universität wien

MASTERARBEIT / MASTER'S THESIS

Titel der Masterarbeit / Title of the Master's Thesis

„The ultimate sensitivity in dark matter direct detection experiments in the presence of an anomalous neutrino source"

verfasst von / submitted by

Marco Nikolic BSc

angestrebter akademischer Grad / in partial fulfilment of the requirements for the degree of

Master of Science (MSc)

Wien, 2019 / Vienna, 2019

Studienkennzahl lt. Studienblatt / degree programme code as it appears on the student record sheet:	A 066 876
Studienrichtung lt. Studienblatt / degree programme as it appears on the student record sheet:	Masterstudium Physik UG2002
Betreut von / Supervisor:	Mag. Dr. Josef Pradler
Mitbetreut von / Co-Supervisor:	

Acknowledgements

At this point, I would like to thank the people who worked with me and supported me during my master thesis. I worked with brilliant scientists.

First of all, I would like to thank my supervisor Josef Pradler at the High Energy Physics Institute (HEPHY), who gave me the opportunity to write my master thesis in dark matter and to publish a paper about the research and results obtained during my thesis. I learned a lot about the universe and different strategies to answer the question of discovering the mysterious dark matter. He has many exciting ideas to solve various problems. I am grateful for the valuable discussions. I also want to thank Walter Grimus for useful explanations about neutrinos.

Special thanks go to Suchita Kulkarni for useful and interesting discussions. She also supervised me during my master thesis and motivated me to understand the neutrino floor. I enjoyed working with her and it was funny. I could always ask her questions, which we discussed in detail. She supported me in applying for my PhD and I learned how to become a good scientist. Furthermore, I would like to thank Wolfgang Waltenberger, who explained to me the statistics needed for my thesis. I attended his course at the University of Technology and extended my knowledge of using statistical methods. I would also like to thank my mates in my office Lukas Matzi, Gerhard Ungersbäck, Lukas Semmelrock, Jui-Lin Kuo and Xiaoyong Chu (other office) who helped me and discussed with me when I had problems to solve. Lukas Semmelrock also proofread parts of my thesis.

Special thanks go to Christiane Schulze. I am grateful for the funny time, and I want to apologize for the times when I was an annoying person to her and especially when I didn't notice it. She helped me in many things, in particular, proofreading my thesis and useful discussion in solving exercises. Finally, I am grateful that my girlfriend and my family motivated and supported me unconditionally.

Abstract

Besides dark matter, the universe may be filled in significant number with a new form of relativistic particles, dark radiation, that have escaped detection to date. One way to look for such particles is by searching for nuclear recoil events in direct detection experiments, where dark matter particles, e.g WIMPs elastically scatter off target nuclei. As is well known, Standard Model neutrinos - also a form of dark radiation - constitute an irreducible background in these searches, ultimately limiting the increase of sensitivity to dark matter in these experiments. This sensitivity limit is termed "neutrino-floor" in the literature. In this work we analyse the sensitivity to dark matter when additional anomalous sources of dark radiation in form of neutrinos are present. Such dark radiation is assumed to be produced from dark matter decays. Since dark radiation may mimic dark matter signals in direct detection experiments, we perform our analysis based on likelihood statistics and hypothesis testing that allows to test the discrepancy between signals and backgrounds. We show that the neutrino floor for xenon-based experiments may be lifted by several orders of magnitude in the presence of extra dark radiation. Assuming that an additional neutrino source produced by a progenitor with mass $m_X = 1$ GeV and a lifetime $\tau_X = 10$ Gyr exists, the neutrino floor is raised by up to four orders of magnitude.

In addition, we explore the sensitivity with respect to neutrino dark radiation from dark matter decay in the presence of Standard Model neutrinos in direct detection experiments. For instance, atmospheric neutrinos may mimic dark radiation with a progenitor mass $m_X = 242$ MeV and a lifetime $\tau_X = 10^5$ Gyr. Given the previous bounds from neutrino experiments, such as Super-Kamiokande, we find that xenon-based dark matter searches with exposures less than 1 ton yr will not be able to probe new regions of the dark matter progenitor mass and lifetime parameter space.

Zusammenfassung

Neben der Dunkler Materie könnte es eine weiter Quelle relativistischer Teilchen im Universium geben - die sogenannte dunkle Strahlung - die bisher nicht entdeckt wurde. Eine Möglichkeit, solche Teilchen zu finden, ist die Suche nach nuklearen Rückstoßereignissen in direkten Detektionsexperimenten, wo Dunkle Materie-Teilchen, z.B. WIMPs, elastisch an Atomkernen streuen. Neutrinos aus dem Standardmodell, die auch eine Form der dunklen Strahlung darstellen, bilden allerdings einen irreduziblen Hintergrund in diesen Experimenten und begrenzen daher die Sensitivität gegenüber der Dunklen Materie. Diese Grenze wird in der Literatur als "neutrino floor" bezeichnet. In dieser Arbeit analysieren wir die Sensitivität der Dunklen Materie-Experimenten, wenn eine zusätzliche anomale Quelle an dunkler Strahlung in Form von Neutrinos vorhanden ist. Dazu nehmen wir an, dass diese dunkle Strahlung aus der Dunklen Materie erzeugt wird. Da dunkle Strahlung Dunkle Materie-Signale in direkten Detektionsexperimenten imitieren kann, führen wir Analysen durch, die auf Likelihood-Statistik und Hypothesen-Tests basieren. Dies ermöglicht uns, die Diskrepanz zwischen Signalen und Hintergründen zu testen. Wir zeigen, dass der "neutrino floor" für Experimente, die Xenon als Detektormaterial verwenden, bei Anwesenheit von dunkler Strahlung um mehrere Größenordnungen angehoben werden kann. So hebt z.B. eine zusätzliche Neutrinoquelle, die von Dunklen Materie-Teilchen mit einer Masse von $m_X = 1$ GeV und einer Lebensdauer von $\tau_X = 10$ Gyr produziert wird, den "neutrino foor" um bis zu vier Größenordnungen.

Darüber hinaus untersuchen wir die Sensitivität von direkten Detektionsexperimenten gegenüber einer solchen dunklen Neutrinostrahlung in Gegenwart von Neutrinos aus dem Standardmodell. So können beispielsweise atmosphärische Neutrinos Signale der dunklen Neutrinostrahlung mit einer Dunklen Materie-Masse von $m_X = 242$ MeV und einer Lebensdauer von $\tau_X = 10^5$ Gyr imitieren. Angesichts der bisherigen Grenzen von Neutrinoexperimenten, wie Super-Kamiokande, stellen wir fest, dass Xenon-basierte Dunkle-Materie-Experimente mit Expositionen unter 1 ton yr nicht in der Lage sein werden, neue Regionen im Parameterraum von Dunkler Materiemasse und Lebensdauer zu untersuchen.

Contents

1 Introduction

In the 20th century the relativistic quantum theory of particles and their interactions were established. Quantum field theory (QFT) predicts the physics of particles and their phenomena at a high precision. One of the best examples is the theory predicted anomalous magnetic moment of electrons, which includes QED, electroweak and hadronic contributions [1–3]

$$\begin{aligned} a_e^{\mathrm{SM}} &= a_e^{\mathrm{QED}} + a_e^{\mathrm{ew}} + a_e^{\mathrm{had}} \\ &= 1\,159\,652\,181.643(25)_{\alpha^4}(23)_{\alpha^5}(16)_{\mathrm{ew+had}}(763)_{\alpha(Rb)} \cdot 10^{-12}, \end{aligned} \tag{1.1}$$

where the respective contributions are given by

$$\begin{aligned} a_e^{\mathrm{QED}} &= 1\,159\,652\,179.908(25)_{\alpha^4}(23)_{\alpha^5}(763)_{\alpha(Rb)} \cdot 10^{-12}, \\ a_e^{\mathrm{ew}} &= 0.0297(5) \cdot 10^{-12}, \\ a_e^{\mathrm{had}} &= 1.706(15) \cdot 10^{-12}. \end{aligned} \tag{1.2}$$

The predicted value is in very good agreement with the experimental value [4]

$$a_e^{\mathrm{exp}} = (1\,159\,652\,180.73 \pm 0.28) \cdot 10^{-12}, \quad a_e^{exp} - a_e^{SM} = 0.822(813) \cdot 10^{-12}. \tag{1.3}$$

Given the success of QFT in the theory description of phenomena, it is generally expected that the Standard Model (SM) is not complete. The last extension of the SM was achieved in 2012. A new particle was discovered by ATLAS [5] and CMS [6], called the Higgs-boson. Its measured mass is $126.0 \pm 0.4(\mathrm{stat}) \pm 0.4(\mathrm{syst.})$ GeV (ATLAS) and $125.3 \pm 0.4(\mathrm{stat.}) \pm 0.5(\mathrm{syst.})$ GeV (CMS). The corresponding theory was formulated long years ago in 1964 by Peter W. Higgs [7] alongside others (Robert Brout, François Englert [8], Gerald Guralnik, Carl R. Hagen and Tom Kibble [9, 10]), who predicted the existence of Higgs bosons as a consequence of spontaneous symmetry breaking (SSB) of gauge groups. Later, the Higgs mechanism was applied to the electroweak theory by Steven Weinberg [11] and Abdus Salam [12]. Although many questions were answered by the introduction of the Higgs Boson, many problems in physics remain unsolved and may be explained by several theories beyond the SM. In this thesis, we focus on dark matter, in particular, on WIMPs (weakly interacting massive particles), that predicts massive stable particles, that are described by QFT.

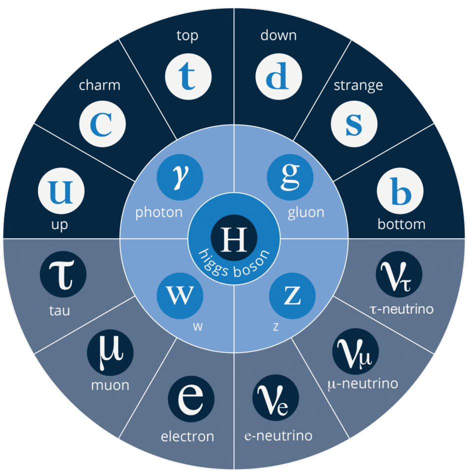

Figure 1: The Standard Model particle content. The blue shaded circle contains the scalar Higgs boson in the center and the four vector bosons surrounding it. The black and grey shaded regions contain quarks and the leptons, which come in six flavors (figure taken from [13]).

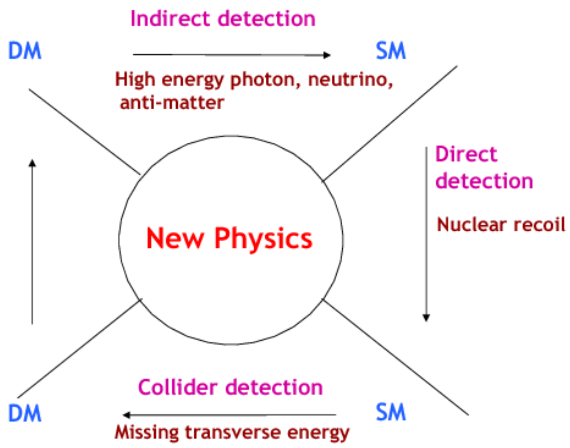

Figure 2: Three different types of DM detection. The direct detection experiments are focused on nuclear recoils, the indirect detection experiments on DM annihilation products and the collider detection experiments on missing energy (figure taken from [14]).

WIMPs are thermally produced in early times of the universe and were in thermal equilibrium with SM particles via annihilation channels $\chi\chi \to$ SM SM and vice versa [15, 16]. With higher expansion rate the universe cooled down and annihilations were less likely until WIMPs decoupled completely from the thermal bath of SM particles at temperatures $T_f = \frac{m_\chi}{20}$, where m_χ is the WIMP mass. Due to the in GeV-scale mass, WIMPs decoupled early enough in the early universe such that their velocity redshift implies that WIMPs today fall into the category of cold dark matter (CDM) with an average velocity $v_\chi \sim 0.3c$.

Today's observations indicate that DM particles formed haloes around galaxies and interact with baryonic matter mainly via gravitational forces. Measurements of velocity curves of stars in galaxies indicate that the gravitational attraction of the additional mass from DM counteracts the centrifugal force of objects within the galaxy. Without DM no rotating galaxy of this form would ever exist and the universe would not have evolved the way we see it today. DM does not couple to photons (except with possible minute charge, "millicharged" DM [17–20]), but are able to interact through the weak force.

The search of DM divides into three categories as illustrated in Fig. 2: direct detection experiments, indirect detection experiments and collider detection experiments. Direct detection experiments are used to measure nuclear recoils of DM particles [21]. They elastically scatter off a target nuclei, e.g. xenon or germanium and produce recoils of few keV. Indirect detection experiments are focused on measuring annihilation products from DM annihilations, in particular, gamma rays, neutrinos and charged leptons travelling through the milky way galaxy [22]. The goal of collider detection experiments is to produce DM particles by colliding SM particles. Then, the DM particle can be identified as missing energy in the detector [23]. In this thesis we focus on direct detection experiments, where experiments as XENON1T [24], LUX [25] and CREEST [26] search for nuclear recoils of WIMPs. The ultimate sensitivity of these experiments, the so called "neutrino floor", depends on irreducible backgrounds caused by neutrinos. Neutrinos coming from the sun, Earth's atmosphere and supernovae explosions may mimic the recoil spectra of WIMPs by coherent scattering. This has an influence on interpreting the measured data. In this case, the sensitivity of an experiment is too low, such that neutrinos and WIMPs are no longer distinguishable. Assuming dark radiation (DR) in the form of neutrinos produced by DM decays (DR neutrinos), the additional anomalous neutrino flux should lead to a further decrease of the ultimate sensitivity in a certain WIMP mass range. We use standard hypothesis tests based on likelihood statistics to discover a WIMP signal statistically in the presence of an irreducible neutrino background and put limits on the WIMP-nucleon cross section σ_n. The sensitivity for different WIMP masses is analysed with and without an additional anomalous neutrino flux.

Instead of searching for DM directly in an experiment, we can also analyse DR in the form of neutrinos in direct detection experiments, that are produced by DM decays [27]. The known SM neutrino background (solar, atmospheric and supernova neutrinos) may also mimic recoil rates of DR neutrinos. In order to detect a signal from DR neutrinos, we derive an ultimate sensitivity and put limits on the progenitor's lifetime for sub-GeV DM masses.

2 Dark matter in the universe

2.1 Observation of dark matter in the universe

Dark matter (DM) has to be stable or should have at least a lifetime greater than the age of the universe. Today's observations conclude that DM interacts mainly only gravitational and does not couple to photons with any appreciable strength. Therefore, DM is not observable in the sense that we cannot see it directly, but indirect observations are possible. In 1933 Fritz Zwicky studied velocities of galaxies inside the Coma cluster and observed that the mean density of mass should be 400 times greater than the observable mass density. He concluded that the amount of invisible matter in the universe has to be much larger than the amount of visible matter [28]. Later, in 1969, Vera Rubin discovered that the mass of visible matter in disk galaxies is not compatible with observations of their velocity rotation curves [29]. In the absence of DM and following Newton's theory, galaxies would not exist in the form we observe it today. The circular velocity of matter orbiting in a galaxy is given by equating the centrifugal force F_C with the force of gravitational attraction F_G [30]

$$F_C = \frac{Mv^2}{r} \stackrel{!}{=} G\frac{mM}{r^2} = F_G \quad \Rightarrow \quad v(r) = \sqrt{G\frac{m(r)}{r}}, \tag{2.1}$$

$$m(r) = \int d^3x\, \rho\,(|\vec{x}\,|) = 4\pi \int_0^r d^3r' \rho(r')\, r'^2, \quad r \equiv |\vec{x}\,|, \tag{2.2}$$

where r is the radial distance from the center, $G \approx 6.67408(31) \cdot 10^{-11}\ \mathrm{m^3kg^{-1}s^{-2}}$ [31] is the Newton's constant, $m(r)$ is the rotating mass and $\rho(r)$ is the mass density depending on the distance r. Measurements of velocity rotation curves imply a galaxy containing invisible matter with a mass density profile $\rho(r) \sim r^{-2}$. A typical example is the disk galaxy M33 [32], which has a radius of about 10 kpc. Typical radii of disk galaxies in the optical range are r_{opt} = 10-60 kpc. Contributions from the stellar disk are not sufficient to explain the observed data as shown in Fig. 3. Therefore, DM has to be introduced. The simplest possible distribution of DM is in the form of a spherical symmetric halo. Further observations indicate, that the observed circular velocity is approximately constant at large radii $r \gtrsim r_{opt}$ (outside the optical range r_{opt}). Therefore, the total mass scales as $m(r) \sim r$, which leads to a mass density profile $\rho(r) \sim r^{-2}$ for $r \gtrsim r_{opt}$. Further observations of DM were successfully achieved by gravitational lensing of galaxies [33, 34] and cosmic microwave background (CMB) measurements [35].

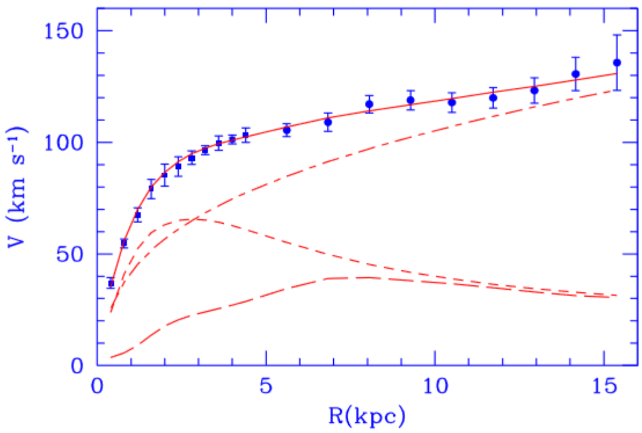

Figure 3: The 21−cm rotation curve of the galaxy M33 represented for radii up to ≈ 16 kpc. The data of M33 is fitted by the velocity curve in [32]. The halo contribution is represented by the dashed-dotted line, the stellar disk by the short-dashed line and the gas contribution by the long-dashed line (figure taken from [32]).

2.2 Dark matter density profile

There exist different DM density profiles [36] characterizing cold dark matter in a halo. For large radii, we already know that the DM density profiles should scale as $\rho(t) \sim r^{-2}$ as shown in Fig. 4. The commonly used profile is the NFW profile constructed by Navarro, Frenk and White [37] via N-body simulations of the formation of galactic halos and galaxy clusters. It is spherical symmetric with a DM density profile given as

$$\rho_{\mathrm{NFW}}(r) = \frac{\rho_s}{\frac{r}{r_s}\left(1+\frac{r}{r_s}\right)^2}, \tag{2.3}$$

where the scaling radius $r_s = 24.42$ kpc and the scaling density $\rho_s = 0.184\ \mathrm{GeV/cm^3}$ are determined by the N-body simulations. In fact, the NFW profile behaves in the correct way for large radii

$$r \ll r_s \ \Rightarrow\ \rho_{\mathrm{NFW}}(r) \sim r^{-1}, \quad r \gg r_s \ \Rightarrow\ \rho_{\mathrm{NFW}}(r) \sim r^{-2}. \tag{2.4}$$

Defining a halo in which the average density is 200 times larger than the critical density ρ_{crit}, the virial radius is obtained by $r_{200} = c\, r_s$ [37, 38]. The parameter c is called the "concentration parameter". In a spherical symmetric halo, the total mass can be derived in two ways. The DM density profile can be integrated over the radius

$$\begin{aligned} M &= 4\pi \int_0^{r_{200}} \rho(r)\, r^2 dr = 4\pi\rho_s r_s^3 \left[\ln\left(\frac{r_s + r_{200}}{r_s}\right) - \frac{r_{200}}{r_s + r_{200}}\right] \\ &= 4\pi\rho_s r_s^3 \left[\ln\left(\frac{1+c}{r_s}\right) - \frac{c}{1+c}\right] \end{aligned} \tag{2.5}$$

or using

$$M = V\rho = \frac{4\pi}{3} r_{200}^3 200 \rho_c. \tag{2.6}$$

Then, the scaling density ρ_s can be expressed as

$$\rho_s = \frac{200}{3} \frac{c^3 \rho_{\mathrm{crit}}}{\left[\ln\left(\frac{1+c}{r_s}\right) - \frac{c}{1+c}\right]} \tag{2.7}$$

comparing the Eq. (2.5) with Eq. (2.6).

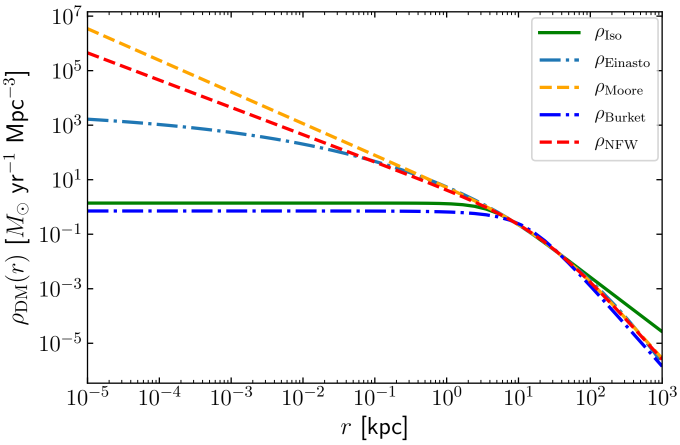

Figure 4: Various models of DM density profiles [36].

2.3 The ΛCDM-model

Assuming a homogeneous, isotropic universe on large scales the amount of cold dark matter in the universe can be approximated by the density parameters Ω obtained from the Friedmann equations [16, 39–41] (derivation of Friedmann equations are given in the App. A)

$$\frac{\dot{a}(t)^2 + K}{a(t)^2} - \frac{\Lambda}{3} = \frac{8\pi G}{3}\rho(t), \qquad \textbf{(1st Friedmann equation)} \tag{2.8}$$

$$\frac{\ddot{a}(t)}{a(t)} = -\frac{4\pi G}{3}\left(3p(t) + \rho(t)\right) + \frac{\Lambda}{3}, \qquad \textbf{(2nd Friedmann equation)} \tag{2.9}$$

where the first Friedmann equation (2.8) is the $((\mu, \nu) = (0, 0))$ component of the Einstein equations using Friedmann Robertson Walker metric (A.1). This is known as the ΛCDM-model, where the cosmological constant $\Lambda \approx 4.33 \cdot 10^{-66}$ eV^2 [42] was first introduced by Einstein as a counterpart of expansion of the universe. Today, Λ characterizes the vacuum energy (known as dark energy) and accounts for the expansion of the universe. The energy density $\rho(t)$ is composed of densities of matter and radiation

$$\rho = \rho_M + \rho_R, \tag{2.10}$$

where $\rho_M = \rho_b + \rho_{\text{cdm}}$ (baryons and cold dark matter), $\rho_R = \rho_\gamma + \rho_\nu$ (photons and neutrinos) plus further contributions in the early universe. The first Friedman equation can then be written in terms of the Hubble constant $H(t) = \frac{\dot{a}(t)}{a(t)}$

$$H^2 = H_0^2\left(\frac{\rho_R}{\rho_{\text{crit}}} + \frac{\rho_M}{\rho_{\text{crit}}} + \frac{\rho_\Lambda}{\rho_{\text{crit}}}\right) - \frac{K}{a^2}, \tag{2.11}$$

where H_0 represents the Hubble constant at present time $t_0 \approx 13.7$ Gyr [43], $\rho_{\text{crit}} = \frac{3H_0^2}{8\pi G}$ is the critical density and $\rho_\Lambda = \frac{\Lambda}{8\pi G}$ is the constant energy density. The last term characterizes the spatial curvature

- $K = +1$ closed sphere,
- $K = 0$ flat,
- $K = -1$ hyperboloid.

Table 1: Different measurements of the Hubble parameter H_0 at present time (table taken from [44]). The Hubble constant H_0 at the present time should be a fixed value and is measured by many collaborations using different techniques. The measurements depend on the cosmological model and all assumptions about the early universe. One of the most successful models is the ΛCDM-model used by Planck collaboration.

H_0 [km/s/Mpc]	method
67.37 ± 0.54	Planck18 [45]
73.48 ± 1.66	Local ladder [46]
70^{+12}_{-8}	GW [47]
68.5 ± 3.5	CC14 [48]
68.5 ± 2.9	CC18 [49]
71.0 ± 2.8	GCs [44]
69.3 ± 2.7	low-met stars [44]

It is convenient to rewrite Eq. (2.11) in terms of density parameters

$$H^2 = H_0^2 \left(\Omega_{R,0}\, a^{-4} + \Omega_{M,0}\, a^{-3} + \Omega_{K,0}\, a^{-2} + \Omega_{\Lambda,0}\right) \tag{2.12}$$

using the evolution of energy densities $\rho_R(t) = \rho_{R,0}\, a^{-4}$, $\rho_M(t) = \rho_{M,0}\, a^{-3}$, $\rho_K(t) = \rho_{K,0}\, a^{-2}$ and $\rho_\Lambda(t) = \rho_{\Lambda,0}$. The index "0" denotes the parameter given at present time t_0. Then, the density parameters at present time [50] are given by

$$\begin{aligned}
\Omega_{M,0} &= \frac{\rho_{M,0}}{\rho_{\text{crit}}} = 0.308 \pm 0.012, \quad \Omega_{R,0} = \frac{\rho_{R,0}}{\rho_{\text{crit}}} = 5.38(15) \cdot 10^{-5}, \\
\Omega_{\Lambda,0} &= \frac{\rho_{\Lambda,0}}{\rho_{\text{crit}}} = 0.692 \pm 0.012, \quad \Omega_{K,0} = -\frac{K}{H_0^2} = 0 \pm 0.02
\end{aligned} \tag{2.13}$$

and characterize the content of the universe. Taking Eq. (2.12) at time t_0 the density parameters satisfy $\Omega_{R,0} + \Omega_{M,0} + \Omega_{K,0} + \Omega_{\Lambda,0} = 1$ ($a(t_0) = 1$), which reduces approximately to $\Omega_{M,0} + \Omega_{\Lambda,0} = 1$ for a matter dominated universe. Cold dark matter at the present time makes up approximately 25.8% of the content of the universe

$$\Omega_{\text{cdm}} = \Omega_{M,0} - \Omega_{b,0} = 0.258(11) \approx 25.8\%, \tag{2.14}$$

where $\Omega_{b,0} = \frac{\rho_{b,0}}{\rho_{\text{crit}}} \approx 0.0484(10)$ is the baryon density [50].

3 WIMP as a dark matter candidate

Observations of the universe confirm that there should exist particles, that have to fulfil specific requirements to explain the phenomenon of DM. A good dark matter candidate should be electrically neutral, its lifetime has to be greater then the age of the universe and its relic density should be close to relic density of the ΛCDM model (2.14) [51]. One of the simplest and most promising DM models predicts particles, which were in a full thermal equilibrium with SM particles and were coupled together. At some point during the radiation dominated era, these DM particles decoupled from the SM particles and cooled down. This is known as the "thermal freeze out". The evolution of the DM number density is obtained by the Boltzmann equation.

3.1 The time evolution of the number density of DM

Let $V = \mathbb{R}^3$ be a vector space over a field $F = \mathbb{R}$ and $\vec{x}, \vec{v}$ be elements of V. Then, the Boltzmann equation[1] describes the evolution of the phase-space density function $f(\vec{x}, \vec{v})$ of a particle species χ. The probability of finding a particle at $\vec{x}$ with velocity $\vec{v}$ in a volume $d^3x \times d^3v$ is given by [52]

$$f_\chi(\vec{x}, \vec{v})\, d^3\vec{x}\, d^3\vec{v} \tag{3.1}$$

with the probability condition

$$\int_v \int_x f_\chi(\vec{x}, \vec{v}) d^3\vec{x}\, d^3\vec{v} = 1. \tag{3.2}$$

If collisions are taken into account, then the Boltzmann equation is given by

$$L[f] = C[f], \tag{3.3}$$

where $C[f]$ is the collision operator [52], which characterizes the interactions between particles. It accounts for the increase and decrease of the number of particles per phase space volume [15]. The Liouville operator $L[f]$ governs the free time evolution of the phase-space density function

$$L[f] = \frac{df}{dt} = \frac{\partial f}{\partial t} + v^\alpha \frac{\partial f}{\partial x^\alpha} + F^\alpha \frac{\partial f}{\partial v^\alpha} \tag{3.4}$$

in the classical non-relativistic limit with $\dot{x}^\alpha = v^\alpha$, $\dot{v}^\alpha = F^\alpha$. The relativistic version of the Liouville operator [16] is given by

$$L[f(p)] = p^\alpha \frac{\partial f}{\partial x^\alpha} - \Gamma^\alpha_{\beta\gamma} p^\beta p^\gamma \frac{\partial f}{\partial p^\alpha}, \tag{3.5}$$

where $p = (t, \vec{p})$ is the four-momentum vector. Applying the transformation $(t, \vec{p}) \to (t, E)$ the Liouville operator for the FRW metric (A.1) can be expressed as

$$L[f(t, E)] = E\frac{\partial}{\partial t} - H|\vec{p}|^2 \frac{\partial f}{\partial E}. \tag{3.6}$$

The number density is given by integrating the phase space density over all momenta and summing over all spins

$$n_\chi(t) = \int dn = \frac{g_\chi}{(2\pi)^3} \int d^3\vec{p}\, f(t, E), \tag{3.7}$$

where g_χ are spin degrees of freedom [15]. Then, by virtue of partial integration, the left-hand side of the Boltzmann equation can be written as

$$\frac{g_\chi}{(2\pi)^3} \int d^3\vec{p}\, \frac{L[f(t, E)]}{E} = \frac{dn_\chi}{dt} + 3Hn_\chi. \tag{3.8}$$

First, consider only two-body annihilation channels $A + B \to 1 + 2$ and vice versa, where A, B are DM particles $\chi, \bar{\chi}$ and $1, 2$ represent SM particles $\phi, \bar{\phi}$. In the end, all annihilation channels will sum

[1] This chapter follows mainly the calculations of P. Gondolo and G. Gelmini [15].

up [53]. The right-hand side of the Boltzmann equation, i.e. the collision operator integrated over the phase space for the reaction $A + B \to 1 + 2$ is given by [15, 16]

$$\begin{aligned}\frac{g_\chi}{(2\pi)^3}\int d^3\vec{p}\,\frac{C[f(t,E)]}{E} &= -\sum_{\text{spins}}\int \frac{d^3\vec{p}_A}{(2\pi)^3 2E_A}\frac{d^3\vec{p}_B}{(2\pi)^3 2E_B}\frac{d^3\vec{p}_1}{(2\pi)^3 2E_1}\frac{d^3\vec{p}_2}{(2\pi)^3 2E_2}\\ &\times (2\pi)^4\delta^{(4)}(p_A+p_B-p_1-p_2)\\ &\times \Big[|M_{AB\to 12}|^2 f_A f_B(1\pm f_1)(1\pm f_2) - |M_{12\to AB}|^2 f_1 f_2 (1\pm f_A)(1\pm f_B)\Big]\,,\end{aligned} \tag{3.9}$$

where $|M_{AB\to 12}|^2, |M_{12\to AB}|^2$ are invariant matrix elements. The sign $(+)$ is taken for bosons and $(-)$ for fermions. In a thermal equilibrium, the phase space distribution of fermions and bosons is given by

$$f(E) = \frac{1}{e^{(E-\mu)/T}\pm 1}, \tag{3.10}$$

where $(-)$ represents bosons and $(+)$ fermions. In the classical limit, the effects of Bose condensation and Fermi degeneracy are neglected. The statistical mechanical factors $(1\pm f_i)\sim 1$, and the Fermi/Bose distribution reduces to the Maxwell-Boltzmann distribution for low temperatures $T < (E-\mu)$

$$f(E) = \frac{1}{e^{(E-\mu)/T}\pm 1} \quad\xrightarrow{\text{classical limit}}\quad f(E) = \frac{1}{e^{(E-\mu)/T}}. \tag{3.11}$$

If all particles are in a thermal equilibrium, i.e. in a kinetic equilibrium and in a chemical equilibrium, then energy conservation $E_A + E_B = E_1 + E_2$ and $\mu_A + \mu_B = \mu_1 + \mu_2$ can be used to replace the densities $f_1 f_2$ by densities at equilibrium of the DM particles (the principle of detailed balance [15])

$$f_1 f_2 = f_1^{eq} f_2^{eq} = \frac{1}{e^{((E_1+E_2)-(\mu_1+\mu_2))/T}} = \frac{1}{e^{((E_A+E_B)-(\mu_A+\mu_B))/T}} = f_A^{eq} f_B^{eq}. \tag{3.12}$$

It is necessary to assume that the SM particles go quickly into the thermal equilibrium. Thus, the collision term reduces to

$$\begin{aligned}\frac{g_\chi}{(2\pi)^3}\int d^3\vec{p}\,\frac{C[f(t,E)]}{E} &= -\sum_{spins}\int \frac{d^3\vec{p}_A}{(2\pi)^3 2E_A}\frac{d^3\vec{p}_B}{(2\pi)^3 2E_B}\frac{d^3\vec{p}_1}{(2\pi)^3 2E_1}\frac{d^3\vec{p}_2}{(2\pi)^3 2E_2}\\ &\times (2\pi)^4\delta^{(4)}(p_A+p_B-p_1-p_2)\Big[|M_{AB\to 12}|^2 f_A f_B - |M_{12\to AB}|^2 f_1 f_2\Big]\\ &= -\sum_{spins}\int \frac{d^3\vec{p}_A}{(2\pi)^3 2E_A}\frac{d^3\vec{p}_B}{(2\pi)^3 2E_B}\frac{d^3\vec{p}_1}{(2\pi)^3 2E_1}\frac{d^3\vec{p}_2}{(2\pi)^3 2E_2}\\ &\times (2\pi)^4\delta^{(4)}(p_A+p_B-p_1-p_2)\Big[|M_{AB\to 12}|^2 f_A f_B - |M_{12\to AB}|^2 f_A^{eq} f_B^{eq}\Big]\,.\end{aligned} \tag{3.13}$$

The integral over the momenta $\vec{p}_1$, $\vec{p}_2$ can now be performed independent of the phase space densities

$$\sum_{spins}\int \frac{d^3\vec{p}_1}{(2\pi)^3 2E_1}\frac{d^3\vec{p}_2}{(2\pi)^3 2E_2}(2\pi)^4\delta^{(4)}(p_A+p_B-p_1-p_2)|M_{AB\to 12}|^2 = 4F\, g_A\, g_B\, \sigma_{AB\to 12}, \tag{3.14}$$

where $F = \sqrt{(p_A\cdot p_B)^2 - m_A^2 m_B^2}$ is the flux factor, g_A, g_B are the spin degeneracy parameters and $\sigma_{AB\to 12}$ is the annihilation cross section. The unitarity condition [15] implies that the matrix element $|M_{AB\to 12}|^2 = |M_{12\to AB}|^2$ and $\sigma = \sigma_{AB\to 12} = \sigma_{12\to AB}$. The definition of the Møller velocity [54] $v_{\text{Møl}} := F/(E_A\, E_B)$ allows to express the Boltzmann equation (3.3) in a compact from

$$\frac{dn_\chi}{dt} + 3Hn_\chi = -\int \sigma v_{\text{Møl}}\,(dn_A dn_B - dn_A^{eq} dn_B^{eq}) = -\int \sigma v_{\text{Møl}}\left(dn_\chi dn_{\bar\chi} - dn_\chi^{eq} dn_{\bar\chi}^{eq}\right). \tag{3.15}$$

The term $v_{\text{Møl}} n_\chi n_\chi$ is Lorentz invariant [15] and the Møller velocity in the comoving frame can be expressed as

$$v_{\text{Møl}} = \sqrt{|\vec{v}_A - \vec{v}_B|^2 - |\vec{v}_A \times \vec{v}_B|^2} \tag{3.16}$$

using the relativistic definition of the velocities $\vec{v} = \vec{p}/E$. Then, the Boltzmann equation can be written in terms of the thermally averaged annihilation rate $\langle \sigma v_{\text{Møl}} \rangle$

$$\frac{dn_\chi}{dt} = -3Hn_\chi - \langle \sigma v_{\text{Møl}} \rangle (n_\chi n_{\bar{\chi}} - n_{\chi,eq} n_{\bar{\chi},eq}), \tag{3.17}$$

where

$$\langle \sigma v_{\text{Møl}} \rangle = \frac{\int \sigma v_{\text{Møl}} dn_\chi^{eq} dn_{\bar{\chi}}^{eq}}{\int dn_\chi^{eq} dn_{\bar{\chi}}^{eq}}. \tag{3.18}$$

The first term on the right-hand side of Eq. (3.17) represents the reduction of the number density in time due to the expansion of the universe. The second term reduces the number of DM particles, because they annihilate to produce SM particles. The creation of DM particles increases the number density, which is given by the third term [55]. In the thermal bath it is also possible that DM particles annihilate via other annihilation channels, e.g. $\chi\bar{\chi} \to$ final state, where the final state does not necessarily have to be a two-body state as before [16]. Fortunately, cross sections of all annihilation channels appearing in the Boltzmann equation (3.3) add together. Therefore, the Boltzmann equation is written in terms of the total annihilation cross section $\sigma_A = \sum_{\substack{\text{final} \\ \text{states}}} \sigma_{AB \to \text{final state}}$

$$\frac{dn_\chi}{dt} = -3Hn_\chi - \langle \sigma_A v_{\text{Møl}} \rangle (n_\chi^2 - n_{\chi,eq}^2), \tag{3.19}$$

where no antimatter asymmetry is assumed $n_\chi = n_{\bar{\chi}}$, if the chemical potential μ is very small. The simplified Boltzmann equation (3.19) characterizes the time evolution of the number density of DM particles, which were once in a thermal bath with SM particles. Following [15] the thermally averaged cross section can be simplified analytically by assuming the Maxwell Boltzmann distribution, as discussed before. Then, $\langle \sigma_A v_{\text{Møl}} \rangle$ is defined as

$$\langle \sigma_A v_{\text{Møl}} \rangle = \frac{\int d^3p_\chi d^3p_{\bar{\chi}}\, \sigma_A v_{\text{Møl}} e^{-E_\chi/T} e^{-E_{\bar{\chi}}/T}}{\int d^3p_\chi d^3p_{\bar{\chi}}\, e^{-E_\chi/T} e^{-E_{\bar{\chi}}/T}}, \tag{3.20}$$

where $E_\chi, E_{\bar{\chi}}$ are energies of the colliding DM particles. The momentum phase space functional can be rewritten as

$$d^3\vec{p}_\chi d^3\vec{p}_{\bar{\chi}} = (4\pi)|\vec{p}_\chi|^2 d|\vec{p}_\chi|(4\pi)|\vec{p}_{\bar{\chi}}|^2 d|\vec{p}_{\bar{\chi}}|\frac{1}{2} d\cos\theta = (4\pi)|\vec{p}_\chi|E_\chi dE_\chi (4\pi)|\vec{p}_{\bar{\chi}}|E_{\bar{\chi}} dE_{\bar{\chi}} \frac{1}{2} d\cos\theta, \tag{3.21}$$

where θ is the angle between the three-momenta $\vec{p}_\chi$ and $\vec{p}_{\bar{\chi}}$. Using the differential form of the energy-momentum relation $|\vec{p}_\chi| d|\vec{p}_\chi| = E_\chi dE_\chi$ the integral boundary change from $[0, \infty]$ to $[m_\chi, \infty]$ (analogue for the antiparticle $\bar{\chi}$). Further variable transformations change the momentum phase space to (see App. B.1)

$$d^3\vec{p}_\chi d^3\vec{p}_{\bar{\chi}} = (2\pi^2) E_\chi E_{\bar{\chi}} dE_+ dE_- ds, \tag{3.22}$$

where $s = (p_\chi . p_{\bar{\chi}}) = 2m_\chi^2 + 2E_\chi E_{\bar{\chi}} - 2|\vec{p}_\chi||\vec{p}_{\bar{\chi}}| \cos\theta$, $E_+ = E_\chi + E_{\bar{\chi}}$ and $E_- = E_\chi - E_{\bar{\chi}}$. In the calculations above the masses of antiparticles and particles are equal $m_\chi = m_{\bar{\chi}}$.

The integral region transforms again to

$$(2\pi^2) \int_{\sqrt{s}}^{\infty} \int_{-E_-^\star}^{E_-^\star} \int_{4m_\chi^2}^{\infty} dE_+ dE_- ds\, E_\chi E_{\bar{\chi}}, \tag{3.23}$$

where $E_-^\star = \sqrt{1-\frac{4m_\chi^2}{s}}\sqrt{E_+^2 - s}$. Taking all simplifications into account the numerator in Eq. (3.20) is given by

$$\begin{aligned}\int d^3\vec{p}_\chi d^3\vec{p}_{\bar\chi}\,\sigma_A v_{\text{Møl}} e^{-E_\chi/T} e^{-E_{\bar\chi}/T} &= (2\pi^2)\int_{\sqrt{s}}^\infty \int_{-E_-^\star}^{E_-^\star}\int_{4m_\chi^2}^\infty dE_+ dE_- ds\, E_\chi E_{\bar\chi}\sigma_A v_{\text{Møl}} e^{-E_+/T} \\ &= 4\pi^2 \int_{4m_\chi^2}^\infty ds\,\sigma_A F(s)\sqrt{1-\frac{4m_\chi^2}{s}}\int_{\sqrt{s}}^\infty dE_+\, e^{-E_+/T}\sqrt{E_+^2 - s},\end{aligned} \tag{3.24}$$

where $F(s) = v_{\text{Møl}} E_\chi E_{\bar\chi} = \frac{1}{2}\sqrt{s(s-4m_\chi^2)}$ is a function of the mandelstam variable s. The integral over E_+ is performed as follows

$$\int_{\sqrt{s}}^\infty dE_+\, e^{-E_+/T}\sqrt{E_+^2 - s} = s\int_1^\infty dx\, e^{-x\sqrt{s}/T}\sqrt{x^2-1} = T\sqrt{s}K_1\left(\frac{\sqrt{s}}{T}\right) \tag{3.25}$$

using the substitution $x = \frac{E_+}{\sqrt{s}}$ and the modified Bessel function of second kind

$$K_n(z) = \frac{\sqrt{\pi}}{\left(n-\frac{1}{2}\right)!}\left(\frac{1}{2}z\right)^n \int_1^\infty dx\, e^{-z\,x}\left(x^2-1\right)^{n-1/2}. \tag{3.26}$$

Thus, the numerator in Eq. (3.20) is written as

$$\int d^3\vec{p}_\chi d^3\vec{p}_{\bar\chi}\,\sigma_A v_{\text{Møl}} e^{-E_\chi/T} e^{-E_{\bar\chi}/T} = 2\pi^2 T\int_{4m_\chi^2}^\infty ds\,\sigma_A\sqrt{s}(s-4m_\chi^2)K_1\left(\frac{\sqrt{s}}{T}\right). \tag{3.27}$$

The denominator in Eq. (3.20) is derived in a similar way

$$\begin{aligned}\int d^3\vec{p}_\chi d^3\vec{p}_{\bar\chi} e^{-E_\chi/T} e^{-E_{\bar\chi}/T} &= (4\pi^2)\int_{m_\chi}^\infty dE_\chi\, |\vec{p}|_\chi E_\chi e^{-E_\chi/T}\int_{m_\chi}^\infty dE_{\bar\chi}\, |\vec{p}|_{\bar\chi} E_{\bar\chi} e^{-E_{\bar\chi}/T} \\ &= (4\pi^2)\int_{m_\chi}^\infty dE_\chi\, \sqrt{E_\chi^2 - m_\chi^2}E_\chi e^{-E_\chi/T}\int_{m_\chi}^\infty dE_{\bar\chi}\, \sqrt{E_\chi^2 - m_\chi^2}E_{\bar\chi} e^{-E_{\bar\chi}/T}.\end{aligned} \tag{3.28}$$

So the integrals can be solved independently using the substitution $x = E_\chi/m_\chi$ and integrating by parts

$$\begin{aligned}\int_{m_\chi}^\infty dE_\chi\, \sqrt{E_\chi^2 - m_\chi^2}E_\chi e^{-E_\chi/T} &= m_\chi^3\int_1^\infty dx\, x\sqrt{x^2-1}\, e^{-\frac{m_\chi}{T}x} \\ &= \frac{m_\chi^4}{3T}\int_1^\infty dx\,\left(x^2-1\right)^{3/2}\, e^{-\frac{m_\chi}{T}x} = m_\chi^2 T K_2\left(\frac{m_\chi}{T}\right),\end{aligned} \tag{3.29}$$

where $\int dx\, x\sqrt{x^2-1} = \frac{1}{3}\left(x^2-1\right)^{3/2}$. In the end, the denominator can be expressed as

$$\int d^3\vec{p}_\chi d^3\vec{p}_{\bar\chi} e^{-E_\chi/T} e^{-E_{\bar\chi}/T} = \left[4\pi m_\chi^2 T K_2\left(\frac{m_\chi}{T}\right)\right]^2. \tag{3.30}$$

Thus, the thermal average of the annihilation rate per unit density [15] is given by

$$\langle\sigma_A v_{\text{Møl}}\rangle = \frac{\int_{4m_\chi^2}^\infty ds\,\sigma_A\sqrt{s}(s-4m_\chi^2)K_1\left(\frac{\sqrt{s}}{T}\right)}{8m_\chi^4 T K_2^2\left(\frac{m_\chi}{T}\right)}. \tag{3.31}$$

The thermal averaged annihilation rate is not frame independent [15]

$$\langle\sigma_A v_{\text{Møl}}\rangle = \langle\sigma_A v_{\text{lab}}\rangle^{\text{lab}} = \frac{1}{2}\left[1+\frac{K_1^2(x)}{K_2^2(x)}\right]\langle\sigma_A v_{\text{cm}}\rangle^{\text{cm}}, \tag{3.32}$$

where $x = m_\chi/T$, "cm" denotes the center of mass frame and "lab" the lab frame. The fully relativistic and fully non-relativistic cases are obtained for $x \to 0$ and $x \to \infty$. For non-relativistic particles $\langle \sigma_A v_{\text{Møl}} \rangle$ can be expanded as

$$\langle \sigma_A v_{\text{Møl}} \rangle = a_0 + \frac{3}{2} a_1 \, x^{-1} + \frac{15}{8} a_2 \, x^{-2} + \frac{35}{16} a_3 \, x^{-3} + O(x^{-4}). \tag{3.33}$$

3.2 Thermal freeze out

It is useful to work in the comoving frame, where the expansion of the universe is scaled out[2]. Since the entropy density per comoving volume sa^3 is conserved, the yield function (number of particles per comoving volume) as a fraction of the number density n_χ and the entropy density s [16, 53] is introduced

$$Y = \frac{n_\chi}{s}. \tag{3.34}$$

Then, the Boltzmann equation (3.19) is written as

$$\frac{dY}{dt} = -s \, \langle \sigma_A v_{\text{Møl}} \rangle \left(Y^2 - Y_{eq}^2 \right), \tag{3.35}$$

where

$$\frac{dY}{dt} = \frac{d}{dt} \left(\frac{n_\chi a^3}{sa^3} \right) = \frac{1}{sa^3} \left(\frac{dn_\chi}{dt} a^3 + 3 n_\chi a^2 \dot{a} \right) = \frac{1}{s} \left(\frac{dn_\chi}{dt} + 3 H n_\chi \right), \quad sa^3 \approx \text{constant}. \tag{3.36}$$

The density and the entropy in the radiation dominated universe are to good approximation given by

$$\rho_R = \sum_j \rho_j = \frac{\pi^2}{30} g_{\text{eff},\rho}(T) \, T^4, \quad s = \frac{p + \rho_R}{T} = \frac{\frac{1}{3}\rho_R + \rho_R}{T} = \frac{4}{3} \frac{\rho_R}{T} = \frac{2\pi^2}{45} g_{\text{eff,s}} \, T^3, \tag{3.37}$$

where the sum goes over all fermions and bosons of the Standard Model [16, 53]. The effective degrees of freedom are given by

$$g_{\text{eff,s}}(T) = \sum_{\text{i=bosons}} g_i \left(\frac{T_i}{T} \right)^3 + \frac{7}{8} \sum_{\text{i=fermions}} g_i \left(\frac{T_i}{T} \right)^3, \tag{3.38}$$

$$g_{\text{eff},\rho}(T) = \sum_{\text{i=bosons}} g_i \left(\frac{T_i}{T} \right)^4 + \frac{7}{8} \sum_{\text{i=fermions}} g_i \left(\frac{T_i}{T} \right)^4. \tag{3.39}$$

The Hubble constant during the radiation dominated universe is a temperature dependent quantity [53]

$$H^2(T) = \frac{8\pi G}{3} \rho_R = \frac{4\pi^3 G}{45} g_{\text{eff},\rho}(T) T^4. \tag{3.40}$$

Since, the entropy per comoving volume is constant $sa^3 \approx$ constant and $s \propto g_{\text{eff,s}}(T) \, T^3$ the photon temperature can be set in in relation with the expansion constant $a^{-1} \propto T$, if $g_{\text{eff,s}}(T) \approx$ constant. Moreover, one can introduce a new dimensionless variable $x = \frac{m_\chi}{T}$, where the derivative is related to the Hubble constant [53]

$$\frac{dx}{dt} = H(T) x^2 \;\text{ obtained by }\; \frac{d}{dt} \left(a x^{-1} \right) \propto \frac{d}{dt} \left(aT \right) \approx \text{constant}. \tag{3.41}$$

Then, the yield equation (3.35) is transformed to

$$\begin{aligned} \frac{dY}{dx} = \frac{dY}{dt} \frac{dt}{dx} = \frac{dY}{dt} \frac{1}{H(T) x} \quad \Rightarrow \quad \frac{dY}{dx} &= -\frac{s}{H(T) x} \langle \sigma_A v_{\text{Møl}} \rangle \left(Y^2 - Y_{eq}^2 \right) \\ &= -\frac{s \, x}{H(m)} \langle \sigma_A v_{\text{Møl}} \rangle \left(Y^2 - Y_{eq}^2 \right), \end{aligned} \tag{3.42}$$

[2] This chapter follows mainly the calculations of D. G. Cerdeño [53] and the book by E. W. Kolb and M. S. Turner [16].

where $H(m)$ is still temperature depended due to $g_{\text{eff},\rho}(T)$[3] given as

$$H(m) = H(T)\,x^2 = \sqrt{\frac{4\pi^3 G}{45}} g_{\text{eff},\rho}^{1/2}(T)\,m^2 = \sqrt{\frac{4\pi^3}{45}} g_{\text{eff},\rho}^{1/2}(T)\,m^2/m_p \tag{3.43}$$

and $m_p = \sqrt{1/G} \approx 1.022 \cdot 10^{19}$ GeV is the Planck mass. The number density at equilibrium of fully relativistic particles ($E(|\vec{p}\,|) \approx |\vec{p}\,|, T \gg m_\chi$) and fully non-relativistic particles ($E(p) \approx m_\chi + \frac{p^2}{2m_\chi}$, $T \ll m_\chi$) can be expressed as (see App. B.2 for detailed calculation and [56])

$$n_{\chi,eq} = \frac{g}{(2\pi)^3}\int d^3\vec{p}\, f(|\vec{p}\,|) = \begin{cases} \frac{g'}{\pi^2}T^3\zeta(3) & \text{for fully relativistic particles,} \\ g\left(\frac{m_\chi T}{2\pi}\right)^{\frac{3}{2}} e^{-m_\chi/T} & \text{for fully non relativistic particles.} \end{cases} \tag{3.44}$$

where $\zeta(3) \approx 1.202$ is the Riemman's zeta function, $g' = g$ for bosons and $g' = \frac{3}{4}g$ for fermions. For non-relativistic particles there is no distinction between bosons and fermions anymore and the Bose/Fermi distribution can be replaced by the Maxwell distribution ($e^{E/T} \gg 1$ for $T \ll m$)

$$f(E) = \frac{1}{e^{E/T} \pm 1} \quad \rightarrow \quad f(E) = \frac{1}{e^{E/T}} \quad \text{for } T \ll m. \tag{3.45}$$

Then, the yield at equilibrium is given by

$$\begin{aligned} Y_{eq} &= \frac{45}{2\pi^4}\frac{g'}{g_{\text{eff,s}}(T)}\zeta(3) \approx 0.278\frac{g'}{g_{\text{eff,s}}(T)} && \text{for fully relativistic particles,} \\ Y_{eq} &= \frac{45}{2\pi^4}\frac{g'}{g_{\text{eff,s}}(T)}\sqrt{\frac{\pi}{8}}x^{\frac{3}{2}}e^{-m_\chi/T} \approx 0.145\frac{g'}{g_{\text{eff,s}}(T)}x^{\frac{3}{2}}e^{-m_\chi/T} && \text{for fully non relativistic particles} \end{aligned} \tag{3.46}$$

using the definition of the entropy (3.37) and the number density (3.44). It is convenient to rewrite the equation (3.42) in terms of the annihilation rate $\Gamma_A = n_{\chi,eq}\langle\sigma_A v_{\text{Møl}}\rangle$ to analyse the yield in the regions of interest (before, at and after the freeze out). In this case, the yield equation (3.42) is given by [16]

$$\frac{x}{Y_{eq}}\frac{dY}{dx} = -\frac{\Gamma_A}{H(T)}\left[\left(\frac{Y}{Y_{eq}}\right)^2 - 1\right]. \tag{3.47}$$

The solutions of this equation are strongly dependent on the ratio $\Gamma_A/H(T)$. Before the freeze out, particles are in a thermal kinetic equilibrium. In this case, particles are more likely to find a partner to annihilate, because the distance between them is small enough and the temperature is very high. This implies that the ratio $\Gamma_A/H(T) \gtrsim 1$. During the expansion, when the Hubble constant increases, the universe cools down and the annihilation becomes less likely, $\Gamma_A/H(T) \lesssim 1$. At the point, where annihilation is approximately equal to the Hubble constant, $\Gamma_A/H(T) \sim 1$, the particles freeze out at a certain temperature $T = T_f$ or equivalently $x = x_f$ and decouple from the thermal bath. Therefore, each particle species decouples from the thermal bath at a different temperature T. The yield function of particles, which are still relativistic after the freeze out, is time independent and depends only on the temperature $T = T_f$, when these particles decouple [53]. Thus, their yield is a constant function after the freeze out [53] and is given by the yield at equilibrium evaluated at $T = T_f$

$$Y \approx Y_{eq} \approx 0.278\frac{g'}{g_{\text{eff,s}}(T = T_f)}. \tag{3.48}$$

The abundance of relativistic particles today is obtained by

$$n_{\text{rel},\infty} = Y_\infty s_\infty \approx Y_{eq}s_\infty = 825.66\frac{g'}{g_{\text{eff,s}}(T = T_f)}\text{cm}^{-3}, \tag{3.49}$$

[3] More precisely, it depends only on the decoupling temperature T_f.

where $Y_\infty \equiv Y(x \to \infty) \approx Y_{eq}$ is the yield and $s_\infty = 2970\,\text{cm}^{-3}$ is the entropy density at present time. Then, the relic density at present time is expressed as

$$\Omega h^2 = \frac{\rho}{\rho_{crit}} h^2 = \frac{m n_{rel,\infty}}{\rho_{crit}} h^2 = \frac{m s_\infty Y_\infty}{\rho_{crit}} h^2, \tag{3.50}$$

where $h = 0.704$ is related to the Hubble constant. Particles with low mass, e.g. neutrinos decouple at a temperature T_f ~MeV [16, 53]. In the case of one neutrino flavor $\nu, \bar{\nu}$, the relic density is obtained by

$$\Omega_{\nu\bar{\nu}} h^2 = \frac{m_R s_\infty Y_\infty}{\rho_{crit}} h^2 \approx \frac{m_\nu}{91.5\text{eV}}, \tag{3.51}$$

where $g' = 2 \cdot (3/4)$, $g_{\text{eff,s}}(T \sim \text{MeV}) = 10.75$ and $\rho_{crit} = 1.054 \cdot 10^{-5} h^2$ GeV cm^{-3} [16]. Applying the cosmological bound $\Omega h^2 \leq 1$, the mass of a neutrino is bounded above

$$m_\nu \leq 91.5 eV. \tag{3.52}$$

Today's experiments reached even smaller upper bounds of neutrino masses $\sum_{i=1}^{3} m_{\nu_i} < 0.15$ eV [57]. For the fully non-relativistic case, a new parametrization is introduced $\Delta_Y = Y - Y_{eq}$ to solve the Boltzmann equation easier [53]. Before the freeze out occurs ($m \ll T \ll T_f$ or $1 \ll x \ll x_f$) the yield is approximately the yield at equilibrium [53]

$$Y \approx Y_{eq} = 0.145 \frac{g'}{g_{\text{eff,s}}(T)} x^{\frac{3}{2}} e^{-m/T}. \tag{3.53}$$

Therefore, $d\Delta_Y/dx = 0$ and

$$\Delta_Y = -\frac{H(m)}{s\,x\,\langle \sigma_A v_{\text{Møl}} \rangle} \frac{\frac{dY_{eq}}{dx}}{2Y_{eq}}. \tag{3.54}$$

At freeze out ($x = x_f$) the Eq. (3.54) reduces to

$$\Delta_Y = \frac{H(m)}{2s\,x_f\,\langle \sigma_A v_{\text{Møl}} \rangle} = \frac{x_f^2}{2\lambda \langle \sigma_A v_{\text{Møl}} \rangle}, \quad \lambda = 0.26 \frac{g_{\text{eff,s}}(T)}{g_{\text{eff},\rho}^{1/2}(T)} m_p m, \tag{3.55}$$

where $\frac{\lambda}{x^2} = \frac{s\,x}{H(m)}$ and $\frac{dY_{eq}}{dx} = -Y_{eq}$ for large x [53]. After the freeze out ($x \gg x_f$) the yield does not match anymore with the yield at equilibrium, $Y \gg Y_{eq}$ ($\Delta_Y \approx Y$), which implies that the yield difference at $x \to \infty$ is given by $\Delta_{Y_\infty} \approx Y_\infty$. Then the Boltzmann equation can be expressed as

$$\frac{d\Delta_Y}{dx} \approx -\frac{s\,x}{H(m)} \langle \sigma_A v_{\text{Møl}} \rangle \Delta_Y^2 = \frac{\lambda}{x^2} \langle \sigma_A v_{\text{Møl}} \rangle \Delta_Y^2. \tag{3.56}$$

This differential equation can be solved by separation of variables

$$\int_{\Delta_{Y_f}}^{\Delta_{Y_\infty}} \frac{d\Delta_Y}{\Delta_Y^2} = \lambda \int_{x_f}^{\infty} \frac{\langle \sigma_A v_{\text{Møl}} \rangle}{x^2} dx. \tag{3.57}$$

Using the first order terms of the expanded annihilation rate (3.33) leads to

$$\Delta_{Y_\infty} \approx Y_\infty = \frac{x_f}{\lambda \left(a_0 + \frac{3}{4} \frac{a_1}{x_f} \right)}, \tag{3.58}$$

which implies an abundance of non relativistic particles today

$$n_{non\,rel,\infty} = Y_\infty s_\infty = \frac{s_\infty\, x_f}{\lambda \left(a_0 + \frac{3}{4} \frac{a_1}{x_f} \right)} = 2970 \frac{x_f}{\lambda \left(a_0 + \frac{3}{4} \frac{a_1}{x_f} \right)} \text{cm}^{-3}. \tag{3.59}$$

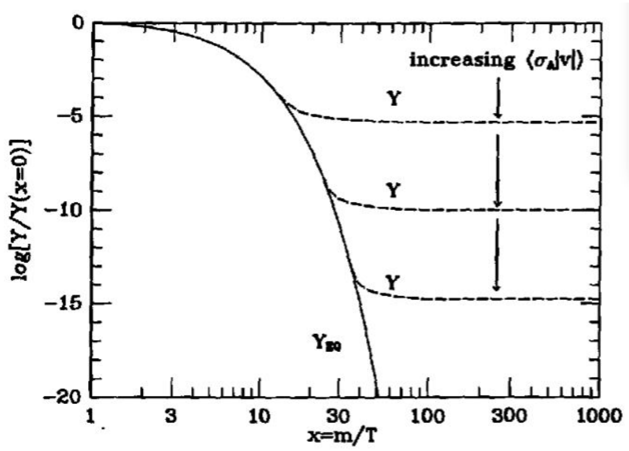

Figure 5: The evolution of the yield for a massive particle. Before the freeze out happens, the yield follows the yield at equilibrium and becomes proportional to the yield at freeze out after decoupling. The yield at equilibrium is suppressed by the Boltzmann factor e^{-x} (figure taken from [16]).

For a enough good approximation the term $1/\Delta_{Y_f}$ can be neglected [53]. Then, the relic density of non relativistic particles is given by

$$\Omega_{cdm}h^2 = \frac{\rho_{cdm}}{\rho_{crit}}h^2 = \frac{m_\chi n_{non\,rel,\infty}}{\rho_{crit}}h^2 = \frac{m_\chi s_\infty Y_\infty}{\rho_{crit}}h^2 \approx \frac{3\cdot 10^{-27}\text{cm}^3}{a_0 + \frac{3}{80}a_1}. \tag{3.60}$$

Since the yield didn't change since the freeze out the relic density didn't change too, $\Omega_{cdm}h^2 \approx 0.1$. In this case the yield at freeze out is approximated by

$$0.1 \approx \Omega_{cdm}h^2 = \frac{m_\chi Y_f s_0 h^2}{\rho_{crit}} \;\Leftrightarrow\; Y_f = 0.1\frac{\rho_{crit}}{s_0 h^2}\frac{1}{m_\chi} = 3.55\cdot 10^{-10}\frac{1}{m_\chi}. \tag{3.61}$$

The point x_f is iteratively derived by the freeze out condition $\Gamma_A(x_f) = n_{\chi,eq}\langle\sigma_A v_{\text{Møl}}\rangle \simeq H(x_f)$, which is equivalently to

$$x_f^{1/2}e^{x_f} \simeq \frac{m_\chi m_p}{2\pi^3}\sqrt{\frac{45}{2}}\frac{g}{g_{\text{eff},\rho}^{1/2}(T)}\langle\sigma_A v_{\text{Møl}}\rangle \tag{3.62}$$

using the expressions (3.43) and (3.44) for fully non relativistic particles. Then, the time of the freeze is found to be $x_f = \frac{m}{T_f} \approx 20$ [16,58].

Cold dark matter constitutes of about 26% of our universe. Assuming the correct DM relic density $\Omega_{cdm}h^2 \approx 0.128$ the thermal averaged annihilation rate can approximately as follows [30,53]

$$\Omega_{\text{cdm}}h^2 \approx \frac{3\cdot 10^{-27}\text{cm}^3\text{s}^{-1}}{\langle\sigma_A v_{\text{Møl}}\rangle} \quad\Rightarrow\; \langle\sigma_A v_{\text{Møl}}\rangle \approx 3\cdot 10^{-26}\text{cm}^3\text{s}^{-1}, \tag{3.63}$$

where $h = 0.704$ is related to the Hubble constant. If the thermal averaged annihilation rate is of order of the weak interaction $\langle\sigma_A v_{\text{Møl}}\rangle \approx G_F^2 m_\chi^2$, then the WIMP mass requires to be of order $O(\text{GeV})$ to obtain the correct relic density for cold dark matter today, where $G_F = 1.1663787(6)\cdot 10^{-5}$ GeV^{-2} is the Fermi coupling constant.

3.3 The isothermal DM halo

Assuming that DM gathered around galaxies in in form of a spherical symmetric halo, then the halo is approximated by an isothermal sphere of ideal gas[4]. Observations of the universe prove that

[4] This chapter follows mainly the book by J. Binney and S. Tremaine [41].

Table 2: Summary of important results before, at and after the freeze out of relativistic and non relativistic particles (calculations reproduced from [16, 53, 58]).

		relativistic	non relativistic
	thermal equilibrium		$T >> m_\chi$
before	$\Gamma_A \gtrsim H$	$Y \approx Y_{eq} \approx 0.278 \frac{g'}{g_{\text{eff,s}}(T)}$	$Y \approx Y_{eq} = 0.145 \frac{g'}{g_{\text{eff,s}}(T)} x^{\frac{3}{2}} e^{-m/T}$
freeze out	$n_\chi \approx n_{\chi,eq}$	$n_{\chi,eq} = \frac{g'}{\pi^2} T^3 \zeta(3)$	$n_{\chi,eq} = g \left(\frac{m_\chi T}{2\pi}\right)^{\frac{3}{2}} e^{-m_\chi/T}$
	matter decouples		$T \sim m_\chi/20$
freeze	at $T = T_f$	$Y \approx Y_{eq} \approx 0.278 \frac{g'}{g_{\text{eff,s}}(T)}$	$Y_f = 3.55 \cdot 10^{-10} \frac{1}{m_\chi}$
out	$\Gamma_A \sim H$	$n_{\text{rel},\infty} = 825.66 \frac{g'}{g_{\text{eff,s}}(T)} \text{cm}^{-3}$	$Y \approx Y_{eq}(x_f) = 0.145 \frac{g'}{g_{\text{eff,s}}(T)} x_f^{\frac{3}{2}} e^{-x_f}$
			$n_{\chi,eq}(x_f) = g \frac{m_\chi^3}{(2\pi)^{3/2}} x_f^{-\frac{3}{2}} e^{-x_f}$
	matter completely		$T << m_\chi$
after	decoupled	$Y \approx Y_{eq} \approx 0.278 \frac{g'}{g_{\text{eff,s}}(T)}$	$Y_{non\,rel,\infty} = \frac{x_f}{\lambda\left(a_0 + \frac{3}{4}\frac{a_1}{x_f}\right)}$
freeze out	$\Gamma_A \lesssim H$	$n_{\text{rel},\infty} = 825.66 \frac{g'}{g_{\text{eff,s}}(T)} \text{cm}^{-3}$	$n_{non\,rel,\infty} = 2970 \frac{x_f}{\lambda\left(a_0 + \frac{3}{4}\frac{a_1}{x_f}\right)} \text{cm}^{-3}$

Dark Matter has to be non-relativistic. Therefore, the hydrostatic equilibrium is given by Newtonian physics [41]

$$\frac{dp(r)}{dr} = \frac{k_B T}{m} \frac{d\rho(r)}{dr} = -\rho \frac{d\Phi(r)}{dr} = -\rho(r) \frac{GM(r)}{r^2}, \tag{3.64}$$

where $\Phi(r)$ is the gravitational potential, k_B is the Botzmann-constant, $p(r)$ is the pressure of the gas, T is the temperature of the gas, m is the mass of a particle within the halo, $\rho(r)$ is the mass density within the halo and $M(r)$ is the total mass of the halo sphere characterized by the radius r. The equation (3.64) can then be differentiated by r

$$\frac{d}{dr}\left(r^2 \frac{d \ln \rho(r)}{dr}\right) = -\rho(r) \frac{4\pi G m}{k_B T} r^2 \tag{3.65}$$

using $dM(r)/dr = 4\pi r^2 \rho(r)$. Due to Jean's theorem [59], a steady state solution ($\partial f/\partial t = 0$) of the collisionless Boltzmann equation $L[f] = 0$ (3.4) is given by the integral of motion in a static potential $\Phi(\vec{x})$ depending on the coordinates $(\vec{x}, \vec{v})$, any function

$$f(E) = f\left(\frac{1}{2}|\vec{v}\,|^2 + \Phi(\vec{x})\right) \tag{3.66}$$

solves the collisionless Boltzmann equation, where E is the non-relativistic energy. Indeed, let $I(\vec{x}, \vec{v})$ be an integral of motion, which is constant along any orbit, then

$$\frac{dI(\vec{x}, \vec{v})}{dt} = v^\alpha \frac{\partial I}{\partial x^\alpha} + \frac{dv^\alpha}{dt} \frac{\partial I}{\partial v^\alpha} = v^\alpha \frac{\partial I}{\partial x^\alpha} - \frac{\partial \Phi(\vec{x}\,)}{\partial x^\alpha} \frac{\partial I}{\partial v^\alpha} = 0, \tag{3.67}$$

where $F^\alpha = -\frac{\partial \Phi(\vec{x})}{\partial x^\alpha}$. This equation is equivalent to the collisionless Boltzmann equation for the function $f(\vec{x}, \vec{v})$. Therefore, $f(\vec{x}, \vec{v})$ is an integral of motion. For instance, the non relativistic energy $E = \frac{1}{2}|\vec{v}\,|^2 + \Phi(\vec{x}\,)$ is an integral of motion [59] shown by

$$\frac{dE}{dt} = v^\alpha \frac{dv^\alpha}{dt} + \frac{\partial \Phi(\vec{x}\,)}{\partial x^\alpha} \frac{dx^\alpha}{dt} = v^\alpha F_\alpha + \frac{\partial \Phi(\vec{x}\,)}{\partial x^\alpha} \frac{dx^\alpha}{dt} = v^\alpha \left(-\frac{\partial \Phi(\vec{x}\,)}{\partial x^\alpha}\right) + \frac{\partial \Phi(\vec{x}\,)}{\partial x^\alpha} v^\alpha = 0. \tag{3.68}$$

Define the relative potential and the relative energy as follows

$$\Psi = -\Phi + \Phi_0, \quad \varepsilon = -E + \Phi_0 = \Psi - \frac{v^2}{2}, \quad \Phi_0 = \text{const.} \tag{3.69}$$

where the constant potential is chosen such that $f > 0$ for $\varepsilon > 0$ and $f = 0$ for $\varepsilon \leq 0$ [59]. Then, the relative potential satisfies the Poisson equation [59]

$$\nabla^2\Psi = -4\pi G\rho, \quad \Psi \;\rightarrow\; \Phi_0 \quad \text{for } |\vec{x}\,| \;\rightarrow\; \infty \tag{3.70}$$

Assume a Maxwell-Boltzmann distribution,

$$f(\varepsilon) = \frac{\rho_1}{(2\pi\sigma_v^2)^{3/2}} e^{\varepsilon/\sigma_v^2} = \frac{\rho_1}{(2\pi\sigma_v^2)^{3/2}} e^{(\Psi(r)-\frac{v^2}{2})/\sigma_v^2}, \tag{3.71}$$

where ρ_1 is constant. Then, the density is obtained by integrating over the velocities

$$\rho(r) = \int d^3v\, f(v) = 4\pi \int_0^\infty dv v^2 f(v) = \rho_1 e^{\Psi(r)/\sigma_v^2}, \tag{3.72}$$

which implies $\Psi(r) = \sigma_v^2 \left(\ln\rho(r) - \ln\rho_1\right)$. The Poisson equation of the relative potential $\Psi(r)$ is then written in the form

$$\frac{1}{r^2}\frac{d}{dr}\left(r^2\frac{d\Psi(r)}{dr}\right) = -4\pi G\rho_1 e^{\Psi(r)/\sigma_v^2} \;\Leftrightarrow\; \frac{d}{dr}\left(r^2\frac{d\ln\rho(r)}{dr}\right) = -\frac{4\pi G}{\sigma_v^2} r^2\rho(r). \tag{3.73}$$

It can be solved by the ansatz $\rho = Cr^{-b}$ [41], which results in

$$\rho(r) = \frac{\sigma_v^2}{2\pi G r^2}, \quad \rho(r) \rightarrow \infty \text{ for } r \rightarrow 0. \tag{3.74}$$

This is known as the singular isothermal sphere [41, 59]. The total mass is given by

$$M(r) = \frac{2\sigma_v^2 r}{G}, \quad M(r) \rightarrow \infty \text{ for } r \rightarrow \infty. \tag{3.75}$$

Comparing Eq. (3.65) with Eq. (3.73) the expressions are identical if

$$\sigma_v^2 = \frac{k_B T}{m}, \tag{3.76}$$

which implies that the theory of an isothermal sphere with an ideal gas is set in relation with the collisionless Boltzmann equation through the factor σ_v^2 [41]. Calculating the mean square velocity of the Maxwell Boltzmann equation (3.71), σ_v is identified as a one dimensional velocity dispersion

$$\langle v^2\rangle = \frac{\int d^3v\, v^2 f(v)}{\int d^3v\, f(v)} = \frac{\int_0^\infty dv\, v^4 \exp\left[\left(\Psi(r) - \frac{v^2}{2}\right)/\sigma_v^2\right]}{\int_0^\infty dv\, v^2 \exp\left[\left(\Psi(r) - \frac{v^2}{2}\right)/\sigma_v^2\right]} = 2\sigma_v^2 \frac{\int_0^\infty dx\, x^4 e^{-x^2}}{\int_0^\infty dx\, x^2 e^{-x^2}} = 2\sigma_v^2 \times \frac{3}{2} = 3\sigma_v^2 \tag{3.77}$$

using the substitution $x = \frac{v^2}{2\sigma_v^2}$. Then the mean circular velocity is written as

$$v_0 \equiv \langle v\rangle = \sqrt{G\frac{M(r)}{r}} = \sqrt{2}\sigma_v. \tag{3.78}$$

Assuming that WIMPs gathered around the Milky way galaxy in a spherical symmetric halo, the total mass of the halo and the local DM density are to be $M(r) \sim 10^{12} M_\odot$ and $\rho_s \approx 0.3\,\frac{\text{GeV}}{\text{cm}^3}$ [60]. The halo radius is approximated by

$$M(r) \approx \frac{4\pi}{3}\rho_s r^3 \quad \Rightarrow\; r \approx 100\text{kpc}. \tag{3.79}$$

In this case, the mean velocity of WIMPs in a halo can be estimated by

$$v_0 = \sqrt{G\frac{M(r)}{r}} \approx 200\frac{\text{km}}{\text{s}}, \tag{3.80}$$

which implies a velocity dispersion of $\sigma_v \approx 141$ km/s.

4 Irreducible neutrino background

Experiments always struggle with background events of all forms, e.g. radioactivity, neutrinos or environmental influences. Often these backgrounds are reducible through different techniques, e.g. shielding with various materials or the difference in time of signals. However, background in form of neutrinos is not reducible, because they interact only weakly with matter in the sense, that the cross section is very small. Neutrinos are leptons with 3 flavors ν_e, ν_μ, ν_τ, which undergo only weak interactions. There exist several neutrino sources. The highest neutrino fluxes on Earth are generated in the sun by fusion processes. Smaller fluxes but highly energetic neutrinos are produced in the atmosphere of the Earth and during the death of a star. Geo- and reactor neutrinos have relatively lower fluxes and can be neglected for the following calculations. All these neutrino sources are grouped in categories indicated by their origin.

4.1 Solar neutrinos

Stars are the main source of neutrinos in the universe[5]. In our solar system, our sun is producing approximately a flux of 10^{11} neutrinos per second and per cm^2. They are produced by fusion processes, where lighter elements fuse into heavier ones [62]. These neutrinos are known as solar neutrinos. Due to the fact, that neutrinos interact extremely weakly, they are able to escape the inner layers of the star. Solar neutrinos are grouped in three pp-chains (ppI,ppII,ppIII) shown in Fig. 6, the CN cycle (I) and the ON cycle (II) shown in Fig. 7. In all of these reactions, energy is released.

In the stellar core, the temperature and density are high enough to start the energy production by fusing protons to deuterium, ^{2}H, mostly by the reaction [61]

$$p + p \quad \rightarrow \quad {}^2\mathrm{H} + e^+ + \nu_e \quad \text{(pp-neutrinos)}\,. \tag{4.1}$$

Alternatively, there is a very small probability that an electron is captured in the proton fusion

$$p + e^- + p \quad \rightarrow \quad {}^2\mathrm{H} + \nu_e \quad \text{(pep-neutrinos)}\,. \tag{4.2}$$

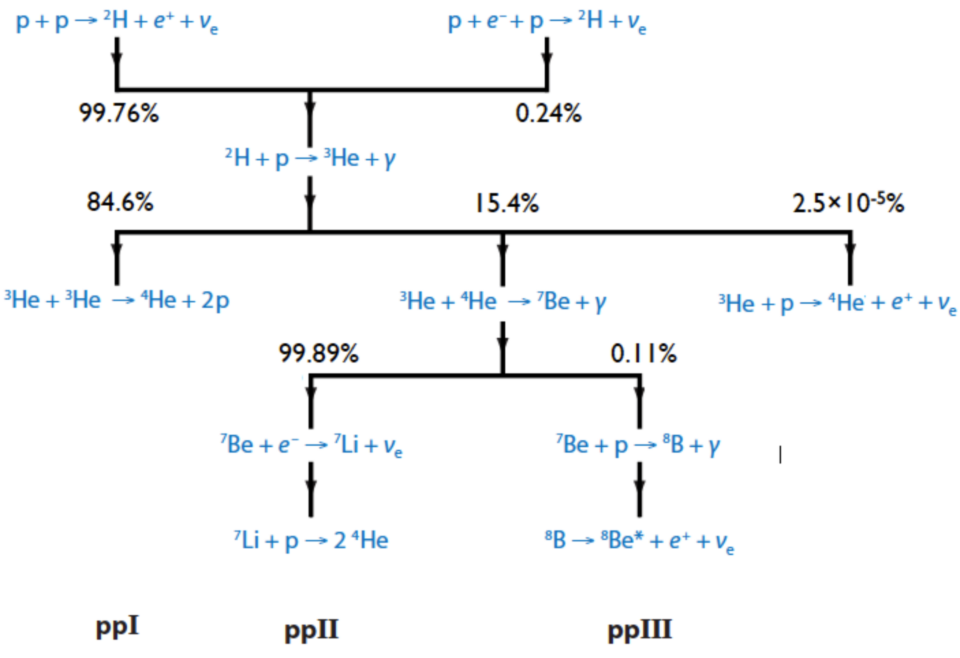

Figure 6: Solar neutrino production in the sun characterized by three chains ppI, ppII, ppIII (figure taken from [63]).

[5] This chapter follows mainly the paper by V. A. Naumov [61].

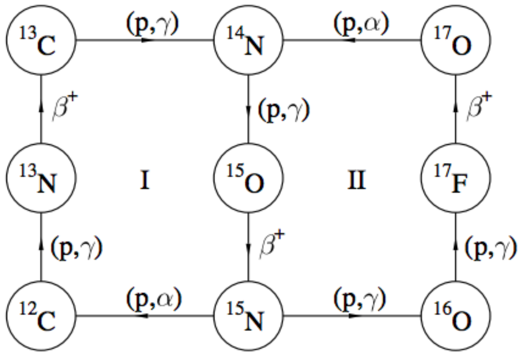

Figure 7: Solar neutrino production in the sun characterized by CN cycle (figure taken from [64]).

In this case, an almost monochromatic neutrino beam is produced with energy smearing caused by Doppler effects and the recoil of the deuteron [61]. The next heavier element, a stable helium isotope ^{3}He is formed by a neutrinoless reaction of deuterium fusion with a proton by

$$^2\mathrm{H} + p \;\; \rightarrow \;\; ^3\mathrm{He} + \gamma. \tag{4.3}$$

The next heavier stable isotope ^{4}He is produced by helium fusion

$$^3\mathrm{He} +^3\mathrm{He} \;\; \rightarrow \;\; ^4\mathrm{He} + 2p, \tag{4.4}$$

which is an additional source for proton fusion. This branch is known as the ppI chain. In the ppII chain helium fusion can also create beryllium via

$$^3\mathrm{He} +^4\mathrm{He} \;\; \rightarrow \;\; ^7\mathrm{Be} + \gamma. \tag{4.5}$$

If a beryllium nucleus captures an electron, lithium is produced and monochromatic neutrinos with two energies 861.3 keV and 384.3 keV are emitted

$$^7\mathrm{Be} + e^- \;\; \rightarrow \;\; ^7\mathrm{Li} + \nu_e \quad \left(^7\mathrm{Be}\ 861.3\ (384.3)\text{-neutrinos}\right). \tag{4.6}$$

The highest energy release is given by lithium proton fusion, which forms first an unstable beryllium isotope ^{8}Be and immediately decays into two ^{4}He

$$^7\mathrm{Li} + p \;\; \rightarrow \;\; ^8\mathrm{Be} \;\; \rightarrow \;\; ^4\mathrm{He} +^4\mathrm{He}. \tag{4.7}$$

The energy release from reactions of ppII chain is comparable with the energy release from reactions of ppI chain for stars with high masses, because the internal temperature is high enough to drive up the production of helium isotopes ^{4}He by fusion of ^{3}He cores [61]. In stars with low masses the fusion of helium cores is less possible due to the low internal temperature. The occurrence of the ppIII chain is less probable than the ppII chain. With a probability of 0.11% beryllium nuclei fuse with protons to form boron by

$$^7\mathrm{Be} + p \;\; \rightarrow \;\; ^8\mathrm{B} + \gamma. \tag{4.8}$$

Neutrinos are emitted by β^+-decays of boron

$$^8\mathrm{B} \;\; \rightarrow \;\; ^8\mathrm{Be}^* + e^+ + \nu_e \quad \left(^8\mathrm{B}\text{-neutrinos}\right) \tag{4.9}$$

with an endpoint neutrino energy of 14.02 MeV. The excited beryllium nucleus $^8\mathrm{Be}^*$ decays again into helium isotopes

$$^8\mathrm{Be}^* \;\; \rightarrow \;\; ^4\mathrm{He} +^4\mathrm{He}. \tag{4.10}$$

The last branch on the right side of Fig. 6 is sometimes called the ppIV chain and contains only one reaction

$$^{3}\mathrm{He} + p \;\rightarrow\; ^{4}\mathrm{Li} \;\rightarrow\; ^{4}\mathrm{He} + e^{+} + \nu_e \quad \text{(hep-neutrinos)}\,, \tag{4.11}$$

where neutrinos are produced. Electron neutrinos are also produced by β^{+}-decays in the CNO cycle (I+II) by the following reactions

$$^{13}\mathrm{N} \;\overset{\beta^{+}}{\rightarrow}\; ^{13}\mathrm{C} + e^{+} + \nu_e, \tag{4.12}$$

$$^{15}\mathrm{O} \;\overset{\beta^{+}}{\rightarrow}\; ^{15}\mathrm{N} + e^{+} + \nu_e, \tag{4.13}$$

$$^{17}\mathrm{F} \;\overset{\beta^{+}}{\rightarrow}\; ^{17}\mathrm{O} + e^{+} + \nu_e. \tag{4.14}$$

The CNO cycle is relevant for higher internal temperatures of about $10^{7}\,\mathrm{K}$ [61].

4.2 Atmospheric neutrinos

Atmospheric neutrinos are produced by primary cosmic rays interacting with the atmosphere of the Earth. Cosmic rays, mostly high energy protons (5% are helium cores) collide with nuclei in the atmosphere (see Ref. [65] and Fig. 8). The resulting hadronic showers consist mostly of protons, neutrons, pions and kaons. Atmospheric neutrinos $\nu_\mu, \bar{\nu}_\mu$ and high energy muons $\mu^{\pm}$ are then produced by the decay channels of pions $\pi^{\pm}$ and kaons $K^{\pm}, K^{0}$ [66–68]:

$$\pi^{-} \;\rightarrow\; \mu^{-} + \bar{\nu}_\mu, \qquad \pi^{+} \;\rightarrow\; \mu^{+} + \nu_\mu, \tag{4.15}$$

$$K^{-} \;\rightarrow\; \mu^{-} + \bar{\nu}_\mu, \qquad K^{+} \;\rightarrow\; \mu^{+} + \nu_\mu, \tag{4.16}$$

$$K^{0} \;\rightarrow\; \pi^{-} + \pi^{+}, \quad K^{0} \;\rightarrow\; \mu^{-} + \mu^{+}, \quad K^{0} \;\rightarrow\; e^{-} + e^{+}. \tag{4.17}$$

With a lifetime of 2.19703±0.00004 μs [69] high energy muons decay into muon- and electron-neutrinos:

$$\mu^{-} \;\rightarrow\; e^{-} + \bar{\nu}_\mu + \nu_e, \qquad \mu^{+} \;\rightarrow\; e^{+} + \nu_\mu + \bar{\nu}_e. \tag{4.18}$$

These channels contribute the bulk of neutrino production in the atmosphere. The production of photons and electrons by neutral pion decays $\pi^{0} \;\rightarrow\; \gamma + \gamma$, annihilation channels $\gamma \;\rightarrow\; e^{-} + e^{+}$, bremsstrahlung, kaon decays and Cherenkov light leads to electromagnetic showers. The observed fluxes at Earth are approximately related as follows [66, 70]

$$\frac{\phi(\nu_\mu + \bar{\nu}_\mu)}{\phi(\nu_e + \bar{\nu}_e)} \approx 2, \quad \phi(\nu_\mu) \approx \phi(\bar{\nu}_\mu), \quad \frac{\phi(\nu_e)}{\phi(\bar{\nu}_e)} \approx \frac{\phi(\mu^{+})}{\phi(\mu^{-})}. \tag{4.19}$$

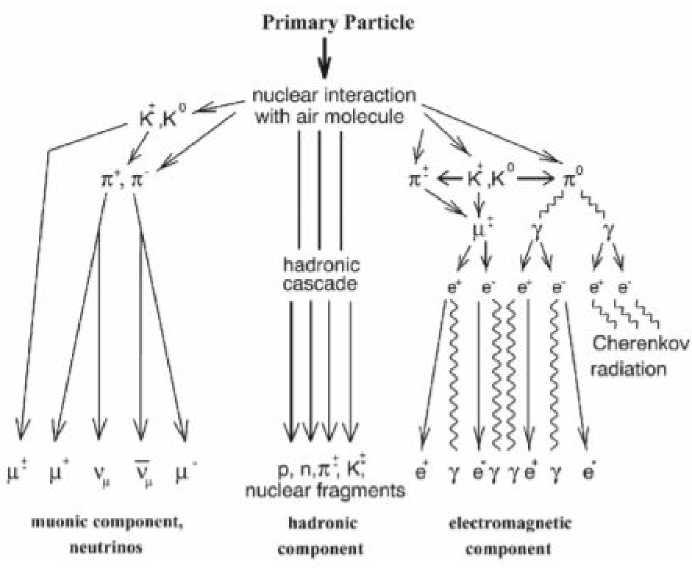

Figure 8: The production of neutrinos in the atmosphere (figure taken from [71]).

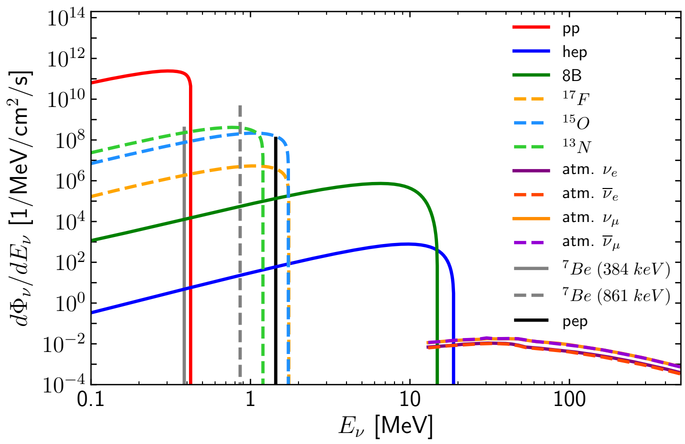

Figure 9: Neutrino fluxes taken from John Bahcall's website [73]. The fluxes for the atmospheric neutrinos are given in [74]. These fluxes can also be approximated by a polynomial of order nine (4.21).

Thus, the amount of neutrinos in the atmosphere is dominated by muon-neutrinos. The amount of tau-neutrinos ν_τ produced in the atmosphere is negligibly small and requires heavy mesons or neutrino oscillation [67]. In the atmosphere also mesons with charm quarks are produced. For instance, D-mesons have a short lifetime and decay immediately into muons and neutrinos. This results in a prompt muon/neutrino flux [72].

4.3 Solar and atmospheric neutrino fluxes

The differential flux of solar and atmospheric neutrinos is given by the differential energy spectrum and its total flux

$$\frac{d\Phi_\nu(E_\nu)}{dE_\nu} = \Phi_\nu \frac{dN_\nu(E_\nu)}{dE_\nu}. \tag{4.20}$$

where the energy spectra of solar neutrinos are taken from John Bahcall's website [73] and the atmospheric fluxes are given in [74]. The fluxes are shown in Fig. 9. An alternative way to obtain the solar neutrino fluxes is to approximate the energy spectrum by a polynomial of order nine [75]

$$\frac{dN_\nu(E_\nu)}{dE_\nu} = \begin{cases} \frac{1}{N}\sum_{k=0}^{8} a_k E_\nu^{k+1} & \text{for } E_\nu < E_\nu^{\max} \\ 0 & \text{for } E_\nu \geq E_\nu^{\max} \end{cases}, \tag{4.21}$$

where $E_\nu^{\max}$ is the maximum energy a neutrino of each type can carry. The normalization constant is given by

$$N = \sum_{k=0}^{8} \frac{1}{k+2} a_k \left(E_\nu^{\max}\right)^{k+2}, \tag{4.22}$$

where the coefficients a_k are taken from the Tab. 3. A negligible small difference between the fitted and measured fluxes in Fig. 9 is noticed in the tail of the ^{8}B neutrinos. The most precise measurement is the pp-flux with an uncertainty of about 0.6% [76] (first reaction in the ppI chain in Fig. 6). The spectra of atmospheric neutrinos are extrapolated for smaller energies. Therefore, a higher uncertainty of 20% is assumed [77]. The total atmospheric neutrino flux is derived by the sum of all four particle spectra and is about $7.3(1 \pm 0.2)$ cm^{-2} s^{-1}. The ^{8}B neutrinos (last reaction in the ppIII chain in Fig. 6) were measured with a high precision by the Sudbury Neutrino observatory (SNO) [78, 79] through three reactions

$$\begin{aligned} &\mathrm{CC}: \nu_e + d \to p + p + e^- - 1.442\,\mathrm{MeV} \\ &\mathrm{NC}: \nu_x + d \to p + n + \nu_x - 2.224\,\mathrm{MeV} \\ &\mathrm{ES}: \nu_x + e^- \to \nu_x + e^- \end{aligned}\;, \tag{4.23}$$

Table 3: The coefficients a_k of the polynomial fit for neutrino fluxes (taken from [75]).

coefficients	pp	hep	^{8}B
a_0[1/MeV]	$-2.87034 \cdot 10^{-1}$	$-2.04975 \cdot 10^{-6}$	$6.01473 \cdot 10^{-4}$
a_1 [1/MeV^2]	$1.63559 \cdot 10^{2}$	$4.22577 \cdot 10^{-3}$	$1.49699 \cdot 10^{-2}$
a_2 [1/MeV^3]	$-1.22253 \cdot 10^{3}$	$-4.70817 \cdot 10^{-4}$	$-2.6481 \cdot 10^{-3}$
a_3 [1/MeV^4]	$1.55085 \cdot 10^{4}$	$2.55332 \cdot 10^{-5}$	$-2.4141 \cdot 10^{-5}$
a_4 [1/MeV^5]	$-1.465140 \cdot 10^{5}$	$-2.81714 \cdot 10^{-6}$	$6.22325 \cdot 10^{-5}$
a_5 [1/MeV^6]	$7.843750 \cdot 10^{5}$	$3.06961 \cdot 10^{-7}$	$-9.84329 \cdot 10^{-6}$
a_6 [1/MeV^7]	$-2.35727 \cdot 10^{6}$	$-1.87479 \cdot 10^{-8}$	$7.51311 \cdot 10^{-7}$
a_7 [1/MeV^8]	$3.71082 \cdot 10^{6}$	$6.01396 \cdot 10^{-10}$	$-2.8606 \cdot 10^{-8}$
a_8 [1/MeV^9]	$2.38308 \cdot 10^{6}$	$-7.88874 \cdot 10^{-12}$	$4.31572 \cdot 10^{-10}$
coefficients	^{17}F	^{15}O	^{13}N
a_0[1/MeV]	$-2.59522 \cdot 10^{-2}$	$-1.36811 \cdot 10^{-2}$	$-6.74473 \cdot 10^{-2}$
a_1 [1/MeV^2]	$1.05228 \cdot 10^{1}$	3.94221	4.63141
a_2 [1/MeV^3]	$-3.2344 \cdot 10^{1}$	-8.55431	$-1.1535 \cdot 10^{1}$
a_3 [1/MeV^4]	$1.33211 \cdot 10^{2}$	$2.36712 \cdot 10^{1}$	$2.85067 \cdot 10^{1}$
a_4 [1/MeV^5]	$-4.11848 \cdot 10^{2}$	$-5.00477 \cdot 10^{1}$	$-5.11664 * \cdot 10^{1}$
a_5 [1/MeV^6]	$7.28405 \cdot 10^{2}$	$6.07542 \cdot 10^{1}$	$5.51102 \cdot 10^{1}$
a_6 [1/MeV^7]	$-7.26105 \cdot 10^{2}$	$-4.15278 \cdot 10^{1}$	$-3.45332 \cdot 10^{1}$
a_7 [1/MeV^8]	$3.8137 \cdot 10^{2}$	$1.49462 \cdot 10^{1}$	$1.1655 \cdot 10^{1}$
a_8 [1/MeV^9]	$-8.21149 \cdot 10^{1}$	-2.20367	-1.62814

where x represents any neutrino flavor ($x = e, \mu, \tau$). Electron neutrinos are only produced in charge current scattering (CC). In neutral current (NC) and neutrino electron elastic scatterings (ES) the total flux of all neutrinos is measured. Following the paper of SNO [78] they obtained the measured ^{8}B fluxes for each reaction

$$\begin{aligned}
\phi_{\mathrm{CC}}^{\mathrm{SNO}} &= 1.59^{+0.08}_{-0.07}(\mathrm{stat})^{+0.06}_{-0.08}(\mathrm{syst}) \cdot 10^6\,\mathrm{cm}^{-2}\,\mathrm{s}^{-1} \\
\phi_{\mathrm{ES}}^{\mathrm{SNO}} &= 2.21^{+0.31}_{-0.26}(\mathrm{stat}) \pm 0.10(\mathrm{syst}) \cdot 10^6\,\mathrm{cm}^{-2}\,\mathrm{s}^{-1} \\
\phi_{\mathrm{NC}}^{\mathrm{SNO}} &= 5.21 \pm 0.27(\mathrm{stat}) \pm 0.38(\mathrm{syst}) \cdot 10^6\,\mathrm{cm}^{-2}\,\mathrm{s}^{-1}\,.
\end{aligned} \tag{4.24}$$

The following calculations take into account an uncertainty of 14% [80] for the ^{8}B neutrinos that concords with the uncertainty of SNO.

Table 4: Neutrino fluxes taken from [80] and the corresponding recoil energies.

	flux Φ_ν [1/cm^2/s]	$E_\nu^{\min}$ [keV]	$E_\nu^{\max}$ [keV]	$E_{R,\nu}^{\max}$ [keV]
pp	$5.98(1 \pm 0.006) \cdot 10^{10}$	5.04	423	$2.94 \cdot 10^{-3}$
hep	$8.04(1 \pm 0.3) \cdot 10^{3}$	18.8	$1.88 \cdot 10^{3}$	5.79
^{17}F	$5.52(1 \pm 0.17) \cdot 10^{6}$	3.48	$1.74 \cdot 10^{3}$	$4.97 \cdot 10^{-2}$
^{15}O	$2.23(1 \pm 0.15) \cdot 10^{8}$	3.46	$1.73 \cdot 10^{3}$	$4.92 \cdot 10^{-2}$
^{13}N	$2.96(1 \pm 0.14) \cdot 10^{8}$	6	$1.20 \cdot 10^{3}$	$2.36 \cdot 10^{-2}$
^{8}B	$5.58(1 \pm 0.14) \cdot 10^{6}$	0	$1.66 \cdot 10^{4}$	4.50
^{7}Be (384 keV)	$4.50(1 \pm 0.07) \cdot 10^{8}$	384.3	384.3	$2.42 \cdot 10^{-3}$
^{7}Be (861 keV)	$5.00(1 \pm 0.07) \cdot 10^{9}$	861.3	861.3	$1.22 \cdot 10^{-2}$
pep	$1.44(1 \pm 0.012) \cdot 10^{8}$	$1.44 \cdot 10^{3}$	$1.44 \cdot 10^{3}$	$3.40 \cdot 10^{-2}$
atm. ν_e	$1.27(1 \pm 0.2)$	$1.30 \cdot 10^{4}$	$9.44 \cdot 10^{5}$	$14.39 \cdot 10^{3}$
atm. $\bar{\nu}_e$	$1.17(1 \pm 0.2)$	$1.30 \cdot 10^{4}$	$9.44 \cdot 10^{5}$	$14.39 \cdot 10^{3}$
atm. ν_μ	$2.46(1 \pm 0.2)$	$1.30 \cdot 10^{4}$	$9.44 \cdot 10^{5}$	$14.39 \cdot 10^{3}$
atm. $\bar{\nu}_\mu$	$2.45(1 \pm 0.2)$	$1.30 \cdot 10^{4}$	$9.44 \cdot 10^{5}$	$14.39 \cdot 10^{3}$
DSNB ν_e	$22.12(1 \pm 0.5)$	0	$\approx 1.0 \cdot 10^{5}$	163
DSNB $\bar{\nu}_e$	$17.69(1 \pm 0.5)$	0	$\approx 1.0 \cdot 10^{5}$	163
DSNB ν_x	$11.06(1 \pm 0.5)$	0	$\approx 1.0 \cdot 10^{5}$	163

4.4 Diffuse supernova neutrino background (DSNB)

"The supernova neutrinos are the dark matter of the neutrino family."

The diffuse supernova neutrino background (DSNB) can be seen as a steady source of all neutrinos and antineutrinos emitted from core collapse supernovae of Type II from the beginning of first stars to today.

Supernova neutrinos were measured directly only in two experiments based on water-Cerenkov detectors, when the blue supergiant Sanduleak-69 202 in the Large Magellanic Cloud exploded in a supernova, which is known as the SN1987A. One of these experiments is Kamiokande-II (Kam-II), which reported 12 neutrino events [81–83]. The second one is the Irvine-Michigan-Brookhaven (IMB) experiment, which reported 8 events [84, 85]. They were actually built to measure proton decays but were also efficient to measure neutrinos by detecting the energy of the electron produced in the inverse beta decay $\bar{\nu}_e + p \to e^+ + n$. The energy of the electron should be close to that of the neutrino

$$E_e = (E_\nu - 1.3\text{MeV})\left(1 - \frac{E_\nu}{m_p}\right) \tag{4.25}$$

where $m_n - m_p \approx 1.3$ MeV and m_p, m_n is the proton mass and neutron mass [86]. In 2012, Super-Kamiokande (SK) set an upper limit for the DSNB flux on electron neutrinos for energies above a threshold of 19.3 MeV [86, 87]

$$\Phi\left(E_\nu > 19.3\text{MeV}\right) \lesssim 1.2\text{cm}^{-2}\text{s}^{-1} \quad (90\% \text{ C.L.}). \tag{4.26}$$

4.4.1 Type II supernova-production of neutrinos

Supernovae are not frequent in our galaxy but very frequent in the universe[6]. Stars with mass less than $8M_\odot$ end up as white dwarfs. The maximum mass of a star that ends as a white dwarf is estimated to be $7.25M_\odot$ [90]. In this case, while helium is fused into carbon the temperature inside the core is not

[6] This chapter follows mainly the book by G. G. Raffelt [89].

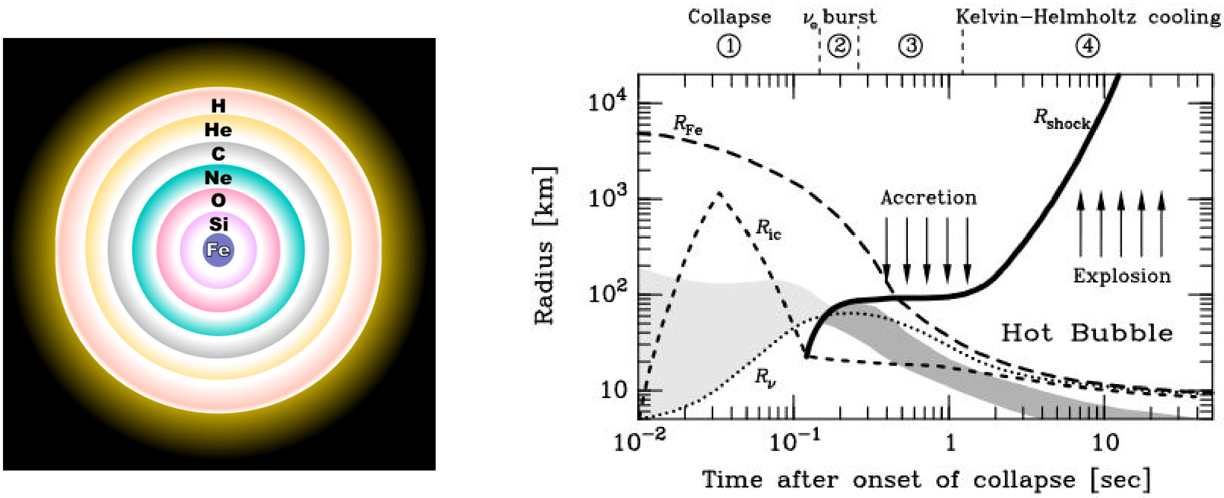

Figure 10: **(left)** Fusion processes in a star that explodes in a Type II supernova (figure taken from [88]). **(right)** 1 core collapse, 2 ν_e burst, 3 protoneutron star mantle cooling and matter accretion, 4 Kelvin-Helmholtz cooling (figure taken from [89]).

high enough to fuse carbon into heavier elements. The core cools down until it becomes the average temperature of the universe. Stars, which exceed this mass limit of $8M_\odot$ explode and produce a large number of neutrinos. This is known as the Type II supernova [91, 92].

Stars fuse hydrogen into helium and release thermal energy. The produced pressure inside the core counteracts the gravity of the star and prevents it from collapsing. Due to low temperatures helium cannot yet be fused to heavier elements. When hydrogen is exhausted, less thermal energy is released and its own gravity contracts the core increasing the temperature again. The fusion of helium to carbon begins. After enough carbon is formed, the star starts to fuse neon into oxygen. Then, it begins to fuse oxygen into silicon and silicon into iron. The core is layered in rings as in Fig. 10, where heavier elements are formed in the center of the core. In each of these fusion processes, thermal energy is released that heats the core up to 10^9 K and keeps the star from collapsing. The inner iron core has a central density of about $3.7 \cdot 10^9$ g cm^{-3}, a temperature $T \approx 0.69$ MeV and approximately an equal number of electrons and baryons $Y_e \approx 0.42$ [89, 93]. When the amount of iron in the core increases, the star begins to fuse iron into cobalt or nickel. However, this fusion process is endothermic and absorbs energy, because iron is the most tight bound nucleus. The core starts to cool down and thermal radiation is no longer released. The consequence is that the star begins to collapse. However, electron degeneracy pressure stops the core from collapsing further. Due to the Pauli exclusion principle, electrons with same the quantum numbers cannot occupy the same state. An enormous pressure builds up against the implosion.

When the mass of the iron core reaches the Chandrasekhar limit of $1.4M_\odot$ electron degeneracy pressure against gravitation can no longer be supported. The core collapses rapidly with a velocity $v/r \sim 400 - 700$ s^{-1}, which is approximately 20% of the speed of light and the temperature increases up to 10^{10} K [89]. The collapse velocity depends on the radius of the core and increases with a higher radius. The core becomes so hot and dense that high energy gamma rays are produced, that destroy iron by photodissociation $\gamma +^{56} Fe \rightarrow 13\alpha + 4n$. This reaction consumes 124.4 MeV of energy, which supports the collapsing process even more. The force of the collapse force electrons to merge with protons and an amount of neutrinos are produced via the inverse beta decay $e^- + p \rightarrow n + \nu_e$. Neutrinos interact very weakly with matter (weakly in the sense that the cross section is very small), but at some point, they can no longer travel freely through the core and are trapped by coherent neutral current scatterings [94] due to high densities in the core and high energies of the neutrinos.

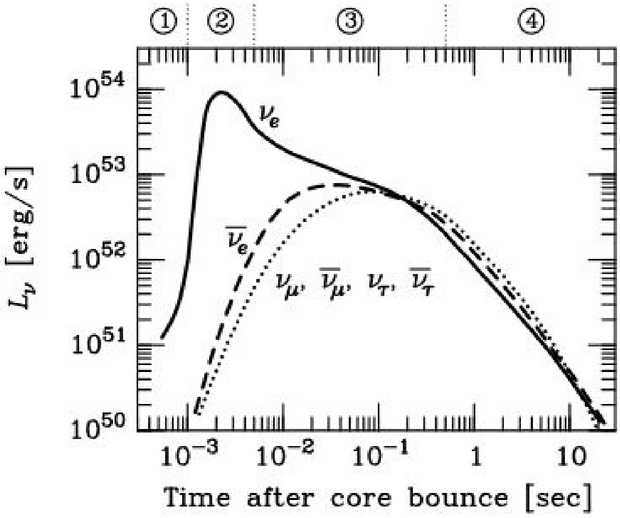

Figure 11: Luminosity of neutrinos emitted during the stages of supernova. 1 core collapse, 2 ν_e burst or shock break out, 3 protoneutron star mantle cooling and matter accretion, 4 Kelvin-Helmholtz cooling (figure taken from [89]).

This sea of neutrinos is known as the neutrino sphere and has a density of about 10^{12} g cm^{-3} for 10 MeV neutrinos [93]. In the neutrino sphere neutrinos are in thermal equilibrium. The lepton number fraction per baryon $Y_L \approx 0.35$ is approximately conserved, because electrons are converted into electron neutrinos and vice versa. If the inner core reaches nuclear density $\rho \approx 3 \cdot 10^{14}$ g cm^{-3} collapsing slows down. The falling material of the outer mantle travels with supersonic speed towards the inner core but slows down within the inner core to subsonic speed [89]. More and more material is gathered around the edge of the inner core. The outer layers bounce onto the inner core and create a shockwave that propagates outward. The shockwave hits the neutrino sphere in a short period of time. As the shockwave propagates trough the neutrino sphere, it dissociates nuclei. Additionally, protons of these dissociated nuclei interact with electrons and produce a big amount of neutrinos by $e^- + p \to n + \nu_e$. Less nuclei and more neutrinos result in the fact, that many neutrinos escape from the neutrino sphere. A prompt ν_e burst or deleptonization burst is released. However, most of the leptons remain trapped.

This shockwave has stored enough energy to blow away the outer parts of the stellar mantle. An explosion known as the supernova occurs. Everything below the shockwave converts to a proton neutron star (PNS). The inner core of the PNS, where the shockwave first formed, consists of proton, neutrons, electrons and neutrinos. It has a lepton number fraction per baryon of about 0.35 [89]. In the outer parts of the PNS many leptons are ejected by the propagation of the shockwave and simultaneously during the deleptonization process. Now the PNS (radius ≈ 30 km) is decoupled from the outer material from the progenitor star. The surface of the PNS cools down slowly. It loses its energy by emitting neutrinos of all flavors as shown in Fig. 11. At the same time, electron neutrinos are released by deleptonization process. After a few seconds the number of leptons within the PNS is reduced to a minimum. This is known as the Kelvin Helmholtz cooling and is responsible for the dominant neutrino emission. The PNS shrinks to a neutron star with a radius of about 10 km as shown in Fig. 10.

4.4.2 DSNB flux

The present number density of DSNB neutrinos with energies $[E_\nu, E_\nu + dE_\nu]$ emitted at redshifts $[z, z + dz]$ is given by [95]

$$\begin{aligned} dn_\nu &= R_{\mathrm{SN}}(z)(1+z)^3\Big|\frac{dt}{dz}\Big|dz\frac{dN}{dE_\nu}\left(E_{\nu,\mathrm{em}}\right)dE_{\nu,\mathrm{em}}(1+z)^{-3} \\ &= R_{\mathrm{SN}}(z)(1+z)\Big|\frac{dt}{dz}\Big|dz\frac{dN}{dE_\nu}\left(E_\nu(1+z)\right)dE_\nu, \end{aligned} \tag{4.27}$$

where

- $E_{\nu,\mathrm{em}} = E_\nu(1+z)$ is the energy at emission and E_ν the energy at observation,
- $R_{\mathrm{SN}}(z)$ is the supernova rate per comoving volume at redshift z,
- $R_{\mathrm{SN}}(z)(1+z)^3$ represents the supernova rate per proper volume at redshift z,
- $\frac{dN}{dE_\nu}\left(E_\nu(1+z)\right)$ is the neutrino spectrum (=neutrino emission per supernova), where neutrinos with energy E_ν were emitted at higher energies $E_\nu(1+z)$,
- the factor $(1+z)^{-3}$ has to be added due to the expansion of the universe,
- the density parameters $\Omega_M \approx 0.3$, $\Omega_\Lambda \approx 0.7$, the Hubble constant $H_0 \approx 70\mathrm{km\,s^{-1}\,Mpc^{-1}}$ and

$$\left|\frac{dt}{dz}\right| = \frac{1}{H(z)} = \frac{1}{H_0(1+z)\sqrt{(1+z)^3\Omega_M + \Omega_\Lambda}} \tag{4.28}$$

  are obtained from Friedman equations.

The DSNB flux measured at the Earth is then written as an integral over redshifts z

$$\frac{d\Phi_\nu}{dE_\nu}\bigg|_{\mathrm{DSNB}} = c\frac{dn_\nu}{dE_\nu} = \frac{c}{H_0}\int_0^{z_{max}} \frac{dz}{\sqrt{(1+z)^3\Omega_M + \Omega_\Lambda}} R_{SN}(z)\frac{dN}{dE_\nu}\left(E_\nu(1+z)\right). \tag{4.29}$$

Assume that the first Type II core collapse supernovae occurred at a redshift $z_{max} \approx 5-6$ [96]. The DSNB flux can be derived in detail similar to the extragalactic flux in Sec. 8.3 replacing $e^{-\Gamma_\lambda t(z)}$ by $R_{\mathrm{SN}}(z)$.

The flux of supernova neutrinos depends strongly on the magnitude and redshift dependence of the core-collapse supernova rate $R_{\mathrm{SN}}(z)$. In the universe the death rate and the birth rate of stars is approximately in equilibrium. Therefore, the supernova rate R_{SN} is obtained from the star formation rate R_{SF} times the fraction of stars in the universe, that end up as Type II core collapse supernovae [86,97]

$$R_{\mathrm{SN}}(z) = R_{\mathrm{SF}}(z)\frac{\int_{8M_\odot}^{50M_\odot}\Psi(m)dm}{\int_{0.1M_\odot}^{125M_\odot}m\Psi(m)dm} \simeq \frac{R_{\mathrm{SF}}(z)}{143M_\odot}, \tag{4.30}$$

where $\Psi(m)$ is known as the initial mass function (IMF), that characterizes the mass distribution of stars in the universe. Due to observations and simulations, the IMF takes the form $\Psi(m) \sim m^n$ (for a Salpeter IMF $n = -2.35$) and is extrapolated for smaller masses [86]. The numerator $\int_{8M_\odot}^{50M_\odot}\Psi(m)dm$ is the number of stars, that end up as a Type II supernova and produce neutrinos. The denominator $\int_{0.1M_\odot}^{125M_\odot}m\Psi(m)dm$ is the total mass in stars in the universe. The lower bound of the upper integral is chosen such that the minimum mass of a star of about $8M_\odot$ is required for a core collapse supernova (the minimum mass $(8.5^{+1}_{-1.5})M_\odot$ is estimated by maximum likelihood analysis [98]). Stars more than $50M_\odot$ collapse immediately to a black hole and no neutrinos are produced. In the lower integral, the smallest star in the universe is assumed to have a minimum mass of about $0.1M_\odot$. The biggest stars have a mass of about $125M_\odot$. There exist few stars with masses above $125M_\odot$, but those can be

cosmic star formation history	$R_{\rm SF}(0)$	α	β	γ
upper	0.0213	3.6	-0.1	-2.5
fiducial	0.0178	3.4	-0.3	-3.5
lower	0.0142	3.2	-0.5	-4.5

Table 5: Analytic fits for a Salpeter IMF [97]. $R_{\rm SF}(0)$ is given in units $[M_\odot\,{\rm yr}^{-1}\,{\rm Mpc}^{-3}]$.

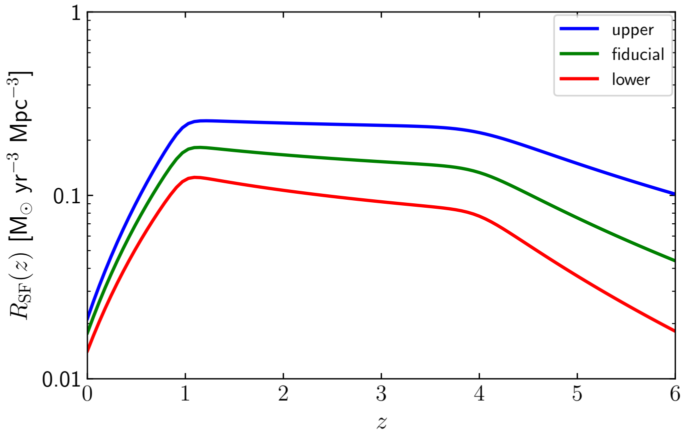

Figure 12: Evolution of the star formation rate density $R_{\rm SF}(z)$ for redshifts z and Salpeter IMF. For redshifts $z < 1$ the ultraviolet data (UV-data) and far-infrared data (FIR-data) are combined due to obscuration of dust. In the region $1 < z < 3$ FIR-data is quite flat and a constant dust correction/FIR-data is added to UV-data (for more details see [99–102]).

neglected. The star formation rate density (SFR) is well measured for low redshifts and can be fitted by an analytic function [97]

$$R_{\rm SF}(z) = R_{\rm SF}(0)\left[(1+z)^{\alpha\eta} + \left(\frac{1+z}{B}\right)^{\beta\eta} + \left(\frac{1+z}{C}\right)^{\gamma\eta}\right]^{1/\eta}, \tag{4.31}$$

where

$$B = (1+z_1)^{1-\alpha/\beta}, \quad C = (1+z_1)^{(\beta-\alpha)/\gamma}\,(1+z_2)^{1-\beta/\gamma} \tag{4.32}$$

with $z_1 = 1$, $z_2 = 4$ as redshift breaks of the SFR density and $\eta = -10$. The analytical fits given in Tab. 5 are shown in the Fig. 12 and characterize an uncertainty width. The uncertainty is greater for higher redshifts due to obscuration of the universe by dust and larger distances. Dust has an effect on the measurements of the luminosity of galaxies in the ultraviolet and optical regions. Therefore, far-infrared data (FIR-data) is added to the observed data in order to determine the SFR density more accurately. The SFR density is well consistent with all observations and constraints in a range $0 < z \lesssim 6$ [99].

The DSNB spectrum can be approximated by a Fermi-Dirac distribution [97,103] (thermal spectrum)

$$\frac{dN}{dE_\nu}(E_{\nu,\rm em}) = \frac{E_\nu^{\rm tot}}{6}\frac{120}{7\pi^4}\frac{(E_{\nu,\rm em})^2}{T_\nu^4}\left(e^{E_{\nu,\rm em}/T_\nu}+1\right)^{-1}, \tag{4.33}$$

where $E_{\nu,\rm em}$ is the neutrino energy at emission and each neutrino and antineutrino carries an equal fraction of the total energy [86,97]

$$E_\nu^{\rm tot} \simeq E_{\rm bind} = 3\times 10^{53}\left(\frac{M_{\rm NS}}{1.4{\rm M}_\odot}\right)^2\left(\frac{R_{\rm NS}}{10{\rm km}}\right)^{-1}{\rm erg}. \tag{4.34}$$

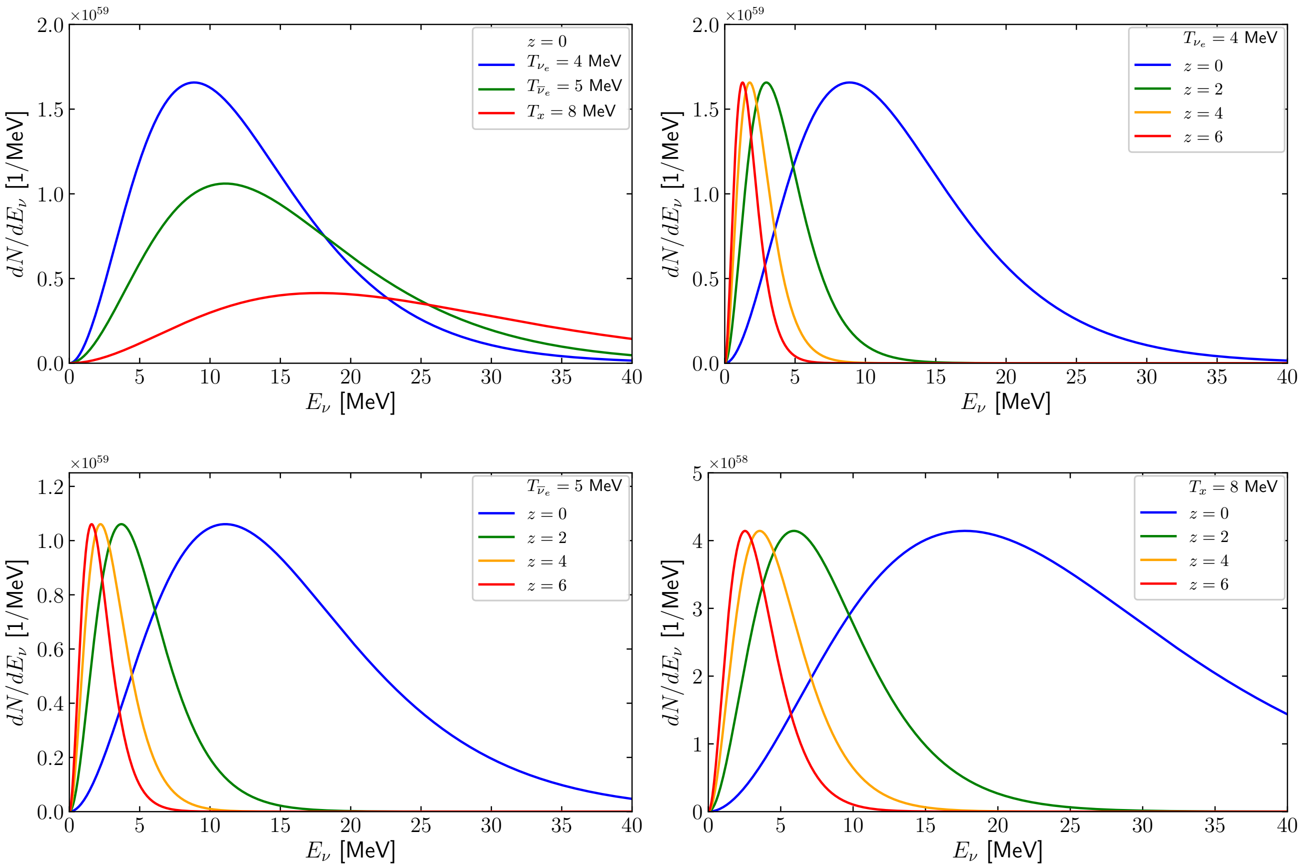

Figure 13: Fermi-Dirac spectra for several redshifts $z = 0, 2, 4, 6$ and for temperatures $T_{\nu_e} \approx 4\,\mathrm{MeV}$, $T_{\bar{\nu}_e} \approx 5\,\mathrm{MeV}$, $T_x \approx 8\,\mathrm{MeV}$ ($x = \nu_\mu, \bar{\nu}_\mu, \nu_\tau, \bar{\nu}_\tau$): The spectra shift to lower energies for higher redshifts and decrease for higher temperatures.

The energy $E_\nu^{\mathrm{tot}}/6$ carried by each neutrino and antineutrino is in good agreement with numerical supernova simulations of the Lawrence Livermore group $E_{\bar{\nu}_e} = 4.7 \cdot 10^{52}\,\mathrm{erg} \approx E_\nu^{\mathrm{tot}}/6$ [104]. The total energy is approximately equal to the gravitational binding energy of the star, because almost all of its gravitational binding energy is converted to high energetic neutrinos. The parameters M_{NS} and R_{NS} are the mass and the radius of a neutron star.

Observationally, the masses of neutron stars M_{NS} may be estimated by observation of X-rays of binaries or radio binary pulsars, where fast rotating neutron stars (pulsars) orbit another neutron star, a white dwarf or a main-sequence star [105]. The measured masses of neutron stars in a binary system, called PSR 1913+16 are $(1.3867 \pm 0.0002)\, M_\odot$ and $(1.4414 \pm 0.0002)\, M_\odot$ [106]. The radius is derived by observations of gravitational waves by LIGO and Virgo [107] detected in 2017 and is estimated to be $(10.8^{+2.0}_{-1.7}\,\mathrm{km})$ and $(10.7^{+2.1}_{-1.5}\,\mathrm{km})$ for two neutron stars colliding in a binary system, where the neutron star with smaller radius has smaller mass. This is in a good agreement with a neutron star with mass $M_{\mathrm{NS}} \approx 1.4 M_\odot$ and radius $R_{\mathrm{NS}} \approx 10\,\mathrm{km}$.

Each neutrino and antineutrino is identified with a certain temperature $T_{\nu_e} \approx 4\,\mathrm{MeV}$, $T_{\bar{\nu}_e} \approx 5\,\mathrm{MeV}$, $T_x \approx 8\,\mathrm{MeV}$ (x denotes the other neutrino flavors $\nu_\mu, \bar{\nu}_\mu, \nu_\tau, \bar{\nu}_\tau$), where the temperature T_{ν_e} is consistent with the upper limit of Super-Kamiokande (see Eq. 4.26 and [86]). The hierarchy $T_{\nu_e} < T_{\bar{\nu}_e} < T_x$ is given by the radii at which the neutrinos decouple. Neutrinos $\nu_\mu, \bar{\nu}_\mu, \nu_\tau, \bar{\nu}_\tau$ decouple at the smallest radius of the protoneutron star and diffuse out with a thermal spectra [108]. The DSNB fluxes and the Fermi-Dirac spectra are shown in Fig. 15 and in Fig. 13. Combining the DSNB fluxes lead to a total flux of about $84(1 \pm 0.5)\ \mathrm{cm}^{-2}\ \mathrm{s}^{-1}$.

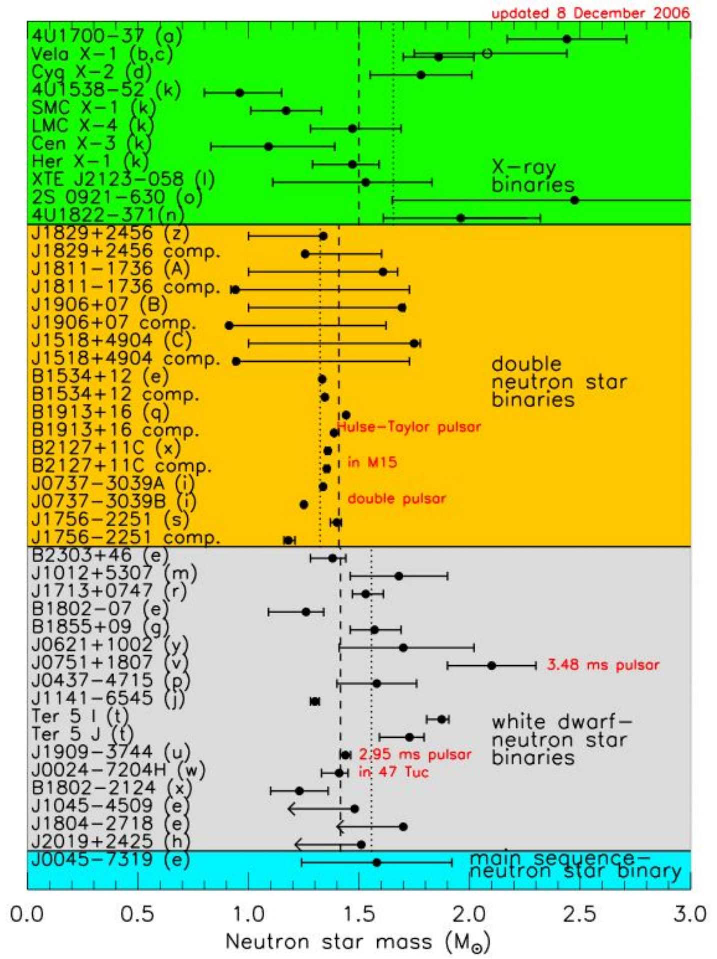

Figure 14: Neutron star mass is estimated by observation of binaries (figure taken from [105]).

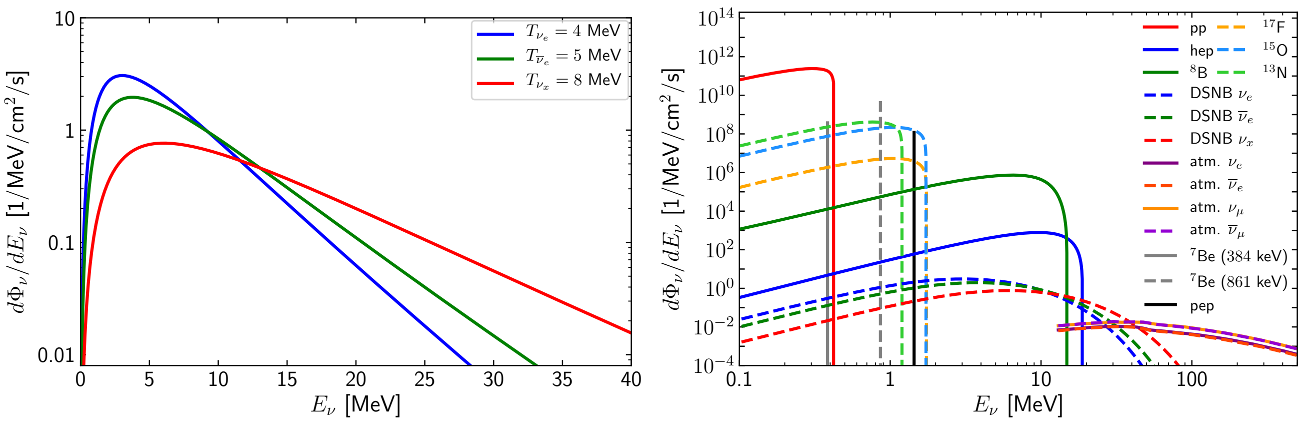

(a) (b)

Figure 15: **(a)** The fluxes of the diffuse supernova neutrino background (DSNB) for temperatures $T_{\nu_e} \approx 4\,\text{MeV}$, $T_{\bar{\nu}_e} \approx 5\,\text{MeV}$, $T_x \approx 8\,\text{MeV}$ ($x = \nu_\mu, \bar{\nu}_\mu, \nu_\tau, \bar{\nu}_\tau$) [86]. **(b)** Neutrino fluxes with diffuse supernova neutrino background (dashed lines: blue, green, red).

5 Detection of neutrinos

In 1930, Wolfgang Pauli postulated a neutral particle [109], which should explain the continuous spectrum of electrons in beta decays[7]. If beta decays are two body decays $n \to p + e^-$, then electrons should have a sharp discrete energy $E_e = \frac{m_n^2 - m_p^2 + m_e^2}{2m_n} \approx 1.29$ MeV. Pauli named the invisible particle neutron, but with the discovery of a more massive neutral particle (today known as the neutron) by James Chadwick in 1932 [111], the postulated particle by Pauli was renamed to neutrino by Enrico Fermi. The existence of neutrinos was confirmed in 1956 by Clyde Cowan and Frederick Reines [112]. They used a reactor to produce a high flux of $\bar{\nu}_e$-neutrinos, that interacted with protons in water tanks and produced positrons and neutrons

$$\bar{\nu}_e + p \quad \to \quad n + e^+. \tag{5.1}$$

The positrons annihilated with electrons and produced gamma rays, which were detected by scintillators. The neutrons were detected by dissolved cadmium in water

$$n +^{108}\mathrm{Cd} \quad \to \quad ^{109\mathrm{m}}\mathrm{Cd} \quad \to \quad ^{109}\mathrm{Cd} + \gamma. \tag{5.2}$$

In the following years many experiments were built to detect all flavors of neutrinos and to explain their interactions with other Standard Model particles. Several techniques are used for neutrino detection [110]:

- radiochemical method,
- method with Cherenkov detectors,
- scintillation technique,
- iron calorimeter (ICAL),
- liquid argon time projection chamber (LArTPC).

5.1 Radiochemical method

In the radiochemical method neutrinos are detected by the inverse beta decay

$$\nu_e +_Z^A X \quad \to \quad e^- +_{Z+1}^A Y, \tag{5.3}$$

where X are target nuclei with atomic mass number/nucleon number A and atomic number/proton number Z. During this reaction neutrons of nuclei X convert to protons and increases the atomic number of produced nuclei Y by one. Experiments, e.g. HOMESTAKE, GALLEX, GNO and SAGE use different target nuclei to measure solar neutrinos. In the HOMESTAKE experiment [113] chlorine was used as the target nucleus, which converts to argon after the interaction with a electron-neutrino

$$\nu_e +_{17}^{37}\mathrm{Cl} \quad \to \quad e^- +_{18}^{37}\mathrm{Ar} \;\; (q = 0.814 \text{ MeV}). \tag{5.4}$$

GALLEX [114] and SAGE [115] exploit the advantage of gallium with which one can achieve very low thresholds of few keV and consider similar reactions

$$\nu_e +_{31}^{71}\mathrm{Ga} \quad \to \quad e^- +_{32}^{71}\mathrm{Ge} \;\; (q = 233 \text{ keV}). \tag{5.5}$$

This allows neutrinos with smaller energies to be observed [110].

[7] This chapter follows mainly the paper by A. Nath and Ng. K. Francis [110].

5.2 Method with Cherenkov detectors

The Cherenkov method [116] is an excellent technique to detect neutrinos. If the phase velocity of a charged particle propagating through a medium (Super-Kamiokande (SK) uses H_2O, Sudbury Neutrino observatory uses heavy water deuterium oxide D_2O [110]) is greater than the speed of light in that medium, then light is emitted in form of a light cone known as Cherenkov cone or Cherenkov light:

$$v > \frac{c}{n}, \tag{5.6}$$

where n is the refractive index ($n \approx 1.33$ for H_2O at room temperature $T \approx 20^\circ$ C). The direction of the radiation related to the flight axis of the propagating particle is given by the Cherenkov angle θ (see Fig. 16a and Ref. [117])

$$\cos\theta = \frac{\overline{AB}}{\overline{AC}} = \frac{\frac{c}{n}\Delta t}{v\Delta t} = \frac{1}{\beta n}, \quad \beta = \frac{v}{c}. \tag{5.7}$$

The maximum angle a particle can reach is obtained if $v = c$ [118]

$$\theta_{\max} = \arccos\left(\frac{1}{n}\right). \tag{5.8}$$

In water the maximum Cherenkov angle is $\theta_{\max}^{H_2O} \approx 41^\circ$. The Cherenkov cone can then be mapped to a two dimensional circle using many photomultiplier-tubes (see Fig. 16b). This technique of Ring-imaging Cherenkov detectors is used in many neutrino experiments [110], e.g. SNO, SK, IceCube, KamLAND, MiniBooNE.

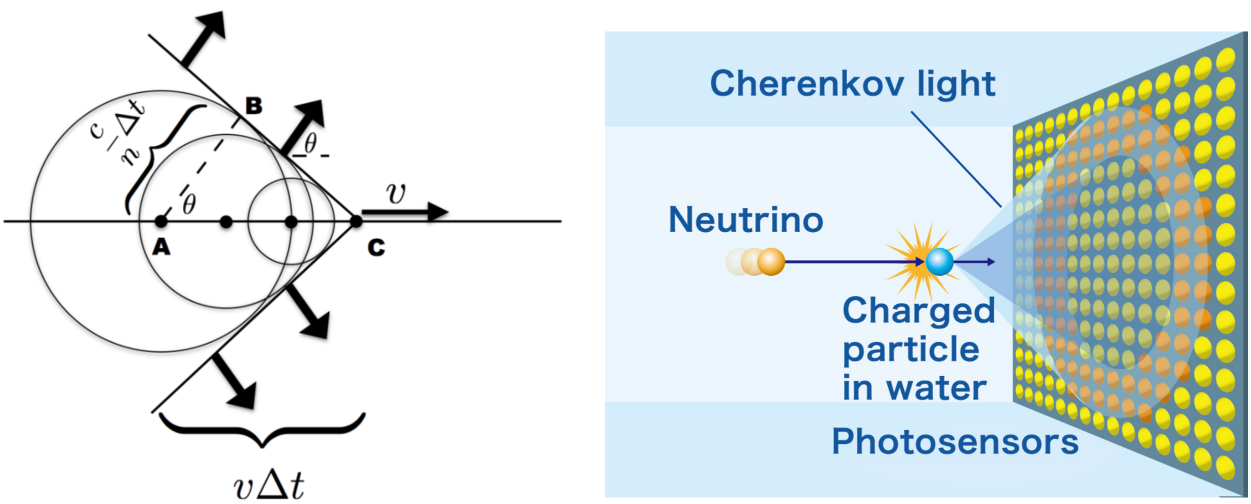

(b)

(a)

Figure 16: **(a)** The Cherenkov cone: The line segment $\overline{AB}$ of emitted light in a medium with index of refraction n is given by $\frac{c}{n}\Delta t$, where Δt is the time. In the same time Δt the particle propagates the line segment $\overline{AC} = v\Delta t$ with velocity v (figure taken from [117]). **(b)** The Cherenkov cone is detected as a ring. The type of particle can be identified by the from of the ring. A propagating electron would produce electromagnetic showers, which lead to fuzzy rings (figure taken from [119]).

5.3 Scintillation technique

Organic or anorganic Scintillators are used to measure charged particles, X-rays or gamma rays. If a particle, X-ray or gamma ray propagates through a scintillator, light is emitted by excitation of the molecules in the scintillator. Mostly, the following three effects contribute to ionization of the scintillator [110]:

1. Photoelectric effect,
2. Compton effect,
3. pair-production.

In each of these processes electrons are produced, which ionize the molecules of the scintillator. This leads to emission of photons. The number of scintillation photons is proportional to the energy deposition of the incoming charged particle, X-ray or gamma ray. Organic scintillators consist mostly of plastic, crystals that are aromatic hydrocarbons containing benzene rings, liquids or polymer solids. Anorganic materials used for scintillators are alkali metal halides, e.g. sodium iodide, alkali halide crystals, e.g. cesium iodide and non-alkali crystals, e.g. barium fluoride or calcium tungstate (scheelite) [120]. Scintillators are used in Borexino, MINOS and KamLAND.

Borexino uses liquid scintillators as target material to study the spectra of solar neutrinos, like hep and ^{8}B neutrinos. Low thresholds also allow the measurements of neutrinos with low energies, e.g, pp, pep, ^{7}Be. The Borexino collaboration considers elastic ν-e^- scatterings

$$\nu_x + e^- \quad \to \quad \nu_x + e^- \quad (x \text{ denotes the three flavors}), \tag{5.9}$$

where free moving electrons produce scintillation light. Liquid scintillators are preferred due to their larger photon yield. The detector KamLAND is a tank filled with pure liquid scintillator studying $\overline{\nu}_e$-disappearance of reactor neutrinos and neutrino oscillations by the reaction

$$\overline{\nu}_e + p \quad \to \quad e^+ + n. \tag{5.10}$$

5.4 Iron calorimeter (ICAL)

A calorimeter measures the energy of a particle that propagates through it [121]. Particles deposit all their energy interacting with the nuclei of the calorimeter and produce particle showers. There are two types of calorimeter which are used in particle physics. One measures particle showers that are produced by electromagnetic interactions. In this case, a lot of electrons, positrons and photons are created by pair-production and bremsstrahlung. The second one measures the hadrons produced by strong interaction. Most of these hadrons are pions. The iron calorimeter belongs to the group of hadronic calorimeters. Neutrinos enter the calorimeter and produce hadrons by interaction with iron nucleons by neutral current (NC) and charge current (CC) [110]

$$\text{NC: } \nu_\mu +^{56}_{26}\text{Fe} \quad \to \quad \nu_\mu + \text{hadrons}, \tag{5.11}$$

$$\text{CC: } \nu_\mu +^{56}_{26}\text{Fe} \quad \to \quad \mu^- + \text{hadrons}, \quad \bar{\nu}_\mu +^{56}_{26}\text{Fe} \quad \to \quad \mu^+ + \text{hadrons}. \tag{5.12}$$

The MINOS collaboration uses iron calorimeter to analyse neutrinos [122, 123].

5.5 Liquid argon time projection chamber (LArTPC)

In 1977, Carlo Rubbia invented a time projection chamber (TPC) with liquid argon [110, 124]. A TPC analyses the path of a charged particle propagating through a volume (see Fig. 17). The volume is normally filled with gas. If a particle propagates through the TPC, the gas is ionized along this path. A high electric field is applied inside the volume to avoid recombination of the ionized atoms. Therefore, produced electrons are accelerated to the anode wire planes on the sides of the TPC and produce a measurable signal, which allows to analyse the path of the particle. Argon has advantageous properties. First, its electronegativity is zero, i.e. the ionized electrons are not attracted by argon and move freely. Second, argon acts also as a scintillator, when a charged particle propagates through it. The density in liquid argon is much higher, i.e. the propagating charged particle interact more with the molecules and produce more ions, which leads to a detailed analysis of the particle's path. The energy

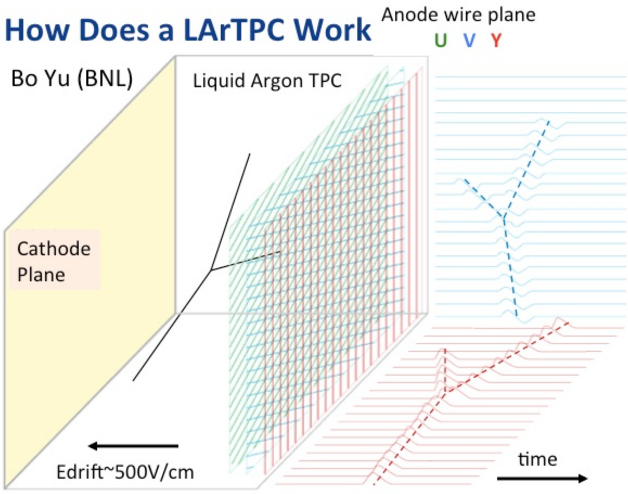

Figure 17: Schematic view of the Liquid argon time projection chamber used in the MicroBooNE experiment. The Anode consists of several wire planes to analyse the tracks of the particles in any direction (figure taken from [126]).

required to ionize molecules in liquid argon is $W_e = 23.6^{+0.5}_{-0.3}$eV. In argon gas more ionization energy is needed $W_e \approx 26.6$eV [125]. The experiment ICARUS uses the detection technique of LArTPC to study processes

$$^{40}\mathrm{Ar} + \nu_e \quad \rightarrow \quad ^{40}\mathrm{K} + e^- \tag{5.13}$$

for observation of neutrinos form different sources and neutrino oscillations.

6 WIMPs and neutrinos in direct detection experiments

6.1 WIMP and neutrino-induced nuclear recoil rates

In direct detection experiments neutrinos of any origin may mimic direct detection signatures of WIMPs. Although such experiments try to avoid background events, neutrinos cannot be shielded by matter. Therefore, the background from neutrinos is irreducible. Dark matter direct detection experiments are mainly sensitive to neutrino-nucleus elastic scattering.

Neutrinos scatter coherently off target nuclei, e.g. xenon or germanium nuclei and may produce recoil spectra similar to WIMPs. The measure of coherence is given by a nuclear form factor $F(|\vec{q}|)$. Coherence is lost, if the momentum transfer $|\vec{q}|$ takes values up to few MeV. A nuclear form factor is introduced to describe the internal structure of an object in a scattering process [127–129]. Then, a differential cross section can be expressed by a product of the point-like cross section and the nuclear form factor

$$\frac{d\sigma}{d\Omega} = |F(|\vec{q}|)|^2 \, \frac{d\sigma}{d\Omega}_{\text{point-like}}. \tag{6.1}$$

The form factor is the Fourier transformation of the nuclear mass density $\rho_{mass}(r)$ weighted by the nucleus mass m_N [129–131]

$$|F(|\vec{q}|)| = \frac{1}{m_N} \int d^3r \; \rho_{\text{mass}}(r) e^{-i\vec{q}\cdot\vec{r}} \tag{6.2}$$

and has to fulfil the condition $F(0) = 1$. In general, the nuclear mass density is proportional to the nuclear charge density

$$\rho_{\text{mass}}(r) = \frac{m_N}{Ze}\rho(r), \tag{6.3}$$

where $\rho(r) \equiv \rho_{\text{charge}}(r)$, Ze is the total charge of a nucleus. The differential coherent cross section of neutrinos is determined by the elastic scattering process via Z-exchange (detailed discussion is given in App. F.2)

$$\nu + N \to \nu + N \tag{6.4}$$

and is given in terms of recoil energies E_R

$$\frac{d\sigma_{N\nu}(E_\nu, E_R)}{dE_R} = \frac{Q_W^2 G_F^2 m_N |F\left(|\vec{q}|\right)|^2}{4\pi} \left[1 - \frac{E_R m_N}{2E_\nu^2}\right], \tag{6.5}$$

where $G_F = 1.1663787(6) \cdot 10^{-5}$ GeV^{-2} is the Fermi constant, $Q_W = (4\sin^2\theta_W - 1)Z + N$ is the weak charge, θ_W is the Weinberg angle ($\sin^2\theta_W \approx 0.23129(5)$ in MS regime [31]) and E_ν is the energy, that the neutrino carries before scattering. Interactions with W-bosons change flavors and photons couple only on charged particles. Therefore, processes including these mediators are excluded. We consider spin-independent scattering. The spin-independent form factor can be approximated by an analytic form, also known as the Helm form factor [128]

$$|F(|\vec{q}|)| \equiv \left|F^{\text{SI}}(|\vec{q}|)\right| = \frac{3j_1(|\vec{q}|R)}{|\vec{q}|R} e^{-|\vec{q}|^2 s^2/2}, \tag{6.6}$$

where

- $j_1(x)$ is the first order spherical Bessel function of the first kind

$$j_1(x) = \frac{\sin(x)}{x^2} - \frac{\cos(x)}{x}, \tag{6.7}$$

- R is the effective nuclear radius

$$R = \sqrt{c^2 + \frac{7}{3}\pi^2 a^2 - 5s^2}, \tag{6.8}$$

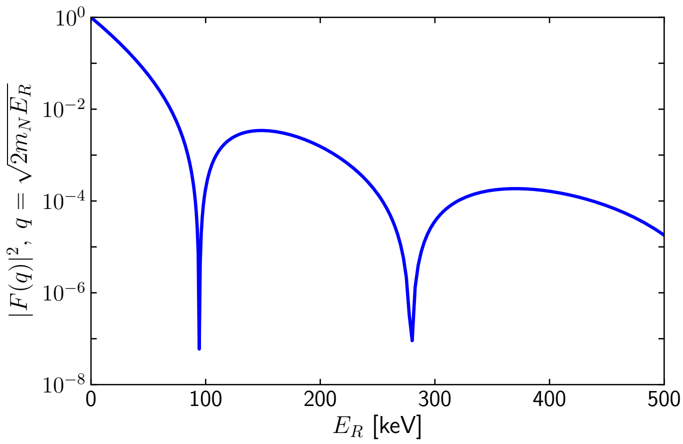

Figure 18: The Helm form factor squared. The cross section is suppressed by the form factor at recoil energies $E_R \geq 50$ keV.

- $c = (1.23A_N^{\frac{1}{3}} - 0.60)$ fm, A_N is the nuclear mass number,
- $s \approx 0.9$ fm is the nuclear skin thickness and $a \approx 0.52$ fm.

The Helm form factor is introduced as the Fourier transformation of a convolution of nuclear charge densities $\rho_u(r)$, $\rho_s(r)$ of the uniform model and a Gaussian smearing to take the soft edge of the nucleus into account [128, 130, 132]

$$\rho_u(r) = \begin{cases} \frac{3Ze}{4\pi R^3} & \text{for } r \leq R \\ 0 & \text{for } r > R \end{cases}, \quad \rho_s(r) = \frac{1}{(2\pi s^2)^{3/2}} e^{-r^2/2s^2}. \tag{6.9}$$

The corresponding Fourier transformations are given by

$$F_u(|\vec{q}|) = \frac{3}{|\vec{q}|R} j_1(|\vec{q}|R), \quad F_s(|\vec{q}|) = e^{-|\vec{q}|^2 s^2/2}. \tag{6.10}$$

Due to the property of Fourier transformation $F_{u,s}[\rho_u * \rho_s] = F_u[\rho_u] \cdot F_s[\rho_s]$ the Helm form factor is a multiplication of the Fourier transformations (6.10)

$$\begin{aligned} |F(|\vec{q}|)| = F_{u,s}[\rho_u * \rho_s] &= \frac{1}{m_N} \int d^3r \; \rho_{u*s}(r) e^{-i\vec{q}\cdot\vec{r}} \\ &= F_u(|\vec{q}|) F_s(|\vec{q}|) = \frac{3j_1(|\vec{q}|R)}{|\vec{q}|R} e^{-|\vec{q}|^2 s^2/2}, \end{aligned} \tag{6.11}$$

where $\rho_{u*s}(r) = \int dr' \; \rho_u(r')\rho_s(r - r')$.

In direct detection the measured quantity are recoil energies E_R. The maximum recoil energy that a neutrino can produce is given by [77]

$$E_{R,\nu}^{\max} = \frac{2(E_\nu^{\max})^2}{2E_\nu^{\max} + m_N} \tag{6.12}$$

and depends on the maximum energy $E_\nu^{\max}$ that a neutrino carries (for more general calculation of Eq. (6.12) see eqs. (E.9) to (E.12) in the appendix). The differential recoil rate of neutrinos given in units [1/keV/ton/yr] is obtained by integrating of the differential flux (4.20) times the differential cross section (6.1) over their neutrino energies E_ν [77]

$$\frac{dR_\nu(E_R)}{dE_R} = N_T \int_{E_{\nu,\min}}^{E_\nu^{\max}} dE_\nu \frac{d\Phi_\nu(E_\nu)}{dE_\nu} \frac{d\sigma_{N\nu}(E_\nu, E_R)}{dE_R}, \tag{6.13}$$

where

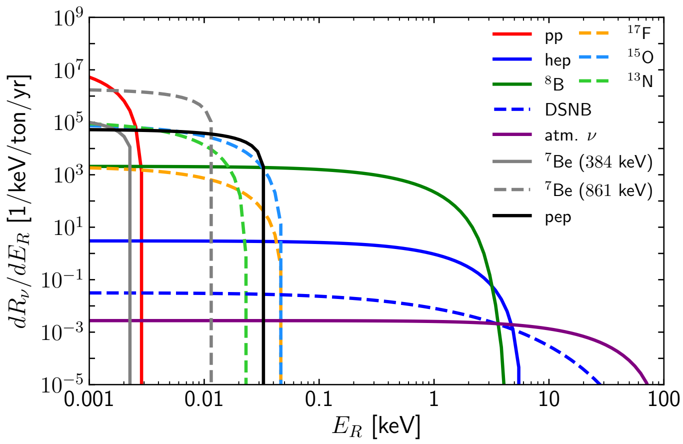

Figure 19: Differential recoil rates of neutrinos in Tab. 4. The spectra of the diffuse supernova neutrino background and the atmospheric neutrinos are combined. The total neutrino fluxes are $\phi_{\text{DSNB}} = 84(1 \pm 0.5)\ \text{cm}^{-2}\ \text{s}^{-1}$ and $\phi_{\text{atm.}\nu} = 7.34(1 \pm 0.2)\ \text{cm}^{-2}\ \text{s}^{-1}$.

- $E_{\nu,\text{min}}$ is the minimum energy that a neutrino produces a recoil E_R

$$E_{\nu,\text{min}} = |\vec{p}_{\nu,\text{min}}| = \sqrt{\frac{E_R m_N}{2}} \tag{6.14}$$

- and N_T is the target number density (number of target nuclei per kg detector mass) given by the Avogadro number $N_A = 6.02 \cdot 10^{23}\ \text{mol}^{-1}$, the molar mass constant $M = 10^{-3}\ \text{kg mol}^{-1}$ and the nuclear mass number A_N

$$N_T = \frac{N_A}{A_N M}. \tag{6.15}$$

The neutrino event rate is written as an integral over recoil energies

$$\mu_\nu = \int_{E_{R_{\text{thr}}}}^{E_{R,\nu}^{\max}} dE_R\, \epsilon_{\text{ff}}(E_R) \frac{dR_\nu(E_R)}{dE_R}, \tag{6.16}$$

where

- $\epsilon_{\text{ff}}(E_R)$ is the detector efficiency
- and $E_{R_{thr}}$ is the threshold energy.

We assume an ideal detector with 100% detector efficiency, i.e. $\epsilon_{\text{ff}}(E_R) = 1$. The differential event rate of WIMPs per unit detector mass [133] depends on the DM density and the velocity distribution explained in Sec. 3.3. It is given by

$$dR = N_T \sigma\, v\, dn, \tag{6.17}$$

where

- dn is the differential particle density

$$dn = n_0 f(\vec{v}, \vec{v}_{\text{lab}})\, d^3v, \tag{6.18}$$

- n_0 is the mean number density

$$n_0 = \frac{\rho_\chi}{m_\chi}, \tag{6.19}$$

- WIMPs follow a Maxwell-Boltzmann distribution

$$f(\vec{v},\vec{v}_{\rm lab}) = \begin{cases} \frac{1}{N_{\rm esc}(2\pi\sigma_v^2)^{3/2}} \exp\left[\frac{-(\vec{v}+\vec{v}_{\rm lab})^2}{2\sigma_v^2}\right] & \text{for } |\vec{v}+\vec{v}_{\rm lab}| < v_{\rm esc} \\ 0 & \text{for } |\vec{v}+\vec{v}_{\rm lab}| \geq v_{\rm esc} \end{cases}, \tag{6.20}$$

- $\sigma_v = v_0/\sqrt{2}$ is the velocity dispersion,
- v_0 is the mean WIMP velocity given in Sec. 3.3,
- $\vec{v}$ is the WIMP velocity relative to the lab frame (Earth),
- $\vec{v}_{\rm lab}$ is the velocity of the lab frame (Earth) relative to the galaxy's rest frame,
- $\vec{v}+\vec{v}_{\rm lab}$ is the velocity of the WIMP relative to the galaxy's rest frame,
- $v_{\rm esc}$ is the escape velocity of the WIMPs in the standard halo model (SHM)
- and $N_{\rm esc}$ is the normalization constant, such that

$$\int_0^{v_{\rm esc}} dv\; f(\vec{v},\vec{v}_{\rm lab}) = 1. \tag{6.21}$$

For a mean WIMP velocity $v_0 = 220\frac{\rm km}{\rm s}$ and an escape velocity $v_{\rm esc} = 544\frac{\rm km}{\rm s}$ [77], one obtains a normalization constant $N_{\rm esc} = 0.993361$. In general, the WIMP velocity relative to the galaxy's rest frame depends on the velocity of the Earth moving around the Sun $\vec{v}+\vec{v}_{\rm lab}+\vec{v}_{\rm E}$, where $\vec{v}_{\rm lab}$ is now the velocity of the solar system relative to the galaxy's rest frame and $\vec{v}_{\rm sun} \approx 30\frac{km}{s}$ is the velocity of the Earth with respect to the rest frame of the solar system. Therefore, the velocity of the lab frame (Earth) changes over the year. Those fluctuations are small and will be neglected for the following calculations (see Sec. 6.2 and [134]). Taking the recoil energies E_R into account one obtains the differential recoil rate [135] as follows

$$\frac{dR_\chi}{dE_R} = N_T \int dn\, \frac{d\sigma}{dE_R} v = N_T \frac{\rho_\chi}{m_\chi}\left\langle \frac{d\sigma}{dE_R} v \right\rangle = N_T \frac{\rho_\chi}{m_\chi} \int_{|\vec{v}|\geq v_{\rm min}} d^3\vec{v}\, f(\vec{v},\vec{v}_{\rm lab}) \frac{d\sigma}{dE_R} v, \tag{6.22}$$

where

- $v_{\rm min}$ is the minimum velocity that a WIMP requires to produce a recoil with energy E_R (for detailed calculation see appendix)

$$v_{\rm min} = \frac{\sqrt{2m_N E_R}}{2\mu_{\chi N}}, \tag{6.23}$$

- and $\mu_{\chi N}$ is the WIMP-nucleus reduced mass

$$\mu_{\chi N} = \frac{m_\chi m_N}{m_\chi + m_N}. \tag{6.24}$$

In an elastic scattering process the WIMP-nucleus cross section related to the mandelsteam variable t is given by

$$\frac{d\sigma}{d|\vec{q}|^2} = \frac{d\sigma}{dt} = \frac{\langle |M|^2 \rangle}{64\pi s |\vec{p}_{\chi,\rm CM}|^2} \quad \text{with } t = -|\vec{q}|^2, \tag{6.25}$$

where

- $\langle |M|^2 \rangle$ is the squared spin averaged WIMP nucleus matrix element,
- $|\vec{p}_{\chi,\rm CM}|$ is the three momentum of the incoming WIMP χ in the center of mass frame (CM),

- and $\vec{q}$ is the momentum transfer.

The three momentum in the center of mass frame is related to the three momentum in the lab frame (rest frame of the nucleus) as follows

$$|\vec{p}_{\chi,\mathrm{CM}}| = \frac{m_N}{\sqrt{s}} |\vec{p}_{\chi,\mathrm{lab}}|. \tag{6.26}$$

Then, the elastic scattering cross section can be written as

$$\frac{d\sigma}{d|\vec{q}|^2} = \frac{d\sigma}{dt} = \frac{\langle |M|^2 \rangle}{64\pi m_N^2 |\vec{p}_{\chi,\mathrm{lab}}|^2} = \frac{\langle |M|^2 \rangle}{64\pi m_N^2 m_\chi^2 v^2}, \tag{6.27}$$

where v is the WIMP velocity in the lab frame. It is convenient to rewrite the cross section (6.27) in terms of cross sections at zero momentum transfer $|\vec{q}| = 0$ and split it in a spin-independent (SI) and spin-depended (SD) part [135, 136]

$$\frac{d\sigma}{dt} = \frac{1}{4\mu_{\chi N}^2 v^2} \left[\sigma_0^{\mathrm{SI}} F^2(|\vec{q}|) + \sigma_0^{\mathrm{SD}} S(|\vec{q}|)/S(0) \right], \tag{6.28}$$

where

- $F^2(|\vec{q}|)$ is the helm form factor given by Eq. (6.6),
- $S(|\vec{q}|)$ is nuclear spin structure function [137]
- and the cross section at zero momentum transfer is obtained by

$$\sigma_0 = \int_0^{4\mu_{\chi N}^2 v^2} d|\vec{q}| \frac{d\sigma(|\vec{q}| = 0)}{d|\vec{q}|^2} = \frac{\mu_{\chi N}^2 \langle |M(|\vec{q}| = 0)|^2 \rangle}{64\pi m_N^2 m_\chi^2}. \tag{6.29}$$

Using $E_R = -\frac{t}{2m_N}$ the cross section (6.28) can then be written in terms of recoil energies E_R

$$\frac{d\sigma}{dE_R} = 2m_N \frac{d\sigma}{dt} = \frac{m_N}{2\mu_{\chi N}^2 v^2} \left[\sigma_0^{\mathrm{SI}} F^2(|\vec{q}|) + \sigma_0^{\mathrm{SD}} S(|\vec{q}|)/S(0) \right]. \tag{6.30}$$

We consider spin-independent scattering and neglect the spin-dependent part. For a spin-independent scattering the WIMP-nucleus cross section σ_0^{SI} is given by [135]

$$\sigma_0^{\mathrm{SI}} = \mu_{\chi N}^2 \left[Z f_p + (A - Z) f_n \right]^2 \simeq A^2 \left(\frac{\mu_{\chi N}}{\mu_{\chi n}} \right)^2 \sigma_n, \tag{6.31}$$

where

- σ_n is the WIMP-nucleon cross section,
- f_n, f_p are effective nucleon couplings ($f_n \simeq f_p$),
- $\mu_{\chi n}$ is the WIMP-nucleon reduced mass,

$$\mu_{\chi n} = \frac{m_\chi m_n}{m_\chi + m_n} \tag{6.32}$$

- and m_n is the neutron mass.

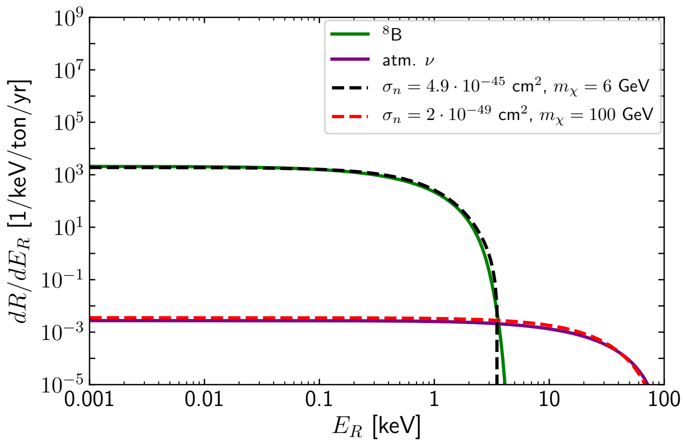

Figure 20: Nuclear recoil rate for ^{131}Xe target with $m_N \approx 122$ GeV. The ^{8}B and atmospheric neutrinos mimic WIMP recoil rates with $m_\chi = 6$ GeV, $m_\chi = 100$ GeV and cross sections $\sigma_n = 4.9 \cdot 10^{-45}$ cm^2, $\sigma_n = 2 \cdot 10^{-49}$ cm^2.

In the end, the differential recoil rate of WIMPs can be expressed as

$$\frac{dR_\chi}{dE_R} = N_T \frac{\rho_\chi}{m_\chi} A^2 F^2(|\vec{q}\,|) \frac{m_N}{2\mu_{\chi n}^2} \sigma_n \int_{v \geq v_{\min}} d^3\vec{v}\, \frac{f(\vec{v}, \vec{v}_{\text{lab}})}{v}, \quad v := |\vec{v}\,|. \tag{6.33}$$

The velocity integral is derived step by step in the App. G.1. The maximum recoil energy E_R produced by a WIMP of mass m_χ in a detector with nucleus mass m_N is derived similar to Eq. (6.12)

$$E_{R,\chi}^{\max} = \frac{2m_N \left((E_\chi^{\max})^2 - m_\chi^2 \right)}{m_N^2 + m_\chi^2 + 2m_N E_\chi^{\max}}, \tag{6.34}$$

where $E_\chi^{\max} = m_\chi + \frac{m_\chi (v_{\text{esc}} + v_{\text{lab}})^2}{2}$ is the maximum energy a WIMP can carry (see Fig. 21). Neutrinos can mimic the differential recoil rates of WIMPs [77]. For instance, ^{8}B-neutrinos mimic a WIMP with $(\sigma_n, m_\chi) = (4.9 \cdot 10^{-45}\ \text{cm}^2, 6\ \text{GeV})$ and the differential recoil rate of atmospheric neutrinos is in good agreement with a WIMP with $(\sigma_n, m_\chi) = (2 \cdot 10^{-49}\ \text{cm}^2, 100\ \text{GeV})$. In that case, neutrinos and WIMPs are no longer distinguishable in a detector as shown in Fig. 20. The size of the cross section is also indicative for which mediator particle takes part in the elastic scattering process between a WIMP χ and a nucleus N [138].

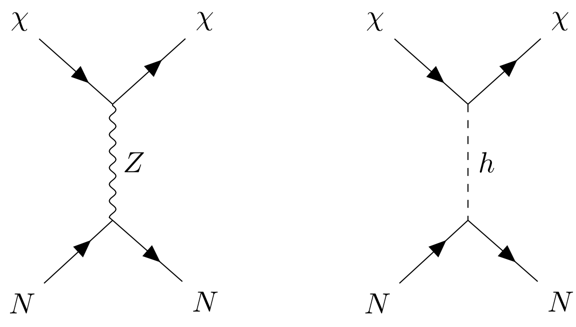

$\sigma_n \sim 10^{-39}$ cm^2 $\sigma_n \sim 10^{-45}$ cm^2

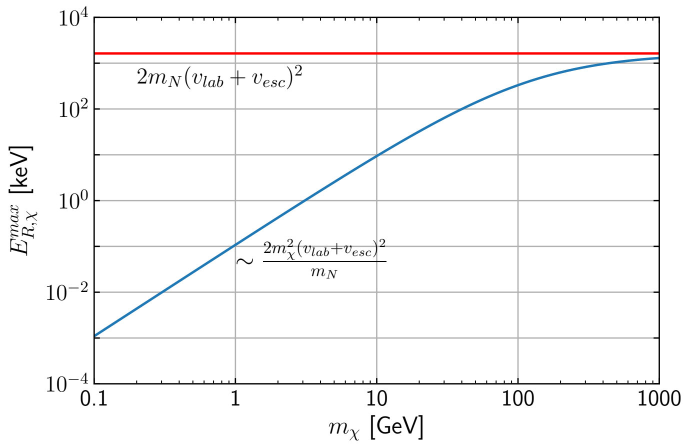

Figure 21: The maximum recoil energy produced by a WIMP in direct detection experiments for different masses m_χ. It converges to $2m_N(v_{\rm lab}+v_{\rm esc})^2$ for higher masses for a ^{131}Xe target with $m_N \approx 122$ GeV.

The total WIMP rate is obtained by integrating over the recoil energies[8]

$$\mu_\chi = \int_{E_{\rm thr}}^{E_{R,\chi}^{\rm max}} dE_R \, \frac{dR_\chi}{dE_R}. \tag{6.35}$$

6.2 Annual modulation in the WIMP rate

Due to the additional circular movement of the Earth around the Sun, the velocity of the Earth with respect to the galaxy's rest frame varies over the year [133, 134, 139]

$$v_{\rm E}(t) = v_{\rm lab}\left(1.05 + 0.07\cos\frac{2\pi(t-t_p)}{1{\rm yr}}\right), \tag{6.36}$$

where t is the time since the 1st January (1 yr= 362.25 d) and t_p is the time elapsed till the 2nd June (152.5 ± 1.3 d). Assuming a spherical symmetric WIMP halo in our galaxy, that is stable and not much rotating, an observer on Earth would feel a wind, because the solar system propagates through the halo as shown in Fig. 22. Therefore, the differential recoil rate of WIMPs changes over the year

$$\frac{dR_\chi(t)}{dE_R} = N_T \frac{\rho_\chi}{m_\chi} \int_{|\vec{v}|\geq v_{\rm min}} d^3\vec{v}\, f\left(\vec{v}, \vec{v}_{\rm E}(t)\right) \frac{d\sigma}{dE_R} v \tag{6.37}$$

and reaches its maximum in June, because the Earth moves in the direction of the solar system and against the WIMP wind. More DM particles leave a detectable signal in the detector. During the winter, the rate decreases and reaches its minimum in December, because the Earth moves against the direction of the solar system and with the WIMP wind. The DAMA experiment [140, 141] measured a ∼ 2% annual modulation, but remains both unconfirmed and ruled out by others (see Fig. 23).

[8] For our purpose we can set $E_{R,\chi}^{\rm max} = 100$ keV as contributions from WIMP with $E_R \geq 100$ keV are negligible.

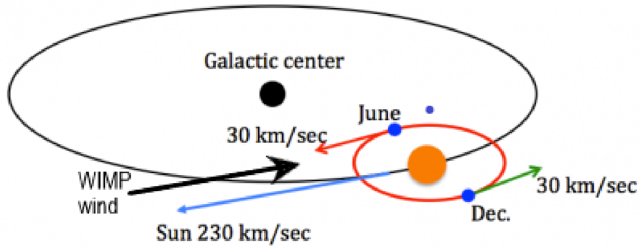

Figure 22: Annual modulation: solar system moving with respect to the galaxy's rest frame. In June, the rate reaches its maximum and in December its minimum (figure taken from [142]).

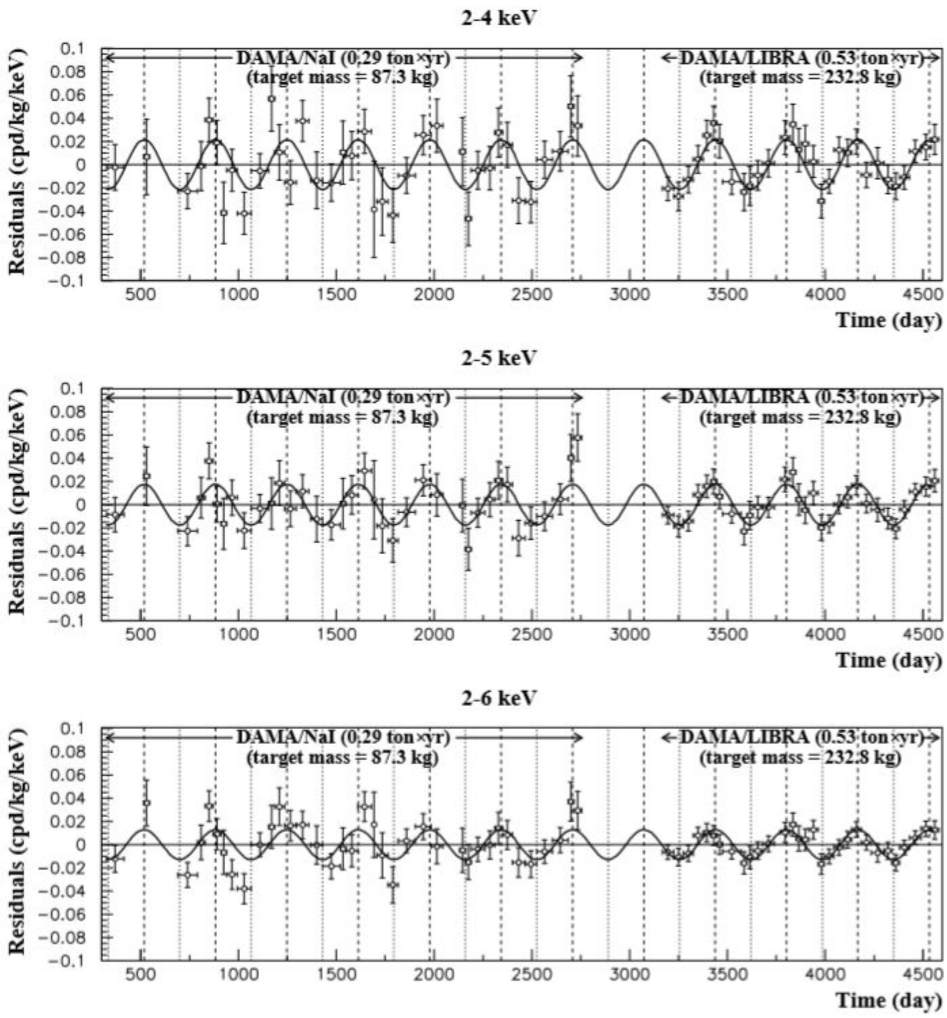

Figure 23: The experimental measurements of DAMA/Nal and DAMA/LIBRA. The residual rates of the single-hit scintillation events are plotted against the time in $(2-4)$ keV, $(2-5)$ keV, $(2-6)$ keV intervals (figure taken from [140] and [141]).

7 The principle reach of DM direct detection experiments

Neutrinos form an irreducible background in direct detection experiments. In order to analyse the principal sensitivity, we deduce exclusion and discovery limits in the presence of such background. For this, we first derive the best background-free sensitivity/exclusion limit, for which no neutrino background is expected. For this purpose, the maximum exposure will be found, such that experiments see their first neutrino event. At this exposure, the minimum WIMP-nucleon cross sections is attained beyond which WIMPs can no longer be excluded. In the second step, we derive discovery limits in the presence of an irreducible neutrino background. For this purpose, based on Monte Carlo generated mock data for a fixed threshold and exposure we reject the neutrino background and set limits on the WIMP-nucleon cross section.

7.1 Exclusion limits

Suppose an experiment measures so long that no events are expected [51, 77]. For this purpose, we adjust the exposure $\varepsilon(E_{R_{\text{thr}}})$, such that the number of expected neutrino events does not exceed one event,

$$1 \overset{!}{=} \varepsilon(E_{R_{\text{thr}}}) \sum_{j=1}^{n_\nu} \mu_\nu^j(E_{R_{\text{thr}}}) \;\Rightarrow\; \varepsilon(E_{R_{\text{thr}}}) = \frac{1}{\sum_{j=1}^{n_\nu} \mu_\nu^j(E_{R_{\text{thr}}})}. \tag{7.1}$$

The sum is over all neutrino sources given in Tab. 4 and

$$\mu_\nu^j(E_{R_{\text{thr}}}) = \int_{E_{R_{\text{thr}}}}^{E_{R,\nu}^{\max}} dE_R \, \frac{dR_\nu^j}{dE_R}, \tag{7.2}$$

where $\mu_\nu^j(E_{R_{\text{thr}}})$ depends on the threshold $E_{R_{thr}}$ and on the endpoint recoil energy $E_{R,\nu}^{\max}$. In Fig. 24 the exposure related to one neutrino event is shown for thresholds from 1 eV to 100 keV. Current DM experiments achieve thresholds of 1 keV and below (LUX $E_{R_{\text{thr}}} \sim 1$ keV [51, 143, 144], CRESST-III Phase 1 $E_{R_{\text{thr}}} = O(0.1)$ keV [145]).

The number of observed WIMP events $N_{\text{obs}}^\chi \sim \text{Pois}(N_{\text{exp}}^\chi)$ in an experiment is Poisson distributed around the expected number of WIMP events $N_{\text{exp}}^\chi = \varepsilon\mu_\chi$, where μ_χ is given by

$$\mu_\chi(\sigma_n; m_\chi) = \int_{E_{R_{\text{thr}}}}^{E_{R,\chi}^{\max}} dE_R \, \frac{dR_\chi(\sigma_n; m_\chi)}{dE_R}, \quad E_{R,\chi}^{\max} \leq 100\,\text{keV}. \tag{7.3}$$

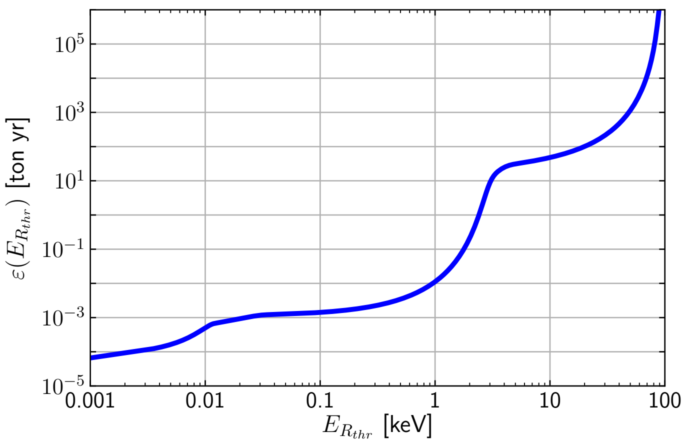

Figure 24: The exposure $\varepsilon(E_{R_{\text{thr}}})$ for one neutrino event. Higher thresholds lead to less neutrino events and therefore, higher exposures are needed.

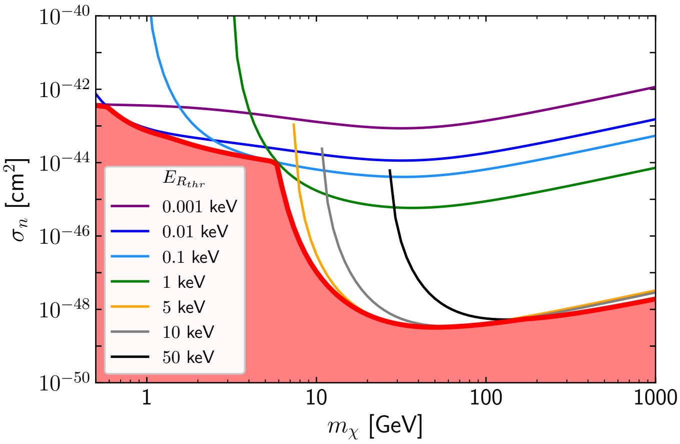

Figure 25: Exclusion limits for different thresholds $E_{R_{\rm thr}}$ and the ultimate sensitivity in red.

If we require a 90% confidence level (C.L.), the number of expected WIMP events should be $N^\chi_{\rm exp} \approx 2.3$,

$$\sum_{k=1}^{\infty} \frac{e^{-N^\chi_{\rm exp}} \left(N^\chi_{\rm exp}\right)^k}{k!} \approx 0.9 \quad \Leftrightarrow \quad e^{-N^\chi_{\rm exp}} \approx 0.1,\ k=0 \ \Rightarrow \ N^\chi_{\rm exp} \approx 2.3. \tag{7.4}$$

In this case, we require that nine of ten random experiments observe at least 1 WIMP event. Then, the exclusion limit on the WIMP nucleon cross section σ_n at 90% C.L. can be derived by

$$\varepsilon(E_{R_{\rm thr}}) = \frac{1}{\sum_{j=1}^{n_\nu} \mu^j_\nu(E_{R_{\rm thr}})}, \qquad \sigma_n^{90}(E_{R_{\rm thr}}, m_\chi) = \frac{2.3}{\varepsilon(E_{R_{\rm thr}}) H_\chi(E_{R_{\rm thr}}, m_\chi)}, \tag{7.5}$$

where the expected differential recoil rate of WIMPs is written as $N^\chi_{\rm exp} = \varepsilon(E_{R_{\rm thr}})\, \sigma_n H_\chi(E_{R_{\rm thr}}, m_\chi)$ and

$$H_\chi(E_{R_{\rm thr}}, m_\chi) = N_T \frac{\rho_\chi}{m_\chi} \frac{m_N}{2\mu^2_{\chi n}} A^2 \int_{E_{R_{\rm thr}}}^{E^{\rm max}_{R,\chi}} dE_R\, F^2(|\vec{q}|) \int_{|\vec{v}|\geq v_{\rm min}} d^3\vec{v}\, \frac{f(\vec{v})}{v}. \tag{7.6}$$

The minimum of all exclusion limits scanned over all thresholds characterizes the ultimate sensitivity as shown in Fig. 25. If the data is fitted by cross sections and WIMP masses below the minimum of all isocontour lines $N^\chi_{\rm exp} \approx 2.3$, WIMPs and neutrinos are no longer distinguishable and the number of WIMP events is not large enough to obtain a significantly large signal.

7.2 Procedure to derive the exclusion limits

1. Fix the threshold $E_{R_{\rm thr}}$.

2. Derive the recoil rate of neutrinos and add them together

$$\sum_{j=1}^{n_\nu} \mu^j_\nu(E_{R_{\rm thr}}) = \sum_{j=1}^{n_\nu} \int_{E_{R_{\rm thr}}}^{E^{\rm max}_\nu} dE_R\, \frac{dR^j_\nu}{dE_R}. \tag{7.7}$$

3. Adjust the exposure $\varepsilon(E_{R_{\rm thr}})$ [ton yr] such that $N^\nu_{\rm exp} = \varepsilon(E_{R_{\rm thr}}) \sum_{j=1}^{n_\nu} \mu^j_\nu(E_{R_{thr}}) \overset{!}{=} 1$ $\Rightarrow\ \varepsilon(E_{R_{\rm thr}}) = 1/\sum_{j=1}^{n_\nu} \mu^j_\nu(E_{R_{\rm thr}})$ (exposure is chosen such that one neutrino event is detected).

4. Calculate the exclusion limit on the WIMP-nucleon cross section σ_n for a fixed threshold and a

90% confidence level by taking $N^{\chi}_{\text{exp}}(\sigma_n; m_\chi) \stackrel{!}{=} 2.3$,

$$\begin{aligned}
N^{\chi}_{\text{exp}}(\sigma_n; m_\chi) &= \varepsilon(E_{R_{\text{thr}}}) \cdot \int_{E_{R_{\text{thr}}}}^{E_{R,\chi}^{\text{max}}} dE_R \, \frac{dR_{\text{DM}}}{dE_R} \\
&= \varepsilon(E_{R_{\text{thr}}}) \cdot N_T \frac{\rho_\chi}{m_\chi} \int_{E_{R_{\text{thr}}}}^{E_{R,\chi}^{\text{max}}} dE_R \int_{|\vec{v}\,| \geq v_{\text{min}}} d^3\vec{v}\, f(\vec{v}\,) \frac{d\sigma}{dE_R} v \\
&= \sigma_n \varepsilon(E_{R_{\text{thr}}}) \underbrace{N_T \frac{\rho_\chi}{m_\chi} \frac{m_N}{2\mu^2_{\chi,n}} A^2 \int_{E_{R_{\text{thr}}}}^{E_{R,\chi}^{\text{max}}} dE_R \, F^2(|\vec{q}\,|) \int_{|\vec{v}\,| \geq v_{\text{min}}} d^3\vec{v}\, \frac{f(\vec{v}\,)}{v}}_{\equiv H_\chi(E_{R_{\text{thr}}}, m_\chi)} \stackrel{!}{=} 2.3
\end{aligned} \tag{7.8}$$

$$\Rightarrow \; \sigma^{90}_n(m_\chi) = \frac{2.3}{\varepsilon(E_{R_{\text{thr}}}) H_\chi(E_{R_{\text{thr}}}, m_\chi)}. \tag{7.9}$$

5. Derive the exclusion limit $\sigma^{90}_n(m_\chi)$ over a broad range of masses, e.g. from 0.5 GeV to 1000 GeV.
6. Repeat 2-5 for all thresholds $E_{R_{\text{thr}}}$ (a region of $E_{R_{thr}} = [0.001, 50]$ keV is sufficient).
7. Take the minimum of all exclusion limits.

7.3 Discovery limits

In order to derive discovery limits, we use likelihood statistics as well as hypothesis testing to set limits on the WIMP nucleon cross section σ_n for each WIMP mass m_χ.

7.3.1 Likelihood functions and maximum likelihood estimators (MLE)

The method of maximum likelihood estimation is one of the most used methods in statistics and data analysis to estimate the most likely parameter of a hypothesis that fits the data the best [146]. Likelihood functions L can be seen as the "inverse" of the probability density function f (PDF)

$$L : \Theta \;\rightarrow\; \mathbb{R}, \quad \theta_1, \theta_2, ..., \theta_n \in \Theta, \tag{7.10}$$

$$L(\theta_1, \theta_2, ..., \theta_n | x_1, x_2, ..., x_n) = f(x_1, x_2, ..., x_n | \theta_1, \theta_2, ..., \theta_n) \equiv f(x_1, x_2, ..., x_n) \tag{7.11}$$

where $x_1, x_2, ..., x_n$ represents the observed data. Given the PDF $f(x_1, x_2, ..., x_n | \theta_1, \theta_2, ..., \theta_n)$ defined by the parameters $(\theta_1, \theta_2, ..., \theta_n)$ one is able to generate data $x_1, x_2, ..., x_n$ (what means that the shape of the PDF is known). However, in Frequentist inference the likelihood $L(\theta_1, \theta_2, ..., \theta_n | x_1, x_2, ..., x_n)$ takes the observed data $x_1, x_2, ..., x_n$ and fits for the parameters $(\theta_1, \theta_2, ..., \theta_n)$. The best fit is found by the maximum likelihood method, which estimates the most likely parameters $(\theta_1, \theta_2, ..., \theta_n)$ by maximizing the likelihood function L for $(\theta_1, \theta_2, ..., \theta_n)$. It is convenient to minimize the negative log-likelihood function $-\ln L$ instead of maximizing the likelihood function L, because products convert to sums of logarithms and many standard methods exist for minimizing a function. This is possible, because the logarithm is a monotonously increasing function and therefore, the log-likelihood function and the likelihood function L itself share the same minimum. In general, the likelihood is not normalized and therefore not a PDF. The maximum likelihood estimator MLE $\hat{\theta}$ is unbiased $\mathbb{E}_\theta[\hat{\theta}] = \theta$ with the smallest possible variance. A simple example of MLE for a Gaussian distribution is given in the Appendix D.1.

7.3.2 Hypotheses testing with profile likelihood ratio test statistics

Hypothesis testing is a way to test the compatibility of hypotheses, statements or theoretical models on the measured data, if results obtained from an experiment can be described by the given model [146]. Mostly, one compares two hypotheses $\text{H}_0 : \theta \in \Theta_0$ and $\text{H}_1 : \theta \in \Theta_0^C$, where one tries to reject the null hypothesis H_0 by the data [147, 148]. The tested model contains parameters $\theta \in \Theta$, where Θ is the parameter space characterizing the whole model. A null hypothesis H_0 is characterized by parameters $\theta \in \Theta_0$, where $\Theta_0 \subset \Theta$ is a subset of the parameter space Θ. The alternative hypothesis H_1 is specified by parameters $\theta \notin \Theta_0$, which describe exactly the complement of Θ_0 implying $H_1 : \theta \in \Theta_0^C$. The likelihood ratio test is one of many statistical tests to compare hypotheses. It is used to find the best fit to the data and is characterized by the test statistics $0 \leq \lambda \leq 1$ given by the ratio of likelihoods [146]

$$\lambda = \frac{\sup_{\theta\in\Theta_0} L(\theta\,|x)}{\sup_{\theta\in\Theta} L(\theta\,|x)} = \frac{L(\tilde{\theta}\,|x)}{L(\hat{\theta}\,|x)}, \tag{7.12}$$

where $\tilde{\theta}$ is the maximum of the likelihood L in Θ_0 and $\hat{\theta}$ denotes the maximum of L in the whole parameter space Θ. A large discrepancy between the null hypothesis H_0 and the alternative hypothesis H_1 is given by smaller values of λ. If H_0 is true, then $\lambda \sim 1$.

Assume the theory is characterized by more parameters than the parameters $\theta \in \Theta$. Let us call them nuisance parameters $\phi \in \Phi$ and $\Theta \cup \Phi$ is now the whole parameter space. Nuisance parameters are parameters, which are part of the theory, but are not of main interest, e.g. background effects. Then, the likelihood has to be maximized in the parameter of interest θ and in the nuisance parameters ϕ [147, 149]

$$\lambda = \frac{\sup\{L(\theta,\phi\,|x),\theta\in\Theta_0,\phi\in\Phi\}}{\sup\{L(\theta,\phi\,|x),\theta\in\Theta,\phi\in\Phi\}} = \frac{L(\tilde{\theta},\tilde{\phi}\,|x)}{L(\hat{\theta},\hat{\phi}\,|x)}. \tag{7.13}$$

For instance, the null hypothesis $H_0 : \theta = 0$ is tested against the alternative hypothesis $H_1 : \theta \neq 0$. Additionally, the tested theories can be characterized by nuisance parameters.

7.3.3 WIMPs vs. SM neutrinos

The purpose of DM experiments is to measure a new signal, which is explainable by known DM models. However, background effects complicate the measurements. It is always a challenge for experimentalists to avoid the background. Mostly, it can be reduced but not completely prevented. Direct detection experiments are designed for measuring nuclear recoil energies of new particles, e.g. WIMPs. However, neutrinos constitute an irreducible background that can mimic recoil rates of WIMPs [77]. In this case, the null Hypothesis $H_0 : \sigma_n = 0$ (only background) is tested against the alternative hypothesis $H_1 : \sigma_n \neq 0$ (signal+background), where σ_n is the WIMP nucleon cross section. Additionally, we consider the neutrino background to be characterized by neutrino fluxes $\vec{\phi}_\nu$ as nuisance parameters. In order to discover a WIMP signal in the presence of the neutrino background, we try to reject the only background hypothesis H_0 [77]. Whether the null hypothesis is rejected or not, is based on the chosen probability p_0.

The p_0-value characterizes the probability, that the null hypothesis H_0 is excluded if the q-value (7.20) is greater than the observed value q_{obs} [150, 151]

$$p_0 = P(q \geq q_{\text{obs}}|H_0) = \int_{q_{\text{obs}}}^{\infty} dq\; f(q\,|H_0), \tag{7.14}$$

where $f(q\,|H_0)$ is the distribution of q-values, that follows asymptomatically a χ^2-distribution with one degree of freedom under the null hypothesis H_0 (see Wilk's theorem [152]). In terms of significance $Z = \sqrt{q}$ the p_0 is obtained by

$$p_0 = P(Z \geq Z_{\text{obs}}|H_0) = \int_{Z_{\text{obs}}}^{\infty} dZ\; f(Z\,|H_0), \tag{7.15}$$

where the distribution of significances $f(Z\,|H_0)$ is twice the right hand side of the Gaussian distribution $\text{No}(0,1)$ due to the restriction $Z \geq 0$. Then, the p_0-value is simply given by the cumulative distribution function $\Phi(x)$ of the standard normal distribution

$$p_0 = 2\times\int_{Z_{\text{obs}}}^{\infty} dZ\; f(Z\,|H_0) = 2\times\int_{Z_{\text{obs}}}^{\infty} dZ\;\frac{1}{\sqrt{2\pi}}e^{-x^2/2} = 2\times\left(1-\Phi(Z_{\text{obs}})\right), \tag{7.16}$$

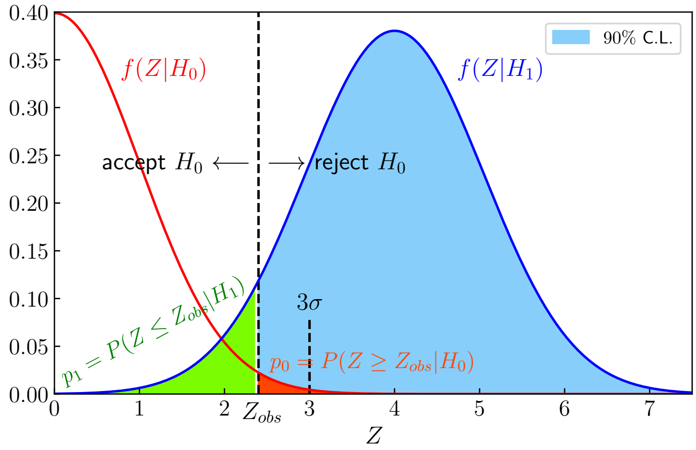

Figure 26: A schematic view of the hypotheses test. A discovery with 3σ is reached, when $Z \geq 3$ or equivalently $p_0 \leq 2 \times 0.00135$.

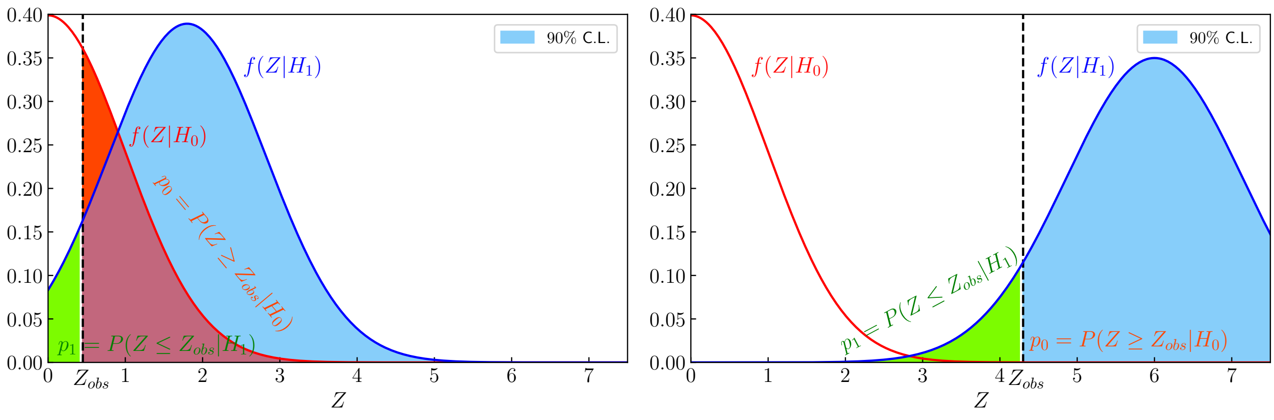

(a) (b)

Figure 27: Two extreme cases are shown: **(a)** The discrepancy between H_0 and H_1 is very small. The data is more compatible with the null hypothesis H_0. **(b)** The data is more compatible with the alternative hypothesis H_1 and the distributions are more distinguishable.

where Z is given in units of standard deviations and $Z_{\mathrm{obs}} = \Phi^{-1}\left(1 - \frac{p_0}{2}\right)$.

For a discovery with 3σ (5σ) significance the corresponding p_0-value is given by $p_0 = 2 \times 0.00135$ ($p_0 = 2 \times 2.9 \cdot 10^{-7}$). Thus, experiments should at least obtain significances $Z_{\mathrm{obs}} \geq 3$ ($Z_{\mathrm{obs}} \geq 5$) to discover a signal. In other words, if data is observed in the critical region $Z_{\mathrm{obs}} \geq 3$ ($Z_{\mathrm{obs}} \geq 5$) or equivalently $p_0 \leq 2 \times 0.00135$ $\left(p_0 \leq 2 \times 2.9 \cdot 10^{-7}\right)$ the null hypothesis H_0 is rejected. The upper bound of the p_0-value is also known as the significance level.

The p_1-value corresponding to the distribution under the alternative hypothesis H_1 quantifies the probability that H_1 is excluded if the q-value (7.20) is less than q_{obs} [150]

$$p_1 = \beta = P(q \leq q_{\mathrm{obs}}|\mathrm{H}_1) = \int_{-\infty}^{q_{\mathrm{obs}}} dq\ f(q\,|\mathrm{H}_1) \tag{7.17}$$

or equivalently in terms of significance $Z = \sqrt{q}$,

$$p_1 = \beta = P(Z \leq Z_{\mathrm{obs}}|\mathrm{H}_1) = \int_{-\infty}^{Z_{\mathrm{obs}}} dZ\ f(Z\,|\mathrm{H}_1). \tag{7.18}$$

The confidence level of the test is given by the statistical power of a hypothesis test [146]

$$1 - \beta = \int_{Z_{\text{obs}}}^{\infty} dZ \; f(Z \,|\mathrm{H}_1) \tag{7.19}$$

and is the probability, that H_1 is accepted, if it is true. It consists of q-values or significances Z, that are not rejected under the alternative hypothesis H_1. Assuming a confidence level of 90% (95%) the alternative hypothesis H_1 is excluded for $\beta = 0.1$ (0.05) [77, 150]. Thus, the significance Z_{obs} is determined by the chosen confidence level $1-\beta$. Higher significances Z_{obs} correspond to a larger discrepancy between the only-background and the signal+background hypothesis. If it reaches the region $Z_{\text{obs}} \geq 3$ ($Z_{\text{obs}} \geq 5$) a signal of 3σ (5σ) is discovered as shown in Fig. 26. Two extreme cases are shown in Fig. 27a and Fig. 27b. It is necessary to note, that two kind of errors are taken into account [151]:

- error of first kind: The null hypothesis H_0 is rejected, although it is true,
- error of second kind: The null hypothesis H_0 is accepted, although it is false.

The probability of making the error of the first kind is given by the p_0-value under the null hypothesis H_0. The probability of making the error of the second kind is given by the p_1-value under the alternative hypothesis H_1.

The discrepancy between the hypotheses H_0 and H_1 is represented in the magnitude of the q-value, which is simply the negative logarithm of the profile likelihood ratio

$$q_0 = -2\ln\lambda(0) = \begin{cases} -2\ln \frac{L(\sigma_n=0,\tilde{\vec{\phi}}_\nu\,|x)}{L(\hat{\sigma}_n,\hat{\vec{\phi}}_\nu\,|x)} & \text{for } \hat{\sigma}_n > 0 \\ \\ 0 & \text{for } \hat{\sigma}_n \leq 0, \end{cases} \tag{7.20}$$

where the $\tilde{\vec{\phi}}_\nu$ maximizes the likelihood for H_0 and $\hat{\sigma}_n, \hat{\vec{\phi}}_\nu$ are the maxima in the case H_1. The maxima are derived by minimizing the negative log-likelihood function $-\ln\mathcal{L}(\sigma_n, \vec{\phi}_\nu\,|x)$. The data x is now the list of recoil energies E_R obtained from an experiment or Monte Carlo simulated data explained in the discovery limit procedure in Sec. 7.4. A larger value of q corresponds to a larger discrepancy between H_0 and H_1, i.e. larger q-values indicate that the data is more compatible with the signal+background hypothesis H_1. A negative cross section σ_n indicates that the data is more compatible with the only background hypothesis H_0, because it has no physical meaning.

The corresponding likelihood function for a fixed WIMP mass m_χ is an extended likelihood [77] given by

$$\begin{aligned} \mathcal{L}(\sigma_n, \vec{\phi}_\nu\,; m_\chi) =& \text{Pois}\left(N_{\text{obs}} \middle| N_\chi(\sigma_n; m_\chi) + \sum_{j=1}^{n_\nu} N_\nu(\phi_\nu^j) \right) \times \prod_{i=1}^{N_{\text{obs}}} \frac{f(E_{R_i}, \sigma_n, \vec{\phi}\,; m_\chi)}{N_\chi(\sigma_n; m_\chi) + \sum_{j=1}^{n_\nu} N_\nu(\phi_\nu^j)} \\ & \times \prod_{j=1}^{n_\nu} L_j(\phi_\nu^j), \end{aligned} \tag{7.21}$$

where the distribution $f(E_{R_i}, \sigma_n, \vec{\phi}; m_\chi)$ is normalized by $N_\chi(\sigma_n; m_\chi) + \sum_{j=1}^{n_\nu} N_\nu(\phi^j)$. The rates $N_\chi(\sigma_n; m_\chi) = \varepsilon\mu_\chi(\sigma_n; m_\chi)$, $N_\nu(\phi_\nu^j) = \varepsilon\mu_\nu(\phi_\nu^j)$ are expected event rates of WIMPs and neutrinos given in Tab. 4,

$$\mu_\chi(\sigma_n; m_\chi) = \int_{E_{R_{thr}}}^{E_{R,\chi}^{\max}} dE_R \frac{dR_\chi\,(\sigma_n; m_\chi)}{dE_R}\,, \quad \mu_\nu(\phi_\nu^j) = \int_{E_{R_{thr}}}^{E_{R,\nu}^{\max}} dE_R \frac{dR_\nu(\phi_\nu^j)}{dE_R}. \tag{7.22}$$

Here is to mention, that the maximum recoil energy $E_{R,\nu}^{\max}$ of course depends on the neutrino source.

The first factor in the likelihood (7.21) appears as a Poisson distribution

$$\mathrm{Pois}\left(N_{\mathrm{obs}}\middle| N_\chi(\sigma_n;m_\chi)+\sum_{j=1}^{n_\nu}N_\nu(\phi^j)\right)=\frac{(N_{\mathrm{exp}})^{N_{\mathrm{obs}}}\,e^{-N_{\mathrm{exp}}}}{N_{\mathrm{obs}}!}, \tag{7.23}$$

where $N_{\mathrm{exp}} = N_\chi(\sigma_n;m_\chi)+\sum_{j=1}^{n_\nu}N_\nu(\phi^j)$ is the total number of expected events. The number of observed WIMP events N_{obs}^χ and the number of observed neutrino events $N_{\mathrm{obs}}^{\nu,j}$ for each neutrino are Poisson distributed around the expected number of events $N_\chi(\sigma_n;m_\chi)$ and $N_\nu(\phi^j)$. Then, the total number of observed events $N_{\mathrm{obs}} = N_{\mathrm{obs}}^\chi + \sum_j^{n_\nu} N_{\mathrm{obs}}^{\nu,j}$ in an experiment is also Poisson distributed with mean N_{exp} (sum of Poisson distributed numbers is again a Poisson distributed number, see App. D.2 and Ref. [146]).

The second factor in the likelihood (7.21) characterizes the probability distribution of observed recoil energies in an experiment

$$f(E_{R_i},\sigma_n,\vec{\phi};m_\chi)=N_\chi(\sigma_n;m_\chi)f_\chi(E_{R_i};m_\chi)+\sum_{k=1}^{n_\nu}N_\nu(\phi^k)f_\nu^k(E_{R_i}). \tag{7.24}$$

The probability distributions $f_\chi(E_{R_i};m_\chi)$, $f_\nu^k(E_{R_i})$ are normalized differential recoil rates obtained by

$$f_\chi(E_{R,i};m_\chi)=\frac{\varepsilon\frac{dR_\chi}{dE_R}(E_{R,i},\sigma_n;m_\chi)}{\varepsilon\mu_\chi(\sigma_n;m_\chi)}=\frac{G_\chi(E_{R,i},m_\chi)}{\int_{E_{R_{thr}}}^{E_R^{max}}dE_R\,G_\chi(E_R;m_\chi)}, \tag{7.25}$$

$$f_\nu^j(E_{R,i})=\frac{\varepsilon\frac{dR_\nu}{dE_R}(E_{R,i};\phi_\nu^j)}{\varepsilon\mu_\nu(\phi_\nu^j)}=\frac{G_\nu^j(E_{R,i})}{\int_{E_{R_{thr}}}^{E_{R,\nu}^{max}}dE_R\,G_\nu^j(E_R)}, \tag{7.26}$$

where $f_\chi(E_{R_i};m_\chi)$ and $f_\nu^j(E_{R_i})$ neither depend on the cross section σ_n, the flux ϕ^j nor on the exposure ε. A better way to see it, is to rewrite the differential recoil rates as $\frac{dR_\chi}{dE_R} = \sigma_n\ G_\chi(E_R,m_\chi)$ and $\frac{dR_\nu^j}{dE_R} = \phi^j\ G_\nu^j(E_R)$. Equation (7.24) can then be reduced to the sum of differential recoil rates

$$f(E_{R_i},\sigma_n,\vec{\phi}\,;m_\chi)=\varepsilon\left(\frac{dR_\chi(E_{R_i},\sigma_n;m_\chi)}{dE_R}+\sum_{j=1}^{n_\nu}\frac{dR_\nu(E_{R_i},\phi_\nu^j)}{dE_R}\right). \tag{7.27}$$

The third factor in the likelihood function (7.21) is a multiplication of probability distributions of the nuisance parameters $\vec{\phi}_\nu$. Neutrino fluxes ϕ_ν^j occurring in a experiment are Gaussian distributed with mean $\overline{\phi}_\nu^j$ and uncertainty σ_j given in Tab. 4. Therefore, the likelihood function (7.21) is extended by further restrictions given as

$$L_j(\phi_\nu^j)=\frac{1}{\sqrt{2\pi\sigma_j^2}}\,e^{\frac{-\left(\overline{\phi}_\nu^j-\phi_\nu^j\right)^2}{2\sigma_j^2}}. \tag{7.28}$$

Taking all the simplifications into account the extended likelihood function (7.21) can be expressed as

$$\mathcal{L}(\sigma_n,\vec{\phi}_\nu\,;m_\chi)=\frac{e^{-\left(N_\chi(\sigma_n;m_\chi)+\sum_{j=1}^{n_\nu}N_\nu(\phi^j)\right)}}{N_{obs}!}\times\prod_{i=1}^{N_{obs}}\left[\varepsilon\left(\frac{dR_\chi(E_{R_i},\sigma_n;m_\chi)}{dE_R}+\sum_{j=1}^{n_\nu}\frac{dR_\nu(E_{R_i},\phi_\nu^j)}{dE_R}\right)\right]$$
$$\times\prod_{j=1}^{n_\nu}L_j(\phi_\nu^j). \tag{7.29}$$

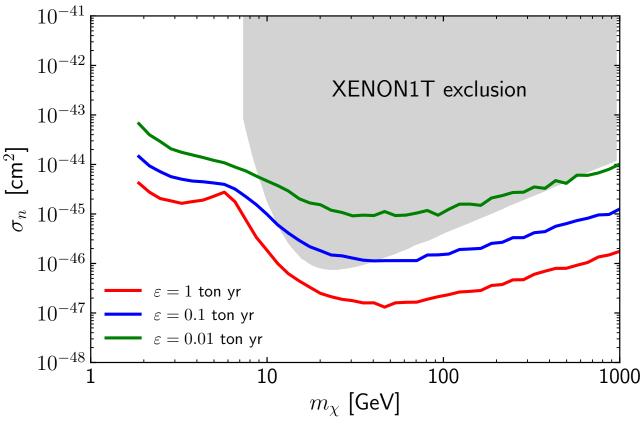

(a)

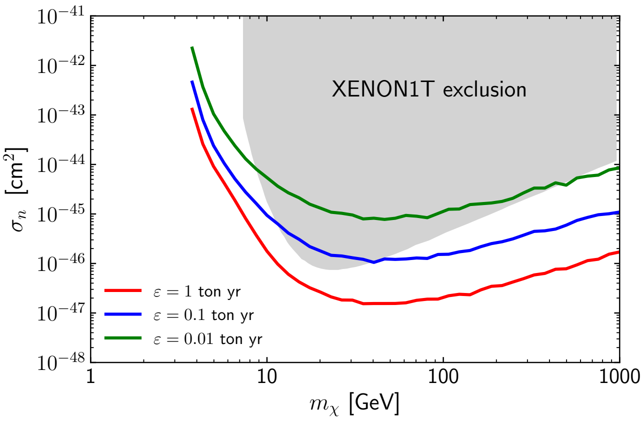

(b)

Figure 28: Discovery limits at 90% C.L. for various exposures and thresholds **(a)** $E_{R_{thr}} = 0.1$ keV, **(b)** $E_{R_{thr}} = 1$ keV. A wide WIMP mass range is excluded by the experiment XENON1T at 90% C.L. [153].

The discovery limits on the WIMP nucleon cross section σ_n are shown in Fig. 28 for different exposures ε and thresholds $E_{R_{thr}}$ assuming a significance level $p_0 \leq 2 \times 0.00135$ (3σ discovery) and a confidence level $1 - \beta = 0.9$ (90% confidence level). In this case, we require that nine of ten experiments measure at least WIMP events with 3σ significance ($\mathrm{H}_1 : \sigma_n \neq 0$ is verified with at least 3σ). As can be seen the sensitivity depends on the exposure and threshold of an experiment. For smaller exposures, less WIMP events are measured. In order to obtain a significant discovery of 3σ, higher cross sections are required to be more compatible with the signal+background hypothesis $\mathrm{H}_1 : \sigma_n \neq 0$ (higher cross sections lead to higher number of WIMP events). It is harder to distinguish between WIMPs and neutrinos when the number of observed signal events is small and the events induced by neutrino fluxes become relevant. The relevant neutrino fluxes occurring in an experiment depend on the chosen threshold $E_{R_{thr}}$ and on the maximum recoil energy the neutrinos can induce as shown in Fig. 19. For thresholds of 0.1 keV and 1 keV hep, ^{8}B, DSNB and atmospheric neutrinos contribute. All other neutrino fluxes produce non-detectable sub-threshold events. In the lower mass range of WIMPs, higher cross sections of about $5 \cdot 10^{-45}$ cm^2 are necessary to fit the data with a significance of 3σ due to the large number of ^{8}B neutrinos. For smaller cross sections ^{8}B neutrinos swamp the WIMP signal. Atmospheric neutrinos and DSNB mimic WIMPs of higher masses. However, they produce low rates and lower cross sections $\sigma_n \in [10^{-47}, 5 \cdot 10^{-46}]$ cm^2 are sufficient to discover a WIMP signal with 3σ significance. For very low thresholds of order about a few eV, the pp and the CNO neutrinos have to be taken into account. In this case, experiments will be sensitive to WIMP masses below 1 GeV.

7.4 Recipe to compute the discovery limits on σ_n

1. Fix the WIMP mass m_χ
2. Fix the exposure ε and the threshold $E_{R_{thr}}$ (We took exposures $\varepsilon = 0.01, 0.1, 1$ ton yr and thresholds $E_{R_{thr}} = 0.1, 1$ keV.)
3. Take a range of cross sections σ_n^{true}, which you want to analyse. We call them true values, because they characterize the WIMP models. (We took 70 points in the range $[10^{-50}, 10^{-42}]$ cm^2 evenly distributed on the log-grid and parametrized the cross section as $\sigma_n = 10^x$ to restrict it to positive physical values.)

Generate DM events

Generate the observed recoil energies E_R in an experiment for one true cross section σ_n^{true} through Monte Carlo sampling.

4. For a fixed WIMP mass m_χ compute the expected number of WIMP events $N_\chi = \varepsilon\mu_\chi$ for one cross section σ_n^{true} given by Eq. (6.33)

$$N_\chi(\sigma_n; m_\chi) = \varepsilon \int_{E_{R_{\text{thr}}}}^{100\ \text{keV}} dE_R \, \frac{dR_\chi(E_R, \sigma_n; m_\chi)}{dE_R}. \tag{7.30}$$

5. Draw from a Poisson distribution with mean N_χ to obtain the observed number of WIMP events, $N_\chi^{\text{obs}} \sim \text{Pois}(N_\chi)$.

Generate neutrino events

6. Generate neutrino fluxes ϕ_j from a Gaussian distribution with mean $\bar{\phi}_j$ and uncertainty σ_ν^j given in the Tab. 4, $\phi^j \sim \text{No}(\bar{\phi}^j, \sigma_\nu^j)$.

7. Derive the expected number of neutrino events $N_\nu^j = \varepsilon\mu_\nu^j$ with the generated fluxes ϕ_j by the equation

$$N_\nu(\phi^j) = \varepsilon \int_{E_{R_{\text{thr}}}}^{E_{R,\nu}^{\max}} dE_R \, \frac{dR_\nu(E_R, \phi^j)}{dE_R}, \tag{7.31}$$

   where $\epsilon_{\text{ff}}(E_R) = 1$ assuming 100% detector efficiency.

8. Draw from a Poisson distribution with mean N_ν^j for each neutrino source to obtain the observed number of neutrino events in one experiment, $N_{\text{obs}}^{\nu,j} \sim \text{Pois}(N_\nu^j)$.

Generate recoil energies

9. Generate recoil energies E_R by drawing $N_{\text{obs}}^\chi, N_{\text{obs}}^{\nu,j}$ times from the PDFs $f_\chi(E_{R_i}, m_\chi), f_\nu^j(E_{R_i})$ (normalized differential recoil rates (7.25), (7.26)) using the inverse transform sampling method explained in App. D.3. (The best way to deal with the inverse of the cumulative distribution function (CDF) $F(E_R)$ of f_χ, f_ν^j is to evaluate the CDF $F(E_R)$ for the observed recoil energy range $[0, 100]$ keV. We took 10000 points in this range. For each $u \sim \text{U}([0,1])$ drawn from the standard uniform distribution, one can find the nearest value, where $F(E_R) \approx u$. Then, one can extract the corresponding recoil energy E_R.)

10. Combine the generated recoil energies in one list. This is our data set for one cross section, i.e. for one mock experiment.

Derive the significance Z_{obs} for a 90% confidence level

The next step is to estimate the cross section σ_n and the fluxes ϕ^j from our generated data to see which hypothesis fits better the data.

11. Minimize the negative log-likelihood function $(-\ln L)$ in σ_n and the fluxes ϕ_j for the only background hypothesis $\text{H}_0 : \sigma_n = 0$ and for signal+background hypothesis $\text{H}_1 : \sigma_n \neq 0$ for one mock experiment/one data set containing the generated recoil energies. For the hypothesis H_0 one minimizes only in the fluxes ϕ_j by setting σ_n to zero.

12. Obtain the q-value by deriving the likelihood ratio test (7.20) and calculate the corresponding significance $Z = \sqrt{q}$.

13. Generate an ensemble of 500 mock experiments for the same cross section $\sigma_n^{\rm true}$ to obtain a statistical set of significances Z by repeating the points 4-12. Thereby one obtains the distribution $f(Z\,|\mathrm{H}_1)$ from the ensemble of 500 mock experiments.

14. Derive the significance $Z_{\rm obs}$ for a 90% confidence level for this ensemble by deriving the statistical power (7.19).

Deriving the discovery limits with 3σ

15. Repeat the points 4-14 for several cross sections $\sigma_n^{\rm true}$ in the range explained in 3.

16. Derive $Z_{\rm obs}$ for each true cross section $\sigma_n^{\rm true}$. The $Z_{\rm obs}$ should increase with higher cross sections. (For low cross sections, where data is more compatible with the only background hypothesis H_0 the observed significances $Z_{\rm obs}$ may fluctuate.)

17. Terminate the calculation once $Z_{\rm obs} \geq 5$ is reached.

18. Interpolate a function in the plane $(\sigma_n^{\rm true}, Z_{\rm obs})$ to determine the $\sigma_n^{\rm true}$ for $Z_{\rm obs} = 3$. This corresponds to a 3σ WIMP event.

Alternative way of deriving the discovery limits for one mass

Instead of working with the significances, one can work with the q-values.

(i) The procedure remains the same until the point 12, but we don't compute the significances.

(ii) Generate an ensemble of 500 mock experiments for the same cross section $\sigma_n^{\rm true}$ to obtain a statistical set of q-values by repeating the points 4-12 (without computing Z).

(iii) Repeat the points 4-12 and (i)-(ii) for several cross sections $\sigma_n^{\rm true}$ in the range explained in 3. Now one obtains the distribution $f(q\,|\mathrm{H}_1)$.

(iv) Derive the observed q-value $q_{\rm obs}$ for a 90% confidence level for this ensemble by deriving the statistical power (7.19) related to q.

(v) Derive $q_{\rm obs}$ for each true cross section $\sigma_n^{\rm true}$ and terminate the calculation once $q_{\rm obs} \geq 10$ is reached.

(vi) Interpolate a function in the plane $(\sigma_n^{\rm true}, q_{\rm obs})$ to determine the $\sigma_n^{\rm true}$ for $q_{\rm obs} = 9$. This corresponds to a 3σ WIMP event.

8 Dark Radiation from decaying Dark Matter

Whereas DM constitutes $\sim 26\%$ of the energy budget of the universe, the number budget is unknown [154]. Under the assumption that a fraction of DM particles decay, the energy budget of dark radiation (DR) may be small, but the number of DR quanta may take large values and can even be the most populous species in our universe. The total DR flux may be large enough to leave a detectable signal in experiments, such as XENON1T [24] and CREEST [26]. The flux is generally composed of a galactic and an extragalactic component.

8.1 Galactic particle flux

Consider a small fraction $\kappa = 0.1$ of DM particles X, that are unstable and decay into particles λ within our galaxy. For simplicity, assume the progenitor X has one decay channel with decay rate $\Gamma_X = 1/\tau_X$, where τ_X is the lifetime of the progenitor. The number of decays in a volume element dV is given by

$$\Gamma_X \frac{\kappa\rho_X(r(s,\theta))e^{-\frac{t_0}{\tau_X}}}{m_X} dV, \tag{8.1}$$

where $\rho_X(r(s,\theta))$ is the DM density at distance s and for an observation angle θ , m_X is the progenitor mass and $t_0 = 13.7$ Gyr [43] is the age of the universe. Then, the total number of particles λ per energy originating from dV at distance s is obtained by

$$\frac{dN}{dE_\lambda}\Gamma_X \frac{\kappa\rho_X(r(s,\theta))\, e^{-\frac{t_0}{\tau_X}}}{m_X} dV, \tag{8.2}$$

where $\frac{dN}{dE_\lambda}$ is their energy spectrum. The energy differential galactic flux is given by

$$\frac{d\Phi_{\lambda,\mathrm{gal.}}}{dE_\lambda} = \frac{1}{dA}\frac{dN}{dE_\lambda}\Gamma_X \frac{\kappa\rho_X(r(s,\theta))\, e^{-\frac{t_0}{\tau_X}}}{m_X} dV, \tag{8.3}$$

where the particles λ are crossing through an area dA. Consider a full angle observation and integrate over the whole area of the sphere ($dA \to 4\pi s^2$, $dV = s^2\, ds d\Omega$). Then, we find

$$\begin{aligned}\frac{d\Phi_{\lambda,\mathrm{gal.}}}{dE_\lambda} &= \frac{1}{4\pi}\frac{dN}{dE_\lambda}\frac{\kappa\Gamma_X\, e^{-\frac{t_0}{\tau_X}}}{m_X}\int_{\Delta\Omega}\int_{\mathrm{l.o.s}} \rho_X(r(s,\theta)) ds\, d\Omega = \frac{1}{4\pi}\frac{dN}{dE_\lambda}\frac{\kappa\Gamma_X\, e^{-\frac{t_0}{\tau_X}}}{m_X} r_\odot\rho_\odot \int_{\Delta\Omega} J_{\mathrm{dec}}(\theta) d\Omega \\ &= \frac{dN}{dE_\chi}\frac{\kappa\Gamma_X\, e^{-\frac{t_0}{\tau_X}}}{m_X} r_\odot\rho_\odot \langle J_{\mathrm{dec}}(\theta)\rangle,\end{aligned} \tag{8.4}$$

where the J-factor is averaged,

$$\langle J_{\mathrm{dec}}(\theta)\rangle = \frac{1}{4\pi}\int_{\Delta\Omega} J_{\mathrm{dec}}(\theta) d\Omega = \frac{1}{4\pi}\int_0^{2\pi}\int_{-1}^{1} J_{\mathrm{dec}}(\theta)\; d\cos\theta\, d\phi \quad \forall\, \theta, \phi. \tag{8.5}$$

8.2 J-factor

The J-factor is an integral along the line of sight s. For decaying DM particles the J-factor [36] is given by

$$J_{\mathrm{dec}}(\theta) = \frac{1}{r_\odot\rho_\odot}\int_{l.o.s} ds\, \rho(r(s,\theta)) \tag{8.6}$$

and is proportional to the density weighted by the distance $r_\odot = 8.33$ kpc from the observer (Earth) to the galactic center and the local dark matter density $\rho_\odot = 0.3$ GeV/cm^3. The distance between the galactic center and the observation window $\Delta\Omega$ is $r(s,\theta) = \sqrt{s^2 + r_\odot^2 - 2sr_\odot\cos\theta}$ (see galactic

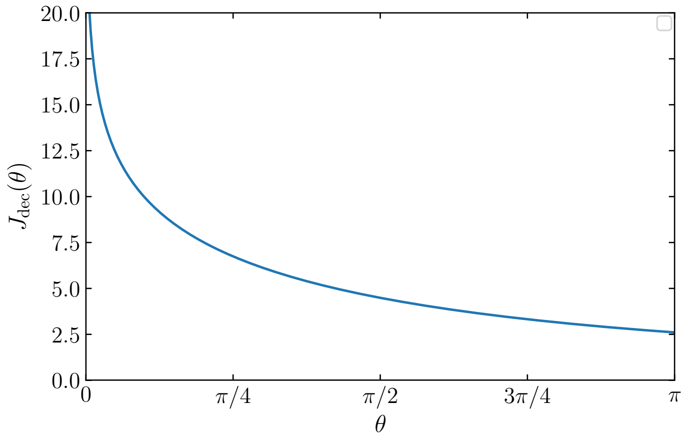

Figure 29: The J-factor $J_{\mathrm{dec}}(\theta)$ for decay.

coordinates in App. C.1). The J-factor $J_{\mathrm{dec}}(\theta)$ is rotation invariant along the axis of $r_\odot$ [36]. For a detector with no directional sensitivity as is the case for DM detectors, one averages over the whole angles [27]

$$\Delta\Omega = \int_0^{2\pi}\int_0^{\pi} d\varphi\, d\theta \sin\theta = 4\pi, \qquad \langle J_{\mathrm{dec}}(\theta)\rangle = \frac{1}{\Delta\Omega}\int_0^{2\pi}\int_0^{\pi} d\varphi\, d\theta \sin\theta J_{\mathrm{dec}}(\theta). \tag{8.7}$$

Choosing the NFW-profile we obtain an average J-factor $\langle J_{\mathrm{dec}}(\theta)\rangle = 2.1885$.

8.3 Extragalactic particle flux

Consider particles λ coming from the universe from larger distances outside our milky way galaxy. In this case, the redshift of the momentum $|\vec{p}_{\lambda,\mathrm{em}}|$ of particles λ has to be taken into account ($|\vec{p}_{\lambda,\mathrm{em}}|$ is the momentum at emission). The flux of these particles is derived in the FWR metric [16, 39, 40, 155]

$$ds^2 = g_{\mu\nu}dx^\mu dx^\nu = dt^2 - a^2(t)\left[\frac{dr^2}{1-Kr^2} + r^2 d\theta^2 + r^2\sin^2\theta\, d\varphi^2\right] = dt^2 - a^2(t)\left[\frac{dr^2}{1-Kr^2} + r^2 d\Omega^2\right], \tag{8.8}$$

where r, θ, φ are comoving coordinates, $t = s$ is the proper time and $a(t)$ is a time dependent scale factor following a radial ray (θ, φ constant $\Rightarrow d\theta = d\varphi = 0$) to an comoving object at distance r. The proper distance (distance in the FRW metric $g_{\mu\nu}dx^\mu dx^\nu$) is given by

$$d_p(t,r) = \int_0^r \sqrt{|g_{rr}|}dr = a(t)\int_0^r \frac{dr}{\sqrt{1-Kr^2}}dr = a(t)\int_0^\chi d\chi = a(t)\chi. \tag{8.9}$$

The distance χ is known as the comoving distance and is time independent, where the expansion rate is scaled out. The proper volume element dV_p defined by the proper distance $d_p(t,r)$ at a time t is given by [16, 155]

$$dV_p = d_p^2\, dd_p\, d\Omega = [a(t)\chi]^2\, a(t)d\chi d\Omega = a(t)^3\chi^2 d\chi d\Omega = \frac{a^3(t_0)}{(1+z)^3}\chi^2 d\chi d\Omega, \tag{8.10}$$

where dd_p is an infinitesimal element of the proper distance. In equation (8.10) the redshift relation $\frac{a(t_0)}{a(t)} = (1+z)$ is used, where $a(t_0) = 1$ is the scale factor today at $t_0 = 13.7$ Gyr and z is the redshift factor [16].

The number of decaying particles X per unit time, is given by the Eq. (8.1) and can be used to obtain the number of decays at redshift z

$$\begin{aligned}\Gamma_X \frac{\kappa\rho_X(r(s,\theta))e^{-\Gamma_X t(z)}}{m_X} dV_p &= \Gamma_X \frac{\kappa\rho_{\mathrm{m},0} a^{-3}(z) e^{-\Gamma_X t(z)}}{m_X} \frac{a^3(t_0)}{(1+z)^3}\chi^2 d\chi d\Omega \\ &= \Gamma_X \frac{\kappa\rho_{\mathrm{m},0} e^{-\Gamma_X t(z)}}{m_X}\chi^2 d\chi d\Omega,\end{aligned} \tag{8.11}$$

where $\rho_X(r(s,\theta)) = \rho_{\mathrm{m}}(z) = \rho_{m,0}a^{-3}(z)$ is the redshifted density and $\rho_{\mathrm{m},0}$ is the density at present time. Here we assume that only a fraction κ of total DM density decays, where $\kappa = \frac{\rho_X(t)}{\Omega_{\mathrm{dm}}\rho_{\mathrm{crit}}}\Big|_{t\ll\tau_X}$ is consistent with cosmological constraints [156] and τ_X is the lifetime of the progenitor X.

The energy-differential extragalactic flux of λ at observation (Earth), is then given by

$$\begin{aligned}\frac{d\Phi_{\lambda,\mathrm{e.g.}}}{dE_\lambda} &= \frac{1}{\int dA}\frac{dN}{dE_\lambda}\Gamma_X \frac{\kappa\rho_{\mathrm{m},0} e^{-\Gamma_X t(z)}}{m_X}\chi^2 d\chi d\Omega = \frac{1}{4\pi d_p^2}\frac{dN}{dE_\lambda}\Gamma_X \frac{\kappa\rho_{\mathrm{m},0} e^{-\Gamma_X t(z)}}{m_X}\chi^2 d\chi d\Omega \\ &= \frac{1}{4\pi a^2(z)\chi^2}\frac{dN}{dE_\lambda}\Gamma_X \frac{\kappa\rho_{\mathrm{m},0} e^{-\Gamma_X t(z)}}{m_X}\chi^2 d\chi d\Omega = \frac{1}{4\pi a^2(t_0)\chi^2}\frac{dN}{dE_\lambda}\Gamma_X \frac{\kappa\rho_{\mathrm{m},0} e^{-\Gamma_X t(z)}}{m_X}\chi^2 d\chi d\Omega,\end{aligned} \tag{8.12}$$

where E_λ is the energy $\frac{dN}{dE_\lambda}$ is the energy spectrum at observation. The redshifted particles coming from a volume dV_p propagate through an area $\int dA = 4\pi a^2(t)\chi^2 = 4\pi a^2(t_0)\chi^2$ of the detector at $z = 0$. Integrating over the whole sphere $\int d\Omega = 4\pi$, because of isotropy and setting $a(t_0) = 1$ the extragalactic flux at observation reduces to

$$\frac{d\Phi_{\chi,\mathrm{e.g.}}}{dE_\lambda} = \int d\chi \frac{dN(E_{\mathrm{em}})}{dE_\lambda}\Gamma_X \frac{\kappa\rho_{\mathrm{m},0} e^{-\Gamma_X t(z)}}{m_X}. \tag{8.13}$$

The spectrum depends on the energy at emission E_{em}, where the corresponding three momentum at emission $|\vec{p}_{\lambda,\mathrm{em}}| = |\vec{p}_\lambda|(1+z)$ is obtained by redshifting the three momentum at observation $|\vec{p}_\lambda|$. For massless particles $m_\lambda = 0$ the energy at emission $E_{\mathrm{em}} = E_\lambda(1+z)$ is simply given by the reshifted energy at observation E_λ. For a radial γ-ray ($d\Omega = 0, ds^2 = 0$) one obtains a relation between the proper time and the comoving distance [157]

$$dt = a(t)d\chi \quad \text{(for a flat universe } K = 0\text{)}. \tag{8.14}$$

Let the crest of a wave be emitted at (t_e, p_e) (choose the origin) and be observed at (t_o, p_o), then the comoving distance is given by [157]

$$\int_{\chi(p_e)=0}^{\chi(p_o)} d\chi' = \int_{t_e}^{t_o}\frac{dt}{a(t)} = \int_{a_e}^{a_o}\frac{da}{a^2(t)H(t)} = -\int_z^0 \frac{dz'}{H(z')} = \int_0^z \frac{dz'}{H(z')}, \tag{8.15}$$

where from $H = \frac{\dot{a}}{a} \Rightarrow dt = \frac{da}{aH}$ and from $a = \frac{1}{(1+z)}$ with $a(t_0) = 1 \Rightarrow da = -\frac{1}{(1+z)^2}dz = -a^2 dz$. In the end the extragalactic flux of massless particles can be written as

$$\frac{d\Phi_{\lambda,\mathrm{e.g.}}}{dE_\lambda} = \Gamma_X \frac{\kappa\Omega_{\mathrm{dm}}\rho_{\mathrm{crit}}}{m_X}\int_0^{z_f}\frac{dz}{H(z)}\frac{dN(E_\lambda(1+z))}{dE_\lambda}e^{-\Gamma_X t(z)} \tag{8.16}$$

with the Hubble expansion rate $H(z) = H_0\sqrt{(1+z)^3\Omega_M + \Omega_\Lambda}$ $(\Omega_k = 0)$, $\rho_{m,0} = \Omega_{\mathrm{dm}}\rho_{\mathrm{crit}}$ and ρ_{crit} is the critical density.

For massive particles the extragalactic flux gets an additional factor, the redshifted velocity at emission $v_{\mathrm{em}}(z)$

$$\frac{d\Phi_{\lambda,\mathrm{e.g.}}}{dE_\lambda} = \Gamma_\lambda \frac{\kappa\Omega_{\mathrm{dm}}\rho_{\mathrm{crit}}}{m_X}\int_0^{z_f}\frac{dz}{H(z)}\frac{dN(E_{\mathrm{em}})}{dE_\lambda}e^{-\Gamma_\lambda t(z)}v_{\mathrm{em}}(z) \tag{8.17}$$

using the expression

$$d\chi = \frac{d\chi}{dd_p}\frac{dd_p}{dt}dt = v_{\rm em}(t)\frac{dt}{a(t)} \quad \Rightarrow \quad \int_{\chi(p_e)=0}^{\chi(p_o)} d\chi' = \int_0^z \frac{dz'}{H(z')}v_{\rm em}(z) \tag{8.18}$$

and $E_{\rm em} = \sqrt{|\vec{p}_{\lambda,\rm em}|^2 + m_\lambda^2} = \sqrt{|\vec{p}_\lambda|^2(1+z)^2 + m_\lambda^2}$. For the lookback time $t(z)$ for a flat universe ($\Omega_K = 0$) we find

$$t(z) = \int_z^\infty \frac{dz'}{(1+z')H(z')} = \frac{2}{3H_0}\int_{u(z)}^\infty \frac{du}{u^2 - \Omega_\Lambda} = \frac{1}{3H_0\sqrt{\Omega_\Lambda}} \ln\left|\frac{\sqrt{1+(1+z)^3\frac{\Omega_M}{\Omega_\Lambda}}+1}{\sqrt{1+(1+z)^3\frac{\Omega_M}{\Omega_\Lambda}}-1}\right|, \tag{8.19}$$

where the substitution $u = \frac{H(z')}{H_0} = \sqrt{(1+z')^3\Omega_M + \Omega_\Lambda}$ was used and $u(z) = \sqrt{(1+z)^3\Omega_M + \Omega_\Lambda}$.

8.4 Dark Radiation from two-body decays

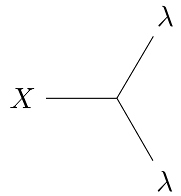

(8.20)

The injection spectrum for a two-body decay $X \to \lambda\lambda$ is given by a delta function [27]

$$\left.\frac{dN(E_{\rm em})}{dE_\lambda}\right|_{2\text{ body}} = N_\lambda \delta(E_{\rm em} - E_{\rm in}), \tag{8.21}$$

where $E_{\rm in} = \frac{m_X}{2}$ is the injection energy of particles λ and $N_\lambda = 2$ is the number of particles λ produced at decay. The velocity dispersion effects are negligible and X decays at rest. In the two-body decay the redshift integral of the extragalactic flux (8.17) can be evaluated directly, if the delta-function is rewritten as

$$\begin{aligned}\delta(E_{\rm em} - E_{\rm in}) &= \delta\left(\sqrt{|\vec{p}_\lambda|^2(1+z)^2 + m_\lambda^2} - E_{\rm in}\right) = \frac{\sqrt{|\vec{p}_{\rm in}|^2 + m_\lambda^2}}{|\vec{p}_\lambda||\vec{p}_{\rm in}|}\delta\left(z - \left(\frac{|\vec{p}_{\rm in}|}{|\vec{p}_\lambda|} - 1\right)\right) \\ &= \frac{\sqrt{|\vec{p}_{\rm in}|^2 + m_\lambda^2}}{|\vec{p}_\lambda||\vec{p}_{\rm in}|}\delta\left(z + 1 - \alpha\right),\end{aligned} \tag{8.22}$$

where $\alpha = \frac{|\vec{p}_{\rm in}|}{|\vec{p}_\lambda|} \geq 1$ and $|\vec{p}_{\rm in}| = \sqrt{E_{\rm in}^2 - m_\lambda^2} = \sqrt{\left(\frac{m_X}{2}\right)^2 - m_\lambda^2}$ is the injected momentum. Then, the extragalactic flux is derived by the following calculation

$$\begin{aligned}\frac{d\Phi_{\lambda,\rm e.g.}}{dE_\lambda} &= \Gamma_X \frac{\kappa\Omega_{\rm dm}\rho_{\rm crit}}{m_X}\int_0^{z_f}\frac{dz}{H(z)}\frac{dN(E_{\rm em})}{dE_\lambda}e^{-\Gamma_\lambda t(z)}v_{\rm em}(z) \\ &= N_\lambda\Gamma_X\frac{\kappa\Omega_{\rm dm}\rho_{\rm crit}}{m_X}\int_0^{z_f}\frac{dz}{H(z)}\delta(E_{\rm em} - E_{\rm in})e^{-\Gamma_X t(z)}v_{\rm em}(z) \\ &= N_\lambda\Gamma_X\frac{\kappa\Omega_{\rm dm}\rho_{\rm crit}}{m_X}\int_{-\infty}^{\infty}\theta(z)\,\theta(z_f - z)\frac{dz}{H(z)}\frac{\sqrt{p_{\rm in}^2 + m_\lambda^2}}{|\vec{p}_\lambda||\vec{p}_{\rm in}|}\delta\left(z+1-\alpha\right)e^{-\Gamma_X t(z)}v_{\rm em}(z) \\ &= N_\lambda\Gamma_X\frac{\kappa\Omega_{\rm dm}\rho_{\rm crit}}{H_0\, m_X}\frac{\sqrt{|\vec{p}_{\rm in}|^2 + m_\lambda^2}}{|\vec{p}_\lambda||\vec{p}_{\rm in}|}\frac{e^{-\Gamma_X t(\alpha-1)}v_{\rm em}(\alpha-1)}{\sqrt{\alpha^3\Omega_M + \Omega_\Lambda}}\theta(\alpha-1)\,\theta(z_f - (\alpha-1)),\end{aligned} \tag{8.23}$$

where the boundaries of the integral are adapted by theta-functions and the Hubble constant at any redshift is given by $H(z) = H_0\sqrt{(1+z)^3\Omega_M + \Omega_\Lambda}$. The theta-function $\theta(z_f - (\alpha - 1))$ can be neglected, because $z_f = 10^4$ is always greater than $\alpha - 1$. In the end the differential extragalactic flux of a two-body decay at observation is expressed as

$$\frac{d\Phi_{\lambda,\text{e.g.}}}{dE_\lambda} = N_\lambda \Gamma_\lambda \frac{\kappa \Omega_{\text{dm}} \rho_{\text{crit}}}{H_0\, m_X} \frac{\sqrt{|\vec{p}_{\text{in}}|^2 + m_\lambda^2}}{|\vec{p}_\lambda||\vec{p}_{\text{in}}|} \frac{e^{-\Gamma_\lambda t(\alpha-1)} v_{\text{em}}(\alpha-1)}{\sqrt{\alpha^3 \Omega_M + \Omega_\Lambda}} \theta(\alpha-1), \tag{8.24}$$

where the velocity $v_{\text{em}}(z)$ of the particles λ at emission is given by

$$v_{\text{em}}(z) = \frac{p_{\text{em}}}{E_{\text{em}}} = \frac{|\vec{p}_\lambda|(1+z)}{\sqrt{|\vec{p}_\lambda|^2(1+z)^2 + m_\lambda^2}}. \tag{8.25}$$

Rewriting the velocity as

$$v_{\text{em}}(\alpha-1) = v_{\text{em}}\left(\frac{|\vec{p}_{\text{in}}|}{|\vec{p}_\lambda|} - 1\right) = \frac{|\vec{p}_{in}|}{E_{\text{in}}} = \frac{\sqrt{E_{\text{in}}^2 - m_\lambda^2}}{E_{\text{in}}} \tag{8.26}$$

the extragalactic flux reduces to a compact form

$$\frac{d\Phi_{\lambda,\text{e.g.}}}{dE_\lambda} = N_\lambda \Gamma_\lambda \frac{\kappa \Omega_{\text{dm}} \rho_{\text{crit}}}{H_0\, m_X} \frac{1}{|\vec{p}_\lambda|} \frac{e^{-\Gamma_\lambda t(\alpha-1)}}{\sqrt{\alpha^3 \Omega_M + \Omega_\Lambda}} \theta(\alpha-1). \tag{8.27}$$

The massless case $m_\lambda = 0$ is obtained by putting $v_{\text{em}}(\alpha - 1) = c = 1$

$$\left.\frac{d\Phi_{\lambda,\text{e.g.}}}{dE_\lambda}\right|_{m_\lambda=0} = N_\lambda \Gamma_\lambda \frac{\kappa \Omega_{\text{dm}} \rho_{\text{crit}}}{H_0\, m_X} \frac{1}{|\vec{p}_\lambda|} \frac{e^{-\Gamma_\lambda t(\alpha-1)}}{\sqrt{\alpha^3 \Omega_M + \Omega_\Lambda}} \theta(\alpha-1), \tag{8.28}$$

which lead to an equivalent form of the Eq. (8.27) since $|\vec{p}_\lambda| = E_\lambda$. The differential fluxes for DM-progenitors with $m_X = 50$ MeV and $m_X = 500$ GeV decaying into particles with various masses m_λ are shown in Fig. 30.

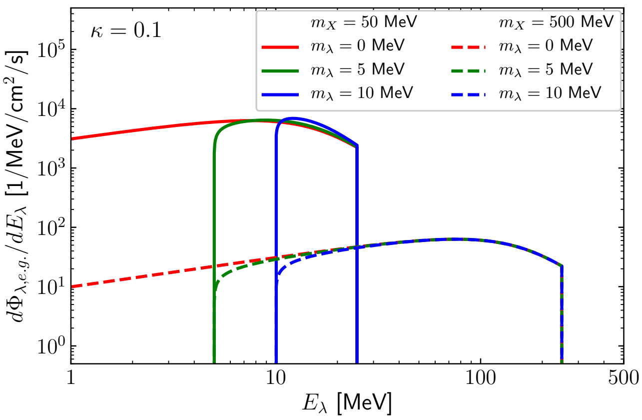

(a)

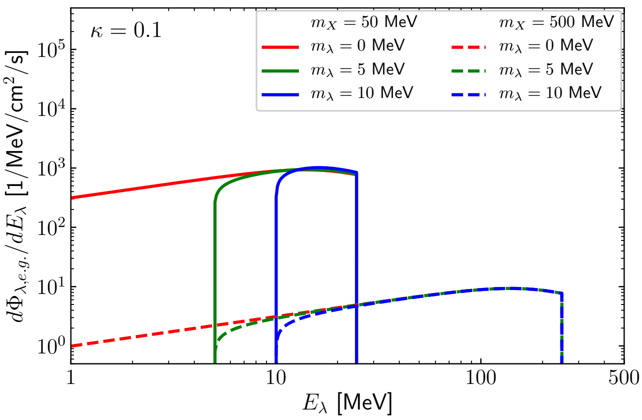

(b)

Figure 30: Differential fluxes from a two body decay of DM-progenitors with $m_X = 50$ MeV and $m_X = 500$ GeV decaying into particles with various masses m_λ: **(a)** $\tau_X = 10$ Gyr, **(b)** $\tau_X = 100$ Gyr.

9 SM neutrinos as dark radiation

An ample possibility is that DR is made from SM neutrinos. Neutrinos are nearly massless, hence progenitor of at most any mass can decay into DR. There exist few scenarios, where SM neutrinos can occur as DR. We consider DM particles decaying directly to neutrinos [27] as reactions $X \to \nu + \overline{\nu}$ (X vector/scalar boson) and $X \to \nu + Y$ (X fermion, Y vector/scalar boson). Additional visible energy injection, e.g. by electron pairs in reactions such as $X \to \nu\bar{\nu}e^-e^+$ are strongly suppressed for (sub-)GeV scale X. In this thesis the focus lies on the two-body decay $X \to \nu\overline{\nu}$, where X is a scalar boson[9]. A scalar particle decaying into two photons $X \to \gamma\gamma$ does not exist at the tree level and is suppressed by quantum loop corrections.

Assume that a scalar DM particle X decays into a neutrino pair

$$X \quad \to \quad \nu\bar{\nu} \tag{9.1}$$

where we may assume that each neutrino flavor is equal weighted, for simplicity. Then, the differential galactic and extragalactic flux for neutrinos $m_\lambda = m_\nu = 0$ is obtained by

$$\frac{d\Phi_{\nu,\text{gal.}}}{dE_\nu} = N_\nu \frac{\kappa \Gamma_X e^{-\frac{t_0}{\tau_X}}}{m_X} r_\odot \rho_\odot \langle J_{\text{dec}}(\theta)\rangle \delta(E_\nu - E_{\text{in}}), \tag{9.2}$$

$$\frac{d\Phi_{\nu,\text{e.g.}}}{dE_\lambda} = N_\nu \frac{\kappa \Omega_{\text{dm}} \rho_{\text{crit}}}{H_0 m_X} \frac{1}{E_\nu} \frac{\Gamma_X e^{-\frac{t(\alpha-1)}{\tau_X}}}{\sqrt{\alpha^3 \Omega_M + \Omega_\Lambda}} \theta(\alpha - 1), \tag{9.3}$$

where $\alpha = E_{\text{in}}/E_\nu$, $E_{\text{in}} = \frac{m_X}{2}$ and $E_\nu = |\vec{p}_\nu|$. The total galactic flux is obtained by evaluating the delta function

$$\Phi_{\nu,\text{gal.}} = N_\nu \frac{\kappa \Gamma_X e^{-\frac{t_0}{\tau_X}}}{m_X} r_\odot \rho_\odot \langle J_{\text{dec}}(\theta)\rangle. \tag{9.4}$$

In the massless case, the total extragalactic flux can be derived analytically (for more details see App. C.2)

$$\Phi_{\nu,\text{e.g.}} = N_\nu \frac{\kappa \Omega_{\text{dm}} \rho_{\text{crit}}}{m_X} \left[1 - \left(\frac{\sqrt{\Omega_M/\Omega_\Lambda + 1} + 1}{\sqrt{\Omega_M/\Omega_\Lambda + 1} - 1} \right)^{-\frac{1}{3H_0\sqrt{\Omega_\Lambda}\tau_X}} \right] \propto \left(1 - e^{-\tilde{t}/\tau_X}\right), \tag{9.5}$$

where $\tilde{t} = \frac{1}{3H_0\sqrt{\Omega_\Lambda}} \ln x_\star$ and $x_\star = \frac{\sqrt{\Omega_M/\Omega_\Lambda+1}+1}{\sqrt{\Omega_M/\Omega_\Lambda+1}-1}$. In Fig. 31 the total extragalactic flux is shown for various progenitor masses m_X. For small lifetimes $\tau_X \leq 10$ Gyr it is constant, whereas it decreases for higher lifetimes. Then, the total DR flux is given by

$$\Phi_{X2\nu} = \Phi_{\nu,\text{gal.}} + \Phi_{\nu,\text{e.g.}}. \tag{9.6}$$

The differential recoil rate in direct detection experiments is then given by

$$\frac{dR_{X2\nu}(E_R)}{dE_R} = N_T \sum_{i=\text{gal,e.g.}} \int_{E_{\nu,\min}}^{E_{\text{in}}} dE_\nu \, \frac{d\Phi_{\nu,i}(E_\nu)}{dE_\nu} \frac{d\sigma_{N\nu}(E_\nu, E_R)}{dE_R}, \tag{9.7}$$

where $E_{\nu,\min} = \sqrt{E_R m_N/2}$ is the minimum energy a neutrino needs to produce a recoil energy. An analytic form exists for the extragalactic differential recoil rate for massless final states [10](for more

[9] It could also be $X \to \nu\nu$, if X is a majorana.

[10] It is important to mention that the difference of two hypergeometric functions does not necessarily have to converge and can cause numerically problems for some lifetimes and masses. In this case, we derived the integral numerically.

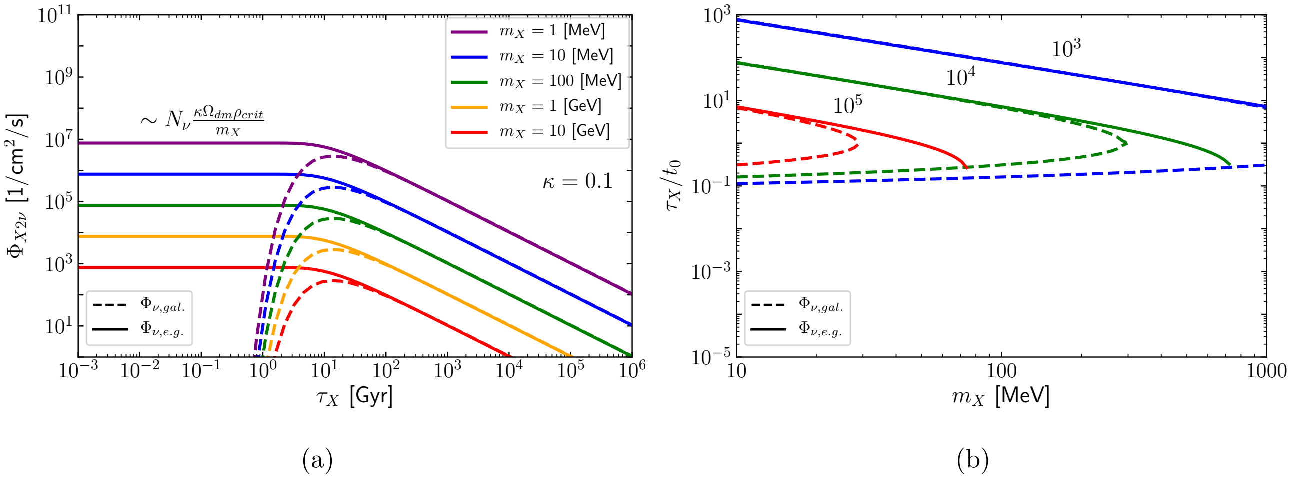

Figure 31: **(a)** The total neutrino flux of the extragalactic component for different DM masses m_X. For small lifetimes $\tau_X \leq 10$ Gyr the flux scales as $1/m_X$. **(b)** Contour lines of fluxes $10^3, 10^4, 10^5$ cm^{-2} s^{-1}. The maximum DR flux is obtained for a lifetime of about the age of the universe $t_0 = 13.7$ Gyr.

details see App. C.3),

$$\frac{dR^{\text{e.g.}}_{X2\nu}}{dE_R} = N_T \frac{Q_W^2 G_F^2 m_N F(q)^2}{4\pi} N_\nu \frac{\kappa \Omega_{\text{dm}} \rho_{\text{crit}}}{m_X} \times \left(x^d_{\text{min}}(E_R) - x^d_\star + \frac{2^{1/3}}{H_0\sqrt{\Omega_\Lambda}\tau_X} \left(\frac{\Omega_\Lambda}{\Omega_M}\right)^{\frac{2}{3}} \frac{E_R m_N}{E^2_{\text{in}}} \frac{{}_2F_1\left(-\frac{1}{3}, \frac{1}{3} - d, \frac{2}{3}; 1 - x\right)}{\sqrt[3]{-1+x}} \Bigg|^{x_\star}_{x_{\text{min}}(E_R)} \right), \tag{9.8}$$

where

$$x_{\text{min}}(E_R) = \frac{\sqrt{\frac{E^3_{\text{in}}}{E^3_{\text{min}}} \frac{\Omega_M}{\Omega_\Lambda} + 1} + 1}{\sqrt{\frac{E^3_{\text{in}}}{E^3_{\text{min}}} \frac{\Omega_M}{\Omega_\Lambda} + 1} - 1}, \quad x_\star = \frac{\sqrt{\frac{\Omega_M}{\Omega_\Lambda} + 1} + 1}{\sqrt{\frac{\Omega_M}{\Omega_\Lambda} + 1} - 1}, \quad d = -\frac{1}{3H_0\sqrt{\Omega_\Lambda}\tau_X}. \tag{9.9}$$

The function ${}_2F_1(a, b, c; z)$ is the Gaussian hypergeometric function and

$$\frac{{}_2F_1\left(-\frac{1}{3}, \frac{1}{3} - d, \frac{2}{3}; 1 - x\right)}{\sqrt[3]{-1+x}} \Bigg|^{x_\star}_{x_{\text{min}}(E_R)} = \frac{{}_2F_1\left(-\frac{1}{3}, \frac{1}{3} - d, \frac{2}{3}; 1 - x_\star\right)}{\sqrt[3]{-1+x_\star}} - \frac{{}_2F_1\left(-\frac{1}{3}, \frac{1}{3} - d, \frac{2}{3}; 1 - x_{\text{min}}(E_R)\right)}{\sqrt[3]{-1+x_{\text{min}}(E_R)}}. \tag{9.10}$$

The differential recoil rate for the galactic component is straight forward to derive

$$\frac{dR^{\text{gal.}}_{X2\nu}}{dE_R} = N_T \frac{Q_W^2 G_F^2 m_N F(q)^2}{4\pi} N_\nu \frac{\Gamma_X e^{-\frac{t_0}{\tau_X}}}{m_X} r_\odot \rho_\odot \langle J_{\text{dec}}(\theta)\rangle \left[1 - \frac{2E_R m_N}{m_X^2}\right]. \tag{9.11}$$

The total expected differential recoil rates in a detector for various lifetimes and masses using xenon as target material ($m_N \approx 122$ GeV for ^{131}Xe) are shown in Fig. 33. The recoil rate is then given by

$$\mu_{X2\nu} = \int_{E_{R_{\text{thr}}}}^{E^{\text{max}}_{R,X2\nu}} dE_R \, \frac{dR_{X2\nu}}{dE_R}. \tag{9.12}$$

The maximum recoil energy 6.12 depends on the mass of the progenitor X

$$E^{\text{max}}_{R,X2\nu} = \frac{m_X^2}{2(m_X + m_N)}, \quad E^{\text{max}}_{R,X2\nu} \simeq \begin{cases} \frac{m_X}{2m_N} & \text{for } m_X \ll m_N \\ \frac{m_X}{2} & \text{for } m_X \gg m_N, \end{cases} \tag{9.13}$$

where $E_\nu^{\max} = E_{\rm in} = \frac{m_X}{2}$ is the maximum energy that neutrinos can carry (see Fig. 32).

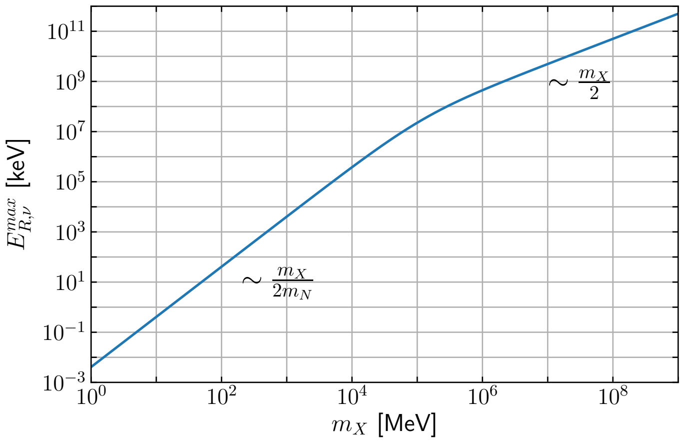

Figure 32: The maximum recoil energy that neutrinos from a two body decay can reach in coherent scattering with a ^{131}Xe target with $m_N \approx 122$ GeV.

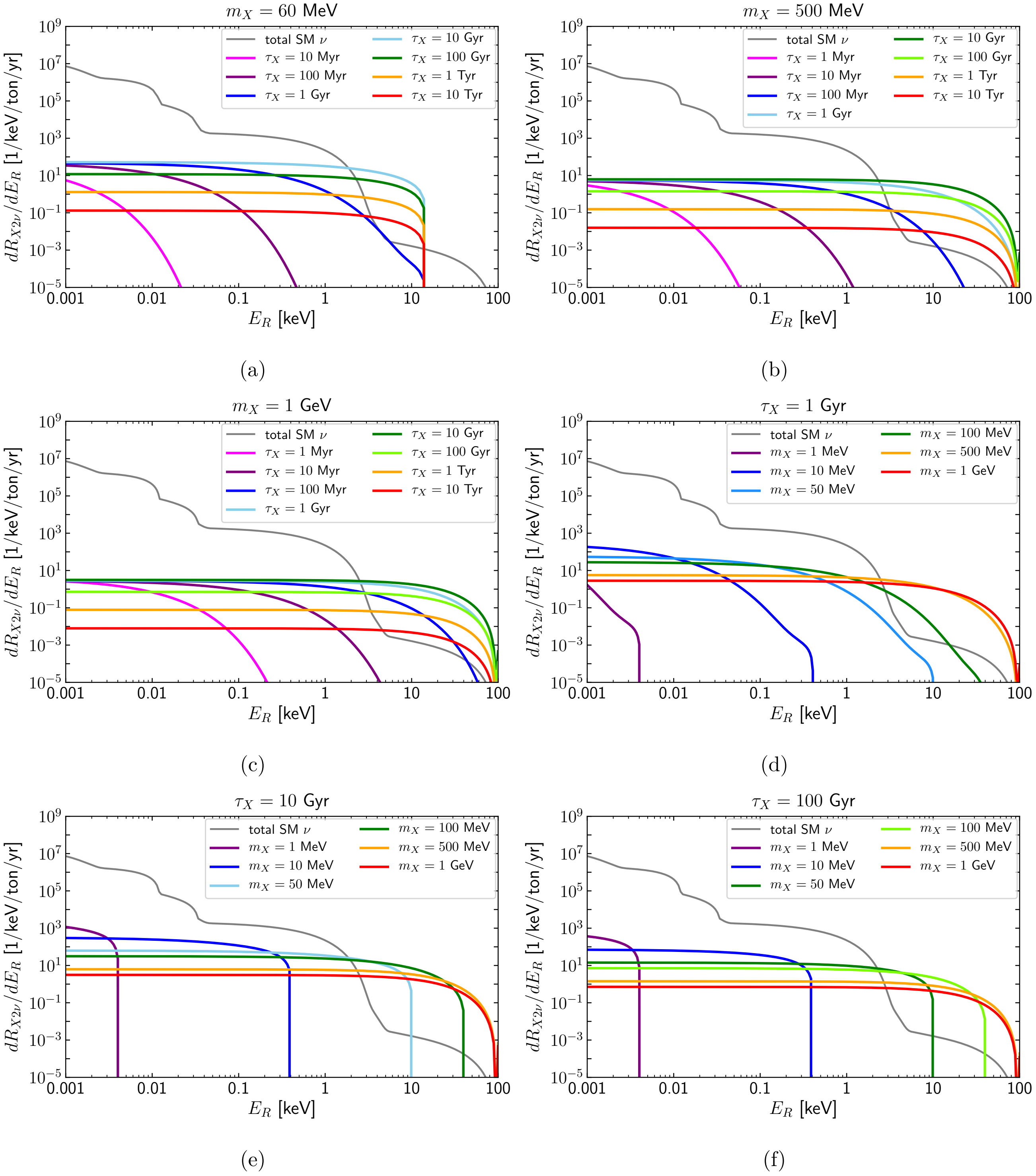

Figure 33: Differential recoil rates for various lifetimes τ_X and masses m_X: **(a)** $m_X = 60$ MeV, **(b)** $m_X = 500$ MeV, **(c)** $m_X = 1$ GeV, **(d)** $\tau_X = 1$ Gyr, **(e)** $\tau_X = 10$ Gyr, **(f)** $\tau_X = 100$ Gyr.

10 WIMPs vs. SM neutrinos and DR neutrinos

In Sec. 8.4 we introduced the new anomalous neutrino flux produced by two-body decays of a DM particle X. Taking into account that DR neutrinos can also mimic WIMPs in their elastic scattering in a detector as shown in Fig 34, the sensitivity on WIMPs decreases even more for certain WIMP masses. In the background-free approach, the exclusion limit at 90% C.L. ($N^{\chi}_{exp} = 2.3$) is shown in Fig. 35 for several masses and lifetimes. In Fig. 36 the exposure is scaled up to the point that one neutrino event is measured as explained in Sec. 7.2, where the neutrino fluxes contain DR contribution. An increase by few orders of magnitude of the position of the neutrino floor in σ_n is noticed for WIMP masses above 6 GeV. As shown in Fig. 33 the DR-induced rates dominate at high recoil energies, beyond the ^{8}B neutrino endpoint. Therefore, in the region between the ^{8}B neutrino peak at $m_\chi = 6$ GeV and the DSNB and atmospheric neutrino contributions at high masses above $m_\chi = 100$ GeV, the DR-induced recoil rates may give the largest contribution. For a small DM mass $m_X = 60$ MeV, the neutrino background does not change at high recoil energies. Therefore, the exclusion limit remains the same for WIMP masses $m_\chi \geq 80$ GeV. Increasing the DM mass, higher recoil energies can be produced and the exclusion limits are pushed to larger values of the WIMP mass, once the DR-induced rates exceed the SM neutrino background. Taking $m_X = 1$ GeV shows that the sensitivity decreases for WIMP masses above 6 GeV. The lifetime can be understood as a scale factor, which increases and decreases the exclusion limits.

The discovery limits take the neutrino background into account. In this case, the sensitivity is again obtained by testing the background-only hypothesis $\mathrm{H}_0 : \sigma_n = 0$ against the signal+background hypothesis $\mathrm{H}_1 : \sigma_n \neq 0$ on the data. The discrepancy is again given by the q-value (7.20) and the corresponding extended likelihood (7.29) is described in Sec. 7.3.3, where the neutrino background is extended by DR contributions.

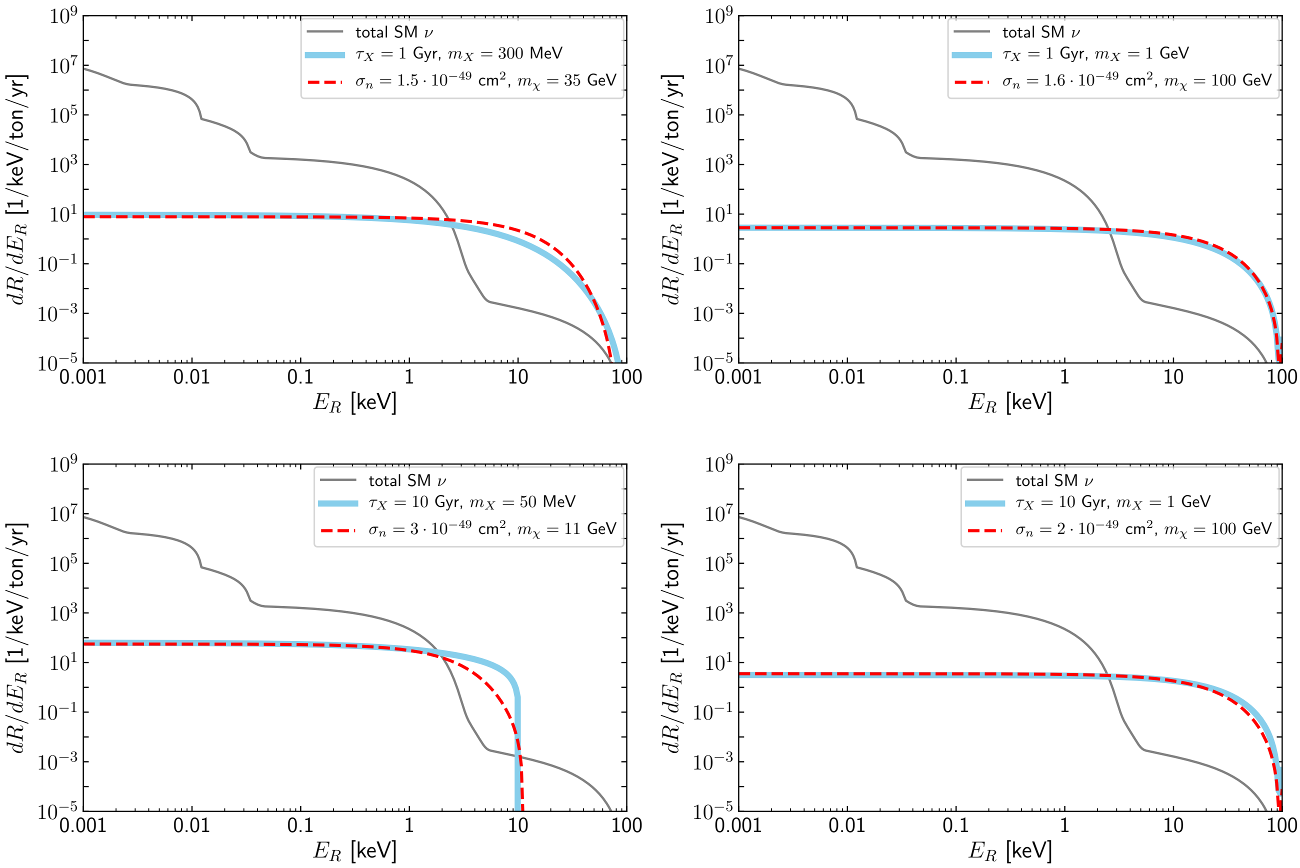

Figure 34: Few examples, where anomalous neutrinos mimic WIMPs in direct detection experiments.

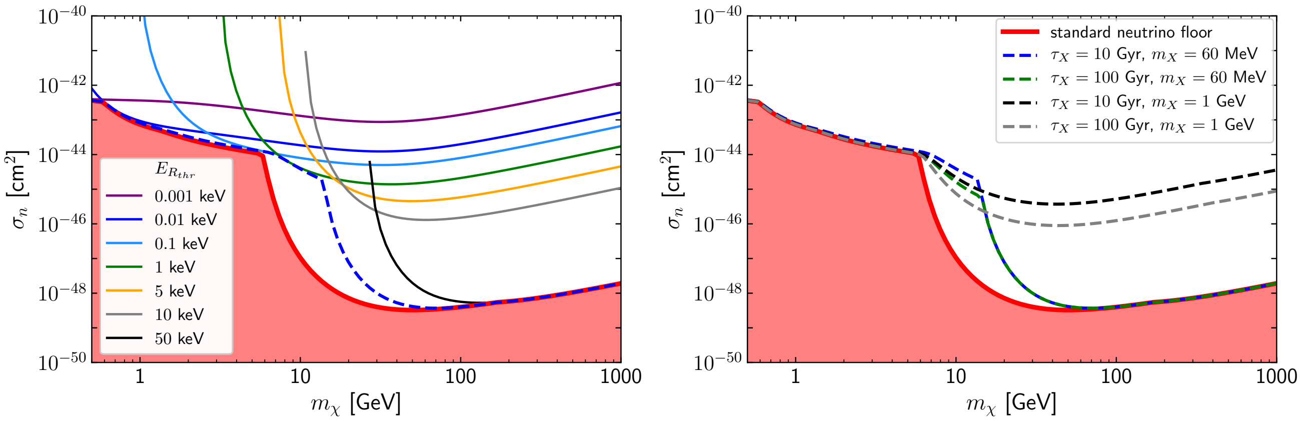

Figure 35: The modified exclusion limit. The standard neutrino floor increases significantly by few orders of magnitude in the region $m_\chi \geq 6$ GeV. In this region the sensitivity decreases and higher cross sections are necessary. In the left picture the blue dashed line correspond to an anomalous recoil rate with $\tau_X = 10$ Gyr and $m_X = 60$ MeV.

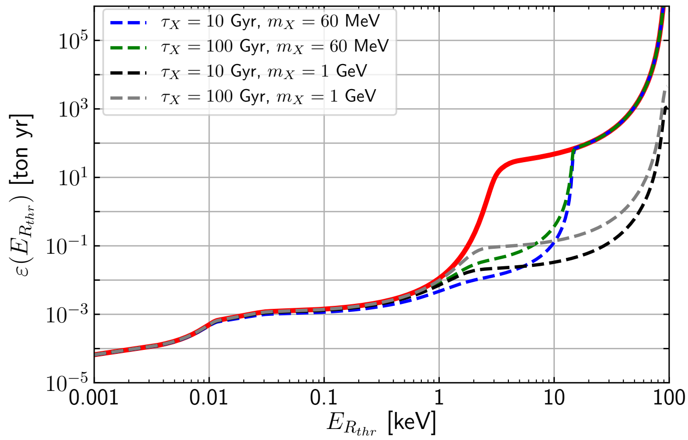

Figure 36: The exposure in the exclusion limit changes with an additional neutrino flux. For higher recoil energies smaller exposures are necessary to measure one neutrino. The exposure for the standard exclusion limit in Sec. 7.1 is shown in red.

Following the same recipe as for the standard neutrino floor (see Sec. 7.4), the discovery limits for several lifetimes τ_X and masses m_X are shown in Fig. 37. In Fig. 37a and Fig. 37b we fixed the lifetime τ_X and the DM mass m_X. Then, the DR flux and the DR-induced recoil rate $\mu_{X2\nu}$ are constant in τ_X and m_X. The differential recoil rate depends only on the recoil energies E_R. The likelihood function is extended by the contribution from DR and is given by

$$\begin{aligned}\mathcal{L}(\sigma_n, \vec{\phi}_\nu\,; m_\chi) = {} & \frac{e^{-\left(N_\chi(\sigma_n; m_\chi) + \sum_{j=1}^{n_\nu} N_\nu(\phi^j) + N_{X2\nu}\right)}}{N_{\text{obs}}!} \\ & \times \prod_{i=1}^{N_{\text{obs}}} \left[\varepsilon\left(\frac{dR_\chi(E_{R_i}, \sigma_n; m_\chi)}{dE_R} + \sum_{j=1}^{n_\nu} \frac{dR_\nu(E_{R_i}, \phi_\nu^j)}{dE_R} + \frac{dR_{X2\nu}(E_{R_i})}{dE_R}\right)\right] \\ & \times \prod_{j=1}^{n_\nu} L_j(\phi_\nu^j),\end{aligned} \tag{10.1}$$

where $\vec{\phi}_\nu$ contains SM neutrino fluxes and $N_{X2\nu} = \varepsilon\mu_{X2\nu}$ is constant for fixed τ_X and m_X. In this case, no Gaussian distribution appears in the likelihood function. In Figs. 37c, 37d we fixed the shape of the particle spectrum for a lifetime τ_X and a DM mass m_X and let $\phi_{X2\nu}$ act now as a scaling parameter similar to the SM neutrino background,

$$\frac{d\phi_{X2\nu}(E_\nu)}{dE_\nu} = \phi_{X2\nu}\frac{dM_{X2\nu}(E_\nu)}{dE_\nu}. \tag{10.2}$$

The constant particle spectrum is derived by

$$\frac{dM_{X2\nu}(E_\nu)}{dE_\nu} = \frac{1}{\Phi_{X2\nu}}\frac{d\Phi_{X2\nu}(E_\nu, \tau_X, m_X)}{dE_\nu}, \tag{10.3}$$

where $\Phi_{X2\nu} = \Phi_{\nu,\text{gal.}} + \Phi_{\nu,\text{e.g.}}$ is fixed in τ_X and m_X. We denote $\phi_{X2\nu}$ as a free explicit parameter and $\Phi_{X2\nu} \equiv \Phi_{X2\nu}(\tau_X, m_X)$ as a function depending on the lifetime and mass given by the Eq. (9.6). Assuming that the total flux $\phi_{X2\nu}$ is also distributed by a Gaussian function with an uncertainty $\sigma_{X2\nu} = 0.3$, the likelihood function (7.29) is extended, $n_\nu \to n_\nu + 1$ and the neutrino flux vector $\vec{\phi}_\nu$ consists now of SM neutrinos and additionally the anomalous flux $\phi_{X2\nu}$.

In both cases, the discovery limits in Fig. 37 are increased in the mass region above $m_\chi = 6$ GeV by the contributions of the anomalous neutrino flux. In this region, the anomalous rates are large enough to achieve a difference in sensitivity, especially when the anomalous rates are dominant in presence of hep, DSNB and atmospheric neutrinos. Below a WIMP mass of $m_\chi = 6$ GeV, the anomalous recoil rates are always too low in contrast to the dominant contributions of pp, ^{8}B neutrinos and neutrinos from the CNO cycle (see Fig. 34 and Fig. 39). Smaller DM masses m_X lead to a larger reduction of the sensitivity for WIMP masses between 10 GeV and 100 GeV. However, higher DM masses m_X produce DR neutrinos with higher energies, that generate higher recoil energies. In this case, we obtain larger contributions from the anomalous rates than from the DSNB and the atmospheric neutrinos. Thus, the sensitivity is also decreased at higher WIMP masses m_χ. Assuming that the DR flux is Gaussian distributed with an uncertainty $\sigma_{X2\nu} = 0.3$, the sensitivity decreases even more, because the flux may take large values, which lead to larger event rates.

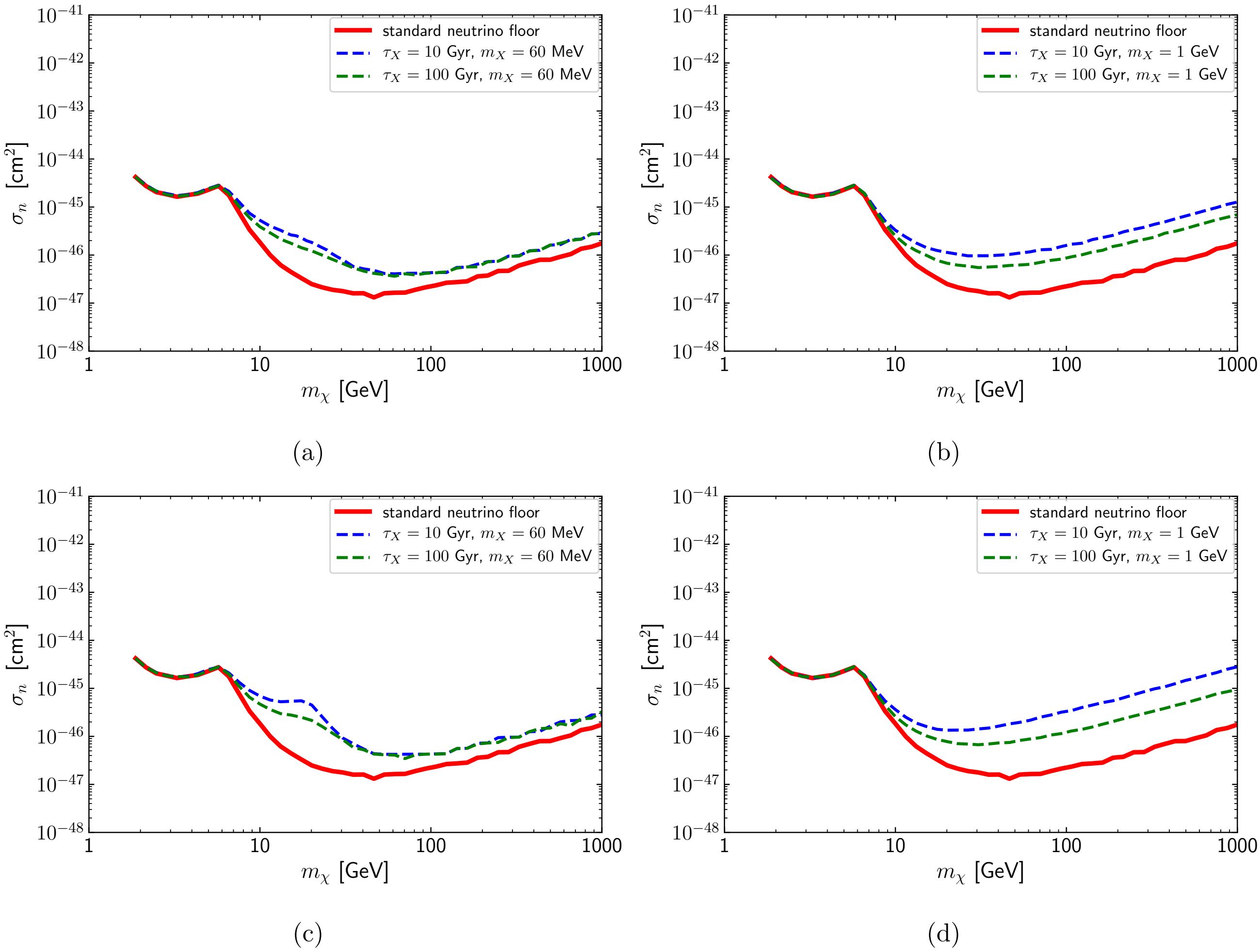

Figure 37: The modified neutrino floor at 90% C.L. for a threshold $E_{R_{\rm thr}} = 0.1$ keV. **(top)** $\Phi_{X2\nu} =$ const. for a lifetime τ_X and DM mass m_X, **(bottom)** $\phi_{X2\nu} \sim \mathrm{No}(\bar{\Phi}_{X2\nu}, \sigma_{X2\nu})$, where $\bar{\Phi}_{X2\nu}$ is fixed for a lifetime τ_X and DM mass m_X.

11 DR neutrinos vs. SM neutrinos

Instead of searching for DM by its interaction with the detector's material, one can analyse the final states of DM decays, as it is not for granted, that DM is stable at cosmological time scales. Moreover, if DM interacts very weakly with SM, DR may be the only way to probe the dark sector directly. Such dark radiation (DR) can leave a noticeable signal in the detector. Assume DM particles X decay into two equal final states, e.g. neutrinos (DR neutrinos). If the DR flux is high enough, DR neutrinos can be measured in direct detection experiments. At the same time, the irreducible background of SM neutrinos may mimic DR neutrinos and reduce the sensitivity to DR.

Similar to the standard neutrino floor calculation [77] we derive exclusion limits and discovery limits in the (τ_X, m_X)-plane for direct detection experiments. In the background-free approach, the exclusion limits at a 90% C.L. ($N_{\text{exp}}^{X2\nu} = 2.3$) are shown in Fig. 38 solving the equation

$$2.3 = \varepsilon(E_{R_{\text{thr}}})\mu_{X2\nu}(E_{R_{\text{thr}}}, \tau_X, m_X) \tag{11.1}$$

for the lifetime τ_X, where $\mu_{X2\nu}$ is the DR-induced recoil rate given by Eq. (9.12). The exposure is scaled up to the point that one SM neutrino is measured as in Sec. 7.1,

$$\varepsilon(E_{R_{\text{thr}}}) = \frac{1}{\sum_{j=1}^{n_\nu} \mu_\nu^j(E_{R_{\text{thr}}})}, \tag{11.2}$$

where $\mu_\nu^j(E_{R_{\text{thr}}})$ are SM neutrino rates given in Eq. (7.2) and n_ν is the number of SM neutrinos given in Tab. 4. For a given threshold $E_{R_{\text{thr}}}$ the outer region in Fig. 38 is excluded by higher SM neutrino events. In this case, DR neutrinos and SM neutrinos are no longer distinguishable. Smaller thresholds lead to larger exclusion regions, because the ^{8}B neutrinos start to become dominant and overshoot the rates of DR neutrinos as shown in Fig. 39. For thresholds below 1 keV and an exposure of 0.01 ton yr, DR and SM neutrino signals are no longer distinguishable. Taking the minimum of all exclusion limits, we obtain the ultimate sensitivity shown by the red dashed line. This corresponds to the maximum sensitivity, that can be reached in direct detection experiments. However, Super-Kamiokande (SK) already put constraints on the lifetime of the DM particle at 95% C.L. from measurements of solar, atmospheric and supernova neutrinos under the assumption, that DR in form of neutrinos is produced by two body decays $X \to \nu\overline{\nu}$ [27, 158–161]. These exclusion regions cover a wide mass range between 30 MeV and at least 1 GeV. The possibility to measure a signal from DR neutrinos in direct detection experiments under the background free approach is almost completely superseded by SK constraints.

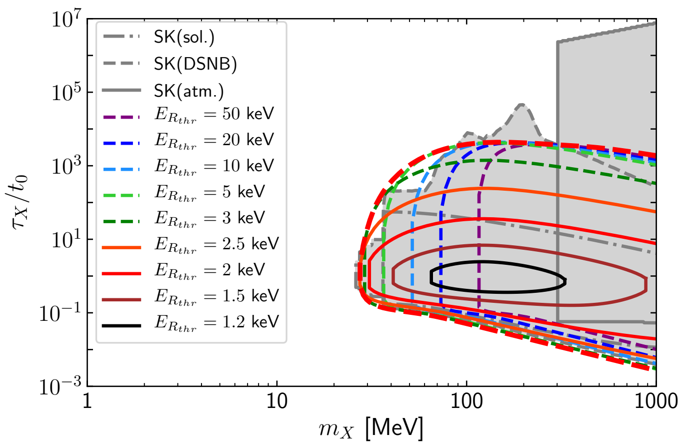

Figure 38: The exclusion limits under the model $X \to \nu\overline{\nu}$ in the background free approach. Lower thresholds lead to larger exclusion regions due to the dominant solar fluxes. The ultimate sensitivity is shown by the dashed red line. The grey shaded regions show exclusions from SK [158–161].

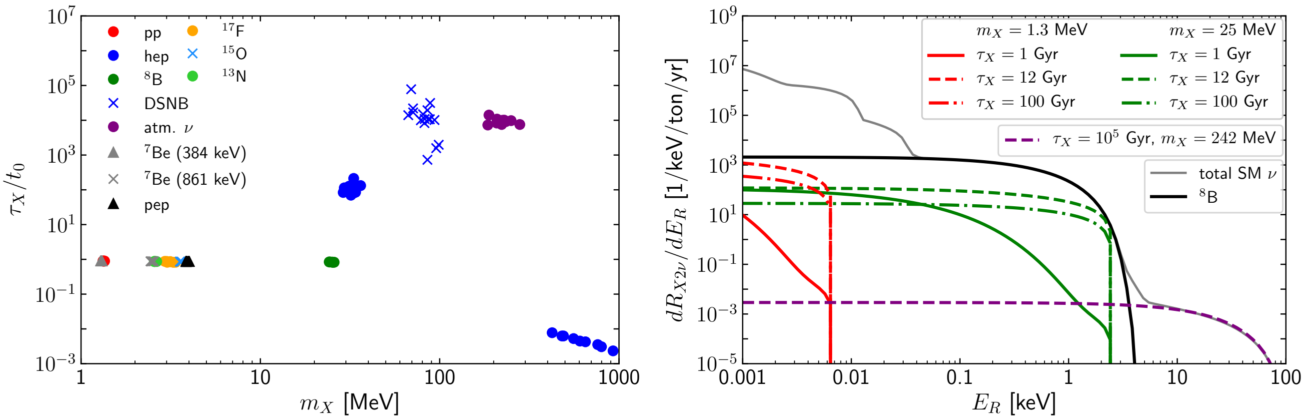

(a) (b)

Figure 39: **(a)** The best fits under the only signal hypothesis for each neutrino background. The dominant solar contributions are best fitted by DR neutrinos with low masses, whereas hep, atmospheric and supernova neutrinos are fitted for larger masses. A threshold of 1 eV was chosen. **(b)** The best fits for the backgrounds pp,^{8}B and atmospheric neutrinos (dashed lines). Higher and lower lifetimes relative to the best fits result in lower rates.

Only small regions of parameter space remain prospective in which direct detection experiments can probe DR. The only signal likelihood function for DR neutrinos

$$\mathcal{L}(\Gamma_X; m_X) = \frac{e^{-N_{X2\nu}(\Gamma_X;m_X)}}{N_{\text{obs}}!} \times \prod_{i=1}^{N_{\text{obs}}} \left[\varepsilon \frac{dR_{X2\nu}(E_{R_i}, \Gamma_X; m_X)}{dE_R}\right], \tag{11.3}$$

is used to analyse which DR neutrino rate is misinterpreted as SM neutrinos rates given in Tab. 4. In order to determine the best fits, we generate recoil spectra for each SM neutrino source by Monte Carlo experiments and maximize (11.3) for each neutrino source to obtain the corresponding lifetime τ_X and progenitor mass m_X. For this purpose, we changed the experiment's exposure for each neutrino source such that 500 events are measured. Then, the maximum likelihood estimators are plotted in the (τ_X, m_X)-plane as shown in Fig. 39a.

The achievable low DM masses are fitted by dominant solar contributions (pp,^{17}F,^{15}O,^{13}N, ^{8}B, pep). However, DR neutrino rates are too small to mimic solar neutrinos reasonably well as shown in Fig. 39b. The neutrino background pp (dashed red line) and ^{8}B (dashed green line) are fitted by rates with progenitor masses $m_X = 1.3, 25$ MeV and a lifetime $\tau_X = 12$ Gyr. In addition, we plotted the rates for lifetimes $\tau_X = 1, 100$ Gyr in order to show, that the best possible fits are obtained for $\tau_X \approx 12$ Gyr. On the flipside, contributions from hep, atmospheric and supernova neutrinos (DSNB) are well fitted by the signal model $X \to \nu\bar{\nu}$. Atmospheric neutrinos mimic DR neutrinos produced by a DM particle with lifetime $\tau_X = 10^5$ Gyr and a mass $m_X = 242$ MeV (dashed purple line).

In presence of an irreducible SM neutrino background the discovery limits are obtained by testing the null hypothesis $\text{H}_0 : \Gamma_X = 0$ (SM neutrino background with fluxes $\vec{\phi}_\nu$) against the alternative hypothesis $\text{H}_1 : \Gamma_X \neq 0$ (DR neutrino signal+SM neutrino background) on the data, where $\Gamma_X = 1/\tau_X$ is the decay width and τ_X the lifetime of the progenitor DM particle X. Following the same procedure as in sections 7.3.3 and 7.4, we try to reject the null hypothesis H_0 using the test statistics given by the profile likelihood ratio test

$$q_0 = -2\ln\lambda(0) = \begin{cases} -2\ln\frac{L(\Gamma_X=0,\tilde{\vec{\phi}}_\nu;m_X|x)}{L(\hat{\Gamma}_X,\hat{\vec{\phi}}_\nu;m_X|x)} & \text{for } \hat{\Gamma}_X > 0 \\ 0 & \text{for } \hat{\Gamma}_X \leq 0, \end{cases} \tag{11.4}$$

where $\tilde{\tilde{\vec{\phi}}}_\nu$ maximizes the likelihood for $\mathrm{H}_0 : \hat{\Gamma}_X = 0$ and $\hat{\Gamma}_X, \hat{\hat{\vec{\phi}}}_\nu$ are maxima in the case $\mathrm{H}_1 : \hat{\Gamma}_X \neq 0$. Larger q-values correspond to a larger discrepancy between the hypotheses H_0 and H_1. In this case, the data is more compatible with the alternative hypothesis H_1. However, smaller q-values lead to better compatibility with the null hypothesis H_0 and the data is better characterized by SM neutrinos alone. The null hypothesis is rejected if the q-value is greater than a observed value q_{obs} [150, 151]

$$p_0 = P(q \geq q_{\mathrm{obs}} | \mathrm{H}_0) = \int_{q_{\mathrm{obs}}}^{\infty} dq \; f(q \,| \mathrm{H}_0), \tag{11.5}$$

where $f(q\,|\mathrm{H}_0)$ is asymptotically a χ^2-distribution with one degree of freedom under the null hypothesis H_0 (see Wilk's theorem [152]). In terms of significance $Z = \sqrt{q}$ in units of standard deviations, the χ^2-distribution transforms to a Gaussian No$(0, 1)$ and the p_0-value is given by $p_0 = 2 \times (1 - \Phi(Z_{\mathrm{obs}}))$ as in Eq. 7.16[11]. A discovery with 3σ is achieved if data is observed in the critical region $Z_{\mathrm{obs}} \geq 3$ ($q_{\mathrm{obs}} \geq 9$) or equivalently $p_0 \leq 2 \times 0.00135$ and the null hypothesis H_0 is rejected. The extended likelihood function for a fixed progenitor mass m_X is given by

$$\begin{aligned}
\mathcal{L}(\Gamma_X, \vec{\phi}_\nu \,; m_X) = & \frac{\left(N_{X2\nu}(\Gamma_X; m_X) + \sum_{j=1}^{n_\nu} N_\nu(\phi^j)\right)^{N_{\mathrm{obs}}} \; e^{-\left(N_{X2\nu}(\Gamma_X; m_X) + \sum_{j=1}^{n_\nu} N_\nu(\phi^j)\right)}}{N_{\mathrm{obs}}!} \\
& \times \prod_{i=1}^{N_{\mathrm{obs}}} \frac{f(E_{R_i}, \Gamma_X, \vec{\phi}\,; m_X)}{N_{X2\nu}(\Gamma_X; m_X) + \sum_{j=1}^{n_\nu} N_\nu(\phi_\nu^j)} \\
& \times \prod_{j=1}^{n_\nu} L_j(\phi_\nu^j),
\end{aligned} \tag{11.6}$$

where $N_{X2\nu}(\Gamma_X; m_X)$ is the expected number of events under the model $X \to \nu\bar{\nu}$ explained in Sec. 9

$$N_{X2\nu}(\Gamma_X; m_X) = \varepsilon \int_{E_{\mathrm{thr}}}^{E_{X2\nu}^{\max}} dE_R \; \frac{dR_{X2\nu}}{dE_R}. \tag{11.7}$$

Similarly, in the second factor of the likelihood function the distribution becomes

$$\begin{aligned}
f(E_{R_i}, \Gamma_X, \vec{\phi}_\nu \,; m_X) &= N_{X2\nu}(\Gamma; m_X) f_{X2\nu}(E_{R_i}; m_\chi) + \sum_{k=1}^{n_\nu} N_\nu(\phi_\nu^k) f_\nu^k(E_{R_i}) \\
&= \left[\varepsilon \left(\frac{dR_{X2\nu}(E_{R_i}, \Gamma_X; m_X)}{dE_R} + \sum_{j=1}^{n_\nu} \frac{dR_\nu(E_{R_i}, \phi_\nu^j)}{dE_R}\right)\right],
\end{aligned} \tag{11.8}$$

where $f_{X2\nu}(E_{R_i}; m_\chi)$, $f_\nu^k(E_{R_i})$ are normalized recoil rates of DR neutrinos and SM neutrinos. Then, the likelihood simplifies to a more compact form

$$\begin{aligned}
\mathcal{L}(\Gamma_X, \vec{\phi}_\nu \,; m_X) = & \frac{e^{-\left(N_{X2\nu}(\Gamma_X; m_X) + \sum_{j=1}^{n_\nu} N_\nu(\phi_\nu^j)\right)}}{N_{\mathrm{obs}}!} \\
& \times \prod_{i=1}^{N_{\mathrm{obs}}} \left[\varepsilon \left(\frac{dR_{X2\nu}(E_{R_i}, \Gamma_X; m_X)}{dE_R} + \sum_{j=1}^{n_\nu} \frac{dR_\nu(E_{R_i}, \phi_\nu^j)}{dE_R}\right)\right] \\
& \times \prod_{j=1}^{n_\nu} L_j(\phi_\nu^j).
\end{aligned} \tag{11.9}$$

[11] The factor 2 occurs due to the restriction $Z \geq 0$.

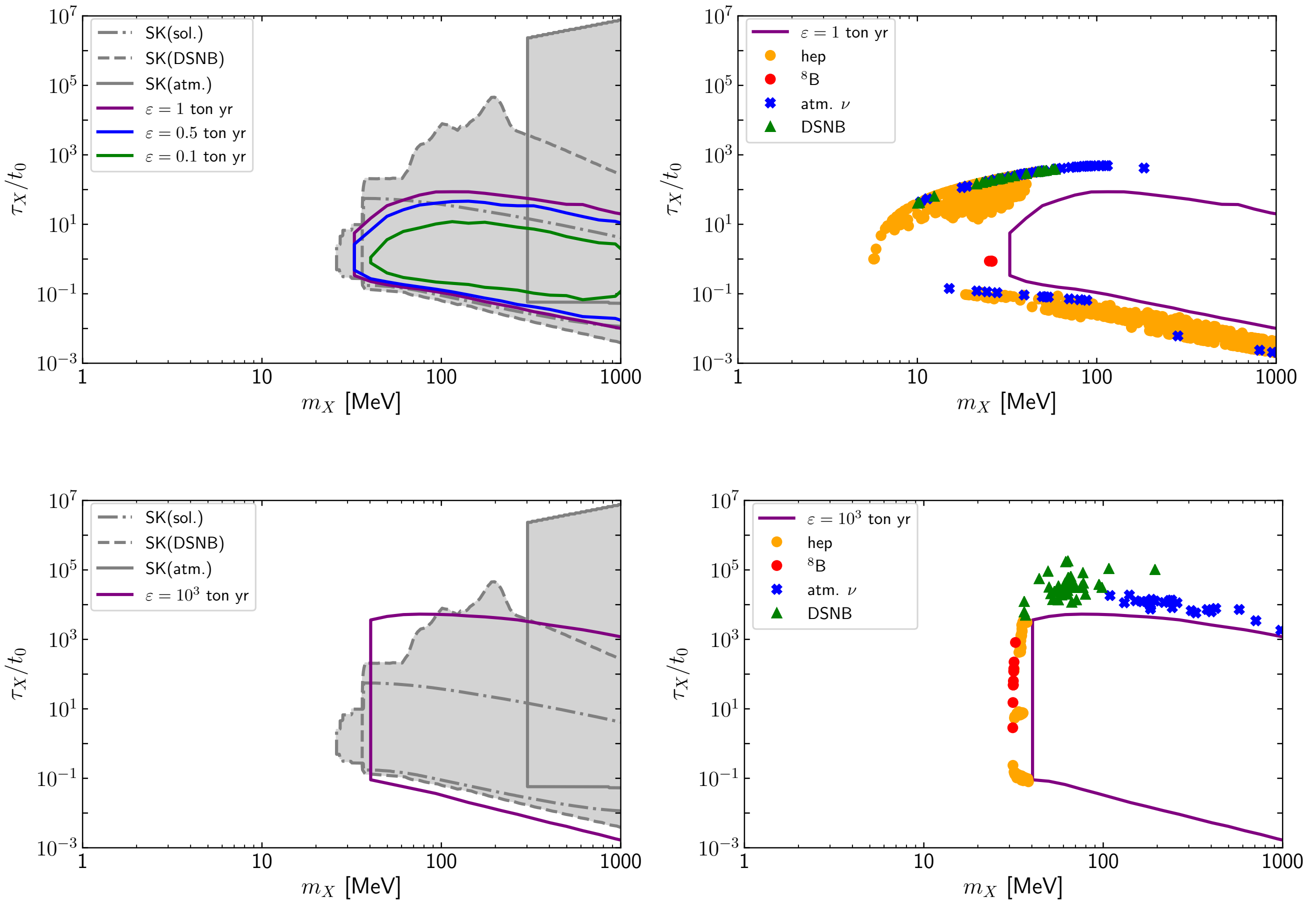

Figure 40: **(left)** Discovery limits at a 90% C.L., **(right)** Contributions from each neutrino source (best fits) determining the shape of the discovery limit, **(top)** $E_{R_{\rm thr}} = 0.1$ keV, **(bottom)** $E_{R_{\rm thr}} = 4$ keV.

The discovery limits at a 90% C.L. are shown in Fig. 40 for thresholds of 0.1 keV and 4 keV. We took 200-250 data sets to determine the distribution of significances $f(Z|\mathrm{H}_1)$ under the signal+background hypothesis as shown in Eq. (7.18). The inner region represents the discovery region, where a signal of a DR neutrino can be distinguished from the irreducible SM neutrino background. Lower thresholds should not improve the sensitivity a lot, because the dominant contributions of the solar neutrinos, especially the ^{8}B neutrinos always exceeds the DR-induced rates as exemplified in Fig. 39b. Therefore, the DR neutrino flux is more likely distinguishable at higher recoil energies above few keV, where the ^{8}B rates are very low. A xenon based experiment with low thresholds and exposures of 1 ton yr will not be able to detect a signal, because it is already excluded by SK. However, increasing the exposure leads to larger discovery regions, that eventually exceed the SK constraints. For a threshold of 4 keV, the exposure $\varepsilon = 10^3$ ton yr was chosen such that approximately 40 nuclear recoils of neutrinos in one experiment are observed to have high enough rates for statistics. At this threshold, the supernova neutrinos as well as the atmospheric neutrinos become dominant. However, due to many numerical calculations for smaller lifetimes, the lower bound m_X is not accurate enough and is estimated to be uncertain within a factor of 2. The upper bound of the discovery limit is very well determined by the dominant fluxes as shown in Fig. 40. However, neither an experiment today nor a next generation experiment will be able to achieve such a large exposure.

12 Conclusion and Outlook

We explored background-free exclusion limits and the discovery potential of future xenon-based ton-scale direct detection experiments by Monte Carlo simulating data and determined the maximum sensitivity that can be reached in these experiments. This limit on the sensitivity is a consequence of the irreducible neutrino backgrounds originating from the Sun, the Earth's atmosphere and supernova explosions, which may mimic dark matter- or dark radiation-induced signals.

In the first part of this thesis, we established the minimum spin-independent WIMP-nucleon cross section σ_n at each WIMP mass m_χ, where nuclear recoils between neutrino backgrounds and WIMP-induced signals are still distinguishable. In some cases, the WIMP-induced recoil events may be misinterpreted as SM neutrino rates. For this purpose, in the first approach, we determined the best background-free sensitivity/exclusion limit by scaling the experiment's exposure, such that one neutrino event is measured for various thresholds. This is illustrated in Fig. 25. Below the one neutrino-event line (region in red), neutrinos become an important background in direct detection experiments. In this region, the number of WIMPs are no longer detectable because their signal is superseded by neutrino-induced events. In the second approach, we develop the proper statistical formalism based on likelihood ratio tests to determine the limits for discovery on σ_n at each WIMP mass m_χ in order to discover a WIMP at least with 3σ significance in the presence of neutrino backgrounds as shown in Fig. 28. Solar neutrinos are the most important background in limiting the sensitivity to WIMP masses below 10 GeV. We found that a cross section of about 10^{-43} cm^2 is the smallest conceivable value to discriminate between WIMPs and neutrinos. For WIMP masses above 10 GeV the DM cross section may be as low as 10^{-48} cm^2. This is because the event rates of the diffuse supernova neutrino background and the atmospheric neutrinos are comparatively lower.

In the second part of this thesis, we introduced a dark radiation flux, that originates from DM two-body decay. We further assume that this dark radiation (DR) is in form of neutrinos. Then, we explored the limits of exclusion and discovery potentials on the spin-independent WIMP-nucleon cross section σ_n at each WIMP mass m_χ in the presence of DR in addition to the standard neutrino background. Hence, similarly to before, we obtained the minimum spin-independent WIMP-nucleon cross section σ_n, where WIMPs and neutrinos are no longer distinguishable. The best background-free sensitivity deteriorates by up to four orders of magnitude. This is illustrated in Fig. 35. In the presence of the SM neutrino background and neutrino dark radiation, the sensitivity in WIMP discovery is decreased for WIMP masses greater than 6 GeV as shown in Fig. 37. Adding a DR-induced rate with a progenitor mass $m_X = 60$ MeV and a lifetime $\tau_X = 10$ Gyr to the standard neutrino background, increases the experimental limits of σ_n at a WIMP mass $m_\chi = 20$ GeV from $2 \cdot 10^{-47}$ cm^2 to $5 \cdot 10^{-46}$ cm^2. For WIMP masses smaller than 6 GeV, the maximum DR-induced recoil rates are much smaller than the recoil rates of the solar neutrinos. Therefore, no increase is noticed in the light WIMP-mass region. We reached our conclusions above by considering two cases. In the first case, the DR flux is constant and the shape of the differential recoil rate is fixed. In the second case, the anomalous flux is assumed to be Gaussian distributed with an uncertainty of 30%. Taking the uncertainty into account, the sensitivity decreases even more due to broaden fluctuations of the DR fluxes.

In the third part of this thesis, we investigated the detectability of DR itself. Hence, we explored background-free exclusion limits and discovery potentials on the lifetime τ_X at each progenitor mass m_X for DR neutrino fluxes. In direct detection experiments SM neutrinos may mimic neutrino dark radiation, which may lead to a misinterpretation of the measured data. Therefore, we established the minimum lifetime corresponding to the smallest DR flux at each progenitor mass, where DR and SM neutrinos are still distinguishable. The maximum reachable sensitivity assuming a background-free experiment is again obtained by scaling the exposure, such that one neutrino event is measured. We found that the maximum sensitivity is already almost completely superseded by existing Super-Kamiokande (SK) constraints. Only small regions still allow for a detectability of DR signals at lifetimes of about $\tau_X = 10^4$ Gyr and progenitor masses in the ballpark of $m_X = 50$ MeV as well as for lifetimes around $\tau_X = 10^3$ Gyr and masses around $m_X = 30$ MeV. The discovery potentials were derived for thresholds of 0.1 keV and 4 keV. In xenon-based direct detection experiments with a threshold of 0.1 keV and an exposure of 1 ton yr or less, the region where DR can be discovered with 3σ significance is excluded by SK. In principle increasing the exposure would lead to a larger discovery region, which may eventually exceed the exclusion limits of SK. At a threshold of 4 keV and with a futuristic exposure of $\varepsilon = 10^3$ ton yr a total of 40 neutrino events would constitute a high enough statistics to make a discovery of DR. We also found that lowering the threshold of these experiments in order to obtain a broader coverage of the measured spectra does not increase the prospects to discover neutrino DR. This is because solar neutrinos backgrounds contribute strongly in the soft part of the spectra.

We highlight few avenues of how the sensitivity could be improved. First, a better understanding of the neutrino background will reduce the uncertainties on the fluxes and thereby reduce the statistical fluctuations of SM induced backgrounds. Second, using different target materials allows to add additional information to discriminate neutrinos from WIMPs. The ultimate discrimination between WIMPs and neutrinos would be to measure the direction of nuclear recoils, since the solar neutrino background is an anisotropic source at Earth.

Finally, we may broaden the analysis by considering more general types of DR. First, DR could be a new particle scattering with different strength than neutrinos, e.g. sterile neutrinos. Second, DR could have different energy characteristics, if it is originated from a multi-body decay of DM. Third, DR could come from other sources than DM-decays, e.g. evaporating primordial black holes or DR emerging from supernova explosions.

A Friedmann equations

Consider the FRW metric [16, 39, 40]

$$\begin{aligned} ds^2 = g_{\mu\nu}(x)dx^\mu dx^\nu &= dt^2 - a^2(t)\left[\frac{dr^2}{1-Kr^2} + r^2 d\theta^2 + r^2\sin^2\theta\, d\varphi^2\right] = dt^2 - a^2(t)\left[\frac{dr^2}{1-Kr^2} + r^2 d\Omega^2\right] \\ &= dt^2 - a^2(t)\gamma_{ij}dx^i dx^j = dt^2 + g_{ij}dx^i dx^j, \end{aligned} \tag{A.1}$$

where r, θ, φ are comoving coordinates and

$$g_{ij} = -a^2(t)\gamma_{ij} \quad \text{with} \quad \gamma_{ij} = \begin{pmatrix} \frac{1}{1-Kr^2} & 0 & 0 \\ 0 & r^2 & 0 \\ 0 & 0 & r^2\sin^2\theta \end{pmatrix} \tag{A.2}$$

is the 3-dimensional induced metric on a maximally symmetric manifold, where Greek letters run over $\mu, \nu, \lambda, ... = 0, 1, 2, 3$ and Latin letters over $i, j, k, ... = 1, 2, 3$. The coordinates $i, j, k, ...$ characterize the spatial part of the metric $g_{\mu\nu}$. The time coordinate t coincides with the proper time s for a free falling observer (observer with constant space coordinates $dx^i = 0$)

$$ds^2 = dt^2 - a^2(t)\gamma_{ij}dx^i dx^j \quad \overset{dx^i=0}{\Rightarrow} \quad ds^2 = dt^2 \quad \Rightarrow \quad s = t. \tag{A.3}$$

Often it is convenient to write the metric in the form

$$ds^2 = dt^2 - a^2(t)\left[d\chi^2 + \left\{\begin{array}{ll} \sinh^2\chi & \text{for } K = -1 \\ \chi^2 & \text{for } K = 0 \\ sin^2\chi & \text{for } K = +1 \end{array}\right\} d\Omega^2\right], \tag{A.4}$$

using the substitution $d\chi^2 = \frac{dr^2}{1-Kr^2}$. The Friedmann equations are derived from the Einstein equations [162]

$$R_{\mu\nu} - \frac{1}{2}Rg_{\mu\nu} - \Lambda g_{\mu\nu} = 8\pi G T_{\mu\nu} \tag{A.5}$$

using the FRW metric (A.1) and the energy momentum tensor of a perfect fluid

$$T_{\mu\nu} = \begin{pmatrix} \rho(t) & 0 & 0 & 0 \\ 0 & -p(t) & 0 & 0 \\ 0 & 0 & -p(t) & 0 \\ 0 & 0 & 0 & -p(t) \end{pmatrix}. \tag{A.6}$$

The Ricci tensor $R_{\mu\nu}$ and the Ricci scalar R are calculated from the Christoffel symbols [16, 162, 163]. The general from of the Christoffel symbols are given by

$$\Gamma^\lambda{}_{\mu\nu} = \frac{1}{2}g^{\lambda\alpha}\left(\partial_\mu g_{\alpha\nu} + \partial_\nu g_{\alpha\mu} - \partial_\alpha g_{\mu\nu}\right) \quad \text{with } \Gamma^\lambda{}_{\mu\nu} = \Gamma^\lambda{}_{\nu\mu} \text{ (torsion free connection)} \tag{A.7}$$

Choosing the first component of the Christoffel symbol as the time coordinate ($\lambda = 0$), the Eq. (A.7) reduces to

$$\Gamma^0{}_{\mu\nu} = \frac{1}{2}g^{0\alpha}\left(\partial_\mu g_{\nu\alpha} + \partial_\nu g_{\mu\alpha} - \partial_\alpha g_{\mu\nu}\right) \overset{\alpha=0}{=} \frac{1}{2}\underbrace{g^{00}}_{=1}(\underbrace{\partial_\mu g_{\nu 0}}_{=0} + \underbrace{\partial_\nu g_{\mu 0}}_{=0} - \partial_0 g_{\mu\nu}) = -\frac{1}{2}\partial_0 g_{\mu\nu}. \tag{A.8}$$

Due to the fact, the FRW-metric is diagonal ($g_{\mu\nu} = 0$ for $\mu \neq \nu$) the following Christoffel symbols are zero

$$\Gamma^0{}_{00} = 0, \quad \Gamma^0{}_{i0} = 0. \tag{A.9}$$

Therefore, the only non zero Christoffel symbol for $\lambda = 0$ is obtained for $(\mu\nu) = (ij)$

$$\Gamma^0{}_{ij} = -\frac{1}{2}\partial_0 g_{ij} = \frac{1}{2}\partial_0 a^2(t)\gamma_{ij} = a(t)\dot{a}(t)\gamma_{ij} = a^2(t)H(t)\gamma_{ij}. \tag{A.10}$$

The other Christoffel symbols are derived by choosing λ as a spatial coordinate (choose $\lambda = i$)

$$\Gamma^{i}{}_{\mu\nu} = \frac{1}{2} g^{i\alpha} \left(\partial_\mu g_{\nu\alpha} + \partial_\nu g_{\mu\alpha} - \partial_\alpha g_{\mu\nu}\right) \overset{\alpha=j}{=} \frac{1}{2} g^{ij} (\partial_\mu g_{\nu j} + \partial_\nu g_{\mu j} - \partial_j g_{\mu\nu}), \tag{A.11}$$

where $\alpha = 0$ leads to the metric component g^{i0}, which is zero, because the metric g is diagonal. This implies

$$\Gamma^{i}{}_{k0} = \frac{1}{2} g^{ij} (\underbrace{\partial_k g_{0j}}_{=0} + \partial_0 g_{kj} - \underbrace{\partial_j g_{k0}}_{=0}) = \frac{1}{2} g^{ij} \partial_0 g_{kj} = \frac{1}{2} \frac{1}{a^2(t)} \gamma^{ij} \partial_0 a^2(t) \gamma_{kj} = \frac{\dot{a}}{a} \gamma^{ij} \gamma_{kj} = H(t) \delta^{i}{}_{k}, \tag{A.12}$$

$$\Gamma^{i}{}_{00} = \frac{1}{2} g^{ij} (\underbrace{\partial_0 g_{0j}}_{=0} + \underbrace{\partial_0 g_{0j}}_{=0} - \underbrace{\partial_j g_{00}}_{=0}) = 0, \tag{A.13}$$

$$\Gamma^{i}{}_{kl} = \frac{1}{2} g^{ij} (\partial_k g_{lj} + \partial_l g_{kj} - \partial_j g_{kl}) = \frac{1}{2} \gamma^{ij} (\partial_k \gamma_{lj} + \partial_l \gamma_{kj} - \partial_j \gamma_{kl}), \tag{A.14}$$

where $\gamma^{ij}\gamma_{kj} = \gamma^{ij}\gamma_{jk} = \delta^{i}{}_{k}$ using that the induced metric γ_{kj} is symmetric. The Christoffel symbols in Eq. (A.14) can be performed explicitly for $i, j, k, l = 1, 2, 3$:

$$\Gamma^{1}{}_{11} = \frac{Kr}{1 - Kr^2}, \quad \Gamma^{1}{}_{22} = -r(1 - Kr^2), \quad \Gamma^{1}{}_{33} = -r(1 - Kr^2)\sin^2\theta, \tag{A.15}$$

$$\Gamma^{2}{}_{21} = \Gamma^{2}{}_{12} = \frac{1}{r}, \quad \Gamma^{2}{}_{33} = -\sin\theta\cos\theta, \tag{A.16}$$

$$\Gamma^{3}{}_{31} = \Gamma^{3}{}_{13} = \frac{1}{r}, \quad \Gamma^{3}_{32} = \Gamma^{3}_{23} = \frac{1}{\tan\theta}. \tag{A.17}$$

All remaining Christoffel symbols are zero. In summary one obtains the following non zero Christoffel symbols

$$\begin{aligned}
&\Gamma^{0}{}_{00} = 0, \quad \Gamma^{0}{}_{i0} = \Gamma^{0}{}_{0i} = 0, \quad \Gamma^{0}{}_{ij}, = \Gamma^{0}{}_{ji} = a^2(t) H(t) \gamma_{ij}, \\
&\Gamma^{i}{}_{k0} = \Gamma^{i}{}_{0k} = H(t)\delta^{i}{}_{k}, \quad \Gamma^{i}{}_{00} = 0 \\
&\Gamma^{1}{}_{11} = \frac{Kr}{1 - Kr^2}, \quad \Gamma^{1}{}_{22} = -r(1 - Kr^2), \quad \Gamma^{1}{}_{33} = -r(1 - Kr^2)\sin^2\theta, \\
&\Gamma^{2}{}_{21} = \Gamma^{2}{}_{12} = \frac{1}{r}, \quad \Gamma^{2}{}_{33} = -\sin\theta\cos\theta, \\
&\Gamma^{3}{}_{31} = \Gamma^{3}{}_{13} = \frac{1}{r}, \quad \Gamma^{3}_{32} = \Gamma^{3}_{23} = \frac{1}{\tan\theta}.
\end{aligned} \tag{A.18}$$

Once the Christoffel symbols are derived, the Ricci tensor is given by

$$R_{\mu\nu} = \partial_\alpha \Gamma^{\alpha}{}_{\nu\mu} - \partial_\nu \Gamma^{\alpha}{}_{\alpha\mu} + \Gamma^{\alpha}{}_{\alpha\beta}\Gamma^{\beta}{}_{\nu\mu} - \Gamma^{\alpha}{}_{\nu\beta}\Gamma^{\beta}{}_{\alpha\mu}. \tag{A.19}$$

The components of the Ricci tensor are given as follows

$$\begin{aligned}
R_{00} &= \partial_\alpha \Gamma^{\alpha}{}_{00} - \partial_0 \Gamma^{\alpha}{}_{\alpha 0} + \Gamma^{\alpha}{}_{\alpha\beta}\Gamma^{\beta}{}_{00} - \Gamma^{\alpha}{}_{0\beta}\Gamma^{\beta}{}_{\alpha 0} = -\partial_0 \Gamma^{i}{}_{i0} - \Gamma^{i}{}_{0k}\Gamma^{k}{}_{i0} \\
&= -\partial_0 H(t)\delta^{i}{}_{i} - H(t)^2 \delta^{i}{}_{i} = -3(\dot{H}(t) + H^2(t)) = -3\frac{\ddot{a}(t)}{a(t)},
\end{aligned} \tag{A.20}$$

$$\begin{aligned}
R_{0i} = R_{i0} &= \partial_\alpha \Gamma^{\alpha}{}_{0i} - \partial_i \Gamma^{\alpha}{}_{\alpha 0} + \Gamma^{\alpha}{}_{\alpha\beta}\Gamma^{\beta}{}_{i0} - \Gamma^{\alpha}{}_{i\beta}\Gamma^{\beta}{}_{\alpha 0} = \partial_k \Gamma^{k}{}_{0i} - \partial_i \Gamma^{k}{}_{k0} + \Gamma^{l}{}_{lk}\Gamma^{k}{}_{i0} - \Gamma^{k}{}_{il}\Gamma^{l}{}_{k0} \\
&= \Gamma^{l}{}_{lk}\Gamma^{k}{}_{i0} - \Gamma^{k}{}_{il}\Gamma^{l}{}_{k0} = H(t)\Gamma^{l}{}_{lk}\delta^{k}{}_{i} - H(t)\Gamma^{k}{}_{il}\delta^{l}{}_{k} = H(t)\left(\Gamma^{l}{}_{li} - \Gamma^{k}{}_{ik}\right) = H(t)\left(\Gamma^{l}{}_{li} - \Gamma^{l}{}_{li}\right) = 0
\end{aligned} \tag{A.21}$$

using $\partial_k \Gamma^{k}{}_{0i} = \partial_k (H(t)\delta^{k}{}_{i}) = 0$, $\partial_i \Gamma^{k}{}_{k0} = \partial_i (H(t)\delta^{k}{}_{k}) = 3\partial_i H(t) = 0$ and the torsion free property of the connection $\Gamma^{k}{}_{ik} = \Gamma^{k}{}_{ki}$. The spatial part of the Ricci tensor is obtained by choosing spatial coordinates ($\mu = i, \nu = j$)

$$\begin{aligned}
R_{ij} = R_{ji} &= \partial_\alpha \Gamma^{\alpha}{}_{ji} - \partial_j \Gamma^{\alpha}{}_{\alpha i} + \Gamma^{\alpha}{}_{\alpha\beta}\Gamma^{\beta}{}_{ji} - \Gamma^{\alpha}{}_{j\beta}\Gamma^{\beta}{}_{\alpha i} \\
&= \partial_0 \Gamma^{0}{}_{ji} + \partial_k \Gamma^{k}{}_{ji} - \partial_j \Gamma^{k}{}_{ki} + \Gamma^{k}{}_{k0}\Gamma^{0}{}_{ji} + \Gamma^{k}{}_{kl}\Gamma^{l}{}_{ji} - \Gamma^{0}{}_{jl}\Gamma^{l}{}_{0i} - \Gamma^{k}{}_{j0}\Gamma^{0}{}_{ki} - \Gamma^{k}{}_{jl}\Gamma^{l}{}_{ki} \\
&= (\ddot{a}(t)a(t) + 2\dot{a}^2(t))\gamma_{ij} + \partial_k \Gamma^{k}{}_{ji} - \partial_j \Gamma^{k}{}_{ki} + \Gamma^{k}{}_{kl}\Gamma^{l}{}_{ji} - \Gamma^{k}{}_{jl}\Gamma^{l}{}_{ki}
\end{aligned} \tag{A.22}$$

using the relations

$$\partial_0 \Gamma^0{}_{ij} = \partial_0(a^2(t)H(t))\gamma_{ij} = (\ddot{a}(t)a(t) + \dot{a}^2(t))\gamma_{ij}, \tag{A.23}$$

$$\Gamma^k{}_{k0}\Gamma^0{}_{ji} = a^2(t)H(t)^2\delta^k{}_k\gamma_{ij} = 3\dot{a}^2(t)\gamma_{ij}, \tag{A.24}$$

$$\Gamma^0{}_{jl}\Gamma^l{}_{0i} = a^2(t)H(t)^2\delta^l{}_i\gamma_{jl} = a^2(t)H(t)^2\gamma_{ji} = \dot{a}^2(t)\gamma_{ij}, \quad (\gamma_{ij} \text{ is symmetric, i.e. } \gamma_{ij} = \gamma_{ji}) \tag{A.25}$$

$$\Gamma^k{}_{j0}\Gamma^0{}_{ki} = a^2(t)H(t)^2\delta^k{}_i\gamma_{kj} = \dot{a}^2(t)\gamma_{ij}. \tag{A.26}$$

All non zero components of the Ricci tensor are given by

$$\begin{aligned}
R_{11} &= (\ddot{a}(t)a(t) + 2\dot{a}^2(t))\gamma_{11} + \partial_k\Gamma^k{}_{11} - \partial_1\Gamma^k{}_{k1} + \Gamma^k{}_{lk}\Gamma^l{}_{11} - \Gamma^k{}_{l1}\Gamma^l{}_{k1} \\
&= (\ddot{a}(t)a(t) + 2\dot{a}^2(t))\gamma_{11} + \partial_1\Gamma^1{}_{11} - \partial_1\Gamma^k{}_{k1} + \Gamma^k{}_{1k}\Gamma^1{}_{11} - \Gamma^k{}_{l1}\Gamma^l{}_{k1} \\
&= (\ddot{a}(t)a(t) + 2\dot{a}^2(t))\gamma_{11} + \partial_1\Gamma^1{}_{11} - \partial_1\Gamma^1{}_{11} - \partial_1\Gamma^2{}_{21} - \partial_1\Gamma^3{}_{31} + \Gamma^1{}_{11}\Gamma^1{}_{11} + \Gamma^2{}_{12}\Gamma^1{}_{11} \\
&+ \Gamma^3{}_{13}\Gamma^1{}_{11} - \Gamma^1{}_{11}\Gamma^1{}_{11} - \Gamma^2{}_{21}\Gamma^2{}_{21} - \Gamma^3{}_{31}\Gamma^3{}_{31} \\
&= (\ddot{a}(t)a(t) + 2\dot{a}^2(t))\gamma_{11} + \frac{2}{r^2} + 2\frac{2K}{1-Kr^2} - \frac{2}{r^2} \\
&= (\ddot{a}(t)a(t) + 2\dot{a}^2(t))\gamma_{11} + \frac{2K}{1-Kr^2} \\
&= (\ddot{a}(t)a(t) + 2\dot{a}^2(t) + 2K)\gamma_{11},
\end{aligned} \tag{A.27}$$

$$\begin{aligned}
R_{22} &= (\ddot{a}(t)a(t) + 2\dot{a}^2(t))\gamma_{22} + \partial_k\Gamma^k{}_{22} - \partial_2\Gamma^k{}_{k2} + \Gamma^k{}_{lk}\Gamma^l{}_{22} - \Gamma^k{}_{l2}\Gamma^l{}_{k2} \\
&= (\ddot{a}(t)a(t) + 2\dot{a}^2(t))\gamma_{22} + \partial_1\Gamma^1{}_{22} - \partial_2\Gamma^3{}_{32} + \Gamma^1{}_{11}\Gamma^1{}_{22} + \Gamma^2{}_{12}\Gamma^1{}_{22} + \Gamma^3{}_{13}\Gamma^1{}_{22} \\
&- \Gamma^1{}_{22}\Gamma^2{}_{12} - \Gamma^2{}_{12}\Gamma^1{}_{22} - \Gamma^3{}_{32}\Gamma^3{}_{32} \\
&= (\ddot{a}(t)a(t) + 2\dot{a}^2(t))\gamma_{22} - 1 + 2Kr^2 + \frac{1}{\tan\theta}\frac{(-\cos^2\theta + 1)}{\cos^2\theta} \\
&= (\ddot{a}(t)a(t) + 2\dot{a}^2(t))\gamma_{22} - 1 + 2Kr^2 + \frac{1}{\tan\theta}\frac{\sin^2\theta}{\cos^2\theta} \\
&= (\ddot{a}(t)a(t) + 2\dot{a}^2(t))\gamma_{22} - 1 + 2Kr^2 + \frac{1}{\tan\theta}\tan\theta \\
&= (\ddot{a}(t)a(t) + 2\dot{a}^2(t))\gamma_{22} + 2Kr^2 \\
&= (\ddot{a}(t)a(t) + 2\dot{a}^2(t) + 2K)\gamma_{22},
\end{aligned} \tag{A.28}$$

$$\begin{aligned}
R_{33} &= (\ddot{a}(t)a(t) + 2\dot{a}^2(t))\gamma_{33} + \partial_k\Gamma^k{}_{33} - \partial_3\Gamma^k{}_{k3} + \Gamma^k{}_{lk}\Gamma^l{}_{33} - \Gamma^k{}_{l3}\Gamma^l{}_{k3} \\
&= (\ddot{a}(t)a(t) + 2\dot{a}^2(t))\gamma_{33} + \partial_1\Gamma^1{}_{33} + \partial_2\Gamma^2{}_{33} + \Gamma^1{}_{11}\Gamma^1{}_{33} + \Gamma^2{}_{12}\Gamma^1{}_{33} + \Gamma^3{}_{13}\Gamma^1{}_{33} \\
&- 2\Gamma^1{}_{33}\Gamma^3{}_{13} - 2\Gamma^2{}_{33}\Gamma^3{}_{23} \\
&= (\ddot{a}(t)a(t) + 2\dot{a}^2(t))\gamma_{33} - (-1 - Kr^2)\sin^2\theta + 2Kr^2\sin^2\theta + \sin^2\theta \\
&+ \frac{Kr}{1-Kr^2}(-r)(1-Kr^2)\sin^2\theta - Kr^2\sin^2\theta \\
&= (\ddot{a}(t)a(t) + 2\dot{a}^2(t))\gamma_{33} + (-1 + 3Kr^2 + 1)\sin^2\theta - Kr^2\sin^2\theta \\
&= (\ddot{a}(t)a(t) + 2\dot{a}^2(t))\gamma_{33} + 2Kr^2\sin^2\theta \\
&= (\ddot{a}(t)a(t) + 2\dot{a}^2(t) + 2K)\gamma_{33}.
\end{aligned} \tag{A.29}$$

The Ricci tensor for the FRW metric is diagonal with

$$\begin{aligned}
&R_{00} = -3\frac{\ddot{a}(t)}{a(t)}, \\
&R_{ij} = (\ddot{a}(t)a(t) + 2\dot{a}^2(t) + 2K)\gamma_{ij} \;\text{ for } i = j, \\
&R_{ij} = 0 \;\text{ for } i \neq j.
\end{aligned} \tag{A.30}$$

The Ricci scalar R is obtained by multiplying the Ricci tensor with the metric

$$\begin{aligned} R = g^{\mu\nu}R_{\mu\nu} = g^{00}R_{00} + g^{ij}R_{ij} &= -3\frac{\ddot{a}(t)}{a(t)} - \frac{1}{a^2(t)}\gamma^{ij}(\ddot{a}(t)a(t) + 2\dot{a}^2(t) + 2K)\gamma_{ij} \\ &= -\frac{6}{a(t)}\left(\ddot{a}(t)a(t) + \dot{a}^2(t) + K\right), \end{aligned} \tag{A.31}$$

using $\gamma^{ij}\gamma_{ij} = \delta^j{}_j = 3$.

The $(\mu,\nu) = (0,0)$ component of the Einstein equations leads to the so called 1st Friedmann equation

$$\frac{\dot{a}(t)^2 + K}{a(t)^2} - \frac{\Lambda}{3} = \frac{8\pi G}{3}\rho(t). \qquad \textbf{(1st Friedmann equation)} \tag{A.32}$$

The $(\mu,\nu) = (i,j)$ component of the Einstein equation leads to the equation

$$2\frac{\ddot{a}(t)}{a(t)} + \frac{\dot{a}^2(t)}{a^2(t)} + \frac{K}{a^2(t)} - \Lambda = -8\pi G p(t). \tag{A.33}$$

Subtracting Eq. (A.32) from Eq. (A) we obtain the 2nd Friedmann equation

$$\frac{\ddot{a}(t)}{a(t)} = -\frac{4\pi G}{3}(3p(t) + \rho(t)) + \frac{\Lambda}{3}, \qquad \textbf{(2nd Friedmann equation)}. \tag{A.34}$$

B WIMP model

B.1 Variable transformation of the two-body momentum phase space

The two body momentum phase space is given by

$$d^3\vec{p_\chi} d^3 p\vec{\bar\chi} = (4\pi)|\vec{p}_\chi|^2 d|\vec{p}_\chi|(4\pi)|\vec{p}_{\bar\chi}|^2 d|\vec{p}_{\bar\chi}|\frac{1}{2}d\cos\theta = (4\pi)|\vec{p}_\chi|E_\chi dE_\chi(4\pi)|\vec{p}_{\bar\chi}|E_{\bar\chi}dE_{\bar\chi}\frac{1}{2}d\cos\theta, \tag{B.1}$$

where θ is the angle between the three momenta $\vec{p}_\chi$ and $\vec{p}_{\bar\chi}$. Changing the variable

$$(E_\chi, E_{\bar\chi}, \cos\theta) \;\; \rightarrow \;\; \begin{cases} E_+ = E_\chi + E_{\bar\chi} \\ E_+ = E_\chi - E_{\bar\chi} \\ s = (p_\chi{\cdot}p_{\bar\chi}) = 2m_\chi^2 + 2E_\chi E_{\bar\chi} - 2|\vec{p}_\chi||\vec{p}_{\bar\chi}|\cos\theta \end{cases} \tag{B.2}$$

the determinant of the Jacobian matrix is obtained as follows

$$dE_\chi dE_{\bar\chi} d\cos\theta = \det\left(\frac{\partial(E_\chi, E_{\bar\chi}, \cos\theta)}{\partial(E_+, E_-, s)}\right) dE_+ dE_- ds = \frac{1}{4|\vec{p}_\chi||\vec{p}_{\bar\chi}|}, \tag{B.3}$$

where the Jacobian matrix is given by

$$\frac{\partial(E_\chi, E_{\bar\chi}, \cos\theta)}{\partial(E_+, E_-, s)} = \begin{pmatrix} \frac{1}{2} & \frac{1}{2} & 0 \\ \frac{1}{2} & -\frac{1}{2} & 0 \\ a & b & -\frac{1}{2|\vec{p}_\chi||\vec{p}_{\bar\chi}|} \end{pmatrix}. \tag{B.4}$$

The elements a, b are any terms, which are unnecessary to derive. In this case, the two body momentum phase space can be written as

$$d^3\vec{p}_\chi d^3\vec{p}_{\bar\chi} = (2\pi^2)E_\chi E_{\bar\chi} dE_+ dE_- ds. \tag{B.5}$$

B.2 Number density, energy density and pressure of relativistic and non-relativistic particles

For simplicity, the chemical potential of χ in the early universe is set to zero, $\mu = 0$. The number density [16, 56] is given by

$$n_\chi = \frac{g}{(2\pi)^3}\int d^3p\, f(p), \quad p := |\vec{p}\,|, \tag{B.6}$$

where one distinguishes between bosons and fermions by the phase space distribution

$$f(p) = \frac{1}{e^{E(p)/T} \pm 1}. \tag{B.7}$$

The number density of relativistic and non-relativistic particles can be derived explicitly using the assumptions about their energy

$$\begin{aligned} E(p) &= \sqrt{p^2 + m^2} \approx p && \text{for relativistic particles,} \\ E(p) &= \sqrt{p^2 + m^2} \approx m + \tfrac{p^2}{2m} && \text{for non relativistic particles.} \end{aligned} \tag{B.8}$$

In the relativistic case, the phase space integral can be solved using substitution $p' = \frac{p}{T}$ and the definition of the Riemann's zeta function $\zeta(3)$,

$$\begin{aligned} n_\chi &= \frac{g}{(2\pi)^3}\int d^3p\, f(|\vec{p}\,|) = \frac{g}{2\pi^2}\int_0^\infty dp\, \frac{p^2}{e^{p/T} \pm 1} \\ &= \frac{g}{2\pi^2}T^3 \int_0^\infty dp'\, \frac{p'^2}{e^{p'} \pm 1} = \begin{cases} \frac{g}{2\pi^2}T^3\zeta(3) & \text{for bosons,} \\ \frac{3g}{4\pi^2}T^3\zeta(3) & \text{for fermions,} \end{cases} \end{aligned} \tag{B.9}$$

where

$$\int_0^\infty dp\,\frac{p^2}{e^p-1} = 2\zeta(3), \quad \int_0^\infty dp\,\frac{p^2}{e^p+1} = \frac{3}{2}\zeta(3) \quad \text{and } \zeta(3) \approx 1.202. \tag{B.10}$$

In non relativistic case, the temperature is proportional to the kinetic energy of the particles, $T \propto \frac{p^2}{2m}$. Since, p^2 is very small, the temperature is much smaller than the mass, $T \ll m$ and the exponential $e^{E(p)/T} \approx e^{m/T}e^{-\frac{p^2}{2m}} \gg 1$. Therefore, the Bose/Fermi distribution can be approximated by a Maxwell distribution

$$f(p) = \frac{1}{e^{E(p)/T} \pm 1} \approx e^{-E(p)/T} \approx e^{-m/T}e^{-\frac{p^2}{2m}}. \tag{B.11}$$

Then, in the non relativistic limit the number density is simply derived

$$\begin{aligned} n_\chi &= \frac{g}{(2\pi)^3}\int d^3p\, f(|\vec{p}\,|) = \frac{g}{2\pi^2}e^{-m/T}\int_0^\infty dp\, p^2 e^{-\frac{p^2}{2mT}} \\ &= \frac{g}{2\pi^2}(2mT)^{\frac{3}{2}}\int_0^\infty dx\, x^2 e^{-x^2} = \frac{g}{2\pi^2}(2mT)^{\frac{3}{2}}e^{-m/T}\frac{\Gamma(\frac{3}{2})}{2} \\ &= g\left(\frac{mT}{2\pi}\right)^{\frac{3}{2}} e^{-m/T} \end{aligned} \tag{B.12}$$

using $x = \frac{p}{\sqrt{2mT}}$ and the solution of the Gaussian integral

$$\int_0^\infty dx\, x^n e^{-ax^2} = \frac{\Gamma\left(\frac{n+1}{2}\right)}{2a^{\frac{n+1}{2}}} \quad \text{for } n = 2. \tag{B.13}$$

The energy density is given by

$$\rho = \frac{g}{(2\pi)^3}\int d^3p\, f(p)E(p), \tag{B.14}$$

where $f(p)$ is the Bose/Fermi distribution (B.7) and $E(p) = \sqrt{p^2+m^2}$ is the energy. For relativistic particles with energy $E(p) \approx p$ one obtains

$$\begin{aligned} \rho &= \frac{g}{(2\pi)^3}\int d^3p\, f(p)E(p) = \frac{g}{2\pi^2}\int_0^\infty dp\,\frac{p^3}{e^{p/T}\pm 1} \\ &= \frac{g}{2\pi^2}T^4\int_0^\infty dp'\,\frac{p'^3}{e^{p'}\pm 1} = \begin{cases} \frac{g}{2\pi^2}T^4\zeta(4)\Gamma(4) = \frac{\pi^2}{30}gT^4 & \text{for bosons,} \\ \frac{7}{8}\frac{g}{2\pi^2}T^4\zeta(4)\Gamma(4) = \frac{7}{8}\frac{\pi^2}{30}gT^4 & \text{for fermions,} \end{cases} \end{aligned} \tag{B.15}$$

where $p' = \frac{p}{T}$, $\zeta(4) = \frac{\pi^4}{90}$, $\Gamma(4) = 6$ and

$$\begin{aligned} \int_0^\infty dp\,\frac{p^3}{e^p-1} = \zeta(4)\Gamma(4), \quad \int_0^\infty dp\,\frac{p^3}{e^p+1} &= \int_0^\infty dp\,\frac{p^3}{e^p-1} - \int_0^\infty dp\,\frac{p^3}{e^{2p}-1} \\ &= \zeta(4)\Gamma(4) - \frac{1}{8}\zeta(4)\Gamma(4) = \frac{7}{8}\zeta(4)\Gamma(4). \end{aligned} \tag{B.16}$$

This implies, that $\rho_{fermion} = \frac{7}{8}\rho_{boson}$. The relativistic pressure is derived in a similar way

$$P = \frac{g}{(2\pi)^3}\int d^3p\, f(p)\frac{p^2}{3E(p)} = \omega\rho, \tag{B.17}$$

where $\omega = \frac{1}{3}$.

Analogously, for non relativistic particles ($E(p) \approx m + \frac{p^2}{2m}$) the integral is simplified to

$$\begin{aligned}
\rho &= \frac{g}{(2\pi)^3}\int d^3p\, f(p)E(p) = \frac{g}{2\pi^2}e^{-m/T}\int_0^\infty dp\, p^2 e^{-\frac{p^2}{2mT}}\left(m + \frac{p^2}{2m}\right) \\
&= \frac{g}{2\pi^2}(2mT)^{\frac{3}{2}}e^{-m/T}\int_0^\infty dx\, x^2 e^{-x^2}\left(m + Tx^2\right) = \frac{g}{2\pi^2}(2mT)^{\frac{3}{2}}e^{-m/T}\left(\frac{m}{2}\Gamma\left(\frac{3}{2}\right) + \frac{T}{2}\Gamma\left(\frac{5}{2}\right)\right) \\
&= g\left(\frac{mT}{2\pi}\right)^{\frac{3}{2}}e^{-m/T}\left(m + \frac{3T}{2}\right) \approx g\left(\frac{mT}{2\pi}\right)^{\frac{3}{2}} me^{-m/T} \quad \text{for } m \gg T
\end{aligned} \tag{B.18}$$

using the solution of the integral (B.13) and $x = \frac{p}{\sqrt{2mT}}$, $\Gamma\left(\frac{3}{2}\right) = \frac{\sqrt{\pi}}{2}$, $\Gamma\left(\frac{5}{2}\right) = \frac{3\sqrt{\pi}}{4}$. Thus, the energy density is related to the number density (B.12) as $\rho = mn_\chi$. The non relativistic pressure is also related to the number density as follows

$$P = \frac{g}{(2\pi)^3}\int d^3p\, f(p)\frac{p^2}{3E(p)} = n_\chi T \approx 0 \quad \text{for } m \gg T. \tag{B.19}$$

C Dark radiation

C.1 Galactic coordinates

Galactic coordinates are useful celestial coordinates in astronomy. Spiral galaxies are located approximately in a 2-dimensional plane (see Fig. 41). Therefore, galactic observations from the Earth can be described by the longitude angle l and the latitudinal angle b. The observation line is called the line of sight with distance s. The distance between the Earth (or Sun) and the galactic center is denoted as $r_\odot$. On sphere with the galactic center as midpoint, the distance $r(s,\theta)$ between the galactic center and the edge of the sphere can be expressed by the law of cosines [36]

$$r(s,\theta) = \sqrt{s^2 + r_\odot^2 - 2sr_\odot \cos\theta}, \tag{C.1}$$

where $\cos\theta = \cos l \cos b$.

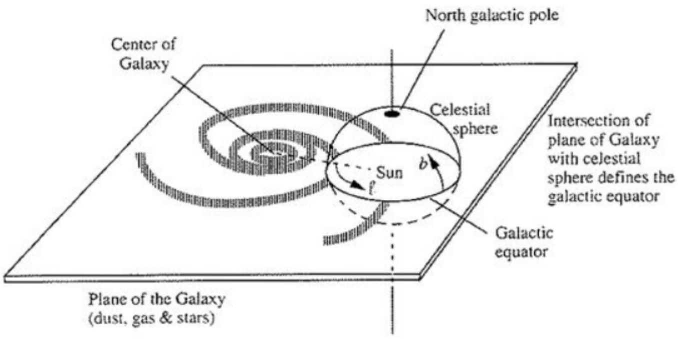

Figure 41: Galactic coordinates (figure from [164]).

C.2 Analytic from of the extragalactic flux for the 2 body decay (massless ν)

The differential form of the extragalactic flux was derived in section 8.3 and is given by

$$\frac{d\Phi_{\nu,\text{e.g.}}}{dE_\nu} = N_\nu \Gamma_X \frac{\kappa \Omega_{\text{dm}} \rho_{\text{crit}}}{m_X\, H_0} \frac{1}{|\vec{p}_\nu|} \frac{e^{-\Gamma_X t(\alpha-1)}}{\sqrt{\alpha^3 \Omega_M + \Omega_\Lambda}} \theta(\alpha - 1), \tag{C.2}$$

where $|\vec{p}_\nu| = E_\nu$ and $\alpha = E_{\text{in}}/E_\nu$ for the massless case. The look-back time is obtained by

$$t(z) = \int_z^\infty \frac{dz'}{(1+z')H(z')} = \frac{1}{3H_0\sqrt{\Omega_\Lambda}} \ln \left| \frac{\sqrt{1+(1+z)^3 \frac{\Omega_M}{\Omega_\Lambda}} + 1}{\sqrt{1+(1+z)^3 \frac{\Omega_M}{\Omega_\Lambda}} - 1} \right|. \tag{C.3}$$

Using the substitution $u = \sqrt{\frac{E_{in}^3}{E_n u^3} \frac{\Omega_M}{\Omega_\Lambda} + 1}$ the extragalactic flux can be expressed as

$$\begin{aligned} \Phi_{\nu,\text{e.g.}} &= \int dE_\nu \, \frac{d\Phi_{\nu,\text{e.g.}}}{dE_\nu} \\ &= N_\nu \Gamma_X \frac{\kappa \Omega_{\text{dm}} \rho_{\text{crit}}}{m_X\, H_0 \sqrt{\Omega_\Lambda}} \left(-\frac{2}{3}\right) \int_\infty^{\sqrt{\Omega_M/\Omega_\Lambda + 1}} du \, \left[\frac{u+1}{u-1}\right]^{-1/(3H_0\sqrt{\Omega_\Lambda}\tau_X)} \frac{1}{u^2-1}. \end{aligned} \tag{C.4}$$

The remaining integral can be solved using the substitution $x = \frac{u+1}{u-1}$

$$\begin{aligned} \int_\infty^{\sqrt{\Omega_M/\Omega_\Lambda+1}} du \, \left[\frac{u+1}{u-1}\right]^d \frac{1}{u^2-1} &= -\frac{1}{2}\int_1^{x_\star} x^{d-1} = -\frac{x^d}{2d}\bigg|_1^{x_*} \\ = -\frac{1}{2d}\left(\frac{u+1}{u-1}\right)^d \bigg|_\infty^{\sqrt{\Omega_M/\Omega_\Lambda+1}} &= \frac{1}{2d}\left[1 - \left(\frac{\sqrt{\Omega_M/\Omega_\Lambda+1}+1}{\sqrt{\Omega_M/\Omega_\Lambda+1}-1}\right)^d\right], \end{aligned} \tag{C.5}$$

where $x_\star = \frac{\sqrt{\Omega_M/\Omega_\Lambda+1}+1}{\sqrt{\Omega_M/\Omega_\Lambda+1}-1}$ and $d = -\frac{1}{3H_0\sqrt{\Omega_\Lambda}\tau_X}$. In the end, the extragalactic flux is given by

$$\Phi_{\nu,\text{e.g.}} = N_\nu \frac{\kappa\Omega_{\text{dm}}\rho_{\text{crit}}}{m_X}\left[1-\left(\frac{\sqrt{\Omega_M/\Omega_\Lambda+1}+1}{\sqrt{\Omega_M/\Omega_\Lambda+1}-1}\right)^{-\frac{1}{3H_0\sqrt{\Omega_\Lambda}\tau_X}}\right]. \tag{C.6}$$

C.3 Analytic form of the extragalactic differential recoil rate for a 2 body decay (massless ν)

In the massless case, the extragalactic differential recoil rate for a 2 body decay is given by

$$\begin{aligned}\frac{dR^{\text{e.g.}}_{X2\nu}}{dE_R} &= N_T\int_{E_{\min}}^{E_{\text{in}}} dE_\nu\,\frac{d\Phi_{\nu,\text{e.g.}}}{dE_\nu}\frac{d\sigma(E_\nu,E_R)}{dE_R}\\ &= N_T\frac{Q_W^2G_F^2m_NF(q)^2}{4\pi}\int_{E_{\min}}^{E_{\text{in}}} dE_\nu\,\frac{d\Phi_{\nu,\text{e.g.}}}{dE_\nu}\left(1-\frac{E_Rm_N}{2E_\nu^2}\right)\\ &= N_T\frac{Q_W^2G_F^2m_NF(q)^2}{4\pi}\left(\int_{E_{\min}}^{E_{\text{in}}} dE_\nu\,\frac{d\Phi_{\nu,\text{e.g.}}}{dE_\nu}-\frac{E_Rm_N}{2}\int_{E_{\min}}^{E_{\text{in}}} dE_\nu\,\frac{d\Phi_{\nu,\text{e.g.}}}{dE_\nu}\frac{1}{E_\nu^2}\right),\end{aligned} \tag{C.7}$$

where $E_{\text{in}} = \frac{m_X}{2}$ is the energy particles have immediately after the decay of the progenitor X with mass m_X and $E_{\min} = \sqrt{\frac{E_Rm_N}{2}}$ is the minimum energy a particle have to carry to produce a recoil off the nucleus with mass m_N. The solution of the first integral is derived in a similar way as in the appendix C.2. One obtains

$$\int_{E_{\min}}^{E_{\text{in}}} dE_\nu\,\frac{d\Phi_{\nu,\text{e.g.}}}{dE_\nu} = N_\nu\frac{\kappa\Omega_{\text{dm}}\rho_{\text{crit}}}{m_X}\left[\left(\frac{\sqrt{\frac{E_{in}^3}{E_{min}^3}\frac{\Omega_M}{\Omega_\Lambda}+1}+1}{\sqrt{\frac{E_{in}^3}{E_{min}^3}\frac{\Omega_M}{\Omega_\Lambda}+1}-1}\right)^d-\left(\frac{\sqrt{\frac{\Omega_M}{\Omega_\Lambda}+1}+1}{\sqrt{\frac{\Omega_M}{\Omega_\Lambda}+1}-1}\right)^d\right], \tag{C.8}$$

where

$$d = -\frac{1}{3H_0\sqrt{\Omega_\Lambda}\tau_X},\quad x_{\min}(E_R) = \frac{\sqrt{\frac{E_{\text{in}}^3}{E_{\text{min}}^3}\frac{\Omega_M}{\Omega_\Lambda}+1}+1}{\sqrt{\frac{E_{\text{in}}^3}{E_{\text{min}}^3}\frac{\Omega_M}{\Omega_\Lambda}+1}-1},\quad x_\star = \frac{\sqrt{\frac{\Omega_M}{\Omega_\Lambda}+1}+1}{\sqrt{\frac{\Omega_M}{\Omega_\Lambda}+1}-1}. \tag{C.9}$$

In the calculation of the second integral the same substitutions are used and one is left with the expression

$$\int_{E_{\min}}^{E_{\text{in}}} dE_\nu\,\frac{d\Phi_{\nu,\text{e.g.}}}{dE_\nu}\frac{1}{E_\nu^2} = -N_\nu\frac{\kappa\Omega_{\text{dm}}\rho_{\text{crit}}}{m_XH_0\sqrt{\Omega_\Lambda}\tau_X}\frac{2^{4/3}}{E_{\text{in}}^2}\left(\frac{\Omega_\Lambda}{\Omega_M}\right)^{\frac{2}{3}}\frac{{}_2F_1\left(-\frac{1}{3},\frac{1}{3}-d,\frac{2}{3};1-x\right)}{\sqrt[3]{-1+x}}\Bigg|_{x_{\min}(E_R)}^{x_\star}, \tag{C.10}$$

where ${}_2F_1\left(a,b,c;z\right)$ is the Gaussian hypergeometric function and

$$\frac{{}_2F_1\left(-\frac{1}{3},\frac{1}{3}-d,\frac{2}{3};1-x\right)}{\sqrt[3]{-1+x}}\Bigg|_{x_{\min}(E_R)}^{x^\star} = \frac{{}_2F_1\left(-\frac{1}{3},\frac{1}{3}-d,\frac{2}{3};1-x_\star\right)}{\sqrt[3]{-1+x_\star}}-\frac{{}_2F_1\left(-\frac{1}{3},\frac{1}{3}-d,\frac{2}{3};1-x_{\min}(E_R)\right)}{\sqrt[3]{-1+x_{\min}(E_R)}}. \tag{C.11}$$

Combining these two result leads to an analytic form of the differential recoil rate

$$\begin{aligned}\frac{dR^{\text{e.g.}}_{X2\nu}}{dE_R} &= N_T\frac{Q_W^2G_F^2m_NF(q)^2}{4\pi}N_\nu\frac{\kappa\Omega_{\text{dm}}\rho_{\text{crit}}}{m_X}\\ &\times\left(x_{\min}^d(E_R)-x_\star^d+\frac{2^{1/3}}{H_0\sqrt{\Omega_\Lambda}\tau_X}\left(\frac{\Omega_\Lambda}{\Omega_M}\right)^{\frac{2}{3}}\frac{E_Rm_N}{E_{\text{in}}^2}\frac{{}_2F_1\left(-\frac{1}{3},\frac{1}{3}-d,\frac{2}{3};1-x\right)}{\sqrt[3]{-1+x}}\Bigg|_{x_{\min}(E_R)}^{x_\star}\right).\end{aligned} \tag{C.12}$$

D Probability theory

D.1 Maximum likelihood estimation of Gaussian distribution

Let $x_1, x_2, ..., x_n$ be data[12] from a Gaussian distribution $N(\mu, \sigma^2)$ with expected value μ and variance σ^2. Then, the likelihood function is given by [146, 165]

$$L(\mu, \sigma^2|x_1, x_2, ..., x_n) = f(x_1, x_2, ...x_n|\mu, \sigma^2) = \prod_{i=1}^{n} f(x_i|\mu, \sigma^2) = \prod_{i=1}^{n} \left[\frac{1}{\sqrt{2\pi\sigma^2}} e^{-\frac{(x_i-\mu)^2}{2\sigma^2}} \right]. \tag{D.1}$$

The maximum of the negative log-likelihood function for μ and σ^2

$$-\ln L(\mu, \sigma^2) = \sum_{i=1}^{n} \left[\frac{1}{2} \ln\Big(2\pi\sigma^2\Big) + \frac{(x_i - \mu)^2}{2\sigma^2} \right] \tag{D.2}$$

is obtained by differentiating with respect to μ and σ^2 and setting to zero

$$-\frac{\partial \ln L(\mu, \sigma^2)}{\partial \mu} = -\sum_{i=1}^{n} \frac{(x_i - \mu)}{\sigma^2} \stackrel{!}{=} 0 \quad \Rightarrow \hat{\mu} = \frac{1}{n} \sum_{i=1}^{n} x_i, \tag{D.3}$$

$$-\frac{\partial \ln L(\mu, \sigma^2)}{\partial \sigma^2} = \frac{n}{2\sigma^2} - \sum_{i=1}^{n} \frac{(x_i - \mu)^2}{2(\sigma^2)^2} \stackrel{!}{=} 0 \quad \Rightarrow \hat{\sigma}^2 = \frac{1}{n} \sum_{i=1}^{n} (x_i - \mu)^2. \tag{D.4}$$

It is convenient to denote the estimators with a hat. The estimators $\hat{\mu}$ and $\hat{\sigma}^2$ are unbiased by the following calculations

$$\mathbb{E}[\hat{\mu}] = \frac{1}{n} \sum_{i=1}^{n} \mathbb{E}[x_i] = \frac{1}{n} n\, \mathbb{E}[x_i] = \mathbb{E}[x_i] = \mu, \tag{D.5}$$

$$\mathbb{E}[\hat{\sigma}^2] = \frac{1}{n} \sum_{i=1}^{n} \mathbb{E}[(x_i - \mu)^2] = \mathbb{E}[(x_i - \mu)^2] = \sigma^2. \tag{D.6}$$

D.2 Poisson distribution

Consider random variables X_1, X_2 which are Poisson distributed with parameters λ_1, λ_2. Then, the sum of the random variables is again Poisson distributed with parameter $\lambda_1 + \lambda_2$ [146, 166]. This can be shown by a discrete convolution of Poisson distributions.

Let $X_1 \sim \text{Pois}(\lambda_1)$ and $X_2 \sim \text{Pois}(\lambda_2)$ then

$$\begin{aligned} P(X_1 + X_2 = k) &= \sum_{l=0}^{k} P(X = l) P(Y = k - l) = \sum_{l=0}^{k} \frac{\lambda_1^l}{l!} e^{-\lambda_1} \frac{\lambda_2^{(k-l)}}{(k-l)!} e^{-\lambda_2} \\ &= e^{-(\lambda_1+\lambda_2)} \sum_{l=0}^{k} \frac{\lambda_1^l \lambda_2^{(k-l)}}{l!(k-l)!} = \frac{1}{k!} e^{-(\lambda_1+\lambda_2)} \underbrace{\sum_{l=0}^{k} \frac{k!}{l!(k-l)!} \lambda_1^l \lambda_2^{(k-l)}}_{(\lambda_1+\lambda_2)^k} \\ &= \frac{(\lambda_1 + \lambda_2)^k}{k!} e^{-(\lambda_1+\lambda_2)} \quad \Rightarrow X_1 + X_2 \sim \text{Pois}(\lambda_1 + \lambda_2). \end{aligned} \tag{D.7}$$

[12] $x_1, x_2, ..., x_n$ are independent

D.3 Inverse transform sampling method

Let $f(x)$ be a probability distribution function (PDF) then

$$F(x) = P(X \leq x) = \int_{-\infty}^{x} dx'\ f(x') \qquad \forall x \in \mathbb{R} \tag{D.8}$$

is the cumulative distribution function (CDF) of $f(x)$.

With the inverse transform sampling method one is able to generate a sample from an arbitrary one dimensional PDF [146]. It transforms a sample from a uniform distribution on an interval $[0, 1]$ to a sample related to the customized PDF $f(x)$.

The inverse transform sampling method works as follows [167]:

1. Draw a sample u from a uniform distribution on the interval $[0, 1] \quad \Rightarrow u_i \sim \mathrm{U}([0, 1])$
2. Solve the equation $F(x_i) = u_i \Leftrightarrow x_i = F^{-1}(u_i)$ for each u_i from the sample u, where the inverse $F^{-1}(u_i) = \inf\{x_i|F(x_i) \geq u_i\}$ is the inverse of F. Then, $x = \{x_i\}_{i\geq 1}$ is the sample of the customized PDF $f(x)$.

D.3.1 Example: Exponential distribution

If $X \sim \mathrm{Exp}(\tau)$ then the PDF [146] is given by

$$f(x|\tau) = \begin{cases} \frac{1}{\tau} e^{-\frac{x}{\tau}} & x \geq 0 \\ 0 & x \leq 0 \end{cases} . \tag{D.9}$$

Let $X \sim \mathrm{Exp}(1)$, then the CDF is derived by the integral

$$F(x) = \int_{0}^{x} dx'\ e^{-x'} = 1 - e^{-x}. \tag{D.10}$$

The sample x of the Exponential distribution is obtained by performing the inverse of the CDF on $u \sim U([0, 1])$

$$x = F^{-1}(u) = -\ln(1 - u). \tag{D.11}$$

E Kinematics for a $2 \to 2$ elastic scattering

E.1 $2 \to 2$ elastic scattering in the lab frame

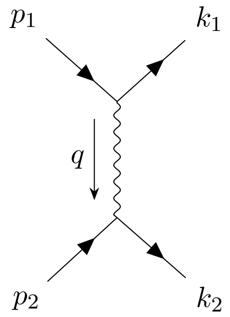

The momenta of the incoming particles are given by

$$p_1 = \begin{pmatrix} E_1 \\ \vec{p}_1 \end{pmatrix}, \quad p_2 = \begin{pmatrix} m_2 \\ \vec{0} \end{pmatrix}, \tag{E.1}$$

where the heavier particle with mass m_2 be at rest ($\vec{p}_2 = 0$). The outgoing momenta in terms of recoil energies E_R are given by

$$k_1 = \begin{pmatrix} E_3 \\ \vec{k}_1 \end{pmatrix} = \begin{pmatrix} E_1 - E_R \\ \vec{k}_1 \end{pmatrix}, \quad k_2 = \begin{pmatrix} E_4 \\ \vec{p}_1 \end{pmatrix} = \begin{pmatrix} E_R + m_2 \\ \vec{p}_1 \end{pmatrix}. \tag{E.2}$$

Using the energy momentum conservation

$$p_1 + p_2 = k_1 + k_2 \Rightarrow \begin{cases} E_1 + m_2 = E_3 + E_4 \\ \vec{p}_1 = \vec{k}_1 + \vec{k}_2 \quad (\vec{p}_2 = 0) \end{cases} \tag{E.3}$$

and the definition of the recoil energy $E_R = E_4 - m_2, E_R = E_1 - E_3$ the mandelstam variables s, t, u can be be expressed in the following ways:

$$\begin{aligned} s &= (p_1 + p_2)^2 = m_1^2 + m_2^2 + 2p_1.p_2 = m_1^2 + m_2^2 + 2E_1 m_2 \\ s &= (k_1 + k_2)^2 = m_1^2 + m_2^2 + 2k_1.k_2 = m_1^2 + m_2^2 + 2E_1 m_2 \end{aligned} \Rightarrow \begin{cases} p_1.p_2 = E_1 m_2 \\ k_1.k_2 = E_1 m_2 \end{cases}, \tag{E.4}$$

$$\begin{aligned} t &= (p_1 - k_1)^2 = 2m_1^2 - 2p_1.k_1 \\ t &= (k_2 - p_2)^2 = 2m_2^2 - 2k_2.p_2 = 2m_2^2 - 2E_4 m_2 \end{aligned} \Rightarrow \begin{cases} p_1.k_1 = m_1^2 + E_R m_2 \\ k_2.p_2 = E_4 m_2 = (E_R + m_2) m_2 \\ t = -2E_R m_2 \end{cases}, \tag{E.5}$$

$$\begin{aligned} u &= (p_1 - k_2)^2 = m_1^2 + m_2^2 - 2p_1.k_2 \\ u &= (p_2 - k_1)^2 = m_2^2 + m_1^2 - 2p_2.k_1 = m_2^2 + m_1^2 - 2m_2 E_3 \end{aligned} \Rightarrow \begin{cases} p_2.k_1 = m_2(E_1 - E_R) \\ p_1.k_2 = m_2 E_3 = m_2(E_1 - E_R) \end{cases}. \tag{E.6}$$

The momentum transfer is obtained by the relation

$$p_1 - k_1 = q = k_2 - p_2, \tag{E.7}$$

from which the following identities can be deduced,

$$\begin{aligned} &p_1.q = -E_R m_2, \quad k_1.q = E_R m_2, \\ &p_2.q = E_R m_2, \quad k_2.q = -E_R m_2 \\ &(p_2 + k_2).q = 0, \quad q^2 = -2E_R m_2. \end{aligned} \tag{E.8}$$

Then, the recoil energy in the lab frame can be derived by solving the equation for E_R

$$(p_1 - k_2)^2 = (p_2 - k_1)^2 \quad \Leftrightarrow \quad -2E_1 E_4 + 2E_1 |\vec{k}_2| \cos\theta_4 = m_2^2 - 2m_2 E_3 \tag{E.9}$$

using $E_4 = m_2 + E_R$ and $E_3 = E_1 - E_R$. The result is

$$E_R = \frac{2E_1^2 m_2 \cos^2\theta_4}{(E_1+m_2)^2 - E_1^2\cos^2\theta_4}, \tag{E.10}$$

where $0 < \theta_4 < \frac{\pi}{2}$ is the angle between the incoming and outgoing particle with mass m_2. The maximum recoil energy is given for $\theta_4 = 0$

$$E_R^{max} = \frac{2E_1^2}{2E_1 + m_2} \tag{E.11}$$

and the minimal recoil energy for $\theta_4 = \frac{\pi}{2}$

$$E_R^{min} = 0. \tag{E.12}$$

E.2 $2 \to 2$ elastic scattering in CMS frame

The center of mass is at rest

$$\vec{X} = \frac{m_1\vec{x}_1 + m_2\vec{x}_2}{m_1+m_2} = \frac{\vec{p}_1+\vec{p}_2}{m_1+m_2} = 0 \quad \Rightarrow \quad \vec{p}_1 = -\vec{p}_2, \quad \vec{k}_1 = -\vec{k}_2, \quad |\vec{p}_1| = |\vec{p}_2|, \quad |\vec{k}_1| = |\vec{k}_2|. \tag{E.13}$$

This implies that the incoming momenta p_1, p_2 and outgoing momenta k_1, k_2 are given by

$$p_1 = \begin{pmatrix} E_1 \\ \vec{p}_1 \end{pmatrix}, \quad p_2 = \begin{pmatrix} E_2 \\ -\vec{p}_1 \end{pmatrix}, \quad k_1 = \begin{pmatrix} E_3 \\ \vec{k}_1 \end{pmatrix}, \quad k_2 = \begin{pmatrix} E_4 \\ -\vec{k}_1 \end{pmatrix}. \tag{E.14}$$

Then, in the elastic scattering:

$$\begin{cases} m_1 = m_3 \\ m_2 = m_4 \end{cases} \Rightarrow \begin{cases} E_1 = E_3 \\ E_2 = E_4 \end{cases} \tag{E.15}$$

the momenta can be expressed as

$$\Rightarrow \quad p_1 = \begin{pmatrix} E_1 \\ \vec{p}_1 \end{pmatrix}, \quad p_2 = \begin{pmatrix} E_2 \\ -\vec{p}_1 \end{pmatrix}, \quad k_1 = \begin{pmatrix} E_1 \\ \vec{k}_1 \end{pmatrix}, \quad k_2 = \begin{pmatrix} E_2 \\ -\vec{k}_1 \end{pmatrix}. \tag{E.16}$$

Similar to the lab frame, we can use mandelstam variables to derive the following relations. The mandestam variable s is obtained by

$$s = (p_1+p_2)^2 = (E_1+E_2)^2 \quad \Rightarrow \quad \sqrt{s} = (E_1+E_2). \tag{E.17}$$

Using

$$\left.\begin{array}{l} E_1^2 = |\vec{p}_1|^2 + m_1 \\ E_2^2 = |\vec{p}_2|^2 + m_2 = |\vec{p}_1|^2 + m_2 \end{array}\right\} \quad \Rightarrow \quad E_1^2 - E_2^2 = m_1^2 - m_2^2 \tag{E.18}$$

one obtains

$$\begin{aligned} E_1 = E_3 &= \frac{1}{2\sqrt{s}}\left(s + m_1^2 - m_2^2\right) \\ E_2 = E_4 &= \frac{1}{2\sqrt{s}}\left(s + m_2^2 - m_1^2\right) \end{aligned} \tag{E.19}$$

Moreover, if we use the energy momentum conservations for each incoming and outgoing momenta

$$E_1^2 - |\vec{p}_1| = m_1^2, \quad E_3^2 - |\vec{k}_1| = m_1^2 \quad \Rightarrow \quad |\vec{p}_1| = |\vec{k}_1|, \tag{E.20}$$

$$E_2^2 - |\vec{p}_2| = m_2^2, \quad E_4^2 - |\vec{k}_2| = m_2^2 \quad \Rightarrow \quad |\vec{p}_2| = |\vec{k}_2|, \tag{E.21}$$

the absolute values of all three momenta are equal, $|\vec{p}_1| = |\vec{p}_2| = |\vec{k}_1| = |\vec{k}_2|$. Further simplifications lead to an expression of the incoming momentum p_1 in the center of mass frame

$$\begin{aligned}
|\vec{p}_1|^2 = E_1^2 - m_1^2 &= \frac{1}{4s}\left[(s+m_1^2-m_2^2)^2 - 4sm_1^2\right] \\
&= \frac{1}{4s}\left(s^2+m_1^4+m_2^4-2sm_1^2-2sm_2^2-2m_1^2m_2^2\right) \\
&= \frac{1}{4s}\lambda(s,m_1^2,m_2^2) \\
&\Rightarrow |\vec{p}_{1,\mathrm{CM}}|^2 = \frac{1}{4s}\lambda(s,m_1^2,m_2^2),
\end{aligned} \tag{E.22}$$

where $\lambda(s,m_1^2,m_2^2)$ is the Källen function, which is symmetric in exchanging of s, m_1^2, m_2^2. The mandelstam variable t can be written as

$$\begin{aligned}
t =&(p_1-k_1)^2 = -(\vec{p}_1-\vec{k}_1)^2 = -|\vec{p}_1|^2 - |\vec{k}_1|^2 + 2\vec{p}_1\cdot\vec{k}_1 \\
&= -2|\vec{p}_1|^2(1-\cos\theta_{\mathrm{CM}}) \\
&\Rightarrow t = -2|\vec{p}_{1,\mathrm{CM}}|^2(1-\cos\theta_{\mathrm{CM}})
\end{aligned} \tag{E.23}$$

The momentum transfer is related as follows

$$q^2 = (p_1-k_1)^2 = -(\vec{p}_1-\vec{k}_1)^2 = -|\vec{q}|^2 = -2|\vec{p}_{1,\mathrm{CM}}|^2(1-\cos\theta_{\mathrm{CM}}). \tag{E.24}$$

Using $t = -2E_R m_N$ the recoil energy in the center of mass frame can be expressed as

$$E_R = \frac{|\vec{p}_{1,\mathrm{CM}}|^2}{m_2}(1-\cos\theta_{\mathrm{CM}}). \tag{E.25}$$

Then, the incoming three momentum of a non relativistic particle is approximated as

$$|\vec{p}_{1,\mathrm{CM}}| = \frac{m_2}{\sqrt{s}}|\vec{p}_{1,\mathrm{lab}}| \approx \frac{m_2 m_1 v}{(m_1+m_2)} = \mu v \tag{E.26}$$

using $E_1 \approx m_1\left(1-\frac{v^2}{2}\right) \approx m_1$ and μ is the reduced mass.

F Cross section

F.1 Differential cross section

The differential cross section of a $2 \to 2$ scattering is given by

$$d\sigma = \frac{1}{4\sqrt{(p_1.p_2)^2 - m_1^2m_2^2}}\frac{d^3k_1}{(2\pi)^3 2k_1^0}\frac{d^3k_2}{(2\pi)^3 2k_2^0}(2\pi)^4\delta^{(4)}(p_1+p_2-k_1-k_2)\langle|M|^2\rangle. \tag{F.1}$$

First, we concentrate on particle phase space and go to the center of mass frame,

$$\begin{aligned}
&\int \frac{d^3k_1}{2k_1^0}\frac{d^3k_2}{2k_2^0}\delta^{(4)}(p_1+p_2-k_1-k_2) = \int \frac{d^3k_1}{2k_1^0}d^4k_2\theta(k_2^0)\delta(k_2^2-m_2^2)\delta^{(4)}(p_1+p_2-k_1-k_2) \\
&= \int \frac{d^3k_1}{2k_1^0}\theta(p_1^0+p_2^0-k_1^0)\delta((p_1+p_2-k_1)^2-m_2^2) \\
&= \int \frac{d|\vec{k}_1||\vec{k}_1|^2}{2k_1^0}d\Omega\,\theta(p_1^0+p_2^0-k_1^0)\delta((p_1+p_2-k_1)^2-m_2^2) \\
&= \int_0^\infty\int_0^{2\pi}\int_{-1}^{1}\frac{d|\vec{k}_1||\vec{k}_1|^2}{2k_1^0}d\varphi\,d\cos(\theta)\,\theta(\sqrt{s}-k_1^0)\delta(m_1^2-m_2^2+s-2\sqrt{s}k_1^0).
\end{aligned} \tag{F.2}$$

If we use the following substitution

$$(k_1^0)^2 - |\vec{k}|^2 = m_1^2 \quad \Rightarrow \quad 2k_1^0 - 2|\vec{k}|\frac{d|\vec{k}|}{dk_1^0} = 0 \quad \Leftrightarrow \quad \frac{1}{2}dk_1^0 = \frac{d|\vec{k}|}{2k_1^0}|\vec{k}|, \tag{F.3}$$

we obtain

$$\begin{aligned}
&\int_0^\infty \int_0^{2\pi} \int_{-1}^1 \frac{d|\vec{k}_1||\vec{k}_1|^2}{2k_1^0} d\varphi\, d\cos(\theta)\, \theta(\sqrt{s} - k_1^0)\delta(m_1^2 - m_2^2 + s - 2\sqrt{s}k_1^0) \\
&= \int_{m_1}^\infty \int_0^{2\pi} \int_{-1}^1 \frac{dk_1^0|\vec{k}_1|}{2} d\varphi\, d\cos(\theta)\, \theta(\sqrt{s} - k_1^0)\delta(m_1^2 - m_2^2 + s - 2\sqrt{s}k_1^0) \\
&= \int_{m_1}^\infty \int_0^{2\pi} \int_{-1}^1 \frac{dk_1^0\sqrt{(k_1^0)^2 - m_1^2}}{2} d\varphi\, d\cos(\theta)\, \theta(\sqrt{s} - k_1^0)\delta(m_1^2 - m_2^2 + s - 2\sqrt{s}k_1^0) \\
&= \int_{-\infty}^\infty \int_0^{2\pi} \int_{-1}^1 \frac{dk_1^0\sqrt{(k_1^0)^2 - m_1^2}}{2} d\varphi\, d\cos(\theta)\, \theta(k_1^0 - m_1)\, \theta(\sqrt{s} - k_1^0)\delta(m_1^2 - m_2^2 + s - 2\sqrt{s}k_1^0).
\end{aligned} \tag{F.4}$$

Next, we can modify the delta function,

$$m_1^2 - m_2^2 + s - 2\sqrt{s}k_1^0 = 0 \quad \Leftrightarrow \quad \frac{m_1^2 - m_2^2 + s}{2\sqrt{s}} = k_1^0, \tag{F.5}$$

$$\delta(m_1^2 - m_2^2 + s - 2\sqrt{s}k_1^0) \quad \rightarrow \quad \frac{1}{2\sqrt{s}}\delta\left(k_1^0 - \frac{m_1^2 - m_2^2 + s}{2\sqrt{2}}\right) \tag{F.6}$$

such that we can integrate over k_1^0,

$$\begin{aligned}
&\int_{-\infty}^\infty \int_0^{2\pi} \int_{-1}^1 \frac{dk_1^0\sqrt{(k_1^0)^2 - m_1^2}}{2} d\varphi\, d\cos(\theta)\, \theta(k_1^0 - m_1)\, \theta(\sqrt{s} - k_1^0)\delta(m_1^2 - m_2^2 + s - 2\sqrt{s}k_1^0) \\
&= \int_{-\infty}^\infty \int_0^{2\pi} \int_{-1}^1 \frac{dk_1^0\sqrt{(k_1^0)^2 - m_1^2}}{4\sqrt{s}} d\varphi\, d\cos(\theta)\, \theta(k_1^0 - m_1)\, \theta(\sqrt{s} - k_1^0)\delta\left(k_1^0 - \frac{m_1^2 - m_2^2 + s}{2\sqrt{s}}\right) \\
&= \int_0^{2\pi} \int_{-1}^1 d\varphi\, d\cos(\theta) \frac{1}{4\sqrt{s}} \sqrt{\left(\frac{m_1^2 - m_2^2 + s}{2\sqrt{s}}\right)^2 - m_1^2}\; \theta\left(\frac{m_1^2 - m_2^2 + s}{2\sqrt{s}} - m_1\right) \theta\left(\sqrt{s} - \frac{m_1^2 - m_2^2 + s}{2\sqrt{s}}\right).
\end{aligned} \tag{F.7}$$

The theta functions can be simplified to

$$\theta\left(\frac{m_1^2 - m_2^2 + s}{2\sqrt{s}} - m_1\right) = \theta\left(\frac{m_1^2 - m_2^2 + s - 2\sqrt{s}m_1}{2\sqrt{s}}\right) = 1 \quad \text{for} \quad \lambda(s, m_1^2, m_2^2) \geq 0, \tag{F.8}$$

$$\theta\left(\sqrt{s} - \frac{m_1^2 - m_2^2 + s}{2\sqrt{s}}\right) = \theta\left(\frac{s - m_1^2 + m_2^2}{2\sqrt{s}}\right) = 1 \quad \text{for} \quad s \geq m_1^2 + m_2^2. \tag{F.9}$$

Thus, the integral reduces to

$$\begin{aligned}
&\int_0^{2\pi} \int_{-1}^1 d\varphi\, d\cos(\theta) \frac{1}{4\sqrt{s}} \sqrt{\left(\frac{m_1^2 - m_2^2 + s}{2\sqrt{s}}\right)^2 - m_1^2} \\
&= \int_0^{2\pi} \int_{-1}^1 d\varphi\, d\cos(\theta) \frac{1}{4\sqrt{s}} \sqrt{\frac{m_1^4 + m_4^4 + s^2 - 2sm_1^2 - 2sm_2^2 - 2m_1^2m_2^2}{4s}} \\
&= \int_0^{2\pi} \int_{-1}^1 d\varphi\, d\cos(\theta) \frac{1}{8s} \sqrt{\lambda(s, m_1^2, m_2^2)} = \int_{-1}^1 d\cos(\theta) \frac{\pi}{4s} \sqrt{\lambda(s, m_1^2, m_2^2)}.
\end{aligned} \tag{F.10}$$

In the end, the phase space integral is given by the Källen function

$$\int \frac{d^3k_1}{2k_1^0}\frac{d^3k_2}{2k_2^0}\delta^{(4)}(p_1+p_2-k_1-k_2) = \int_{-1}^{1} d\cos(\theta)\frac{\pi}{4s}\sqrt{\lambda(s,m_1^2,m_2^2)} \tag{F.11}$$

The term $4\sqrt{(p_1.p_2)-m_1^2m_2^2}$ can be expressed in the center of mass frame as

$$4\sqrt{(p_1.p_2)^2-m_1^2m_2^2} = 2\sqrt{\lambda(s,m_1^2,m_2^2))} = 4\,|\vec{p}_{1,\mathrm{CM}}|\sqrt{s} \tag{F.12}$$

using the mandelstam variable $s = (p_1+p_2)^2 = m_1^2+m_2^2+2p_1.p_2$. In the lab frame the term[13] simplifies to

$$4\sqrt{(p_1.p_2)^2-m_1^2m_2^2} = 4\sqrt{(E_1.m_2)^2-m_1^2m_2^2} = 4\sqrt{m_2^2(E_1^2-m_1^2)} = 4m_2|\vec{p}_{1,\mathrm{lab}}|, \tag{F.13}$$

which lead to a relation between the center of mass and lab momentum

$$|\vec{p}_{1,\mathrm{CM}}| = \frac{m_2}{\sqrt{s}}\,|\vec{p}_{1,\mathrm{lab}}|, \quad |\vec{p}_{1,\mathrm{CM}}| \approx |\vec{p}_{1,\mathrm{lab}}|, \; \frac{m_2}{\sqrt{s}} \approx 1 \quad \text{for}\, m_2 \gg m_1. \tag{F.14}$$

Then, the differential cross section in the center of mass frame

$$\frac{d\sigma}{d\Omega} = \frac{\langle|M|^2\rangle}{64\pi^2 s} \tag{F.15}$$

can be written as

$$\frac{d\sigma}{d\cos\theta_{CM}} = \frac{d\sigma}{dt}\frac{dt}{d\cos\theta_{\mathrm{CM}}} = \frac{d\sigma}{dt}2|\vec{p}_{1,\mathrm{CM}}|^2, \tag{F.16}$$

where $\langle|M|^2\rangle = \frac{1}{2}\sum_{\mathrm{spins}}|M|^2$ is the spin averaged amplitude. According to the mandelstam variable t the differential cross section is expressed as

$$\frac{d\sigma}{dt} = \frac{\langle|M|^2\rangle}{64\pi s|\vec{p}_{1,\mathrm{CM}}|^2}. \tag{F.17}$$

It is common to write the differential cross section in terms of recoil energies E_R

$$\frac{d\sigma}{dE_R} = \frac{d\sigma}{dt}\left|\frac{dt}{dE_R}\right| = \frac{m_2\langle|M|^2\rangle}{32\pi s|\vec{p}_{1,\mathrm{CM}}|^2} \overset{(F.14)}{=} \frac{\langle|M|^2\rangle}{32\pi m_2|\vec{p}_{1,\mathrm{lab}}|^2} \tag{F.18}$$

using $t = -2m_2E_R$.

F.2 Cross section of neutrino nucleus scattering

Consider the elastic scattering of a neutrino off a nucleus with mass m_N

$$\nu + N \to \nu + N. \tag{F.19}$$

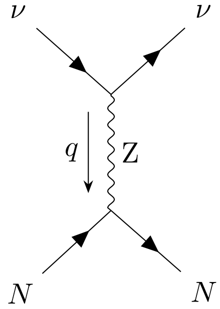

[13] The term is invariant, if the velocity direction vector of both particles lies on the same axes.

	g_V^i	g_A^i
u	$\frac{1}{2} - \frac{4}{3}\sin^2\theta_W$	$\frac{1}{2}$
d	$-\frac{1}{2} + \frac{2}{3}\sin^2\theta_W$	$-\frac{1}{2}$
ν	$\frac{1}{2}$	$\frac{1}{2}$
l	$-\frac{1}{2} + 2\sin^2\theta_W$	$-\frac{1}{2}$

Table 6: Values of vector and axial coupling in the neutral current sector,u...up-quark, d...down-quark, ν...neutrino, l...remaining leptons: e, μ, τ [168].

Denote p_1, p_2 as the four momenta of incoming neutrino and nucleus and k_1, k_2 as the four momenta of outgoing neutrino and nucleus. The mediator particle, that is involved in this scattering, is the Z-boson. Interactions with W-bosons change flavors and photons couple only on charged particles. The neutral current (NC) Lagrangian [168] is given by

$$\mathcal{L}_{NC} = -\frac{g}{2\cos\theta_W}\sum_i \bar{\Psi}_i\gamma^\mu(g_V^i - g_A^i\gamma_5)\Psi_i Z_\mu, \tag{F.20}$$

where

$$g_V^i = t_3^i - 2Q_i\sin^2\theta_W, \quad g_A^i = t_3^i \tag{F.21}$$

are the vector and axial vector couplings, t_3^i is the eigenvalue of isospin T_3 in $SU(2)$ doublet and Q_i is the charge of the interacting particle. The values of the vector and axial vector coupling are given in the Tab. 6. The Z-propagator can be written as

$$-i\frac{g_{\mu\rho} - \frac{q_\mu q_\rho}{M_Z^2}}{q^2 - M_Z^2} \quad \xrightarrow{q^2 \ll M_Z^2} \quad i\frac{g_{\mu\rho}}{M_Z^2} \tag{F.22}$$

using contact interaction $q^2 \ll M_Z^2$. The NC vertex is given by

$$-i\frac{g}{2\cos\theta_W}\gamma^\mu(g_V^i - g_A^i\gamma_5). \tag{F.23}$$

For neutrinos, one obtains

$$-i\frac{g}{2\cos\theta_W}\gamma^\mu\frac{1}{2}(1-\gamma_5) = -i\frac{g}{2\cos\theta_W}\gamma^\mu\gamma_L, \tag{F.24}$$

where the index L denotes left-handed neutrinos. Right handed neutrinos do not exist in the Dirac theory. We consider spin-independent scattering, where the axial-vector part g_A^u, g_A^d is not taken into account. A nucleus has Z protons and N neutrons. Therefore, $2Z+N$ up-quarks and $2N+Z$ down-quarks. Then, the Z-boson couples differently to up-quarks and to down-quarks, which leads to the nucleus vertex [3]

$$-i\frac{g}{2\cos\theta_W}\left[(2Z+N)g_V^u + (2N+Z)g_V^d\right](k_2+p_2)^\rho F^2(q), \tag{F.25}$$

where $\left[(2Z+N)g_V^u + (2N+Z)g_V^d\right]$ is related to the weak charge $Q_W = \left(4\sin^2\theta_W - 1\right)Z + N$,

$$\begin{aligned}
\left[(2Z+N)g_V^u + (2N+Z)g_V^d\right] &= \left[(2Z+N)\left(\frac{1}{2} - \frac{4}{3}\sin^2\theta_W\right) + (2N+Z)\left(-\frac{1}{2} + \frac{2}{3}\sin^2\theta_W\right)\right] \\
&= \left[\frac{1}{2}\left(1 - 4\sin^2\theta_W\right)Z - N\right] \\
&= -\frac{1}{2}Q_W.
\end{aligned} \tag{F.26}$$

Thus, the scattering amplitude for a neutrino nucleus scattering is given by

$$\begin{aligned} iM =& -i\frac{g}{2\cos\theta_W}\bar{u}_\nu(k_1,r_1)\gamma^\mu\gamma_L u_\nu(p_1,s_1)\left(-i\frac{g_{\mu\rho}-\frac{q_\mu q_\rho}{M_Z^2}}{q^2-m_V^2}\right)i\frac{g}{2\cos\theta_W} \\ &\times\frac{1}{2}Q_W 2m_2F(q)\bar{u}_N(k_2,r_2)\frac{(p_2+k_2)^\nu}{(p_2+k_2)^2}u_N(p_2,s_2), \end{aligned} \tag{F.27}$$

where s_1, s_2, r_1, r_2 are spins of the neutrino and nucleus We consider point interaction, then the amplitude reduces to

$$M = -2m_2F(q)Q_W\frac{G_F}{\sqrt{2}}\bar{u}_\nu(k_1,r_1)\gamma^\mu\gamma_L u_\nu(p_1,s_1)g_{\mu\rho}\bar{u}_N(k_2,r_2)\frac{(p_2+k_2)^\rho}{(p_2+k_2)^2}u_N(p_2,s_2) \tag{F.28}$$

using the definition of the Fermi constant $\frac{G_F}{\sqrt{2}} = \frac{g^2}{8M_W^2} = \frac{g^2}{8M_Z^2\cos^2\theta_W}$. Taking the absolute value and summing over the spins one obtains

$$\begin{aligned} \sum_{\text{spins}}|M|^2 =& \sum_{\text{spins}} Q_W^2G_F^2 2m_N^2F(q)^2(\bar{u}_\nu(k_1,r_1)\gamma^\mu\gamma_L u_\nu(p_1,s_1)\bar{u}_N(k_2,r_2)\frac{(p_2+k_2)_\mu}{(p_2+k_2)^2}u_N(p_2,s_2))^\dagger \\ &\times(\bar{u}_\nu(k_1,r_1)\gamma^\alpha\gamma_L u_\nu(p_1,s_1)\bar{u}_N(k_2,r_2)\frac{(p_2+k_2)_\alpha}{(p_2+k_2)^2}u_N(p_2,s_2)) \\ =& \sum_{\text{spins}} Q_W^2G_F^2 2m_N^2F(q)^2\bar{u}_N(p_2,s_2)\frac{(p_2+k_2)_\mu}{(p_2+k_2)^2}u_N(k_2,r_2)\bar{u}_\nu(p_1,s_1)\gamma^\mu u_\nu(k_1,r_1) \\ &\times\bar{u}_\nu(k_1,r_1)\gamma_R\gamma^\rho u_\nu(p_1,s_1)\bar{u}_N(k_2,r_2)\frac{(p_2+k_2)_\alpha}{(p_2+k_2)^2}u_N(p_2,s_2) \\ =& \frac{Q_W^2G_F^2 2m_N^2F(q)^2(p_2+k_2)_\mu(p_2+k_2)_\alpha}{(p_2+k_2)^4}Tr[(\not{p}_2+m_N)(\not{k}_2+m_N)] \\ &\times Tr[\not{p}_1\gamma_R\gamma^\mu\not{k}_1\gamma^\alpha] \\ =& \frac{Q_W^2G_F^2 2m_N^2F(q)^2(p_2+k_2)_\mu(p_2+k_2)_\alpha}{(p_2+k_2)^4}\left[Tr(\not{p}_2\not{k}_2)+Tr(m_N^2\mathbf{1})\right] \\ &\times\left[Tr(\not{p}_1\gamma^\mu\not{k}_1\gamma^\alpha)+Tr(\not{p}_1\gamma_5\gamma^\mu\not{k}_1\gamma^\alpha)\right] \\ =& \frac{Q_W^2G_F^2 2m_N^2F(q)^2(p_2+k_2)_\mu(p_2+k_2)_\alpha}{(p_2+k_2)^4}\left[4p_2.k_2+4m_N^2\right] \\ &\times[4p_{1\rho}k_{1\epsilon}(g^{\rho\mu}g^{\epsilon\alpha}+g^{\rho\alpha}g^{\mu\epsilon}-g^{\rho\epsilon}g^{\mu\alpha})-8i\epsilon^{\mu\epsilon\alpha\rho}] \\ =& \frac{16Q_W^2G_F^2 2m_N^2F(q)^2(p_2+k_2)_\mu(p_2+k_2)_\alpha}{(p_2+k_2)^4}\left[p_2.k_2+m_N^2\right]\times[p_1^\mu k_1^\nu+p_1^\nu k_1^\mu-(p_1.k_1)g^{\mu\alpha}] \\ =& \frac{16Q_W^2G_F^2 2m_N^2F(q)^2}{(p_2+k_2)^4}\left[p_2.k_2+m_N^2\right]\times\left[2p_1.(p_2+k_2)k_1.(p_2+k_2)-(p_1.k_1)(p_2+k_2)^2\right] \end{aligned} \tag{F.29}$$

using $(\gamma_5)^\dagger = \gamma_5$, $(\gamma^0)^\dagger = \gamma^0, \gamma^0(\gamma^\mu)^\dagger\gamma^0 = \gamma^\mu, \gamma_R = \frac{1}{2}(1+\gamma_5)$ and $(p_2+k_2)_\mu(p_2+k_2)_\alpha\epsilon^{\mu\epsilon\alpha\rho} = 0$, because $(p_2+k_2)_\mu(p_2+k_2)_\alpha$ is symmetric and $\epsilon^{\mu\epsilon\alpha\rho}$ is antisymmetric in μ,α. Express $\sum_{\text{spins}}|M|^2$ in terms of the mandelstam variables s,t,u using the identities in center of mass frame

$$\begin{aligned} &(p_2+k_2)^2 = -t+4m_N^2, \quad p_2.k_2 = -\frac{1}{2}t+m_N^2, \quad p_1.k_1 = -\frac{1}{2}t+m_\nu^2, \\ &q^2 = t, \quad p_1.(p_2+k_2)k_1.(p_2+k_2) = \frac{1}{4}(s-u)^2, \quad s+t+u = 2m_\nu+2m_N, \end{aligned} \tag{F.30}$$

where n is the number of particles, in this case $n = 4$. With the last expression the amplitude can be rewritten into the two mandelstam variables s and t using

$$p_1.(p_2 + k_2)k_1.(p_2 + k_2) = \frac{1}{4}(s-u)^2 = \frac{1}{4}(2s + t - 2m_\nu^2 - 2m_N^2)^2. \tag{F.31}$$

Thus, the averaged amplitude over the spins is given by ($m_\nu = 0$)

$$\begin{aligned}
\sum_{\text{spins}} |M|^2 &= \frac{16Q_W^2 G_F^2 2m_N^2 F(q)^2}{(-t+4m_2^2)^2}\left[-\frac{1}{2}t + 2m_N^2\right] \times \left[\frac{1}{2}(s-u)^2 + \frac{1}{2}t(-t+4m_N^2)\right] \\
&= \frac{16Q_W^2 G_F^2 2m_N^2 F(q)^2}{(-t+4m_N^2)^2}\left[-\frac{1}{2}t + 2m_N^2\right] \times \left[\frac{1}{2}(2s+t-2m_N^2)^2 + \frac{1}{2}t(-t+4m_N^2)\right] \\
&= \frac{8Q_W^2 G_F^2 2m_N^2 F(q)^2}{(-t+4m_N^2)}\left[\frac{1}{2}(2s+t^2-2m_N^2)^2 + \frac{1}{2}t(-t+4m_N^2)\right] \\
&= 4Q_W^2 G_F^2 2m_N^2 F(q)^2 \left[\frac{(2s+t-2m_N^2)^2}{(-t+4m_N^2)} + t\right].
\end{aligned} \tag{F.32}$$

Plugging (E.4) and (E.5) into (F.32) one gets

$$\begin{aligned}
\sum_{spins} |M|^2 &= 4Q_W^2 G_F^2 2m_N^2 F(q)^2 \left[\frac{(2s+t-2m_N^2)^2}{(-t+4m_N^2)} + t\right] \\
&= 16Q_W^2 G_F^2 2m_N^2 F(q)^2 \left[\frac{(4E_\nu^2 m_N^2 - 4E_\nu E_R m_N^2 + E_R^2 m_N^2)}{(2E_R m_N + 4m_N^2)} - \frac{E_R m_N}{2}\right].
\end{aligned} \tag{F.33}$$

The nominator can be approximated by

$$2E_R m_N + 4m_N^2 = 2m_N(E_R + 2m_N) \approx 4m_N^2 + \mathcal{O}\left(\frac{E_R}{m_N}\right) \quad \text{for} \quad E_R \ll 2m_N. \tag{F.34}$$

In this case, the amplitude is written as

$$\langle |M|^2 \rangle \equiv \frac{1}{4}\sum_{spins} |M|^2 = 4Q_W^2 G_F^2 2m_N^2 F(q)^2 \left[E_\nu^2 - \frac{E_R m_N}{2}\right], \tag{F.35}$$

where E_R^2 and $E_1 E_R$ are negligible small. Then, the differential cross section in the lab frame is expressed as

$$\begin{aligned}
\frac{d\sigma}{dE_R} &= \frac{\langle |M|^2 \rangle}{32\pi m_N |\vec{p}_{\nu,\text{lab}}|^2} = \frac{Q_W^2 G_F^2 m_N F(q)^2}{4\pi E_\nu^2}\left[E_1^2 - \frac{E_R m_N}{2}\right] \\
&= \frac{Q_W^2 G_F^2 m_N F(q)^2}{4\pi}\left[1 - \frac{E_R m_N}{2E_\nu^2}\right].
\end{aligned} \tag{F.36}$$

G WIMP detection

G.1 Differential recoil rate

The differential recoil rate of WIMPs is given by

$$\frac{dR}{dE_R} = N_T \frac{\rho_\chi}{m_\chi} \left\langle \frac{d\sigma}{dE_R} v \right\rangle = N_T \frac{\rho_\chi}{m_\chi} \int_{|\vec{v}| \geq v_{\min}} d^3\vec{v}\, f(\vec{v}, \vec{v}_{\rm lab}) \frac{d\sigma}{dE_R} v, \tag{G.1}$$

where $f(\vec{v})$ is the Maxwell-Boltzmann-Distribution

$$f(\vec{v}, \vec{v}_{\rm lab}) = \begin{cases} \frac{1}{N_{\rm esc}(2\pi\sigma_v^2)^{3/2}} \exp\left[\frac{-(\vec{v}+\vec{v}_{\rm lab})^2}{2\sigma_v^2}\right] & \text{for } |\vec{v}+\vec{v}_{\rm lab}| < v_{\rm esc} \\ 0 & \text{for } |\vec{v}+\vec{v}_{\rm lab}| \geq v_{\rm esc} \end{cases} \tag{G.2}$$

and the differential spin-independent cross section is expressed in term of the WIMP-nucleon cross section σ_n,

$$\frac{d\sigma}{dE_R} = \frac{m_N}{2\mu_{\chi,N}^2 v^2} \sigma_0^{\rm SI} F^2(|\vec{q}\,|), \quad \sigma_0^{\rm SI} = A^2 \left(\frac{\mu_{\chi,N}}{\mu_{\chi,n}}\right)^2 \sigma_n. \tag{G.3}$$

We concentrate on the condition $|\vec{v}+\vec{v}_{\rm lab}| < v_{\rm esc}$ to modify the boundaries of the velocity integral

$$\begin{aligned} |\vec{v}+\vec{v}_{\rm lab}| < v_{\rm esc} \quad &\Rightarrow \quad |\vec{v}+\vec{v}_{\rm lab}|^2 = v^2 + v_{\rm lab}^2 + 2\vec{v}\cdot\vec{v}_{\rm lab} = v^2 + v_{\rm lab}^2 + 2vv_{\rm lab}\cos\theta < v_{\rm esc}^2 \\ &\Rightarrow \frac{-v^2 - v_{\rm lab}^2 + v_{\rm esc}^2}{2vv_{\rm lab}} > \cos\theta. \end{aligned} \tag{G.4}$$

The integral over $\cos\theta$ is generally bounded above by 1 and below by -1. However, the boundaries change according the condition, where the velocity integral splits into two cases:

1. The boundary of $\cos\theta$ is greater than 1:

$$\begin{aligned} \frac{-v^2 - v_{\rm lab}^2 + v_{\rm esc}^2}{2vv_{\rm lab}} > 1 \quad &\Rightarrow \quad (v+v_{\rm lab})^2 < v_{\rm esc}^2 \\ &\Rightarrow \quad |v+v_{\rm lab}| < |v_{\rm esc}| \\ &\Rightarrow \quad v+v_{\rm lab} < v_{\rm esc}, \quad \text{because } v+v_{\rm lab} \text{ and } v_{\rm esc} \text{ are always positive} \\ &\Rightarrow \quad v < v_{\rm esc} - v_{\rm lab} \end{aligned} \tag{G.5}$$

2. The boundary of $\cos\theta$ is smaller than 1 and grater than -1:

$$\begin{aligned} \frac{-v^2 - v_{\rm lab}^2 + v_{\rm esc}^2}{2vv_{\rm lab}} < 1 \quad &\Rightarrow \quad (v+v_{\rm lab})^2 > v_{\rm esc}^2 \\ &\Rightarrow \quad |v+v_{\rm lab}| > |v_{\rm esc}| \\ &\Rightarrow \quad v+v_{\rm lab} > v_{\rm esc}, \quad \text{because } v+v_{\rm lab} \text{ and } v_{\rm esc} \text{ are always positive} \\ &\Rightarrow \quad v > v_{\rm esc} - v_{\rm lab}, \end{aligned} \tag{G.6}$$

$$\begin{aligned} \frac{-v^2 - v_{\rm lab}^2 + v_{\rm esc}^2}{2vv_{\rm lab}} > -1 \quad &\Rightarrow \quad (v-v_{\rm lab})^2 < v_{\rm esc}^2 \\ &\Rightarrow \quad |v-v_{\rm lab}| < |v_{\rm esc}| \\ &\Rightarrow \quad \pm(v-v_{\rm lab}) < v_{\rm esc}, \quad \text{because } v-v_{\rm lab} \text{ can be negative} \\ &\qquad\qquad \text{and positive } v_{\rm esc} \text{ is always positive} \\ &\Rightarrow \quad v < v_{\rm esc} + v_{\rm lab} \text{ and } v > v_{\rm lab} - v_{\rm esc}. \end{aligned} \tag{G.7}$$

The constrain $v > v_{\rm lab} - v_{\rm esc}$ is always fulfilled, because $v_{\rm lab} - v_{\rm esc}$ is always negative and v is always positive.

The case, where the boundary of $\cos\theta$ is smaller than -1 is not allowed, because the WIMP's maximum velocity is constraint by the escape velocity v_{esc} as well as $v_{\mathrm{lab}} < v_{\mathrm{esc}}$, $v \geq 0$:

$$\begin{aligned} \frac{-v^2 - v_{\mathrm{lab}}^2 + v_{\mathrm{esc}}^2}{2vv_{\mathrm{lab}}} < -1 \quad &\Rightarrow \quad (v - v_{\mathrm{lab}})^2 > v_{\mathrm{esc}}^2 \\ &\Rightarrow \quad |v - v_{\mathrm{lab}}| > |v_{\mathrm{esc}}| \\ &\Rightarrow \quad \pm(v - v_{\mathrm{lab}}) > v_{\mathrm{esc}}, \quad \text{because } v - v_{\mathrm{lab}} \text{ can be negative} \\ &\qquad\qquad\qquad\qquad\quad \text{and positive } v_{\mathrm{esc}} \text{ is always positive} \\ &\Rightarrow \quad v > v_{\mathrm{esc}} + v_{\mathrm{lab}} \text{ and } v < v_{\mathrm{lab}} - v_{\mathrm{esc}}. \end{aligned} \tag{G.8}$$

For a minimum WIMP velocity v_{min} the integral of the distribution function is rewritten as

$$\begin{aligned} \int_{v_{\mathrm{min}}} d^3\vec{v}\, \frac{f(\vec{v} + \vec{v}_{\mathrm{lab}})}{v} = \frac{2\pi}{N_{\mathrm{esc}}(2\pi\sigma_v^2)^{3/2}} \Bigg(&\int_{v_{\mathrm{min}}}^{\max[v_{\mathrm{min}}, v_{\mathrm{esc}} - v_{\mathrm{lab}}]} d\vec{v}\, \underbrace{\int_{-1}^{1} d\cos\theta\, v \exp\left[\frac{-(\vec{v} + \vec{v}_{\mathrm{lab}})^2}{2\sigma_v^2}\right]}_{1.} \\ &+ \int_{\max[v_{\mathrm{min}}, v_{\mathrm{esc}} - v_{\mathrm{lab}}]}^{\max[v_{\mathrm{min}}, v_{\mathrm{esc}} + v_{\mathrm{lab}}]} d\vec{v}\, \underbrace{\int_{-1}^{\frac{-v^2 - v_{\mathrm{lab}}^2 + v_{\mathrm{esc}}^2}{2vv_{\mathrm{lab}}}} d\cos\theta\, v \exp\left[\frac{-(\vec{v} + \vec{v}_{\mathrm{lab}})^2}{2\sigma_v^2}\right]}_{2.} \Bigg), \end{aligned} \tag{G.9}$$

where the boundaries of the velocity integral were modified such that the minimum velocity v_{min} can be arbitrarily large. If the minimum velocity v_{min} is greater than $v_{\mathrm{esc}} - v_{\mathrm{lab}}$ the first integral goes to zero. The first and second integral goes to zero if $v \geq v_{\mathrm{esc}} + v_{\mathrm{lab}}$. The first integral is simply an integral of an exponential function

$$\begin{aligned} \int_{-1}^{1} d\cos\theta\, v \exp\left[\frac{-(\vec{v} + \vec{v}_{\mathrm{lab}})^2}{2\sigma_v^2}\right] &= v \exp\left[\frac{-(v^2 + v_{\mathrm{lab}}^2)}{2\sigma_v^2}\right] \int_{-1}^{1} d\cos\theta\, \exp\left[\frac{-2vv_{\mathrm{lab}}\cos\theta}{2\sigma_v^2}\right] \\ &= \frac{v_0^2}{2v_{\mathrm{lab}}} \exp\left[\frac{-(v^2 + v_{\mathrm{lab}}^2)}{v_0^2}\right] \left(\exp\left[\frac{2vv_{\mathrm{lab}}}{v_0^2}\right] - \exp\left[\frac{-2vv_{\mathrm{lab}}}{v_0^2}\right] \right) \\ &= \frac{v_0^2}{2v_{\mathrm{lab}}} \left(\exp\left[-\frac{(v - v_{\mathrm{lab}})^2}{v_0^2}\right] - \exp\left[-\frac{(v + v_{\mathrm{lab}})^2}{v_0^2}\right] \right). \end{aligned} \tag{G.10}$$

using $\sigma_v = v_0/\sqrt{2}$. The second integral is expressed as

$$\begin{aligned} &\int_{-1}^{\frac{-v^2 - v_{\mathrm{lab}}^2 + v_{\mathrm{esc}}^2}{2vv_{\mathrm{lab}}}} d\cos\theta\, v \exp\left[\frac{-(\vec{v} + \vec{v}_{\mathrm{lab}})^2}{2\sigma_v^2}\right] \\ &= v \exp\left[\frac{-(v^2 + v_{\mathrm{lab}}^2)}{2\sigma_v^2}\right] \int_{-1}^{\frac{-v^2 - v_{\mathrm{lab}}^2 + v_{\mathrm{esc}}^2}{2vv_{\mathrm{lab}}}} d\cos\theta\, \exp\left[\frac{-2vv_{\mathrm{lab}}\cos\theta}{2\sigma_v^2}\right] \\ &= \frac{v_0^2}{2v_{\mathrm{lab}}} \left(\exp\left[-\frac{(v - v_{\mathrm{lab}})^2}{v_0^2}\right] - \exp\left[-\frac{v_{\mathrm{esc}}^2}{v_0^2}\right] \right). \end{aligned} \tag{G.11}$$

Then, the velocity integral is reduced to

$$\begin{aligned} &\int_{v_{\mathrm{min}}} d^3\vec{v}\, \frac{f(\vec{v} + \vec{v}_{\mathrm{lab}})}{v} \\ &= \frac{1}{N_{\mathrm{esc}}\sqrt{\pi}v_0 v_{\mathrm{lab}}} \Bigg[\int_{v_{\mathrm{min}}}^{\max[v_{\mathrm{min}}, v_{\mathrm{esc}} - v_{\mathrm{lab}}]} d\vec{v} \left(\exp\left[-\frac{(v - v_{\mathrm{lab}})^2}{v_0^2}\right] - \exp\left[-\frac{(v + v_{\mathrm{lab}})^2}{v_0^2}\right] \right) \\ &+ \int_{\max[v_{\mathrm{min}}, v_{\mathrm{esc}} - v_{\mathrm{lab}}]}^{\max[v_{\mathrm{min}}, v_{\mathrm{esc}} + v_{\mathrm{lab}}]} d\vec{v} \left(\exp\left[-\frac{(v - v_{\mathrm{lab}})^2}{v_0^2}\right] - \exp\left[-\frac{v_{\mathrm{esc}}^2}{v_0^2}\right] \right) \Bigg]. \end{aligned} \tag{G.12}$$

From the normalization condition we obtain the normalization constant

$$\int d^3\vec{v} f(\vec{v}) = 1 \quad \Leftrightarrow \quad N_{\text{esc}} = \frac{1}{(2\pi\sigma_v^2)^{3/2}} \int_0^{v_{\text{esc}}} d^3\vec{v}\, \exp\left[\frac{-v^2}{2\sigma_v^2}\right]. \tag{G.13}$$

The integral (G.13) can be derived by using spherical coordinates and Feynman's trick applied on the exponential function

$$\frac{d}{dI} \exp\Big[-I^2v^2\Big] = (-2Iv^2) \exp\Big[-I^2v^2\Big] \longleftrightarrow v^2 \exp\Big[-I^2v^2\Big] = -\frac{1}{2I}\frac{d}{dI} \exp\Big[-I^2v^2\Big], \tag{G.14}$$

where $I = 1/v_0$. Then, the normalization constant is given by

$$\begin{aligned}
N_{esc} &= \frac{1}{(2\pi\sigma_v^2)^{3/2}} \int d^3\vec{v}\, \exp\left[\frac{-v^2}{2\sigma_v^2}\right] = \frac{4}{\sqrt{\pi} v_0^3} \int_0^{v_{esc}} d\vec{v}\, v^2 \exp\left[\frac{-v^2}{v_0^2}\right] = \frac{4I^3}{\sqrt{\pi}} \int_0^{v_{esc}} d\vec{v}\, v^2 \exp\Big[-I^2v^2\Big] \\
&= -\frac{2I^2}{2\sqrt{\pi}} \frac{d}{dI} \left(\int_0^{v_{\text{esc}}} d\vec{v} \exp\Big[-I^2v^2\Big] \right) = -\frac{2I^2}{\sqrt{\pi}} \frac{d}{dI} \left(\frac{1}{I} \frac{\sqrt{\pi}}{2} \operatorname{erf}[Iv_{\text{esc}}] \right) = -I^2 \frac{d}{dI} \left(\frac{1}{I} \operatorname{erf}[Iv_{\text{esc}}] \right) \\
&= -I^2 \left(-\frac{1}{I^2} \operatorname{erf}[Iv_{\text{esc}}] + \frac{1}{I} \frac{2v_{\text{esc}}}{\sqrt{\pi}} \exp\Big[-I^2v_{\text{esc}}^2\Big] \right) = \operatorname{erf}[Iv_{\text{esc}}] - I \frac{2v_{\text{esc}}}{\sqrt{\pi}} \exp\Big[-I^2v_{\text{esc}}^2\Big] \\
&= \operatorname{erf}\left[-\frac{v_{\text{esc}}}{v_0}\right] - \frac{2}{\sqrt{\pi}} \frac{v_{\text{esc}}}{v_0} \exp\left[-\frac{v_{\text{esc}}^2}{v_0^2}\right],
\end{aligned} \tag{G.15}$$

where the substitution $v' = Iv$ was performed and

$$\frac{2}{\sqrt{\pi}} \int_0^{Iv_{\text{esc}}} d\vec{v}\,' \exp\Big[-v'^2\Big] = \operatorname{erf}[Iv_{\text{esc}}], \quad \frac{d}{dI} \operatorname{erf}[Iv_{\text{esc}}] = \frac{2v_{\text{esc}}}{\sqrt{\pi}} \exp\Big[-I^2v_{\text{esc}}^2\Big]. \tag{G.16}$$

References

[1] T. Aoyama, M. Hayakawa, T. Kinoshita, and M. Nio, "Tenth-order electron anomalous magnetic moment: Contribution of diagrams without closed lepton loops," *Phys. Rev. D - Part. Fields, Gravit. Cosmol.* **91** no. 3, (2015) , `arXiv:1412.8284`.

[2] P. J. Mohr, B. N. Taylor, and D. B. Newell, "CODATA recommended values of the fundamental physical constants: 2010," *Rev. Mod. Phys.* **84** no. 4, (2012) 1527–1605, `arXiv:1203.5425`.

[3] H. Neufeld, "Anomalous magnetic moments of $e^{\pm}$ and $\mu^{\pm}$," University of Vienna. `https://particle.univie.ac.at/studies/documents-for-download/`.

[4] D. Hanneke, S. Fogwell, and G. Gabrielse, "New measurement of the electron magnetic moment and the fine structure constant," *Phys. Rev. Lett.* **100** no. 12, (Jan, 2008) , `arXiv:0801.1134`.

[5] G. Aad, T. Abajyan, and B. Abbott et al., "Observation of a new particle in the search for the Standard Model Higgs boson with the ATLAS detector at the LHC," *Phys. Lett. Sect. B Nucl. Elem. Part. High-Energy Phys.* **716** no. 1, (Jul, 2012) 1–29, `arXiv:1207.7214`.

[6] C. Mariotti, "Observation of a new boson at a mass of 125 GeV with the CMS experiment at the LHC," in *13th Marcel Grossmann Meet. Recent Dev. Theor. Exp. Gen. Relativ. Astrophys. Relativ. F. Theor. - Proc. MG13 Meet. Gen. Relativ. 2012*, no. 210699, pp. 352–372. 2015. `arXiv:1207.7235`.

[7] P. W. Higgs, "Broken symmetries and the masses of gauge bosons," *Phys. Rev. Lett.* **13** no. 16, (1964) 508–509. `https://doi.org/10.1103/PhysRevLett.13.508`.

[8] F. Englert and R. Brout, "Broken symmetry and the mass of gauge vector mesons," *Phys. Rev. Lett.* **13** no. 9, (1964) 321–323.

[9] G. S. Guralnik, C. R. Hagen, and T. W. B. Kibble, "Global conservation laws and massless particles," *Phys. Rev. Lett.* **13** no. 20, (1964) 585–587.

[10] T. W. B. Kibble, "Symmetry breaking in non-Abelian gauge theories," *Phys. Rev.* **155** no. 5, (1967) 1554–1561.

[11] S. Weinberg, "A model of leptons," *Phys. Rev. Lett.* **19** no. 21, (1967) 1264–1266.

[12] A. Salam and J. C. Ward, "Weak and electromagnetic interactions," *Nuovo Cim. Ser. 10* **11** no. 4, (1959) 568–577.

[13] ATLAS Collaboration, "Standard Model." `https://atlas.cern/discover/physics`.

[14] X. J. Bi, P. F. Yin, and Q. Yuan, "Status of dark matter detection," *Front. Phys.* **8** no. 6, (Sep, 2013) 794–827, `arXiv:1409.4590`.

[15] P. Gondolo and G. Gelmini, "Cosmic abundances of stable particles: Improved analysis," *Nucl. Physics, Sect. B* **360** no. 1, (1991) 145–179.

[16] E. W. Kolb and M. S. Turner, *The Early Universe.* Front.Phys. 69, 1990.

[17] A. Caputo, L. Sberna, and M. Frías et al., "Constraints on millicharged dark matter and axionlike particles from timing of radio waves," *Phys. Rev. D* **100** no. 6, (2019) , `arXiv:1902.02695`.

[18] J. M. Cline, Z. Liu, and W. Xue, "Millicharged atomic dark matter," *Phys. Rev. D - Part. Fields, Gravit. Cosmol.* **85** no. 10, (2012) , `arXiv:1201.4858`.

[19] A. Berlin, N. Blinov, and G. et al. Krnjaic, "Dark matter, millicharges, axion and scalar particles, gauge bosons, and other new physics with LDMX," *Phys. Rev. D* (2019) , `arXiv:1807.01730`.

[20] C. Creque-Sarbinowski, L. Ji, E. D. Kovetz, and M. Kamionkowski, "Direct millicharged dark matter cannot explain the EDGES signal," *Phys. Rev. D* **100** no. 2, (2019) 1–7, `arXiv:1903.09154`.

[21] M. Schumann, "Direct detection of WIMP dark matter: concepts and status," *J. Phys. G Nucl. Part. Phys.* **46** no. 10, (2019) 103003, `arXiv:1903.03026`.

[22] J. Conrad, "Indirect Detection of WIMP Dark Matter: a compact review," `arXiv:1411.1925`.

[23] F. S. Queiroz, "Dark Matter Overview: Collider, Direct and Indirect Detection Searches," `arXiv:1605.08788`.

[24] X. C. E. Aprile, "The XENON Dark Matter Search," `arXiv:astro-ph/0502279v1`.

[25] C. Ghag, "The LUX direct dark matter search experiment," `arXiv:1412.4660`.

[26] L. Stodolsky, G. Angloher, and M. et al. Bauer, "The CRESST II dark matter search," *J. Phys. Conf. Ser.* **384** no. 1, (2012) , `arXiv:1203.6835`.

[27] Y. Cui, M. Pospelov, and J. Pradler, "Signatures of dark radiation in neutrino and dark matter detectors," *Phys. Rev. D* **97** no. 10, (2018) , `arXiv:1711.04531`.

[28] F. Zwicky, "The Redshift of Extragalactic Nebulae (Die Rotverschiebung von extragalaktischen Nebeln)," *Publ. Helv. Phys. Acta* (1933) 110–127.

[29] V. C. Rubin and J. Ford, W. Kent, "Rotation of the Andromeda Nebula from a Spectroscopic Survey of Emission Regions," *Astrophys. J.* **159** (1970) 379.

[30] J. Schieck and H. Kluck, *Dark Matter*. Lecture notes, Technical University of Vienna.

[31] Particle Data Group, "Physical Constants," 2015. `http://pdg.lbl.gov/2018/reviews/rpp2018-rev-phys-constants.pdf`.

[32] E. Corbelli and P. Salucci, "The extended rotation curve and the dark matter halo of M33," *Mon. Not. R. Astron. Soc.* **311** no. 2, (2000) 441–447, `arXiv:astro-ph/9909252`.

[33] H. Hoekstra, M. Bartelmann, and H. Dahle et al., "Masses of galaxy clusters from gravitational lensing," *Space Sci. Rev.* **177** no. 1-4, (2013) 75–118, `arXiv:1303.3274`.

[34] E. Van Uitert, H. Hoekstra, and T. Schrabback et al., "Constraints on the shapes of galaxy dark matter haloes from weak gravitational lensing," *Astron. Astrophys.* **545** (2012) , `arXiv:1206.4304`.

[35] P. A. Ade, N. Aghanim, and M. Arnaud eta al., "Planck 2015 results: XIII. Cosmological parameters," *Astron. Astrophys.* **594** (2016) , `arXiv:1502.01589`.

[36] M. Cirelli, G. Corcella, and A. Hektor et al., "PPPC 4 DM ID: A poor particle physicist cookbook for dark matter indirect detection," *J. Cosmol. Astropart. Phys.* **2011** no. 3, (2011) , `arXiv:1012.4515`.

[37] J. F. Navarro, C. S. Frenk, and S. D. M. White, "The Structure of Cold Dark Matter Halos," *Astrophys. J.* **462** (1996) 563–575, `arXiv:astro-ph/9508025`. `http://adsabs.harvard.edu/doi/10.1086/177173%7D%7Bdoi:10.1086/177173`.

[38] M. Franx, "Structure of Dark Matter halos,".
`https://home.strw.leidenuniv.nl/$\sim$franx/college/galaxies10/handout4.pdf`.

[39] A. Friedmann, "Über die Möglichkeit einer Welt mit konstanter negativer Krümmung des Raumes," *Zeitschrift für Phys.* **21** no. 1, (1924) 326–332.
`https://doi.org/10.1007/BF01328280`.

[40] A. G. Lematre, "A Homogeneous Universe of Constant Mass and Increasing Radius accounting for the Radial Velocity of Extra-galactic Nebulae," *Mon. Not. R. Astron. Soc.* **91** no. 5, (1931) 483–490. `https://doi.org/10.1093/mnras/91.5.483`.

[41] J. Binney and S. Tremaine, *Galactic dynamics: Second Edition.* Princeton University Press, 2011.

[42] H. Wei, X. B. Zou, H. Y. Li, and D. Z. Xue, "Cosmological constant, fine structure constant and beyond," *Eur. Phys. J. C* **77** no. 1, (2017) , `arXiv:1605.04571`.

[43] Particle Data Group, "Astrophysical Constants and Parameters."
`http://pdg.lbl.gov/2019/reviews/rpp2018-rev-astrophysical-constants.pdf`.

[44] R. Jimenez, A. Cimatti, and L. Verde et al., "The local and distant Universe: Stellar ages and H_0," *J. Cosmol. Astropart. Phys.* **2019** no. 3, (2019) , `arXiv:1902.07081`.

[45] Planck Collaboration, "Planck 2018 results. VI. Cosmological parameters,"
`arXiv:1807.06209`. `http://arxiv.org/abs/1807.06209`.

[46] A. G. Riess, S. Casertano, and W. Yuan et al., "New Parallaxes of Galactic Cepheids from Spatially Scanning the Hubble Space Telescope : Implications for the Hubble Constant," *Astrophys. J.* **855** no. 2, (2018) 136, `arXiv:1801.01120`.

[47] B. P. Abbott, R. Abbott, and T. D. Abbott et al., "A gravitational-wave standard siren measurement of the Hubble constant," *Nature* **551** no. 7678, (2017) 85–98, `arXiv:1710.05835`.

[48] L. Verde, P. Protopapas, and R. Jimenez, "The expansion rate of the intermediate universe in light of Planck," *Phys. Dark Universe* **5-6** no. C, (2014) 307–314, `arXiv:1403.2181`.

[49] B. S. Haridasu, V. V. Luković, M. Moresco, and N. Vittorio, "An improved model-independent assessment of the late-time cosmic expansion," *J. Cosmol. Astropart. Phys.* **2018** no. 10, (2018) , `arXiv:1805.03595`.

[50] M. Tanabashi, K. Hagiwara, and K. Hikasa et al., "Review of Particle Physics," 2018.

[51] Y. F. Perez-Gonzalez, "Massive Neutrinos: Phenomenological and Cosmological Consequences," `arXiv:1712.06675`.

[52] L. Landau, E. Lifshitz, and L. Pitaevskij, *Course of theoretical physics. vol. 10: Physical kinetics.* 1981.

[53] D. G. Cerdeno, "DARK MATTER 101: From production to detection,".

[54] S. R. de Groot, W.A. van Leeuwen, and Ch.G. van Weert, *Relativistic kinetic theory : principles and applications.* Amsterdam ; New York : North-Holland Pub. Co. ; New York : sole distributors for the USA and Canada, Elsevier North-Holland, 1980.

[55] K. Griest, "The Net Advance of Physics: The Nature of Dark Matter." `http://web.mit.edu/$%5Csim$redingtn/www/netadv/specr/6/node3.html#SECTION00012000000000000000`.

[56] T. Wrase, *Cosmology and particle physics.* Lecture notes, lecture 6, Technical University of Vienna, 2016.
`http://hep.itp.tuwien.ac.at/$\sim$wrasetm/files/2016S-Lecture-06.pdf`.

[57] P. F. de Salas, S. Gariazzo, and O. Mena et al., "Neutrino Mass Ordering from Oscillations and Beyond: 2018 Status and Future Prospects," *Front. Astron. Sp. Sci.* **5** (2018) , `arXiv:1806.11051`.

[58] P. D. Serpico, "Introduction to Particle cosmology Wimp paradigm, freeze out (and beyond)," GRASPA School. 2017. `https://indico.in2p3.fr/event/14268/contributions/17512/attachments/14514/17779/Astroparticle_th_SERPICO2.pdf`.

[59] V. Belokurov, *Stellar Dynamics and Structure of Galaxies, Jeans Theorem.* Lent term, Institute of Astronomy, 2016.
`https://www.ast.cam.ac.uk/$\sim$vasily/Lectures/SDSG/sdsg_6_dfs.pdf`.

[60] M. Lisanti, "Lectures on Dark Matter Physics," in *New Front. Fields Strings*, pp. 399–446. 2017. `arXiv:1603.03797v2`.

[61] V. A. Naumov, "Solar neutrinos. Astrophysical aspects," *Phys. Part. Nucl. Lett.* **8** (2011) 683–703.

[62] Q. R. Ahmad, R. C. Allen, and T. C. Andersen et al., "Direct Evidence for Neutrino Flavor Transformation from Neutral-Current Interactions in the Sudbury Neutrino Observatory," *Phys. Rev. Lett.* **89** no. 1, (2002) , `arXiv:nucl-ex/0204008`.

[63] W. C. Haxton, R. G. H. Robertson, and A. M. Serenelli, "Solar Neutrinos: Status and Prospects," *Annu. Rev. Astron. Astrophys.* **51** (Aug, 2012) 21–61, `arXiv:1208.5723`.

[64] M. Wiescher, J. Görres, and E. Uberseder et al., "The Cold and Hot CNO Cycles," *Annu. Rev. Nucl. Part. Sci.* **60** no. 1, (2010) 381–404.

[65] T. Kajita, "Atmospheric Neutrinos," *Adv. High Energy Physics, Artic. ID 504715* **2012** (2012) 24. `https://doi.org/10.1155/2012/504715`.

[66] T. K. Gaisser and M. Honda, "Flux of Atmospheric Neutrinos," *Annu. Rev. Nucl. Part. Sci.* **52** no. 1, (2002) 153–199, `arXiv:hep-ph/0203272`.

[67] R. Enberg, "High energy neutrinos from the atmosphere and astrophysical sources," Uppsala University, NuHoRIzons 09.

[68] C. R. Nave, "Kaons," *Hyperphysics (©C.R. Nave, 2017)* .
`http://hyperphysics.phy-astr.gsu.edu/hbase/Particles/kaon.html#c1`.

[69] S. A. Qetina, T. Conka-Nurdana, and A. Mailova, "MUON LIFETIME MEASUREMENT," *8th ICFA Instrum. Sch. Istanbul - Turkey,* (1999) .

[70] T. K. Gaisser, "Fluxes of atmospheric neutrinos and related cosmic rays," *Nucl. Phys. B - Proc. Suppl.* **77** no. 1-3, (1999) 133–139.

[71] D. C. et al. J. C. Arteaga-Velázquez, K. S. Caballero Mora, "Cosmic Ray Physics at MATHUSLA," *twiki.cern.ch* . `https://twiki.cern.ch/twiki/pub/MATHUSLA/MATHUSLAPublic/cosmic-ray-physics_MATHUSLA.pdf`.

[72] A. Schukraft, "A view of prompt atmospheric neutrinos with IceCube," in *Nucl. Phys. B - Proc. Suppl.*, vol. 237-238, pp. 266–268. 2013. `arXiv:1302.0127`.

[73] J. Bahcall, "Solar Neutrinos-software and data." `http://www.sns.ias.edu/$\sim$jnb/`.

[74] G. Battistoni, A. Ferrari, T. Montaruli, and P. R. Sala, "The atmospheric neutrino flux below 100 MeV: The FLUKA results," *Astropart. Phys.* **23** no. 5, (2005) 526–534.

[75] A. Gütlein, *Feasibility Study for a First Observation of Coherent Neutrino Nucleus Scattering Using Low-Temperature Detectors.* PhD thesis, Technical University Munich, 2013.

[76] G. B. Gelmini, V. Takhistov, and S. J. Witte, "Casting a wide signal net with future direct dark matter detection experiments," *J. Cosmol. Astropart. Phys.* **2018** no. 7, (2018) , `arXiv:1804.01638`.

[77] J. Billard, E. Figueroa-Feliciano, and L. Strigari, "Implication of neutrino backgrounds on the reach of next generation dark matter direct detection experiments," *Phys. Rev. D - Part. Fields, Gravit. Cosmol.* **89** no. 2, (2014) , `arXiv:1307.5458`.

[78] S. N. Ahmed, A. E. Anthony, and E. W. Beier et al., "Measurement of the total active 8 B solar neutrino flux at the Sudbury Neutrino Observatory with enhanced neutral current sensitivity," *Phys. Rev. Lett.* **92** no. 18, (2004) , `arXiv:nucl-ex/0309004`.

[79] B. Aharmim, S. N. Ahmed, and J. F. Amsbaugh et al., "Measurement of the νe and total 8B solar neutrino fluxes with the Sudbury Neutrino Observatory phase-III data set," *Phys. Rev. C - Nucl. Phys.* **87** no. 1, (2013) , `arXiv:1107.2901`.

[80] A. M. Serenelli, W. C. Haxton, and C. Pa-Garay, "Solar models with accretion. I. Application to the solar abundance problem," *Astrophys. J.* **743** no. 1, (2011) , `arXiv:1104.1639`.

[81] M. Koshiba, "Observation of neutrinos from SN1987A by Kamiokande-II," *ESO Work. SN 1987A, Garching, Fed. Repub. Ger. July 6-8, 1987, Proc. (A88-35301 14-90). Garching, Fed. Repub. Ger. Eur. South. Obs. 1987, p. 219-227; Discuss. p. 228. MOESC-supported Res.* . `http://adsabs.harvard.edu/full/1987ESOC...26..219K`.

[82] K. S. Hirata, T. Kajita, and M. Koshiba et al., "Observation in the Kamiokande-II detector of the neutrino burst from supernova SN1987A," *Phys. Rev. D* **38** no. 2, (1988) 448–458. `https://doi.org/10.1103/PhysRevD.38.448`.

[83] M. Koshiba, K. Hirata, and T. Kajita et al., "Supernova neutrino signal and kamiokande-II," *Nucl. Phys. B - Proc. Suppl.* **3** (1988) 441–451. `https://doi.org/10.1016/0920-5632(88)90195-8`.

[84] R. M. Bionta, G. Blewitt, and C. B. Bratton et al., "Observation of a neutrino burst in coincidence with supernova 1987A in the large magellanic cloud," *Phys. Rev. Lett.* **58** no. 14, (1987) 1494–1496. `https://doi.org/10.1103/PhysRevLett.58.1494`.

[85] C. B. Bratton, D. Casper, and A. Ciocio et al., "Angular distribution of events from SN1987A," *Phys. Rev. D* **37** no. 12, (1988) 3361–3363. `https://journals.aps.org/prd/abstract/10.1103/PhysRevD.37.3361`.

[86] J. F. Beacom, "The Diffuse Supernova Neutrino Background," *Annu. Rev. Nucl. Part. Sci.* **60** no. 1, (2010) 439–462, `arXiv:1004.3311`.

[87] M. Malek, M. Morii, and S. Fukuda et al., "Search for Supernova Relic Neutrinos at Super-Kamiokande," *Phys. Rev. Lett.* **90** no. 6, (2003) 5, `arXiv:hep-ex/0209028`.

[88] R. J. Hall, *Where do Type II Supernovae come from?* PhD thesis, CTA-UK. `https://www.cta-observatory.ac.uk/?page_id=1137`.

[89] G. Raffelt, *Stars as Laboratories for Fundamental Physics.* University of Chicago Press, 1996.

[90] K. A. Williams, M. Bolte, and D. Koester, "Probing the lower mass limit for supernova progenitors and the high-mass end of the initial-final mass relation from white dwarfs in the open cluster M35 (NGC 2168)," *Astrophys. J.* **693** no. 1, (2009) 355–369, `arXiv:0811.1577`.

[91] M. van Biezen, "Lecture 8: What Is A Type 2 Supernova Explosion?" `http://www.ilectureonline.com/lectures/subject/ASTRONOMY/2/78/255`.

[92] M. Herant, S. A. Colgate, W. Benz, and C. Fryer, "Neutrinos and Supernovae," *Los Alamos Sci. Number* **25** (1997) . `https://library.lanl.gov/cgi-bin/getfile?00326615.pdf`.

[93] G. E. Brown, H. Bethe, and G. Baym, "Supernova Theory," *Nucl. Phys. A* **375** (1982) 481–532. `https://doi.org/10.1016/0375-9474(82)90025-2`.

[94] T. J. MazurekJ. W. TruranA. G. W. Cameron, "Electron capture in carbon dwarf supernovae," *Astrophys. Space Sci.* **27** no. 2, (1974) 261–291. `https://doi.org/10.1007/BF00643877`.

[95] S. Ando and K. Sato, "Relic neutrino background from cosmological supernovae," *New J. Phys.* **6** (2004) 170, `arXiv:astro-ph/0410061v2`.

[96] R. Möllenberg, F. Von Feilitzsch, D. Hellgartner, L. Oberauer, M. Tippmann, V. Zimmer, J. Winter, and M. Wurm, "Detecting the diffuse supernova neutrino background with LENA," *Phys. Rev. D - Part. Fields, Gravit. Cosmol.* **91** no. 3, (2015) , `arXiv:1409.2240`.

[97] S. Horiuchi, J. F. Beacom, and E. Dwek, "Diffuse supernova neutrino background is detectable in Super-Kamiokande," *Phys. Rev. D - Part. Fields, Gravit. Cosmol.* **79** no. 8, (2009) , `arXiv:0812.3157`.

[98] S. J. Smartt, J. J. Eldridge, R. M. Crockett, and J. R. Maund, "The death of massive stars - I. Observational constraints on the progenitors of Type II-P supernovae," *Mon. Not. R. Astron. Soc.* **395** no. 3, (2009) 1409–1437, `arXiv:0809.0403`.

[99] A. M. Hopkins, "On the Evolution of Starforming Galaxies," *Astrophys. J.* **615** no. 1, (2004) 209–221, `arXiv:astro-ph/0407170v1`.

[100] A. M. Hopkins, "The Star Formation History of the Universe," `arXiv:astro-ph/0611283v1`.

[101] L. Riguccini, E. Le Floc'H, and O. Ilbert et al., "Dust-obscured star formation and the contribution of galaxies escaping UV/optical color selections at z $\sim$ 2," *Astron. Astrophys.* **534** (2011) . `https://doi.org/10.1051/0004-6361/201116950`.

[102] P. A. James, J. H. Knapen, and N. S. Shane et al., "The Hα Galaxy survey," *Astron. Astrophys.* **482** no. 2, (2008) 507–516, `arXiv:0802.4421v1`.

[103] A. M. Hopkins and J. F. Beacom, "On the Normalization of the Cosmic Star Formation History," *Astrophys. J.* **651** no. 1, (2006) 142–154, `arXiv:astro-ph/0601463`.

[104] T. Totani, K. Sato, H. E. Dalhed, and J. R. Wilson, "Future Detection of Supernova Neutrino Burst and Explosion Mechanism," *Astrophys. J.* **496** no. 1, (1998) 216–225, `arXiv:astro-ph/9710203`.

[105] J. M. Lattimer and M. Prakash, "Neutron star observations: Prognosis for equation of state constraints," *Phys. Rep.* **442** no. 1-6, (2007) 109–165, `arXiv:astro-ph/0612440`.

[106] J. M. Weisberg and J. H. Taylor, "Relativistic Binary Pulsar B1913+16: Thirty Years of Observations and Analysis," *ASP Conf. Ser. Vol. TBD, 2004* , `arXiv:astro-ph/0407149`.

[107] LIGO Scientific Collaboration Virgo Collaboration, "GW170817: Measurements of Neutron Star Radii and Equation of State," *Phys. Rev. Lett.* **121** no. 16, (2018) , `arXiv:1805.11581`.

[108] J. F. Beacom and L. E. Strigari, "New test of supernova electron neutrino emission using Sudbury Neutrino Observatory sensitivity to the diffuse supernova neutrino background," *Phys. Rev. C - Nucl. Phys.* **73** no. 3, (2006) , arXiv:hep-ph/0508202.

[109] G. Rajasekaran, "The Story of the Neutrino," arXiv:1606.08715.

[110] A. Nath and N. K. Francis, "Detection techniques and investigation of different neutrino experiments," arXiv:1804.08467.

[111] J. Chadwick, "Possible existence of a neutron," *Nature* **129** no. 3252, (1932) . https://doi.org/10.1038/129312a0.

[112] C. Nave, "Cowan and Reines Neutrino Experiment," *Hyperphysics (©C.R. Nave, 2017)* . http://hyperphysics.phy-astr.gsu.edu/hbase/Particles/cowan.html.

[113] B. T. Cleveland, T. Daily, and R. Davis Jr. et al., "Measurement of the Solar Electron Neutrino Flux with the Homestake Chlorine Detector," *Astrophys. J.* **496** no. 1, (1998) 505–526.

[114] W. Hampel, J. Handt, and G. Heusser et al., "GALLEX solar neutrino observations: Results for GALLEX IV," *Phys. Lett. Sect. B Nucl. Elem. Part. High-Energy Phys.* **447** no. 1-2, (1999) 127–133.

[115] SAGE Collaboration, "Measurement of the solar neutrino capture rate with gallium metal," *Phys. Rev. C - Nucl. Phys.* **60** no. 5, (1999) 32, arXiv:astro-ph/9907113.

[116] G. Ranucci, "Techniques and methods for the low-energy neutrino detection," *Eur. Phys. J. A* **52** no. 4, (Apr, 2016) 79. http://link.springer.com/10.1140/epja/i2016-16079-0.

[117] Casper Berkeley, "Cherenkov Radiation," *Astrobaki* (2017) . https://casper.ssl.berkeley.edu/astrobaki/index.php/Cherenkov_Radiation.

[118] A. A. Watson, "The discovery of Cherenkov radiation and its use in the detection of extensive air showers," *Nucl. Phys. B - Proc. Suppl.* **212-213** (2011) 13–19, arXiv:1101.4535. https://doi.org/10.1016/j.nuclphysbps.2011.03.003.

[119] PhysicsOpenLab, "DIY Water Cherenkov Detector," 2016. http://physicsopenlab.org/2016/04/24/diy-cherenkov-detector/.

[120] M. Krammer, "Scintillators." https://www.hephy.at/fileadmin/user_upload/VO-5-Scintillators.pdf.

[121] M. Krammer, "Calorimeter," Institute of High Energy Physics, Vienna, Austria. https://www.hephy.at/fileadmin/user_upload/VO-6-Calorimeters.pdf.

[122] P. Adamson, K. V. Alexandrov, and G. Alexeev et al., "The MINOS scintillator calorimeter system," *IEEE Trans. Nucl. Sci.* **49** no. 3, (2002) 861–863. https://doi.org/10.1109/NSSMIC.2000.949199.

[123] J. J. Evans, "The MINOS experiment: Results and prospects," *Adv. High Energy Phys.* **2013** (2013) , arXiv:1307.0721.

[124] C. Rubbia, "The Liquid Argon Time Projection Chamber: A New Concept for Neutrino Detectors," *Eur. Organ. Nucl. Res. Cern.* (1977) .

[125] M. Miyajima, T. Takahashi, and S. Konno et al., "Average energy expended per ion pair in liquid argon," *Phys. Rev. A* **9** no. 3, (1974) 1438–1443.

[126] T. Katori, "MicroBooNE, a Liquid Argon Time Projection Chamber (LArTPC) neutrino experiment," in *AIP Conf. Proc.*, vol. 1405, pp. 250–255. 2011. arXiv:1107.5112.

[127] S. Freeman, "FORM FACTORS: Notes and Examples,". https://personalpages.manchester.ac.uk/staff/Sean.Freeman/pc3121/formfactors.pdf.

[128] R. H. Helm, "Inelastic and elastic scattering of 187-MeV electrons from selected even-even nuclei," *Phys. Rev.* **104** no. 5, (1956) 1466–1475. https://doi.org/10.1103/PhysRev.104.1466.

[129] B. Povh, K. Rith, C. Scholz, and F. Zetsche, *Particles and nuclei: an introduction to the physical concepts.* Springer, 5th ed ed., 2006.

[130] G. Dda, A. Kemper, and P. Gondolo, "Model-independent form factors for spin-independent neutralino-nucleon scattering from elastic electron scattering data," *J. Cosmol. Astropart. Phys.* no. 4, (2007) , arXiv:hep-ph/0608035.

[131] Y. Z. Chen, Y. A. Luo, L. Li, H. Shen, and X. Q. Li, "Determining nuclear form factor for detection of dark matter in relativistic mean field theory," *Commun. Theor. Phys.* **55** no. 6, (2011) 1059–1064, arXiv:1101.3049.

[132] J. ENGEL, S. PITTEL, and P. VOGEL, "Nuclear Physics of Dark Matter Detection," *Int. J. Mod. Phys. E* **01** no. 01, (1992) 1–37.

[133] L. Baudis, "Dark Matter Lecture 2: Principles of direct WIMP detection," 2009. http://fma.if.usp.br/$\sim$burdman/DM/Laura_2.pdf.

[134] N. Weiner, "Understanding Dark Matter." https://cosmo.nyu.edu/$\sim$nealw/styled-5/.

[135] J. Kopp, T. Schwetz, and J. Zupan, "Global interpretation of direct Dark Matter searches after CDMS-II results," *J. Cosmol. Astropart. Phys.* **2010** no. 2, (2010) , arXiv:0912.4264.

[136] J. R. Ellis, K. A. Olive, and C. Savage et al., "Hadronic uncertainties in the elastic scattering of supersymmetric dark matter," *Phys. Rev. D* **77** (2008) , arXiv:0801.3656.

[137] S. Scopel, K. H. Yoon, and J. H. Yoon, "Generalized spin-dependent WIMP-nucleus interactions and the DAMA modulation effect," *J. Cosmol. Astropart. Phys.* **2015** no. 7, (2015) , arXiv:1505.01926. https://doi.org/10.1088%2F1475-7516%2F2015%2F07%2F041.

[138] L. Baudis, "Direct detection of WIMPs," COSMO 2014, Chicago. 2014. http://cosmo2014.uchicago.edu/depot/invited-talk-baudis-laura.pdf.

[139] K. Freese, M. Lisanti, and C. Savage, "Colloquium: Annual modulation of dark matter," *Rev. Mod. Phys.* **85** no. 4, (2013) 1561–1581, arXiv:1209.3339.

[140] R. Bernabei, P. Belli, and F. Cappella et al., "First results from DAMA/LIBRA and the combined results with DAMA/NaI," *Eur. Phys. J. C* **56** no. 3, (2008) 333–355, arXiv:0804.2741.

[141] R. Bernabei, P. Belli, and A. Di Marco et al., "DAMA/LIBRA at Gran Sasso," *Phys. Procedia* **37** (2012) 1095–1104. https://doi.org/10.1016/j.phpro.2012.03.731.

[142] COSINE-100 Dark Matter Experiment, "Annual Modulation of Dark Matter." https://cosine.yale.edu/about-us/annual-modulation-dark-matter.

[143] LUX Collaboration, "First results from the LUX dark matter experiment at the sanford underground research facility," *Phys. Rev. Lett.* **112** no. 9, (2014) , arXiv:1310.8214.

[144] I. O. Samblas, "Projected sensitivity of the LUX-ZEPLIN experiment to WIMP dark matter," Preparing for Dark Matter Particle Discovery, Chalmers University, Göteborg, Imperial College London, 2018. https://indico.cern.ch/event/666809/contributions/3029006/attachments/1667168/2673937/LZsens_Chalmers_Ibles.pdf.

[145] C. collaboration, "First results on low-mass dark matter from the CRESST-III experiment," *Conf. C17-07-24* (2017) 6, arXiv:1711.07692.

[146] G. Cowan, *Statistical Data Analysis.* Oxford University Press Inc., New York, 1998. http://www.oup.co.uk/.

[147] P. J. Bickel and K. A. Doksum, *Mathematical statistics: Basic ideas and selected topics, Vol. 2*, vol. 1. Chapman and Hall/CRC, 2nd ed., 2015.

[148] S. Zheng, "Likelihood Ratio Tests," Lecture notes, Math 541: Statistical Theory II. Missouri State University.

[149] M. L. King, "Hypothesis testing in the presence of nuisance parameters," *J. Stat. Plan. Inference* **50** no. 1, (1996) 103–120. https://www.sciencedirect.com/science/article/pii/0378375895000488?via%5C%3Dihub.

[150] T. Junk, "Sensitivity, Exclusion and Discovery with Small Signals, LargeBackgrounds, and Large Systematic Uncertainties," *CDF-8128, CDF-Note-8128* (2006) . http://inspirehep.net/record/1361506/.

[151] G. Cowan, "Some Statistical Tools for Particle Physics," Particle Physics Colloquium, MPI für Physik u. Astrophysik, Munich, 2016.

[152] S. S. Wilks, "The Large-Sample Distribution of the Likelihood Ratio for Testing Composite Hypotheses," *Ann. Math. Stat.* **9** no. 1, (1938) 60–62. http://dx.doi.org/10.1155/2011/968283.

[153] XENON Collaboration, "First Dark Matter Search Results from the XENON1T Experiment," *Phys. Rev. Lett.* **119** (2017) , arXiv:1705.06655. https://doi.org/10.1103/PhysRevLett.119.181301.

[154] J. Pradler, "The photon as new physics mediator," *Humboldt Kolleg, Discov. Open Puzzles Part. Phys. Gravitation, Kitzbühel* . https://indico.cern.ch/event/808763/contributions/3447467/.

[155] L. Bergstrom, P. Ullio, C. Lacey, and J. Edsjö, "Cosmological dark matter annihilations into γ rays: A closer look," *Phys. Rev. D* **66** (2002) , arXiv:astro-ph/0207125. https://doi.org/10.1103/PhysRevD.66.123502.

[156] V. Poulin, P. D. Serpico, and J. Lesgourgues, "A fresh look at linear cosmological constraints on a decaying Dark Matter component," *J. Cosmol. Astropart. Phys.* **2016** no. 8, (2016) , arXiv:1606.02073. https://doi.org/10.1088%2F1475-7516%2F2016%2F08%2F036.

[157] P. T. Crusciel, "General Relativity II," Lecture notes, University of Vienna. https://homepage.univie.ac.at/piotr.chrusciel/publications/publications.html.

[158] C. Garcia-Cely and J. Heeck, "Neutrino lines from majoron dark matter," *J. High Energy Phys.* **2017** no. 5, (2017) , arXiv:1701.07209.

[159] S. Palomares-Ruiz, "Model-independent bound on the dark matter lifetime," *Phys. Lett. Sect. B Nucl. Elem. Part. High-Energy Phys.* **665** no. 1, (2008) 50–53, arXiv:0712.1937.

[160] K. Abe, Y. Hayato, and T. Iida et al., "Solar neutrino results in Super-Kamiokande-III," *Phys. Rev. D - Part. Fields, Gravit. Cosmol.* **83** no. 5, (2011) , arXiv:1010.0118.

[161] K. Bays, T. Iida, and K. Abe et al., "Supernova relic neutrino search at super-Kamiokande," *Phys. Rev. D - Part. Fields, Gravit. Cosmol.* **85** no. 5, (2012) , arXiv:1111.5031.

[162] J. A. Romeu, "Derivation of Friedman equations," *Fac. Física, Univ. Barcelona, Diagon. 645, 08028 Barcelona, Spain* .

[163] T. Wrase, "Deriving the Friedmann equations from general relativity," *Lect. notes 2017S, Inst. Theor. Physics, Vienna Univ. Technol.* . `http://hep.itp.tuwien.ac.at/$\sim$wrasetm/files/`.

[164] Fab.cba.mit.edu, "Derivation - Coordinate systems." `http://fab.cba.mit.edu/classes/863.14/people/amanda_ghassaei/finalProj/finalProj.html`.

[165] S. Zheng, "Maximum Likelihood Estimation," Missouri State University.

[166] E. Croot, "Some notes on the Poisson distribution,". `http://people.math.gatech.edu/$\sim$ecroot/3770/poisson_notes.pdf`.

[167] M. Boon, "2WB05 Simulation Lecture 8: Generating random variables," University of Technology, Eindhoven,Department of Mathematics and Computer Science, 2013. `https://www.win.tue.nl/$\sim$marko/2WB05/lecture8.pdf`.

[168] A. Pich, "The standard model of electroweak interactions," in *2007 Cern. Sch. High-Energy Physics, CLASHEP 2007 - Proc.*, pp. 1–49. 2008. `arXiv:hep-ph/0502010v1`.